

ABSTRACT

Title of dissertation: FUNCTIONAL IMAGING OF PHOTOVOLTAIC MATERIALS AT THE NANOSCALE

Elizabeth M. Tennyson, Doctor of Philosophy, 2018

Dissertation directed by: Professor Marina S. Leite
Department of Materials Science
and Engineering, Institute for Research
in Electronics and Applied Physics

The ideal photovoltaic technology for global deployment must exhibit two key attributes: (i) high power-conversion efficiency, enabling a solar panel with a large power output per area and, (ii) low-cost/W, due to either being derived from earth-abundant materials and/or ease of fabrication. For the past two decades, extensive efforts have been made to boost the efficiency of some of the most promising high performance *and* low-cost photovoltaic materials, such as CdTe, Cu(In,Ga)Se₂ (CIGS), and hybrid organic-inorganic perovskites, to achieve higher efficiency devices. However, improvement in the overall performance is still limited by the open-circuit voltage (V_{oc}). All of the solar cell materials listed above are composed of grains and grain boundaries on the order of micro- and nanometers, respectively, and their nanoscale interfaces can cause electrical charge carriers to become trapped and recombine non-radiatively, reducing the V_{oc} . Therefore, in this thesis, I implement high spatial resolution functional imaging techniques to resolve the local voltage variations in the thin-film polycrystalline and hybrid perovskites materials for pho-

tovoltaic applications.

First, I spectrally and spatially resolve the local photovoltage of CIGS solar cells through confocal optical microscopy to build a qualitative voltage tomography. From these photovoltage results, I discover variations in the electrical response of $>20\%$ that are also on the same length scale as the grains composing the CIGS material. Therefore, by enhancing the spatial resolution beyond the diffraction limit, the electronic properties of individual grains and the interfaces between the grains can be fully resolved. For this, I implement Kelvin probe force microscopy (KPFM), and demonstrate a universal method to directly map the V_{oc} of any photovoltaic material with nanoscale spatial resolution. Next, we extend this ability of KPFM to rapidly image (16 sec/map) the real-time dynamics of perovskite solar cells, which are notorious for their slow and unstable electrical output. Through fast-KPFM imaging, we discover regions within a single grain that show a residual V_{oc} response which pervades for ≈ 9 min, likely caused by a slow ion migration process. Finally, to understand how different perovskite compositions influence the behavior of the nanoscale electrical response, I utilize KPFM to realize both irreversible *and* reversible V_{oc} signals. Compiling all these results discussed above, throughout my Ph.D. I have yielded the following contributions: (i) evidence that the photovoltage of polycrystalline solar cell materials varies at the same length scale as the grains composing them, (ii) a nanoscale imaging platform to directly map the V_{oc} with unprecedented spatial resolution, and (iii) a technique to map the real-time voltage response of many perovskite compositions, ultimately indicating that the elements constituting the perovskite cation and halide positions are both directly related to

their reversible vs. irreversible electrical nature. From these contributions, I foresee the functional imaging methods developed in this thesis to be widely implemented as a diagnostic tool for the rational design of photovoltaics with enhanced electrical performance and lower cost.

FUNCTIONAL IMAGING OF PHOTOVOLTAIC MATERIALS AT THE NANOSCALE

by

Elizabeth M. Tennyson

Dissertation submitted to the Faculty of the Graduate School of the
University of Maryland, College Park, in partial fulfillment
of the requirements for the degree of
Doctorate of Philosophy
2018

Advisory Committee:
Professor Marina S. Leite, Chair/Advisor
Professor Eric D. Wachsman
Professor Richard L. Greene
Professor John Cumings
Professor Gottlieb S. Oehrlein

© Copyright by
Elizabeth M. Tennyson
2018

Acknowledgments

I would like to dedicate this Ph.D. thesis to everyone who has helped and supported me along this graduate school journey. To start, I would like express my gratitude for my adviser Prof. Marina S. Leite. Your guidance has made me a better scientist, writer, presenter, critical thinker, and researcher. You've taught me *countless* useful research skills and tips, and because of your encouragement I know that I will do well after graduate school. Although it wasn't always easy, thank you for the motivating and believing in me. I'd also like to thank the members of my Ph.D. Thesis Committee: Profs. John Cumings, Richard Greene, Gottlieb Oehrlein, and Eric Wachsman for their perspective and ideas.

To past and present Leite Lab members/friends: Chen Gong, Mariama Dias, John Howard, Zack Benson, Allen Chang, Eric Bailey, William Gunnarsson (*i.e.* Brady), Bernardo Neves, Alex Yulaev, Sabrina Curtis, Griffin Godbey, Garrett Wessler, and Zinab Jadidi. I want to express particular emphasis on Chen, who joined the Leite Lab at the same time as I did. You and I helped pioneer the lab and I am very grateful to have you by my side for that, you are/were a brilliant and excellent group member. Also, Mariama Dias, thank you! You are an incredible mentor and I am so glad to have you in my life.

To members/friends/collaborators of the Munday Lab: Joseph Garrett, Lisa Krayner, Yunlu Xu, and Joseph Murray. In particular, I owe a lot of my AFM knowledge and skills to Joe G. Thank you for being patient, a great teacher, and a kind person. I'd also like to give a special thanks Lisa for being an excellent resource and fun person to discuss research and life, with. Lastly, I'd like to thank Prof. Jeremy Munday for letting me to use his lab's instruments, tools, and optics

while Chen, Prof. Leite, and I were still building up the READ Lab.

To the other non-MSE and non-IREAP collaborators that either helped with obtaining a result or provided solar cell samples for the research performed in this Thesis. The folks at Naval Research Lab: Jesse Frantz, Jason Myers, Robel Bekele, and Jasbinger Sanghera. University of Nebraska: Jinsong Huang and Miao Hu. From UMD Aerospace department: Suok-Min Na. From ORNL/CNMS: Liam Collins, Alison Pawlicki, Anton Ievlev, and Stephen Jesse. From HZB: Antonio Abate. From the University of Cambridge: Bart Roose, Mojtaba Abdi Jalebi, Kangyu Ji, and Sam Stranks.

There are also many staff members at the University of Maryland who deserve my gratitude for helping me with research challenges, health care logistics, pay roll, etc. From the MSE Department: Kathleen Hart, Nina Morris (Kay), Mike McNicholas, and Patricia Lorenzana. From SAC: Karen Gaskell. From IREAP: Nolan Ballew, Jay Pyle, Nancy Boone, Dottie Brosius (special shout out for hosting me at Thanksgiving 2016!), Ed Condon, Judi Gorski, Kathryn Tracey Metzler, Taylor Prendergast, and Bryan Quinn. The Nanocenter: Valery Ray, Mark Lecates, Jon Hummel, John Abrahams (rock on), and Tom Loughran (who also always made a special effort to check up on my family).

To UMD-MSE Alumni who proved to me that graduation was possible and provided me with some excellent guidance, advice, and exclusive resources: Travis Dietz, Romaine Isaacs, Josh Taillon, Wonseok Hwang, Sean Fackler, Norvik Voskarian, Dominik Metzler, Jasper Drisko, Rick Suchoski, Alex Kozen, Greg Hitz, Elliot Bartis, Thomas Hays, Adam Jolley, Matthew Murray, Eric Rosenthal, Alex Pearse, and Gary Paradee.

I graciously acknowledge all of the funding agencies and organizations who have awarded me with monetary support so that I could accomplish and complete this dissertation: the James A. Clark School of Engineering, the UMD Dean's Fellowship, the UMD Jacob K. Goldhaber travel grant, the 2015 and 2017 UMD Graduate School Summer Research Fellowship, the 2016-2017 UMD Graduate Deans Dissertation Fellowship, the 2017-2018 Hulka Energy Research Fellowship, and the

2017-2018 All-S.T.A.R. Fellowship. Other monetary awards include: MRS Graduate Student Silver Award, OSA Student Poster Competition, IREAP best speaker award, UMD Researchfest 2015, IEEE 40th PVSC best poster.

To the 2016 Joint US-Africa Materials Institute for giving me the opportunity of a lifetime. In particular, the organizers: Profs. Sossina Haile, Peter Green, and Simon Billinge.

It is also extremely important that I thank the all the professors from the Physics department at my alma mater, University of Wisconsin - La Crosse. There are a particular few that inspired and supported my decision to attend graduate school at Maryland: Profs. Sudha, Seth King, and Shauna Sallmen. The incredible atmosphere that the professors brought to the UWL Physics department is what motivated me to continue on with my education.

I thank all of my dear friends who have either shared my woes, listened to my rants, or helped distract me from my work when I needed a break (some of these brave individuals even held the honor of performing all three of these tasks). Some include: Manatee(Travis Dietz, Katie Frey, Michael Van Order, Andrew Knoll, and Alyson Becker) our Sunday night dinners, will always be cherished by me, and may Zengo forever rest in peace. Some amazing ladies back in the midwest: Kelse Brellenthin (Triplett? It depends when this thesis gets published), Ceejae Lynch, and Smerg, for listening and being my life-long friends, if there is one thing that is a constant in this life it will be our friendship. Kwembur Morks (a.k.a. Morko) for the advice, support, and for sharing a perspective I cannot get anywhere else. Andrew Prudhom, who was the only person who understood my La Crosse to graduate school transition. Katie and Dave Shahin, for the laughs, the games, the competitions, and the ride in the Tesla. Long Nyugen for being my first official office mate, continuing friend, and introducing me to many of your great friends such as Vikram Um and Adria Schwarber who just hijacked your shout out. Tristan McAloon and Sammi for pushing me to stay my first year when I almost did not. Also: Bethany and Patrick Stanley, Teddy Wilson, Pinghsan Luan, Jiaqi Dai, and Andrew Dunkman.

To Travis C. Dietz, PhD, who was with me for every step along the way in

my graduate school adventure. You made the process infinitely better, it is just a shame we won't be able to quantify it. From all-nighters spent studying for exams, to all-nighters spent writing papers/dissertations, and everything in between (Why crystal melt?). Thank you for all the love and laughter you have shared with me these past five years. I look forward to seeing what life brings with you post-graduate school. This is our last chance to figure out the mysterious green Jello conundrum. Let's see how it goes.

I know that I will not be capable of completely expressing my gratitude for my family, but I can try. To Joe: I wish you were here, and to my other siblings: Jason, Dan, Linsey, and Scott, thank you for never asking when I might graduate or what I am doing with my life, because I never knew, and to my siblings' significant others: Marcia, Tiffany, and Chrisshon for their kind words of motivation. To my nieces: Ariana, Aubrey, McKenzy, and Ivy — this is for you, I want you to know that you can live whatever life you want and don't have to settle for anything. Remember to always embrace these wise words from Beyoncé: “Okay ladies now let's get in-formation”. To my nephews: Gabriel, Oliver, and Quentin — Work hard to reach your goals in life, whatever they may end up being, I already know you boys all have your unique abilities. To Dennis and Mike, thanks for expressing your interest in my research, or at least pretending to. To Nicki: for checking in and always remembering to wish me well whenever there was an achievement or event (big or small) related to graduate school. I know you always enjoyed when I sent you my papers. Lastly, to my incredible parents: to say “I wouldn't be here without them” goes beyond just the physical and literal meaning, their undeniable mental encouragement and belief in me was unparalleled. I am astounded by all their love and support. I mean, they read every paper, that's amazing! Thanks Dad for always double checking my results by comparing them to your own sophisticated research.

Elizabeth M. Tennyson

February 2018

College Park, MD

Table of Contents	v
List of Figures	viii
List of Tables	x
1 Introduction to Photovoltaics	1
1.1 The need for photovoltaics	1
1.2 Pursuing high-performance and low-cost PV	2
1.3 Fundamentals of solar cells	3
2 Research Objectives	7
3 Scanning Probe Microscopy of Energy Harvesting Systems	9
3.1 Introduction to scanning probe microscopy	10
3.2 AFM for energy harvesting systems	12
3.2.1 Hybrid perovskites and thin-film materials for PV: opportu- nities and current limitations	13
3.2.2 Probing electrical properties	20
3.2.3 Imaging local chemical properties	29
3.2.4 Optical properties at the nanoscale	33
3.3 Probing dynamic processes in perovskite solar cells	38
3.4 Summary	42
4 Photovoltage Tomography in Polycrystalline Solar Cells	45
4.1 The need for tomography in thin film photovoltaic devices	46
4.2 Experimental methods	48
4.2.1 CIGS solar cell fabrication	48
4.2.2 Device macroscopic characterization	49
4.2.3 Raman spectroscopy mapping	50
4.2.4 Photovoltage imaging	50
4.3 Correlating chemical and electrical maps in CIGS	51
4.4 Spectrally dependent photovoltage imaging results and discussion . .	54
4.5 Conclusion	64

5	Nano-imaging of open-circuit voltage in photovoltaics	67
5.1	Introduction to local voltage mapping in thin-film solar cells	68
5.2	Experimental methods	71
5.2.1	Solar cell fabrication	71
5.2.2	KPFM measurements	72
5.2.3	Macroscopic characterization of devices	72
5.2.4	EQE measurements of GaAs	74
5.2.5	V_{oc} image analysis	75
5.3	Direct imaging of V_{oc} at the nanoscale: results and discussion	75
5.4	Conclusion	87
6	Real-time nanoscale open-circuit voltage dynamics of perovskite solar cells	89
6.1	Introduction to nano-imaging in perovskite solar cells	90
6.2	Experimental methods	92
6.2.1	Perovskite solar cell fabrication	92
6.2.2	Illuminated Kelvin-probe force microscopy V_{oc} derivation	93
6.2.3	KPFM implementation	97
6.2.4	Image analysis	99
6.3	Fast-KPFM results and discussion	99
6.4	Conclusion	109
7	Perovskite composition-dependent nanoscale voltage response	111
7.1	Introduction	112
7.2	Experimental methods	114
7.2.1	ToF-SIMS characterization	114
7.2.2	Raman spectroscopy and microscopy	114
7.2.3	Solar cell synthesis	114
7.2.4	Macroscopic measurements	116
7.2.5	Kelvin probe force microscopy experiments	116
7.3	Composition analysis of perovskites	117
7.4	Probing perovskites' electrical response at the nanoscale	119
7.4.1	Irreversible nanoscale electrical response in MAPbBr ₃	121
7.4.2	Fully reversible and stable Cs-incorporated triple cation perovskites	126
7.5	Conclusion	131
8	Perspective on functional imaging of PV materials	133
8.1	Introduction	134
8.2	Electrons as a source of excitation	134
8.3	Photons as a source of excitation	139
8.4	Probing the degradation of perovskite solar cells	144
8.5	Correlative microscopy and the need for big data analytics	146
8.6	Outlook	147
8.7	Future work	148

A	Products of this research	151
A.1	Awards and honors	151
A.2	Publications	151
A.3	Presentations	152
B	Additional publications	155
C	University of Maryland service	157
C.1	Contributions	157
	Bibliography	159

List of Figures

1.1	NREL 2018 efficiency chart	3
1.2	Macroscopic dark and light J - V curves	4
1.3	Radiative and non-radiative charge carrier recombination	6
3.1	Principle of AFM operation	11
3.2	SEM images of selected polycrystalline materials for photovoltaics	14
3.3	Nanoimaging electrical properties by AFM	21
3.4	Photovoltaic performance at the nanoscale	28
3.5	Nanoimaging chemical properties in solar cell materials by AFM	31
3.6	Nanoimaging optical properties in solar cell materials by AFM	34
3.7	Imaging electrical, chemical, and optical dynamics in perovskites	40
4.1	CIGS polycrystalline solar cells	49
4.2	Scanning photovoltage experimental setup	51
4.3	CIGS electron backscatter diffraction pattern	52
4.4	Chemical composition and local electrical response of CIGS solar cells	53
4.5	Raman microscopy on CIGS: additional region	54
4.6	Laser ON/OFF photovoltage signal verification	55
4.7	Additional photovoltage maps of CIGS solar cells	55
4.8	Spectrally dependent voltage maps on CIGS solar cell	57
4.9	Spectrally dependent voltage histograms	58
4.10	CIGS optical properties	59
4.11	SEM images of as-is vs. polished CIGS grains	59
4.12	Electron, optical, scanning probe microscopy CIGS grains	60
4.13	Voltage distribution of a polished CIGS sample	61
4.14	Mapping voltage with high spatial resolution in CIGS solar cells	63
4.15	Characterization of the mesoscale behavior of CIGS solar cells	64
5.1	Light J - V curves for all solar cell devices	73
5.2	Dark J - V for GaAs solar cell	73
5.3	Angle dependence of external quantum efficiency for GaAs device	74
5.4	Energy diagram of KPFM measurements	76
5.5	Macroscopic characterization of GaAs	79
5.6	V_{oc} vs. photon flux	79
5.7	Comparison of macro- and nanoscale V_{oc} measurements	80
5.8	KPFM performed on four solar cell devices	82

5.9	Directional independent KPFM imaging on Si	83
5.10	Influence of ΔH on voltage response	85
5.11	Quantifying KPFM spatial resolution	86
6.1	Real-time measurements of voltage dynamics in perovskites	93
6.2	Macroscopic characterization of perovskite solar cell device	94
6.3	SEM images of perovskite thin film	94
6.4	Monitoring all relevant signals during FM-KPFM measurements	96
6.5	Environmental conditions during <i>in situ</i> imaging of perovskites	97
6.6	AFM topography images	98
6.7	Imaging nanoscale variations in the V_{oc} of perovskite solar cells	100
6.8	Dynamics of perovskite solar cells at the nanoscale	102
6.9	Voltage profile for fast H-KPFM illumination scans	104
6.10	Spatial and temporal variation of the residual voltage within perovskites	106
6.11	Real-time nanoscale V_{oc} dynamics of perovskite photovoltaics	108
7.1	Chemical composition analysis of perovskites by ToF-SIMS	118
7.2	Raman microscopy on perovskite thin films	119
7.3	Macroscopic output and short-term stability of perovskite devices	120
7.4	Imaging the V_{oc} response in perovskites at the nanoscale	122
7.5	Relative humidity during KPFM measurements	122
7.6	Nanoscale irreversible voltage response in MAPbBr ₃ perovskites	124
7.7	Dynamic, reversible electrical response of MAPbBr ₃	126
7.8	Dynamic, reversible electrical response of MAPbBr ₃ : region 2	127
7.9	Nanoscale reversible voltage responses in Cs-mixed perovskites	128
7.10	Dynamic electrical response of Cs-mixed perovskite	129
7.11	Analysis of perovskites nanoscale electrical stability	131
8.1	Electrons as an excitation source to nano-image PV functionality	135
8.2	Photons as a source of excitation to nano-image PV functionality	141
8.3	Imaging the nanoscale chemical distribution of a perovskite thin-film	149

List of Tables

3.1	Theoretical vs Experimental Solar Cell Parameters	16
8.1	Nanoscale functional imaging methods performed on PV materials . .	137

Chapter 1: Introduction to Photovoltaics

1.1 The need for photovoltaics

To swiftly and effectively replace of fossil energy-based technologies we require a high-efficiency, low-cost, and ubiquitous photovoltaic (PV) technology. Fortunately, renewable energy is expected to become a significant percentage of the global energy sources as the total amount of power consumed globally continues to increase each year. According to the National Renewable Energy Laboratory (NREL) Renewable Electricity Futures Study, 80% of the power generated in the United States could be from renewable sources by 2050. [1] For this to occur PV electricity generation must increase beyond 10% in the US, [2] as only 1-2% of our electricity is currently produced from solar power today. [3] In general, single crystalline PV materials generally outperform their polycrystalline counterparts, [4] yet the extremely high cost associated with monocrystalline epitaxial fabrication methods does not outweigh the benefits of efficient PV devices, hindering implementation. Non-epitaxial compounds, such as hybrid perovskites and thin-film polycrystalline materials are very promising alternatives, but improvement in device stability and power-conversion efficiency (η) are still required for successful deployment, as will be discussed in detail throughout this dissertation.

1.2 Pursuing high-performance and low-cost PV

Polycrystalline materials such as $\text{CuIn}_x\text{Ga}_{(1-x)}\text{Se}_2$ (CIGS), CdTe, or hybrid organic-inorganic perovskites are a potential alternative for low-cost PV, but improvement η is required to ensure low-cost/W, see Figure 1.1. The efficiency chart [5] displays each PV technology's record performance as a function of time. CIGS, CdTe, and perovskites all produce $\eta > 22\%$, however Silicon, which represents $\sim 90\%$ of the solar cell market, boasts $\eta > 25\%$. Extensive efforts have been made to increase the short circuit current density (J_{sc}) of thin-film polycrystalline solar cells. Yet, the performance of the best solar cells is still limited by the open-circuit voltage (V_{oc}), the maximum voltage available from a PV device, which is related to the radiative recombination (photon emission) within the material. The V_{oc} of both well-established and emerging polycrystalline materials is considerably below theoretical predictions. [6–13]

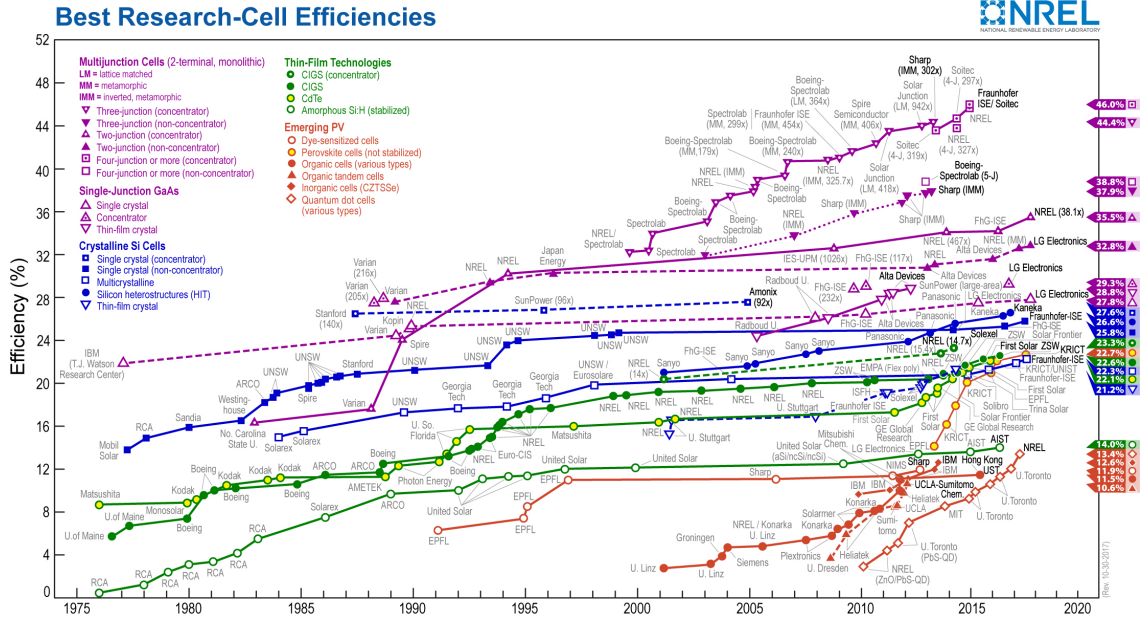


Figure 1.1: NREL 2018 efficiency chart. Accessed online from ref [5].

The key pathway to achieve higher efficiency is through minimizing the non-radiative recombination processes within the semiconductor. [14–23] Therefore, I suggest investigating the V_{oc} , as it is related to the amount of carrier recombination in the material and it plays a key role in the overall performance of solar cells.

1.3 Fundamentals of solar cells

Solar cells are fundamentally governed by the diode equation, where the V_{oc} depends on the dark current (I_0) and on the short-circuit current (I_{sc}) as:

$$V_{oc} = \frac{nkT}{q} \ln \left[\frac{I_{sc}}{I_0} + 1 \right] \approx \frac{nkT}{q} \ln \left[\frac{I_{sc}}{I_0} \right] \quad (1.1)$$

n is the diode ideality factor, k is Boltzmann's constant, T is the temperature, q is

the electronic charge, and I_0 depends on recombination events within the material. Figure 1.2 shows the most common macroscopic characterization technique for PV devices: a dark and light current-voltage (J - V) curve. At zero bias in the dark, a solar cell does not generate any current and will act as a diode, only allowing charge carriers to flow in a specific direction. When excited by photons, the light-absorbing PV material utilizes the energy from the light to produce charge carriers. Ideally, the generated electrons and holes are efficiently separated, swept toward and collected by the electrical contacts, with minimal losses. This process introduces a light-generated current, indicated as J_{sc} in Figure 1.2. The solar cell power-conversion efficiency is calculated by maximum power point (M_{pp}) divided by the incident power.

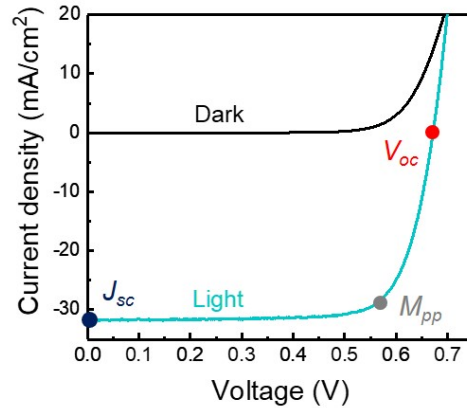


Figure 1.2: **Dark and light J - V curves.** Black curve: Dark J - V , the curve matches that of a standard diode. Blue curve: Light J - V , here the solar cell produces a light-generated current, therefore, performing work at specific external voltage biases. J_{sc} : short-circuit current density, V_{oc} : open-circuit voltage, M_{pp} : maximum power point.

For an ideal PV device, the V_{oc} is only limited by radiative recombination processes and is equal to the material bandgap term ($\frac{E_g}{q}$) in volts minus the thermodynamic losses: $V_{oc} \approx (\frac{E_g}{q}) - 0.4$. [6,24–27] This equation was first derived by Shockley

and Queisser in 1961, and is so-called the Shockley-Queisser limit. [6] Generation and recombination are electronic excitation and relaxation processes that increase and reduce the number of free charge carriers, respectively. The most relevant type of generation in PV is the absorption of a photon. For every generation process there is an equivalent recombination process, which is typically the loss of a carrier through the decay of an electron to a lower energy state. When the energy associated with this decay is released by the emission of a photon that has an equivalent energy to the material bandgap (E_g), the event is termed radiative recombination, see Figure 1.3(a). This thermodynamically necessary process is dominant in direct E_g materials, such as GaAs, perovskites, CIGS, and CdTe, and is not necessarily harmful to the device. [24] Nevertheless, in non-radiative recombination, Figure 1.3(b), electron-hole pairs recombine at defect states, inhibiting the collection of a charge carrier, generating heat, and unavoidably degrading the performance. There are other types of non-radiative recombination events, such as Auger, but here I am highlighting only the most relevant processes for multi-crystalline solar cell materials.

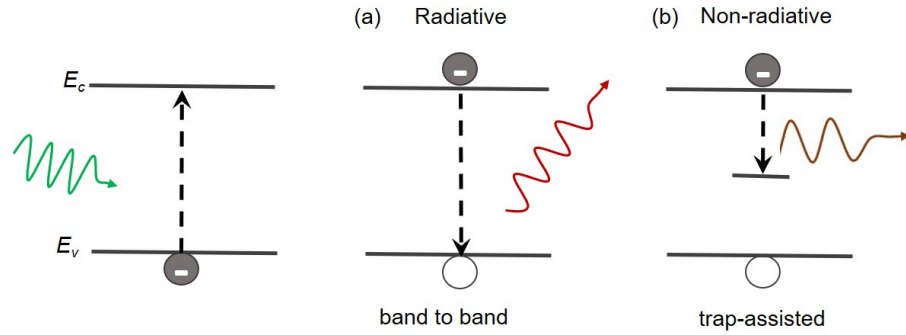


Figure 1.3: **Radiative and non-radiative charge carrier recombination.** Possible recombination events that may occur after an incident photon is absorbed by a solar cell material. (a) Radiative recombination: an electron directly recombines with a hole and emits a photon the same energy as the semiconductor’s bandgap. (b) Trap-assisted non-radiative recombination: an electron relaxes to a defect energy state and emits a photon with an energy much lower than the bandgap.

Polycrystalline light-absorbers are composed of micron-sized grains, and thus, consist of many interfaces or defects, all of which could potentially be sites of trap-assisted recombination. Therefore, while macroscopic light J - V measurements are useful for determining the average device performance, a nanoscale imaging spectroscopy method to spatially resolve the local optical and electrical properties to access charge carrier recombination processes within polycrystalline materials for PV is still missing and is critical for understanding device deficiencies. Throughout this dissertation I advance our understanding of materials for PV by resolving the charge generation and collection with nanoscale resolution. For this, I have implemented novel nanospectroscopic imaging metrologies, such as scanning photovoltage and Kelvin probe force microscopies.

Chapter 2: Research Objectives

In this dissertation I accomplish the following research objectives by developing and implementing functional imaging techniques to map the local electronic charge carrier processes (*i.e.* generation, recombination, and collection) within promising, next-generation PV materials.

(i) **Photovoltage tomography in polycrystalline solar cells.** By selecting the wavelength of the local source of illumination, I build a photovoltage tomography of the PV material, based on its absorption coefficient and the wavelength-dependent SPCM. Our results using scanning confocal microscopy (with a $100\times$ objective lens) show spatial variations in the generation of carriers. The light penetration depth is directly related to the experimentally determined material absorption coefficient ($\alpha = (\frac{4\pi k}{\lambda})$) which establishes a tomography of photovoltage in three dimensions.

(ii) **Nano-imaging of open-circuit voltage in photovoltaics.** Using Kelvin probe force microscopy (KPFM) I locally probe the open-circuit voltage (V_{oc}) with nanoscale resolution of solar cells through a series of dark and illuminated KPFM scans. Since KPFM is a variant of scanning probe microscopy, both the morphology and electrical properties of the solar cell material are simultaneously acquired. KPFM measures the work function difference between the cantilever tip

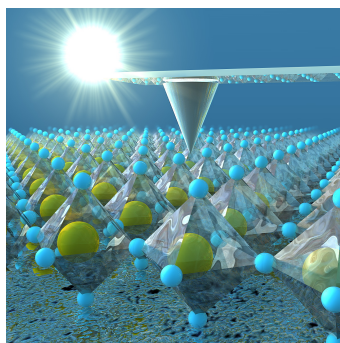
and sample surface. Upon solar cell illumination, the work function shifts, and the local V_{oc} is calculated from this change. Here, I reveal new insights about how the grain boundaries within polycrystalline devices affect the overall performance.

(iii) **Real-time nanoscale open-circuit voltage dynamics of perovskite solar cells.** A variant of KPFM is utilized to rapidly image a specimen with temporal resolution on the order of seconds, more than two orders of magnitude faster than conventional frequency modulated KPFM. By using a scanning probe technique with such high spatial and temporal resolution we realize how the material changes electrically with time. This is especially interesting for perovskite solar cells, as they are known for their electrical instability when exposed to air and/or moisture. Here, I will image the dynamics of perovskite devices in real-time.

(iv) **Imaging fully reversible and stable perovskites at the nanoscale.** With the wide variety of perovskite materials available for PV applications, it is crucial to determine which composition will have the highest electrical stability and moisture tolerance. I leverage my expertise in KPFM and probe multiple perovskite thin-films to measure both irreversible and reversible voltage responses. I further use Fast-KPFM, described in Objective (iii), to track the irreversible electrical signal.

Chapter 3: Scanning Probe Microscopy of Energy Harvesting Systems

Our scientific understanding of the nanoscale world is continuously growing ever since atomic force microscopy (AFM) has enabled us to “see” materials at this length scale. Beyond morphology, functional imaging is becoming standard practice as new AFM-based techniques are continuously extending its capabilities. Resolving material properties with high spatial accuracy is now extremely critical, as future next-generation energy harvesting systems are comprised of complex and intricate nanoscale features. Here, we provide a literature review of recent research discoveries that implemented AFM methods to measure and determine how the electrical, chemical, and/or optical properties influence the overall device behavior. We dedicate a portion of this chapter to perovskite solar cells, which are of primary interest to photovoltaic research, and highlight the remarkable progress made towards understanding and controlling their instabilities. We conclude with a summary and outlook anticipating the most pressing materials related challenges associated with solar cells, and how they will likely be overcome in the near future by nanoimaging through AFM. This chapter is adapted from E.M. Tennyson et. al, *ACS Energy Letters*, **2** 2761-2777 (2017) **Front Cover** [28]



3.1 Introduction to scanning probe microscopy

Imagine gently gliding along the surface of an object with the tip of your index finger — what types of information can you obtain? Most likely, you will feel the texture (surface roughness), temperature, shape, hardness, *etc.*, of the item. All this information is acquired in less than one second by neurons firing from your fingertip to your brain. Atomic force microscopy (AFM) is analogous to this situation; except, replace your fingertip by a nanoscale probe and the neuron reactions with the microscope detection system. AFM is, thus, an extremely powerful tool that probes the morphological, electrical, magnetic, mechanical, chemical, and optical properties of the sample under examination. Since its first implementation in the 1980's, [29] AFM has revolutionized our understanding of a variety of nanoscale PV systems, [30,31], as will be presented in this Chapter.

In most AFM-based setups there is a probe with a radius ranging from 1-100 nm that is positioned very close to or in contact with the surface of a sample, illustrated in Figure 3.1. The spatial resolution of AFM imaging methods is, then, primarily limited by the size of the probe. The interaction between the AFM tip and sample is detected by a photodiode that collects laser light deflected off the back of the cantilever. The photodiode is calibrated with specified x - y coordinates and continuously keeps track of the laser position. Therefore, any minute movement of the probe, whether caused by a small change in sample height or electronic carrier concentration, is detected. The feedback loop system adjusts the cantilever accordingly, depending on the measurement mode of interest. There are many forces and interactions, such as electrostatic, capillary, or chemical potential, that can excite the tip and/or sample causing the deflection laser's x - y coordinates to change. Beyond the surface roughness, [32,33] properties such as the

local electrical, chemical, and optical spatial variations are imaged, which will be discussed in detail later.

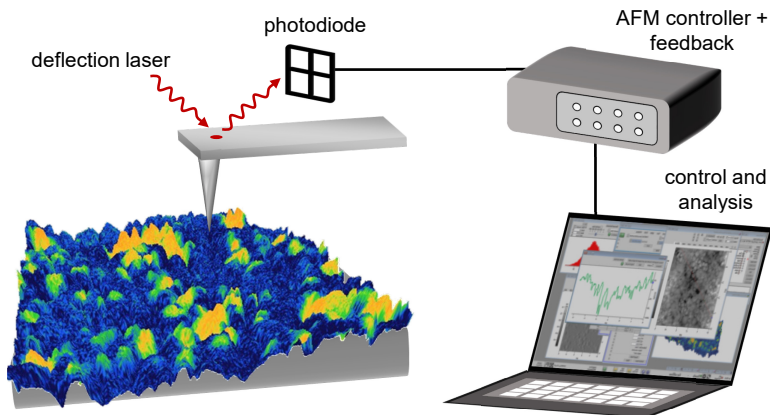


Figure 3.1: **Principle of AFM operation.** Illustration of an AFM probe scanning the surface of a textured, non-uniform sample. A laser is deflected from the back of the probe onto a photodiode and any change in the tip-sample interaction is translated as the laser's coordinates on the photodiode. As a consequence, the feedback system within the AFM adjusts itself accordingly. Out of scale for clarity.

Here, we introduce the remarkable progress made in determining the properties and performance of materials for energy harvesting by AFM through functional and correlative nanoscale imaging. The micro- and nanostructure of heterogeneous photovoltaic (PV) and materials is well known to influence their overall performance. [34, 35] Therefore, understanding the electrical and chemical processes that harm device operation is crucial for future renewable energy generation, conversion, and storage systems. We choose to focus on AFM methods because they encompasses key desirable features such as: the ability to perform measurements in *operando* conditions with 3D nanoscale spatial resolution, is non-destructive, and requires very little sample preparation. Further, AFM is undoubtedly a versatile tool to image the functionality of energy harvesting materials, and its full potential has yet to be realized, as new techniques will shed light on faster, dynamic processes. We target selected AFM-based methods that are specifically implemented to

investigate the nanoscale properties of energy conversion systems that translate into device performance, such as the electrical and optical response of solar cells (through measurements of photovoltage, photon-induced current, and charge carrier lifetime), and chemical composition. In the realm of photovoltaics, we provide an in-depth discussion of each imaging method that has been utilized to probe relevant properties of next-generation solar cells. In particular, we focus on performance mapping and perovskite dynamics as it is at the forefront of interest for scientists and engineers working on PV. These novel scanning methods have the potential to elucidate key open questions about the physical behavior of perovskite devices.

3.2 AFM for energy harvesting systems

The most promising emerging PV materials consist of micro-structured semiconductors with boundaries and interfaces that can lead to undesirable non-radiative recombination of charge carriers, reducing the power-conversion efficiency (η) of the device significantly below its theoretical limit. [34,35] The applications of these heterogeneous materials, including perovskites, CdTe, Cu(In,Ga)Se₂ (CIGS), Cu₂ZnSnS₄ (CZTS), quantum dots, organics, dye-sensitized, *etc.*, are aimed toward lower-cost and/or higher-efficiency solar markets. Often, the devices are fabricated as thin-films ($\leq 3 \mu\text{m}$ thickness), which can be deposited on a variety of surfaces with distinct mechanical properties, including flexible substrates. Despite the potential low cost (\$/kW) of these devices, it is currently not well understood how their structure affects charge carrier generation, recombination, and collection at the nanoscale. Thus, imaging the key physical and chemical properties of these materials is crucial to their further development. In this section of the Thesis I describe how AFM methods have been realized to probe the electrical, chemical, and

optical properties of non-epitaxial materials for PV.

3.2.1 Hybrid perovskites and thin-film materials for PV: opportunities and current limitations

The absorbing layer of halide hybrid perovskites and of most polycrystalline materials for PV (CdTe, CIGS, CZTS, and polycrystalline GaAs) is composed of grains in the microscale range, as shown in Figure 3.2, with well-defined facets, interfaces, and boundaries. The macroscopic performance of the devices strongly depends on these mesoscale constructs, where the behavior of the average density of atoms corresponding to length scales of 5-50 nm (and to a volume commonly comprised of thousands of atoms) is more relevant than the contribution of the individual atoms themselves. [36] Thus, it is imperative to resolve the performance of the device at similar, relevant length scales. While conventional electrical characterization methods are extremely useful, they do not provide information about how each grain and interface contributes to/affects the electrical and optical responses of the PV devices. Scanning probe microscopy (SPM) and scanning (transmission) electron microscopies (STEM and SEM) have been successfully applied to characterize materials for solar cells with high spatial resolution. [37-39] Recently, microscopic techniques have been combined to investigate the structural, optical, chemical, and electrical properties of a variety of relevant materials. [40,41] However, the nanoscale functional imaging of critical mesoscale phenomena in PV materials and in operando devices is still missing. The performance of PV devices is defined by its main figures-of-merit: open-circuit voltage (V_{oc}), short-circuit current density (J_{sc}), fill factor (FF), and η . Thus, the ability to map these quantities with nanoscale spatial resolution will likely unravel the intricate physical and chemical processes that define device functionality at the mesoscale,

elucidating the origin of the modest performance of some technologies, and of the light-induced chemical reactions that take place in perovskites. Below we summarize the major advantages and challenges of the selected non-uniform solar cell materials.

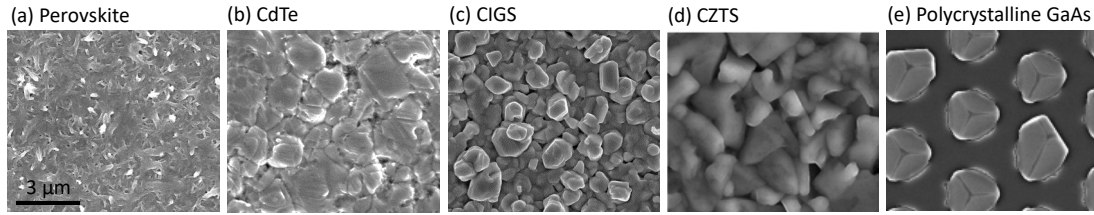


Figure 3.2: **SEM images of selected polycrystalline materials for photovoltaics:** (a) hybrid perovskites, reprinted from ref [42], (b) CdTe, (c) CIGS, (d) CZTS, reprinted from ref [43], and (e) polycrystalline GaAs, reprinted from ref [44]. In all cases, the absorbing layer is composed of micron sized grains or smaller, where their optical and electrical responses vary in the same length scale.

3.2.1.1 Hybrid organic-inorganic perovskites

Since 2009, the research community has witnessed the rise of hybrid halide perovskites as a competitive PV technology. [7,45,46] The perovskite material has the chemical formula ABX_3 , where A is an organic cation (most commonly used is methyl ammonium, $MACH_3NH_3$), B is an inorganic cation (typically Pb or Sn) [47], and X is a halide (typically iodine, but chloride and bromide have also been used). The interchangeability of elements within the compound enables bandgap energy (E_g) tuning from 1.6 eV to 3.2 eV, very appropriate for multi-junction designs. At present, perovskites hold a record power-conversion efficiency similar to CdTe and CIGS, at $\eta = 22.7 \pm 0.8\%$. [35] However, stabilizing the high performance has proven to be a challenge and is one of the main ongoing focuses of research in the field. [48] Scientists have observed PV characteristics change in a matter of seconds [39,49] and the primary processes that cause this instability point towards ion migration. [50] Most perovskites are composed by sub-micron scale grains

(Figure 3.2(a)), where spatial variations in their chemical composition resulting from the spin coating deposition process during the device fabrication are possibly responsible for the spatial electrical variations reported in the literature, [39,51] as well as ion migration. Therefore, imaging electronic charge separation and collection at the numerous interfaces could elucidate the pathways for carrier transport within the material. [52] Full comprehension and control of the time-dependent physical and chemical processes responsible for the commonly observed degradation of perovskites will likely lead to stable, high-efficiency devices. Additionally, by probing the local electrical response of new lead-free perovskite alternatives [53] the community will ultimately identify which materials are stable under PV operation conditions and, thus, suitable for device development, which is currently unknown.

material	E_g (eV)	$V_{oc,theory}$ (V)	$V_{oc,meas}$ (V)	$\frac{V_{oc,meas}}{V_{oc,theory}}$	$J_{sc,theory}$ (mA/cm ²)	$J_{sc,meas}$ (mA/cm ²)	$\frac{J_{sc,meas}}{J_{sc,theory}}$	η (%)
perovskite	1.58	1.325	1.105	0.86	27.2	25.0	0.92	22.7 ± 0.8
CdTe	1.45	1.168	0.887	0.76	30.5	30.25	0.99	22.1 ± 0.5
CIGS	1.15	0.89	0.741	0.83	42.1	87.8	0.90	22.6 ± 0.5
CZTS	1.13	0.884	0.513	0.58	43.3	35.2	0.81	12.6 ± 0.3
poly-GaAs	1.42	1.160	0.994	0.89	31.7	23.2	0.73	18.4 ± 0.5

Table 3.1: Theoretical vs Experimental Solar Cell Parameters

3.2.1.2 CdTe

CdTe/CdS heterojunction solar cells are a mature technology, available on today's PV market. Thus, improving devices' performance for a well-established technology can significantly impact the associated industry. At present, the power-conversion efficiency record of CdTe solar cells is $\eta = 22.1 \pm 0.5\%$ and typical module performance is $\eta = 18.6 \pm 0.6\%$. [4] While the J_{sc} of world record devices has practically achieved its maximum, there is a 25% gap between the theoretical and the measured V_{oc} of polycrystalline CdTe solar cells, see Table 3.1. It has been recently shown that single crystalline CdTe devices (boundaries free) can achieve V_{oc} as high as 1.096 V, [54] corresponding to $\sim 20\%$ voltage improvement over the best values ever obtained for polycrystalline CdTe solar cells (limited at ~ 0.9 V, as shown in Table 3.1). This result strongly indicates that the grain boundaries do indeed negatively impact the recombination rate of charge carriers. However, fabricating monocrystalline CdTe thin films is an extremely slow and expensive process. Therefore, identifying and controlling where carrier recombination events take place within polycrystalline CdTe will facilitate the design of devices with suppressed non-radiative recombination, higher V_{oc} and, thus, performance. It has been recently suggested that not every CdTe GB results in voltage reduction; [37, 55] therefore, the response of individual grains (with $\sim 1 \mu\text{m}$ in diameter, as shown in Figure 3.2(b)) and its interfaces must be resolved, which requires high spatial resolution electrical measurements.

3.2.1.3 $\text{Cu}(\text{In}_{(1-x)}\text{Ga}_x)\text{Se}_2$ (CIGS)

The extensive characterization of CIGS/CdS heterojunction devices strongly indicates that this material can become a marketable PV technology. Currently, CIGS is the

second highest performing thin-film solar cell at $\eta = 22.6 \pm 0.5\%$. [4] The CIGS E_g can be tuned from 1.02 to 1.68 eV as a function of Ga/In content (useful for multi-junction approaches), has high optical absorption, is compatible with flexible substrates, and has the potential for low-cost/W installation. [56] Nevertheless, the V_{oc} and the J_{sc} of these devices can still be improved, as shown in Table 3.1. Note that, recently, the J_{sc} of small cells (0.51 cm²) reached >41 mA/cm² (uncertified), [57] approaching the theoretical value. However, its V_{oc} is still $>20\%$ below the theoretical prediction. The p -doped CIGS absorbing layer is composed of grains with approximately 1 μ m in diameter, see Figure 3.2(c). Voltage variations of $>20\%$ have been observed, shown in the next Chapter, despite the uniform chemical composition of the grains. [40] Therefore, enhanced power conversion efficiencies will require mapping how the different grains and interfaces composing the CIGS layer affect charge carrier generation, recombination, and collection. In particular, the possible correlation between the physical behavior of in operando CIGS devices and its structural properties (resulting from a distribution of grain orientations) is still unclear. [56]

3.2.1.4 Cu(Zn,Sn)(S,Se)₂ (CZTS)

CZTS belongs to a class of material similar to CIGS (see Figure 3.2(d) for grain morphology). The main difference, as the chemical formula suggests, is that the elemental compound does not contain possibly scarce elements like In or Ga, and is purposefully restricted to using earth-abundant elements. Here, the Zn and Sn atoms replace the group III elements (In and Ga), producing a structure with charge neutral valence state. [58,59] Although extensive efforts to increase the performance of CZTS solar cells, its V_{oc} is 50% below the theoretical prediction for this material (Table 3.1). Moreover, improvements in the J_{sc} are also still necessary. As a result of its modest V_{oc} , the record device efficiency is

$\eta = 12.6 \pm 0.3\%$. [4,60] This lower performance is primarily associated with the fabrication of films with high void density or impure phases within the $\text{Cu}_2\text{ZnSnS}_4$, such as Sn_xS_y , [61] despite multiple attempts to optimize the thin film deposition parameters. Determining how these variations in chemical composition affect the local electrical response of CZTS thin films could aid in the fabrication of higher efficiency devices.

3.2.1.5 Polycrystalline GaAs

Single crystalline GaAs offers near-ideal optical and electrical properties. As a result, today's world record single junction devices are made of monocrystalline GaAs, with power-conversion efficiency of $\eta = 28.8 \pm 0.9\%$ under AM1.5 global illumination. [4] Moreover, this semiconductor compound, together with InP and other III-V alloys, has been successfully implemented in high-efficiency multi-junction solar cells for concentrator systems and space applications. [62–64] However, the epitaxial fabrication methods required for manufacturing monocrystalline III-V semiconductor modules have prohibitive costs for terrestrial applications. Polycrystalline GaAs is, thus, an attractive alternative to monocrystalline compounds [44] as they can be fabricated both *n*- and *p*-type by close-spaced vapor transport (CSVV), see Figure 3.2(e). [65, 66] The record cell efficiency for multicrystalline GaAs is $\eta = 18.4 \pm 0.5\%$, [4] which is significantly below its single crystalline counterpart and likely due to either the structural defects in the GaAs polycrystals or surface recombination within the distinct facets. By spatially resolving the J_{sc} and V_{oc} of the GaAs mesoscale constructs we can measure the local response of each crystal facet independently. For instance, it is well known that the GaAs substrate orientation affects the density of defects. [67, 68] Yet, an analysis of the contribution of the individual GaAs polycrystals to charge carrier recombination and collection and, therefore, to the overall

device performance is critical and still missing.

From Table 3.1, it is evident that there is an opportunity for material scientists, electrical engineers, physicists, and chemists to advance the state-of-knowledge of perovskites and polycrystalline materials for PV. As the mesoscale constructs strongly influence the efficiency of charge carrier generation, recombination, and collection events, it is imperative to resolve the relevant performance properties of these materials/devices at similar length scales.

3.2.2 Probing electrical properties

Understanding the nanoscale electrical characteristics of solar cells is the next step towards realizing devices with controlled response and, thus, enhanced performance. In AFM based techniques, the electrical signal is the main diagnostic tool used to indicate whether the local voltage and/or current of a PV device is affected by the materials morphology and how its spatial variation compares with the average, macroscopic device response. Nanoscale electrical characterization can help answer critical, still not fully solved questions such as: “How do the aggregates in perovskite thin films affect overall device morphology and performance?”, [69] “Does the lifetime of charge carriers vary as a function of incident wavelength in organic PV?”, [70] and “What is the specific contribution of grain boundaries in CIGS and CdTe solar cells/ to the local electrical signal?”. [37, 71] we review the most relevant AFM methods that have made contributions towards revealing the effect of the light-absorbing microstructure on the electronic response.

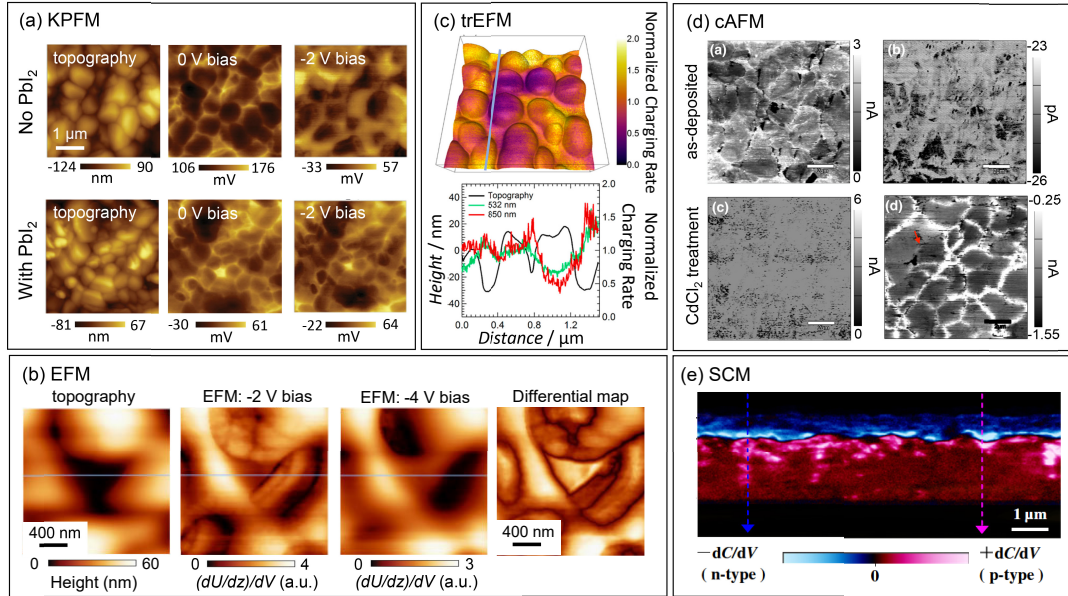


Figure 3.3: **Nanoimaging electrical properties by AFM.** (a) Topography and KPFM of two perovskite solar cells, with and without the incorporation of 5.7 mol% of PbI_2 as function of voltage bias. Illumination conditions: 500 nm incident light and photon flux = 0.3 kW/m^2 . Adapted with permission from ref [69]. ©2015 WILEY-VCH Verlag GmbH & Co. KGaA, Weinheim. (b) AFM and corresponding EFM images of a MDMO-PPV:PCBM (1:4) polymer blend thin film acquired at different applied biases. Far right: differential map of the two biased EFM maps. Adapted from ref [72]. Copyright 2016 The Japanese Journal of Applied Physics. (c) Top: trEFM map overlaid with topography in a polymer half-processed solar cell in a $1.5 \times 1.5 \mu\text{m}^2$ region. Bottom: Profile of topography and relative charging rate acquired for two different photon excitations. Adapted from ref [70]. (d) cAFM maps of the local current signal for both non-passivated and passivated CdTe solar cells in a $10 \times 10 \mu\text{m}^2$ area. Adapted from ref [71]. (e) SCM on the cross-section of a CIGS solar cell defines the location of the p - n junction and qualitatively shows the density of dopants in each respective layer. Adapted with permission from ref [73]. ©2014 IOP Publishing Ltd.

A variant of AFM that measures local voltage with nanoscale spatial resolution is called Kelvin probe force microscopy (KPFM), which we have recently demonstrated to map the open-circuit voltage in solar cells [37,39] (a detailed discussion is presented in the next section and in Chapter 5). KPFM measures the work function difference between a conductive probe and the sample surface, termed the contact potential difference (V_{CPD}). KPFM was theorized by Lord Kelvin in 1898 [74] and first implemented a couple of decades ago to characterize the local electrical signal of metal and semiconductor surfaces. [75,76]

The work function (W) is the energy level difference between the vacuum and Fermi level (E_F). The probe, typically Si coated with a thin conductive metal layer, is assumed to have a constant W in non-contact scanning mode. In equilibrium (no light), the solar cell's W at the surface stays constant; however, in the case of non-uniform, heterogenous materials the work function may vary locally depending on grain orientation, [77] E_F pinning, [78,79] charge trapping, [80] and chemical composition, among other factors. When the sample is illuminated, it generates charge carriers and is, thus, in a non-equilibrium state.

KPFM is frequently used as a diagnostic tool to image the voltage response before and after specific deposition steps, relevant for optimizing the fabrication parameters of the films. In Figure 3.3(a), Seidel's group compared how the electrical signal of $(\text{FAPbI}_3)_{0.85}(\text{MAPbBr}_3)_{0.15}$ (FA = formamidinium, MA = methylammonium) perovskite compounds with and without an additional (5.7 mol%) PbI_2 reacts locally when an external voltage bias (inducing ion migration) is applied, by KPFM. [69] It was found that the V_{CPD} of the sample without the extra treatment step presents a dramatic change as a function of bias, particularly at the grain boundaries, while the V_{CPD} of the device with excess PbI_2 remains constant at both the grain interiors and grain boundaries. These observations were attributed to ionic migration suppression due to the incorporation of excess PbI_2 , which in turn improves the overall electrical properties of the solar cell.

A derivative of KPFM, called either intensity-modulated or illuminated-assisted KPFM, measures the decay of the surface photovoltage (SPV), which is the subtraction between an illuminated- and a dark- KPFM scan in the same location. Here, the V_{CPD} depends on the frequency of the laser pulse, and a transient SPV signal resolved on the order of sub-milliseconds is observed. [81,82] The decay rate of the SPV is related to the minority charge carrier lifetime, as shown in refs [83,84]. Briefly, when the illumination

source is in OFF mode, the PV voltage decays exponentially and is proportional to $e^{-1/\tau}$, where τ is the minority carrier lifetime. These pioneer works yield insights that link the local photovoltage, lifetime, and topography, especially useful for correlating the role of the microstructure to a specific type of recombination mechanism.

Electrostatic force microscopy (EFM), of the same family as KPFM, also measures the electrical signal of the tip-sample interaction while applying a voltage to the tip in non-contact mode. The deflection of the AFM probe is linked to the electrostatic force (FES) between the sample surface and tip. [85, 86] That is, the oscillation path (z -axis) of the cantilever changes depending on the electrical charge distribution located at the sample surface. The electrostatic force is described as:

$$F_{ES} = \frac{1}{2} \frac{dC}{dz} V^2 \quad (3.1)$$

where z is the distance between the tip and sample, C is the tip-to-sample capacitance, and V is a voltage term that encompasses all voltages flowing within the AFM experimental setup. The amount of tip deflection is related to the charge carrier density; therefore, by utilizing EFM one can map electrical properties such as capacitance, surface voltages, or electrostatic potentials. [87] The capability of this technique is exemplified in Figure 3.3(b), where the surface charge of a poly[2-methoxy-5-(3A,7A-dimethyloctyloxy)-1,4-phenylenevinylene] (MDMO-PPV):phenyl-C61-butyric-acid-methyl ester (PCBM) polymer blend thin film is mapped as a function of external voltage. [72] Here, Takuya's group was able to determine how the electrostatic properties of an organic PV system influence device performance. Both the permanent (addition of two EFM maps set at different voltage bias values) and field-induced (differential of two biased EFM maps) charge components were acquired. While the permanent portion of the EFM signal did not affect

performance, the differential map shows sharp, dark contrasts, which could be related to charge trapping.

Time-resolved EFM (trEFM), an extension of traditional EFM, measures the charging rate by tracking the resonance frequency shift that occurs between the probe and the sample due to charge accumulation. [88, 89] Under illumination or external voltage bias a solar cell generates electrons and holes at a specific rate. A faster charging rate implies an increase in charge buildup under the probe, shifting the cantilever frequency further away from its equilibrium resonance peak, dependent on both the incident photon energy and quantum efficiency. Each of these quantities are known for varying spatially in organic heterogenous PV materials. Figure 3.3(c) shows a 3D topography map overlaid with trEFM data on a MDMO-PPV:PCBM (wt/wt 1:4) organic blend cast from toluene. [70] The black curve denotes topography, while the green and red ones are the normalized charging rates under 532 nm (above bandgap) and 850 nm (below bandgap) illumination, respectively. The trEFM line scans present similar spatial trends and, thus, are independent of the incident wavelength. This result suggests that the internal quantum efficiency of the polymer material is equal across a wide range of photon energies. Ginger’s group observed that segregated regions of PCBM have lower charging rates than if the film were to have a completely uniform blend.

One way to measure the current of a PV device at the nanoscale is to probe the sample using conductive- or photoconductive-AFM (cAFM or pcAFM). Here, a conductive AFM probe in contact with the sample surface acts as a local electrode that collects the solar cells dark (cAFM) and/or light-generated current (pcAFM). This mature method has been widely used to image a variety of materials for solar cells, such as perovskites, [51, 90–92] thin-film polycrystalline, [71, 93, 94] and others. [95–99] One pressing question

that cAFM can help answer is: What is the specific role of the CdCl₂ treatment on the electrical properties of CdTe solar cells? It has been ubiquitously demonstrated, at a macroscopic level, that the CdCl₂ improves PV performance by passivating the CdTe grains and interfaces; [100] yet, resolving how it affects the local electrical signal is still not well understood. Thus, cAFM has been applied to elucidate how this extra fabrication step enhances CdTe performance — see in 3.3(d). [71] Here, Rockett’s group imaged two CdTe solar cells, with and without CdCl₂ treatment, under multiple external voltages using a Pt-coated Si probe. Both the top-left and bottom-right maps were obtained at a bias of +6 V while the top-right and bottom-left were acquired at -6 V. Under positive bias the *p-n* junction of the CdTe solar cell experiences reverse breakdown voltage due to the geometry of the measurement. In this case, the current contrast between the grains and grain boundaries in Figure 3.3(d) is accentuated for the CdCl₂ treated sample, caused by injection of electrons into the grain boundaries from the probe. This indicates that the grain boundaries are less *p*-type than the grain interiors in the treated sample. While applying a negative voltage, the sample undergoes forward bias and the current flow in this regime is due to electron injection from the *p-n* junction into the CdTe layer. The magnitude of the current under negative applied bias is limited by the electron collection of the AFM tip and/or by the recombination of charge carriers at the back Schottky contact. While this technique is a great approach to directly map the current generated by a solar cell with nanoscale spatial resolution, much care should be taken when acquiring images, as the thin conductive coating of the probe can be easily removed, producing artifacts in the electrical signal.

Scanning capacitance microscopy (SCM) maps the differential capacitance ($\delta C/\delta V$), enabling dopant concentration imaging in microelectronic systems such as solar cells.

Briefly, the capacitance of a semiconductor can be tuned by applying an alternating electric field to a conductive-coated tip, and is subsequently measured by tracking the third harmonic frequency of the cantilever. [101] The type of doping (n or p) can be deduced based on the sign of $\delta C/\delta V$, while the magnitude of the capacitance is based on carrier concentration. [102] Further, there has been some research effort to quantitatively link $\delta C/\delta V$ to charge carrier concentration in different types of semiconductors materials, such as Si, GaN, and others. [103] Daisnke's group imaged a cross-sectional SCM map of a CIGS solar cell, Figure 3.3(e), showing the qualitative carrier concentration at the CdS/CIGS n-p junction. [73] Both the accumulation and depletion regions were directly mapped, important for determining where the electrons and holes are generated throughout the PV films.

3.2.2.1 Attributing electrical properties to performance

While standard electrical property mapping is an extremely informative way to gain fundamental insights about PV materials and devices, quantifying and relating nanoscale charge carrier phenomena back to device performance is a critical next-step that will lead to the rational design of solar cells with high power-conversion efficiencies. There has been novel research that links the acquired electrical output to a relevant solar cell parameter, namely photovoltage and photocurrent. We recently modified illuminated-KPFM to quantify the local open-circuit voltage (V_{oc}), [37] one of the most important figures-of-merit that define PV performance, discussed in depth in Chapter 5. For this, the AFM probe must be grounded with respect to the bottom electrode of the solar cell and the experimental setup calibrated. In this way, when both a dark and an illuminated KPFM map are acquired on the same region of a sample, and subsequently subtracted,

the remaining value is the quasi-Fermi level ($\Delta\mu$). As seen in Equation 3.2, $\Delta\mu$ is directly proportional to the V_{oc} of the PV device:

$$\Delta\mu = V_{oc} \times q \quad (3.2)$$

where, q is the elementary charge. Figure 3.4(a) shows a V_{oc} map containing two grain boundaries in a CdTe solar cell with distinct and contrasting electrical behavior. The defect highlighted on the left locally reduces the V_{oc} by 60 mV while the grain boundary on the right acts similar to the grain interiors, maintaining a voltage response comparable to its surrounding grains. Here, we determined the quantitative contribution of CdTe grains and grain boundaries to the local V_{oc} . We also revealed local voltage variations in CIGS solar cells as high as 250 mV, demonstrating the large influence that the microstructure can have on the recombination of charge carriers, consistent with other KPFM measurements on CIGS. [104] Overall it was demonstrated that this powerful nanoimaging approach is a universal tool to directly map the local V_{oc} of mono-, polycrystalline, and perovskite solar cell devices, and works in ambient environment. [37, 39] For more information see Chapters 5 and 6.

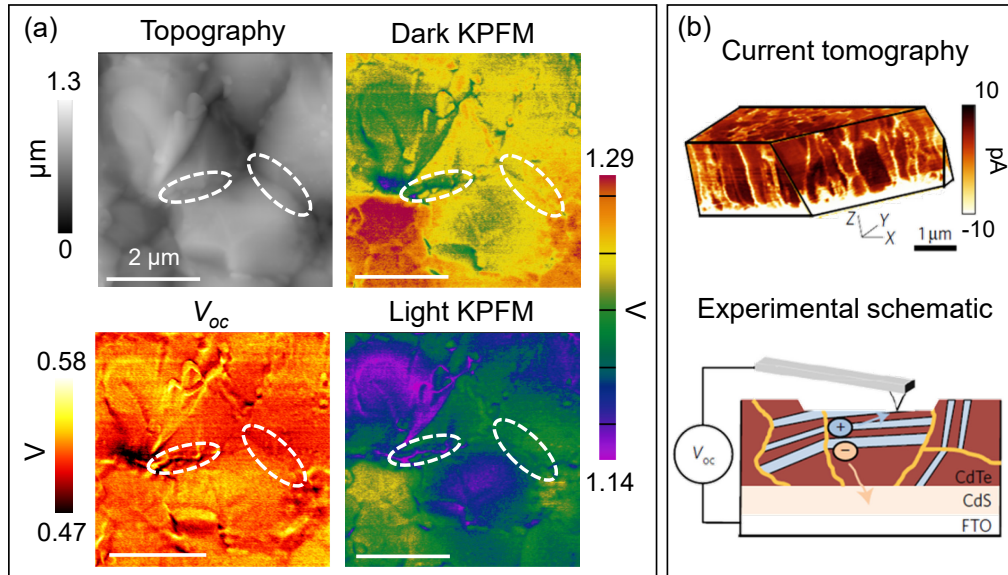


Figure 3.4: **Photovoltaic performance at the nanoscale.** (a) Illuminated-KPFM on a CdTe solar cell results in direct imaging of the local V_{oc} by subtracting an illuminated scan by a dark one. Adapted with permission from ref [37]. ©2015 WILEY-VCH Verlag GmbH & Co. KGaA, Weinheim. (b) A variant of cAFM, conducting tomographic AFM, biased near V_{oc} . A tough diamond-coated probe was used to etch away the top surface layer after each current map of a CdTe solar cell. Adapted by permission from Macmillan Publishers Ltd: Nature Energy [93], copyright 2016.

AFM-based techniques are often limited to imaging properties at the sample surface; however, a method recently developed, conducting tomographic AFM, maps the photocurrent in 3D, demonstrated in Figure 3.4(b). [93] In pcAFM mode, a diamond-coated probe with a high toughness value, iteratively etches away the top few nanometers of the surface to reveal CdTe grains and their respective photo-generated current. While this technique is destructive in the scanned region, charge carrier transport pathways previously hidden, are measured. Using this method, Huey’s group identified inter- and intra-grain planar defects attributed to local wurtzite and zincblende structure variations, consistent with stacking faults imaged with transmission electron microscopy (TEM) of the same sample. Further, by scanning the region biased, grain boundaries with n -type characteristics were resolved.

3.2.3 Imaging local chemical properties

Very recently, researchers have extended AFM to map the chemical information of materials for PV at the nanoscale. [105] Now, more than ever, identifying the elemental distribution with nanoscale spatial resolution is relevant for heterogenous, next-generation PV technologies to improve the state-of-knowledge of crucial unanswered questions, such as: “Where do the Br₃, Cl₃, or I₃ ions segregate in mixed perovskite materials upon illumination?”, [106,107] “Is the non-uniform electrical response of perovskites related to variations in chemical composition?”, [39,51] “Is it possible to chemically resolve where the different species in a block co-polymer thin film preferentially accumulates/segregates?”, [108] “What is the primary substance limiting the electrical conductivity in polymer solar cells?”, [109] and “Are the majority of grain boundaries in CZTS thin-film solar cells of Cu-rich or Cu-poor composition?”. [59]

Tip-enhanced Raman spectroscopy (TERS) is an effective method to image the chemical composition of materials. [110–112] The experimental setup for TERS requires a high-intensity polarized light focused on the apex of a metal-coated AFM probe (*e.g.* Ag or Au) held ~ 20 nm above the sample surface. The interaction between the incident far-field photons and the tip induces a large electromagnetic near-field enhancement, capable of exciting Raman vibration modes. The amplification effect is attributed to localized surface plasmons that are generated by the incident photon energy, which is usually near the resonant peak of the metal coating on the AFM cantilever. [110, 113, 114] The strong excited optical field is coupled into a spectrometer, where each pixel in a TERS map corresponds to a spectrum. TERS is particularly useful when analyzing systems with inhomogeneous chemical composition distribution, such as perovskite and organic

solar cells, as the agglomeration or separation of elemental compounds can deteriorate the electrical performance of the devices. Figure 3.5(a) shows the topography (top) and corresponding TERS image (bottom) of a PCBM (acceptor) and poly-(3-hexylthiophene) (P3HT, donor) polymer solar cell. [109] Meixner's group attributes the bright red feature in the center of the chemical map to a PCBM aggregate that formed on the surface of the polymer due to an unoptimized annealing step. PCBM was identified by both the Raman and photoluminescence (PL) spectra in this region, and the spatial distribution of the chemical trace was only discernable in the TERS imaging. Confocal microscopy was attempted in the same location and no change in the Raman signal was detected. This PCBM aggregate is responsible for the limited electron transfer observed in these polymeric solar cells, resolved by TERS measurements.

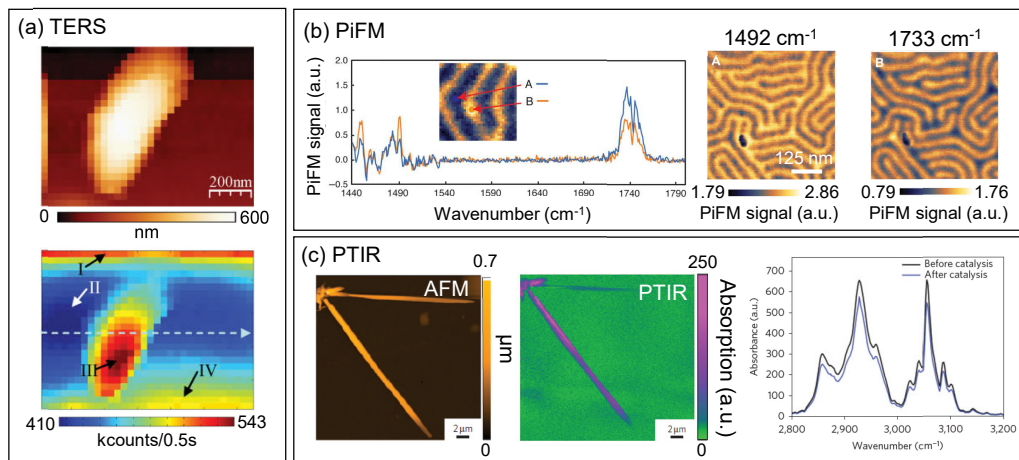


Figure 3.5: **Nanoimaging chemical properties in solar cell materials by AFM.** (a) Topography (top) and near-field TERS map (bottom) of a polymer material, wavenumber range from 283 to 2926 cm^{-1} was integrated. Region III indicates the agglomeration of PCBM molecules. Adapted with permissions from ref [109]. ©2010 WILEY-VCH Verlag GmbH & Co. KGaA, Weinheim. (b) PiFM images acquired at two distinct wavenumber excitations showing the two phases of a co-block polymer material. Reprinted/adapted from [107]. ©The Authors, some rights reserved; exclusive licensee American Association for the Advancement of Science. Distributed under a Creative Commons Attribution NonCommercial License 4.0 (CC BY-NC) <http://creativecommons.org/licenses/by-nc/4.0/>. (c) Topography and PTIR absorption map acquired at 3054 cm^{-1} of a PDPB nanofiber. Corresponding PTIR absorption spectrum of the C-H stretching modes both before and after catalysis. Adapted by permission from Macmillan Publishers Ltd: Nature Materials [115], copyright 2015.

Photo-induced force microscopy (PiFM) is an emerging approach that was developed in 2010. [116] Here, the near-field Raman signal is detected in noncontact mode. Thus, changes in the time averaged force gradient of the tip-sample interaction are measured, rather than a spectrum. [117] During the experiment one (tunable) or two lasers (of different wavelengths) are focused onto the sample; they modulate at frequencies that are selected based on the first and/or second resonance of the cantilever. The external excitation generates a unique response in the force curve that is captured by a lock-in amplifier. [118] In general, the experimental setup is compatible with bottom-illumination with a high numerical aperture objective lens. The spatial resolution of the PiFM image is slightly better than the simultaneously acquired topography map because the PiFM is

both excited and detected in the near-field regime. The signal-to-noise ratio of PiFM is substantially larger than the one of TERS because the latter is detected in the far-field regime. These advantages extend chemical imaging spatial resolution, which can be used to reveal nanoscale domains within composites, or to determine the specific segregation regions in mixed perovskites. [106, 119] As a proof of concept and to demonstrate the power of this technique, Park's group imaged a block co-polymer material, poly(styrene-*b*-methyl methacrylate) (PS-*b*-PMMA), with very well defined Raman molecular signatures and identified each chemical compound with <10 nm resolution, see Figure 3.5(b). [108] A point-by-point PiFM response spectrum is shown on the left, executed by sweeping a quantum cascade laser at the given wavenumber and recording the magnitude of the cantilevers deflection. On the right side of Figure 3.5(b), two PiFM images in the same location are acquired by consecutively exciting the sample at wavenumbers 1492 cm^{-1} (for PS), and 1733 cm^{-1} (for PMMA), where both polymers are clearly resolved. Regions of PS appear brighter in the map using the 1492 cm^{-1} excitation because its near-field Raman signal is stimulating the cantilever at its resonance frequency, detected by lock-in amplification. Note that it is necessary to know the Raman spectrum of the sample under investigation before performing PiFM to ensure appropriate selection of the excitation wavenumber. PiFM is, thus, a very promising AFM-based tool to probe materials for PV ranging from perovskites to CIGS, where local variations in chemical composition might affect carrier recombination and collection.

Photothermal induced resonance (PTIR) microscopy, or AFM-IR, combines precise IR spectroscopy with the spatial resolution of an AFM. [120, 121] Here, an external, tunable IR laser is pulsed while the AFM cantilever is in contact mode. This photon excitation induces local heating of the sample faster than the acquisition of the AFM feedback

and proportional to the thermal expansion coefficient of the material. As each chemical species has a unique thermal expansion coefficient, chemical identification is attainable at the nanoscale. [122,123] In most cases, devices or thin films under investigation are placed on top of a glass prism, where the incident light is reflected up to the sample by total internal reflection. [124] This method has been applied to resolve ferro-elastic domains [125] and the distribution of Cl as a function of wavelength and annealing time, [107] in perovskites. In Figure 3.5(c), both topography and PTIR maps are presented on a UV- and visible-light photocatalytic energy harvesting material, poly(diphenylbutadiyne) (PDPB). [115] Here, the conductive polymer was fabricated as a nanofiber, because the photocatalytic reaction of the one-dimensional design was more efficient than its bulk counterpart. One major challenge with current light harvesters is their long-term stability, thus, Remita's group investigated PDPB, a promising material that does not require any precious metal nanoparticle co-catalyst. Nanoscale PTIR measurements demonstrated the polymer reusability, as any composition degradation would be visualized in the absorption map. Further, the spectra on the right side of Figure 3.5(c) show the reproducible C-H stretching vibration modes at 3054 cm^{-1} both before and after undergoing catalysis. The overlap in the spectra indicates that there was no change in chemical composition, indicative of a stable, photocatalytic material. This chemical mapping technique could also extend to metallic nanostructures for energy harvesting, [126] not possible with TERS or PiFM, as many metals (e.g. Ag and Au) do not have a clear Raman response.

3.2.4 Optical properties at the nanoscale

Combining the information gained from a traditional optical microscope with the spatial resolution of an AFM yields a highly impactful imaging approach that can reveal

optical phenomena (i.e. reflection, absorption, and transmission), and electrical properties of materials for energy harvesting. Acquiring an optical response at the nanoscale requires a small antenna (or probe) that either excites and/or collects the near-field optical signal, entitled near-field scanning optical microscopy (NSOM, or SNOM). Here, the optical information obtained is beyond the diffraction limit of light, restricted instead to the diameter of the NSOM probe. [127] Through NSOM measurements scientists are beginning to answer questions such as: “Does the migration of MA^+ and I^- ions in perovskites impact the index of refraction of the material?”, [128] “How can one efficiently couple far- to near-field light in order to image radiative recombination in nanoscale structures of optoelectronic devices?”, [129] “What is the spectral dependence on the local photocurrent enhancement in CdTe and CZTS grain boundaries?”, [130, 131] and “What is the correlation between the facets of GaAs polycrystals and their carrier radiative emission rate?”. [44, 66]

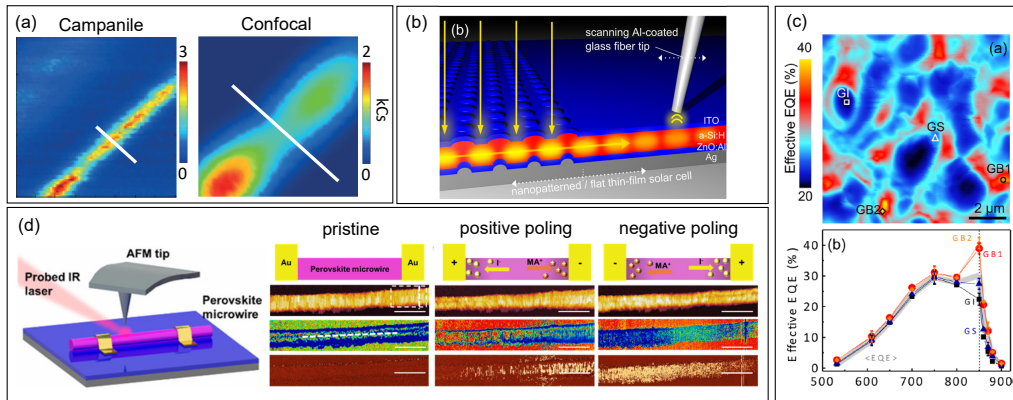


Figure 3.6: Nanoimaging optical properties in solar cell materials by AFM. Clockwise: (a) PL maps acquired with a near-field campanile probe and confocal objective, respectively, of an InP nanowire in a $2 \times 2 \mu\text{m}^2$ region. From [129]. Reprinted with permission from AAAS. (b) Illustration of NSOM in collection mode utilizing an aluminum-coated glass fiber tip to compare the near-field optical resonance of nanopatterned region vs. a flat region on an a-Si device. [132] (c) Effective EQE map measured at 850 nm (top) and average spectrally-dependent EQE graph (bottom) calculated from NSOM-LBIC images of a CdTe solar cell. Adapted from ref [130]. (d) Left: schematic of s-NSOM. Right: s-NSOM measurements on a perovskite microwire under different poling conditions, used to measure ion migration; scale bar is 500 nm. In the s-NSOM amplitude maps: red = high signal, blue = low signal. Adapted from ref [128].

In near-field optics the distance between the illumination/collection source (the NSOM probe) and the sample surface is significantly less than the wavelength of light (~ 10 nm). The theoretical description of the near-field effect was introduced in the 1920's [133] but was realized more than half a century later. [134, 135] The major experimental innovations that led to the successful implementation of NSOM are: (i) depositing a thin metal coating over the NSOM probe to help guide light into the nanoscale aperture, and (ii) including a feedback loop to continuously monitor/adjust the tip-sample distance. NSOM can be performed in multiple configurations, [136] ranging from excitation-only to reflection+collection. Below, we review the two most useful NSOM modes for solar cells: (i) collection and/or excitation and (ii) apertureless, where there is a discussion about how these methods can be extended to determine relevant information about PV device performance.

In NSOM-PL, also detailed in Chapter 8, the probe acts as both a collection and an excitation source. For this, incident light passes through the small hole in the NSOM probe and the subsequent photon emission caused by the radiative recombination of charge carriers in the solar cell is collected back through the same aperture. One example of high-efficiency, bidirectional far-to-near field coupling is presented in Figure 3.6(a), [129] where Weber-Bargioni's group employed a new probe design shaped similar to a campanile bell tower, to promote a more effective waveguide for far-to-near field coupling in a wide spectral range. In Figure 3.6(a), NSOM and confocal PL maps of an InP nanowire (NW) are compared; each pixel represents the amplitude of the emission signal at 802 nm. It is immediately apparent that the image acquired with the campanile probe has much higher spatial resolution, elucidating the spatial distribution of PL within a single NW. The non-uniform emission is associated to trap-state modifications of the localized excitons,

an important discovery if InP NWs are to be implemented into light-harvesting devices. Since this study, there have been more NSOM-PL investigations [137] of the optoelectronics properties of solar cell materials including perovskites [138] and InGaN/GaN, [139] each presenting novel insights about the local distribution of radiative and non-radiative recombination mechanisms.

NSOM using an aperture in the collection-only configuration illuminates a large region of the sample and gathers the evanescent fields of photons propagating through the surface of the device. The NSOM probe is maintained at a distance of ~ 20 nm above the sample, close enough to allow tunneling of the guided photons. In the example shown in Figure 3.6(b), [132] Paetzold *et al.* have used NSOM in collection mode to resolve the near-field enhancement induced by patterned nanostructures within a solar cell as a function of both wavelength and light polarization. [132] Their results complement the macroscopic measurements of external quantum efficiency (EQE) improvement due to the addition of metallic nanostructures. [140]

One application of NSOM in excitation-only mode is light beam induced current (LBIC) microscopy, where the photogenerated current can be spatially resolved at the nanoscale. [141] A spot size equivalent to the diameter of the aperture illuminates a solar cell and locally generates a flow of charge carriers. The photocurrent signal is typically detected by using the macroscopic contacts of the device. Resolving the light-generated current at the nanoscale is relevant when the feature size that composes a solar cell material is of a similar dimension, *e.g.* grain boundaries. [131] In Figure 3.6(c) spectrally-dependent NSOM-LBIC is applied to a CdTe solar cell. [130] Nanoscale spatial variations of the EQE (calculated from photocurrent measurements) at grain boundaries (GB) vs. grain cores (GC) were measured. Overall, Leite *et al.* found that GBs generate more photocurrent,

hypothesized to be a local reduction in bandgap. One advantage of this optical technique over pcAFM is that it is performed in non-contact mode. Thus, contact artifacts from the tip are reduced. However, the signal-to-noise ratio is substantially lower in NSOM-LBIC, and more sensitive current detectors are required.

Apertureless NSOM or scattering-NSOM (s-NSOM) follows similar operating principles as collection-only mode, *i.e.* excitation uses far-field light and the optical response from the sample is collected in the near-field. [142] However, here, the probe is not hollow, but instead a sharp, metallic tip (most cases an AFM probe) kept <20 nm from the illumination spot. The apex enhances and disperses the near-field interaction induced by the incident light occurring at the sample surface, the signal is then acquired with far-field detectors. To further increase the near-field enhancement effect, it is suggested to use an AFM probe that is coated with a thin layer of Au. [143] Because in s-NSOM the tip no longer wields an aperture, the spatial resolution is equivalent to standard AFM. As previously mentioned, ion migration in perovskite materials is hypothesized to induce instabilities and degradation in the overall electrical performance. In Figure 3.6(d), Bao's group implemented apertureless NSOM to nanoimage, in situ, how the electric-field poling direction of a perovskite device influences MA^+ and I^- ion migration. [128] A microwire is used to isolate and confine the direction of the ions. Near-field optical maps were obtained under mid-IR ($11.7 \mu\text{m}$) illumination to map the index or refraction and free-charge carrier distribution. On the left of Figure 3.6(d) an illustration of the experimental setup is shown. The top portion of the right three images displays a schematic of the observed phenomenon occurring in the microwire under pristine (no applied voltage), positive poling (+10 V), and negative poling (-10 V) conditions. The topography, near-field optical amplitude, and phase images under these three conditions are presented

for comparison, respectively. According to the topography maps, the perovskite material expands in the poling direction, which is also in the same orientation as the migration of the MA⁺ ions. The authors calculate that the material expansion is 4.4%; the measured shrinking-swelling effect in the perovskite structure could be one source of device degradation. Further, the near-field amplitude (here, representing the local carrier density) response is uniform under pristine conditions, but during poling the distribution of charge carrier changes: MA⁺ ions accumulate near the negative side and I⁻ shifts toward the positive electrode, possibly generating a temporary *p-i-n* junction. In the near-field phase maps (related to the perovskites refractive index), the negative electrode has a much larger signal, indicating a decrease in absorption due to the swelling of the perovskite. Although very informative, this microscopy method suffers from high background noise due to the far-field excitation. Therefore, double lock-in or other background-suppression methods should be implemented to extract the near-field signal. [136]

3.3 Probing dynamic processes in perovskite solar cells

Due to the high interest in perovskites for energy harvesting, this Chapter section is dedicated to cutting-edge research that investigates the electrical, chemical, and/or optical properties of these intriguing materials with nanoscale spatial resolution. With promising, single-junction power conversion efficiencies >22% [4] and a new record tandem perovskite/Si solar cell of 23.9%, [144] the prospect for commercializing this PV technology is approaching fruition. Moreover, there has been a recent article by Nazeeruddin's group announcing a one-year stable perovskite solar cell, [145] indicating that our ability to optimize and control these complex materials is increasing. Yet, there are still many challenges that lie ahead and we are continuing to discover answers to important scientific

questions such as: “Can we capture the real-time effects of light illumination on the local V_{oc} of perovskites?”, [39] “How do the radiative recombination distributions of charge carriers in MAPbI₃ vs. MAPbBr₃ perovskite compounds differ?”, [138] “Are Cs-containing triple-cation perovskites more stable than conventional ones?”, [146, 147] “What is the role of humidity on the perovskite local electrical response?”, [50, 148] and “What are the perovskite material options that are stable upon illumination?”. [149, 150]

Perovskite solar cells experience performance instabilities caused by transient processes upon material illumination, [151] and exposure to humidity and oxygen. [152, 153] Imaging these dynamical events at relevant length scales have become an important next-step towards identifying stable materials and devices. Rapid temporal mapping will likely elucidate the transport of charge carriers after excitation, spatially identifying where trap-states are located. In Figure 3.7(a), our group measured the real-time, photo-induced voltage response of a MAPbI₃ perovskite solar cell before, during, and after illumination with fast-KPFM. [39] More details will be discussed in Chapter 6, but briefly, each KPFM map (left of image) is acquired in 16 seconds (two orders of magnitude faster than conventional methods), therefore, it is possible to capture how the electrical signal changes as a function of time. Immediately after the light is turned OFF the photo-generated voltage ceases. However, the charge distribution is very different from the initial dark scan, as seen by comparing both the KPFM map and the voltage histograms (right side of panel). In fact, the perovskite’s electrical performance remains out of equilibrium for nine minutes, until finally stabilizing and returning to its initial dark conditions. While perovskite performance instability on the time scale of several minutes has been observed macroscopically, [49] by imaging with nanoscale spatial resolution, two distinct regions with contrasting voltage decay rates were found to coexist within a single MAPbI₃ grain,

resulting from ion migration. [39] The next step is to identify the relationship between this dynamic electrical response with local chemical composition variations. This point will be addressed in more detail in the future work portion of this thesis.

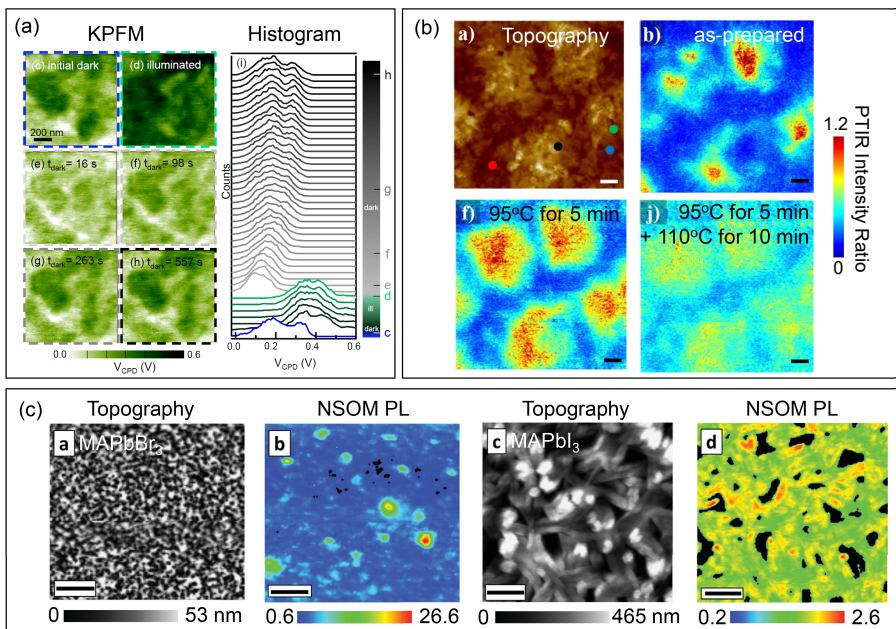


Figure 3.7: **Imaging electrical, chemical, and optical dynamics in perovskite solar cells by AFM.** (a) Sequence of fast KPFM on a perovskite solar cell under dark and illuminated conditions; each map takes 16 seconds. Right graph shows voltage histograms for 42 fast-KPFM maps. [39] (b) Topography and three PTIR maps measured at different annealing temperatures of a thin-film perovskite, where the blue regions of the map refer to high Cl concentration; scale bar is 1 μm . Adapted from [107]. (c) NSOM topography and simultaneous PL images of two perovskite compositions, MAPbBr₃ and MAPbI₃, scale bar = 4 μm . Reproduced with permission. [138] Copyright the authors, published under CC-BY 4.0 license 2015.

Mapping the local elemental distribution in perovskites is of major interest for the PV community to help determine where ions are segregating and/or migrating. For example, in Figure 3.7(b), a MAPbI_{3-x}Cl_x sample is annealed in situ and the AFM (top left) and PTIR signals are acquired during each thermal step. By identifying the PTIR proportion between high and low incident photon energies, local changes in the perovskite bandgap are distinguished. It is well understood that the addition of Cl increases the bandgap energy of the MAPbI₃, therefore, regions of high Cl concentration are discerned

(blue in the PTIR maps, red indicates Cl-poor areas). Local increases in bandgap in the as-prepared sample as high as 0.3 eV were measured. However, upon further annealing the bandgap continuously decreases, indicating that Cl content is reduced with temperature, likely caused by MA₂Cl sublimation. Additional spectrally-dependent PTIR imaging with high spatial resolution on the wide variety of perovskite materials would be extremely informative, particularly to determine the role of absorption of different elements causing the instabilities of solar cell efficiency. Recently, a novel AFM-based chemical imaging method called peak-force infrared microscopy mapped the distribution of methylammonium in a MAPbBr₃ nanocrystal. [154]

To image the radiative recombination centers in perovskite materials, Deschler's group implemented NSOM-PL on both MAPbI₃ and MAPbBr₃ thin films. Figure 3.7(c) displays the simultaneously acquired topography and PL maps for each sample. The sample containing Br₃ has a more homogenous morphology, while the I₃ film has needle-like features with 25% of the scanned region comprised of voids. The PL signal shows localized hot spots (two orders of magnitude increase) in the Br₃ sample that are not correlated with the topography. However, the I₃ containing thin film displays some PL variation, but the brighter regions are not nearly as dramatic as in the Br₃ one. Their results, in combination with time-resolved PL measurements on the same samples, revealed that regions of high radiative recombination for both thin films have slower charge carrier decay rates. The authors concluded that the areas with higher PL emission are decoupled from the low PL regions through either a slow diffusion process or energy barrier that prevents the charge carriers from moving laterally in the perovskite layer. It is also hypothesized that higher luminescent sites are regions of enhanced structural order and better crystalline quality. AFM is a vital tool set for advancing the state-of-knowledge

of the dynamic responses of perovskites when exposed to ambient environment, where measurements prior to full device development are extremely important for the screening and classification of stable alternatives.

3.4 Summary

In this introductory chapter, we presented selected AFM methods that led to recent discoveries related to the electrical, chemical, and optical responses of materials and devices for the most promising polycrystalline PV materials. Revealing the fundamental properties of these systems is crucial to increase our understanding of the underlying mechanisms that define device performance at the nanoscale. Ultimately, we envision that high spatial resolution investigations will lead to the redesign of materials with improved performance, as well as devices.

In this summary section we provide an outlook of how AFM can be further implemented to address pressing problems in materials for photovoltaics and energy storage. First, we speculate how fast AFM methods could be used to help elucidate the role of the ambient environment onto the degradation of perovskites. Then, we discuss the need for advancing NSOM-based methods which, to date, are not widely implemented. Measurements using NSOM are particularly relevant to tackle open questions in polycrystalline PV.

Nanoscale mapping of performance through KPFM and cAFM can potentially deconvolute the role of humidity, oxygen, illumination, bias, and temperature on perovskites degradation, including their effect on both grains and grain boundaries. These measurements are likely to redefine the design of solar cells using conventional and emerging perovskites, considering their contact interfaces. We anticipate the nanoimaging of per-

ovskites through “fast” AFM techniques, such as heterodyne-KPFM [34, 39, 155], KPFM G-mode extension, [156] or 2ω D-KPFM [157] to elucidate their dynamic electrical behavior at relevant length scales, critical to identify the driving forces behind its instabilities. In particular, we expect researchers to correlate the changes in the optoelectrical properties (photovoltage, photocurrent, and PL) with possible chemical composition variations through correlative microscopy (KPFM + cAFM + PiFM) on the very same grains. AFM experiments where one can elucidate the effects of ambient environment on the local electrical and optical properties will probably focus on correlative microscopy, in order to define how each parameter affects charge carrier generation, recombination, and collection, all critical for device performance. We also expect NSOM-PL, KPFM, and TERS to help us identify which perovskites compositions are stable under illumination. While extensive effort has focused on determining the ideal synthesis parameters for optimized device performance, substantial work lies ahead to identify what triggers ion migration and/or material segregation upon sample illumination and exposure to ambient conditions. This class of material has ~ 100 options, [149] thus, measurements on thin films will accelerate a high throughput and effective material selection, prior to device processing development.

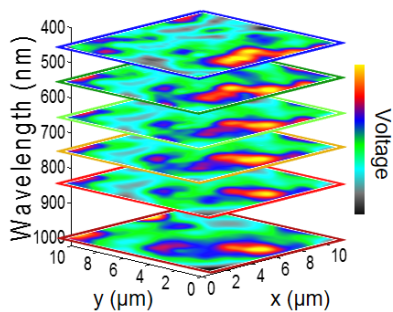
Concerning polycrystalline materials for PV, direct measurements of light-matter interactions through underutilized NSOM-based techniques are critical for tackling relevant open questions. For local optical measurements, better NSOM probes are being designed and engineered to optimize the far-to-near field light coupling, as the current transmission loss is still 3-6 orders of magnitude. [158, 159] More efficient probes will allow for mapping on a broader variety of low-emission materials, including CIGS and CZTS. NSOM-PL will further impact polycrystalline GaAs fabrication, [160] as the dependency

of radiative recombination on different types grain facets could be resolved. We also anticipate KPFM measurements combined with scanning electron microscopy to become more common, [161] where one can correlate, in situ, the electrical response of grains and grain boundaries with their crystalline orientations. To probe the p - n junction in inorganic solar cells, such as CdTe and CIGS, KPFM and cAFM should be applied in cross-section after cleaning the sample in an oxygen-free environment, to prevent surface recombination due to the material's exposure to air. For that, it's best practice to operate the AFM inside a glove box, where the samples can also be cleaved.

In the past three decades AFM has become the standard characterization tool to image the morphology of a specimen. In the years following its conception, scientists have modified the instrumentation to image beyond its typical measurement mode, and unleashed an array of new research opportunities to map other material properties. We have no doubt that novel adaptations will continue to develop, as speculated above. It's all at the tips of our fingers!

Chapter 4: Photovoltage Tomography in Polycrystalline Solar Cells

To date, the performance of all polycrystalline photovoltaics is limited by their V_{oc} , an indicator of charge carrier recombination within the semiconductor layer. Thus, the successful implementation of high efficiency and low-cost solar cells require the control and suppression of non-radiative recombination centers within the material. In this Chapter, we spectrally and spatially resolve the photovoltage of polycrystalline thin-film CIGS solar cells. Micro-Raman and EDX maps obtained on the same grains showed that the chemical composition of the CIGS layer is very uniform. Surprisingly, we observed concurrent spatial variations in the photovoltage generated across the device, strongly indicating that structural properties are likely responsible for the non-uniform mesoscale behavior reported here. We build a tomography of the photovoltage response at 1-sun global illumination, mimicking the operation conditions of solar cells. Further, we spatially resolve the voltage within the CIGS grains, where we found variations $>20\%$. Our functional characterization could be implemented to identify where non-radiative recombination preferentially takes place, enabling the implementation of non-uniform materials for future devices with higher V_{oc} . This chapter is adapted from E.M. Tennyson et. al, *ACS Energy Letters*, **1** 899905 (2016) [40]



4.1 The need for tomography in thin film photovoltaic devices

This chapter investigates thin film Cu(In,Ga)Se₂ (CIGS) solar cells, as they are a practical alternative to commercially available Si photovoltaic (PV) devices due to their low cost and high efficiency. [162, 163] Further, these technologies have the advantage of being fabricated on top of either a rigid or flexible substrate, extending solar cell devices towards a variety of applications. To date, the record CIGS device has an efficiency of $\eta = 22.6\%$ and open-circuit voltage of $V_{oc} = 741$ mV, which was fabricated using the well-established multi-stage co-evaporation technique. [164] However, the sequential deposition steps substantially increase the overall production cost of CIGS, preventing its wide commercialization. [165, 166] An alternative fabrication technique is the sputter deposition of CIGS through a single quaternary target. [167–169] This method can be implemented in large-scale applications and also avoids a necessary but toxic post-deposition selenization step. [170] Despite the advantages of the quaternary target method, the typical V_{oc} of the PV devices is ~ 500 mV, well below the Shockley-Queisser theoretical limit (~ 813 mV for CIGS with $E_g = 1.213$ eV). [6, 7] Thus, as discussed in Chapters 1 and 3, the V_{oc} is currently restricting the performance of CIGS solar cells. Because the CIGS absorbing layer is inhomogeneous and composed of micro-scale grains, it has been speculated that the electrical response of the material could be limited either by composition variations within the grains or by the different interfaces throughout the thin film polycrystalline layer. [56, 171]

In order to probe the local structural and electrical characteristics of materials for PV, scanning probe and electron microscopies have been widely implemented. [56, 172, 173]

The local electrical response of these inhomogeneous materials have been determined by laser-beam [95, 174–176] and electron-beam induced current, (EBIC) [55, 177–179] conductive-atomic force microscopy, [180–183] Kelvin probe force microscopy, (KPFM) [37, 180, 184] scanning probe microwave capacitance, [185] near-field scanning optical microscopy, [130–132, 186, 187] cathodoluminescence, [188, 189] and photoluminescence. [190–195] Further, spectroscopic methods, including electron energy loss spectroscopy (EELS) [196] and X-ray microscopy, [197, 198] have been implemented to reveal how chemical composition variations within the active layers affect the electrical response of the devices. Recently, micro-Raman mapping also became a tool to link material composition to optoelectronic properties. [11, 199] Nevertheless, a high spatial resolution ($<1 \mu\text{m}$) spectroscopic imaging platform to resolve possible photovoltage variations of polycrystalline solar cells that does not require special sample preparation or an inert environment is still missing.

Here, we spectrally and spatially resolved the photovoltage of polycrystalline thin film CIGS solar cells from a quaternary target, which is related to the charge carrier recombination events within the absorbing layer of the device. Micro-Raman maps obtained on the same grains revealed that the chemical composition of the CIGS layer is very uniform, in agreement with our energy-dispersive X-ray spectroscopy (EDX) results. Surprisingly, we observed concurrent spatial variations in the photovoltage generated across the device, strongly indicating that structural properties are likely responsible for the non-uniform mesoscale behavior reported here. We built a qualitative tomography of the photovoltage through a sequence of spectrally dependent voltage scans at low photon injection level, mimicking realistic operation conditions of photovoltaic devices. The mesoscale electrical response of the material varied at the same length scale as the grains, and different

sites (interfaces and groups of grains) showed distinct photovoltage, depending on wavelength (λ), where voltage variations $>20\%$ were measured. These results demonstrate that the of CIGS solar cells is limited by the types of interfaces existing between the grains composing the active layer of the devices. Further, we provide a universal and direct method to map voltage with high spatial resolution without the use of a scanning probe or vacuum environment that can be applied to other optoelectronic devices, such as LEDs, photodetectors, *etc.*

4.2 Experimental methods

4.2.1 CIGS solar cell fabrication

The CIGS solar cell samples were fabricated via sputtering from a quaternary target. [167] The substrate for all samples was soda lime glass coated with 700 nm of Mo. coated with 2.0 μm thick *p*-type CIGS films deposited by RF magnetron sputtering. Then, a chemical bath deposition of 50 nm thick *n*-type CdS layer was performed, and a 500 nm transparent conductive top contact with ZnO and Al:ZnO was sputter deposited to enhance current collection. Lastly, Ni/Al grids were evaporated to serve as the top contact. The samples were scribed by hand to obtain individual cells, each with an area of approximately 0.54 cm^2 . Figure 4.1(a) shows a schematic of the CIGS devices. The inset of Figure 4.1(b) is a photograph of six electrically isolated CIGS devices on a single 1 \times 1 in^2 glass substrate.

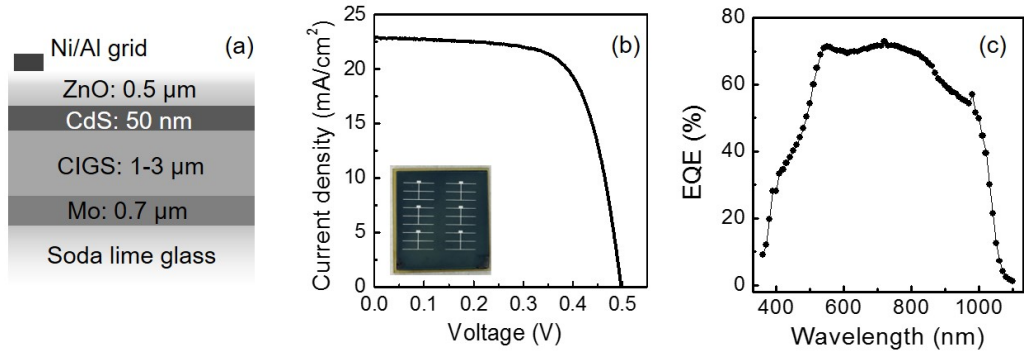


Figure 4.1: **CIGS polycrystalline solar cells fabricated by sputter deposition from a quaternary target.** (a) Schematic of CIGS solar cell, out of scale for clarity. (b) Representative light J - V curve for device illuminated with AM1.5G at 1-sun, yielding $V_{oc} = 490$ mV and $\eta = 7.77\%$. The inset shows a photograph of six solar cells electrically isolated on a single 1×1 in² glass substrate. (c) EQE measurement of the same device shown in (b).

4.2.2 Device macroscopic characterization

Light J - V curves were acquired using a Xenon lamp solar simulator, with 2.0×2.0 in² (50.8×50.8 mm²) output, and an Air Mass 1.5G filter (see Figure 4.1(b) for light J - V curve). The output power of the lamp was set to 1.0-sun (100 mW/cm²). The light source was calibrated with a 20×20 mm² reference monocrystalline Si solar cell with a fused silica window. For the EQE measurement Figure 4.1(c), a xenon arc lamp was directed into a monochromator. Two silicon diodes were initially used: one as a reference and the other for calibration. A beam splitter guided half of the light to the fixed reference diode; the remaining light was directed through another optical path and collected at the position of either the calibration diode or the solar cell sample. Independent measurements using the silicon calibration diode were performed before each EQE measurement was acquired. The ratio of the spectral responses between the solar cell and the calibration diode was computed every 10 nm. The EQE for CIGS was determined between 390 nm and 1100 nm. The low EQE for wavelengths <500 nm results from the expected light absorption

by the ZnO (with $E_g \sim 3.3$ eV) layer and the CdS n -layer (with $E_g = 2.4$ eV) [200].

4.2.3 Raman spectroscopy mapping

A 532 nm laser beam was focused onto the sample using a $100\times$ microscope objective lens (0.75 NA), the scattered light was collected and collimated by the same objective. The scattered signal was then collected by a spectrometer and detected with a liquid nitrogen-cooled charge-coupled-device (CCD). The sample was mounted on an x - y piezo scan stage for the map acquisition. Thus, a Raman spectrum was obtained for each pixel in an image. By applying selective wavenumber filters we produced Raman maps for the relevant vibrations of CIGS.

4.2.4 Photovoltage imaging

Incident light was coupled in to a $25\ \mu\text{m}$ multimode fiber attached to the optical microscope and transmitted through a $100\times$ objective lens, $\text{NA} = 0.75$, focusing a $\sim 1\ \mu\text{m}$ diameter spot onto the surface of the solar cell. The incident photon flux was 1.9×10^{23} photons/ m^2/s for the photovoltage maps shown in Figures 4.4, 4.6, and 4.13, and $>10^{25}$ photons/ m^2/s for Figures 4.8, 4.9, and 4.14. The charge carriers generated by the controlled illumination were collected through their corresponding contacts, one connected to ground, and the other connected to a lock-in amplifier, used to read the electrical output directly from the device at a high signal-to-noise ratio. In all cases, the top contact was $<25\ \mu\text{m}$ away from the scanned region. Here, the lock-in amplifier inherently subtracted the dark current signal from the illuminated scans [174]; thus, the acquired voltage maps refer to an effective open-circuit voltage. A piezo scanner was used to acquire the photovoltage maps for each position of the solar cell, with high spatial resolution. Figure 4.2 displays

a schematic of the experimental setup described here. Because the acquisition of each voltage map took ~ 1 hr, we corrected the drift after each scan to ensure the validity of our wavelength dependent analysis, where the center of the scanned area was recalibrated with the spatial resolution of the piezo scanner (< 100 nm). The average between two neighboring points was taken for all maps shown in this Chapter.

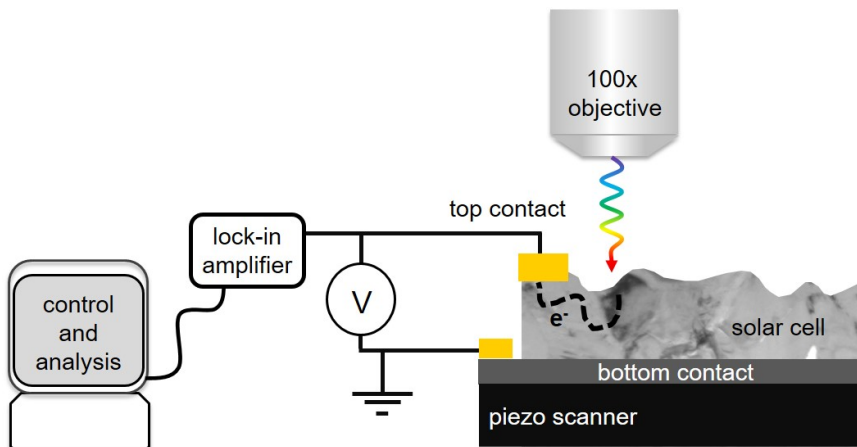


Figure 4.2: **Scanning photovoltage experimental setup.** Incident light is coupled in to a $25 \mu\text{m}$ multimode fiber attached to the optical microscope. The light is transmitted through a $100\times$ objective, $\text{NA} = 0.75$, focusing a $\sim 1 \mu\text{m}$ diameter spot onto the surface of the solar cell. The charge carriers are collected by their corresponding macroscopic contacts, one connected to ground, and the other connected to a lock-in amplifier, which reads the electrical output directly from the device at a high signal-to-noise ratio. A piezo scanner is used to map the voltage signal for each position of the device, resulting in a map with lateral spatial resolution < 500 nm, defined by the beam spot size.

4.3 Correlating chemical and electrical maps in CIGS

We utilize standard characterization methods to obtain the macroscopic photovoltaic performance of the CIGS solar cells investigated here as described in the Experimental Methods section and in ref [167]. The CIGS layer is composed of grains with $\sim 1 \mu\text{m}$ in size, preferentially orientated along the $\langle 112 \rangle$ direction (see Figure 4.3 for a representative SEM and electron back scatter diffraction (EBSD) map).

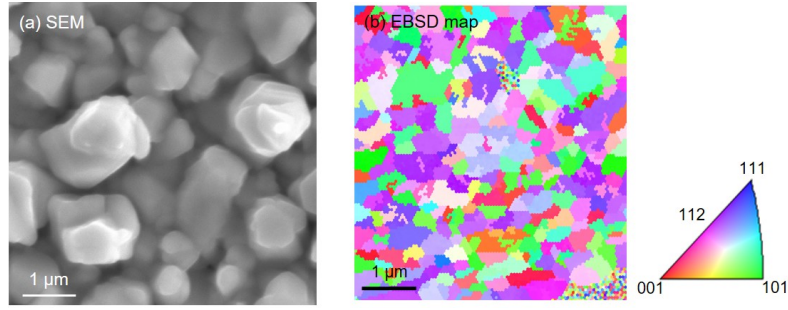


Figure 4.3: **CIGS electron backscatter diffraction pattern.** (a) SEM image of CIGS grains. (b) EBSD map along the normal direction of the CIGS surface showing preferential grain orientation along $\langle 112 \rangle$ direction, as indicated by the color scale on the right.

We investigate the relationship between the chemical composition and the electrical properties of the CIGS devices by micro-Raman imaging and EDX in conjunction with scanning photovoltage microscopy on the *same grains*. For the scanning photovoltage measurements a $100\times$ objective lens is used to focus the local source of excitation, see Experimental Methods.

Remarkable variations in the photovoltage were measured with high spatial resolution, as shown in Figure 4.4. Note that the average voltage signal is small (<2 mV) because of the confined volume of excitation during the measurements (spot area equal $0.95 \mu\text{m}^2$ compared to the total area of the device, equal to 0.54 cm^2), causing a voltage drop to occur between the dark and light regions of the cell. [201, 202] Yet, the electrical variation in the scanned area is 0.5 mV, considerably higher than the noise ($<10 \mu\text{V}$). The representative Raman spectrum with both the strong Cu_{2-x}Se and the chalcopyrite peaks is presented in Figure 4.4(c) (Raman shifts at 295 cm^{-1} and 172 cm^{-1} highlighted in gray and brown, respectively), [203, 204] where the inset refers to the optical micrograph of the region mapped. The micro-Raman images corresponding to the Cu_{2-x}Se and chalcopyrite peaks were acquired on the same location as the voltage map and exhibit uniform surface

chemical composition (despite surface segregation of Cu_{2-x}Se); see Figure 4.4(d,e) (see Figure 4.5 for additional Raman maps). The EDX maps of Cu, Ga, In and Se presented in Figure 4.4(f)-(i) show very uniform elemental distribution in all cases (within the spatial resolution of the SEM probe used). Our chemical composition measurements strongly indicate that the spatial variation observed in the CIGS electrical response is likely due to the distribution of grain orientation or grain boundary types, which could result in areas of high rates of charge carrier recombination. [55, 205]

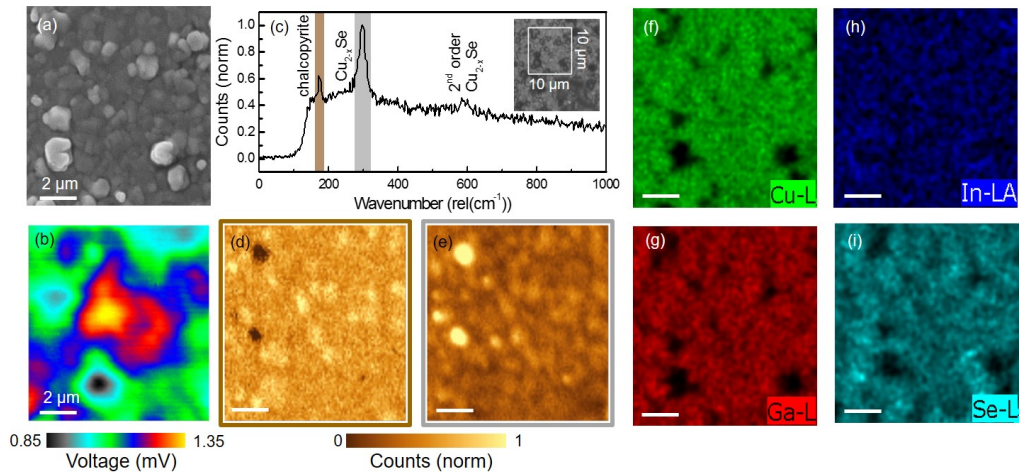


Figure 4.4: **Chemical composition and local electrical response of CIGS solar cells.** (a) SEM image of CIGS. (b) Photovoltage map showing spatial variation $>15\%$; illumination conditions: $100\times$ objective, $\lambda = 575 \pm 3 \text{ nm}$ and incident power $= 298 \pm 3 \mu\text{W}$. (c) Representative Raman spectrum. Inset: optical micrograph indicating the region where EDX, photovoltage, and Raman measurements were acquired (white box). Raman maps of (d) Cu_{2-x}Se peak (grey filter in (c)) and (e) chalcopyrite peak (brown filter in (c)). Illumination conditions for Raman: $\lambda = 532 \text{ nm}$ and incident power $= 100 \pm 5 \mu\text{W}$. EDX maps showing (f) Cu, (g) Ga, (h) In, and (i) Se uniform distribution.

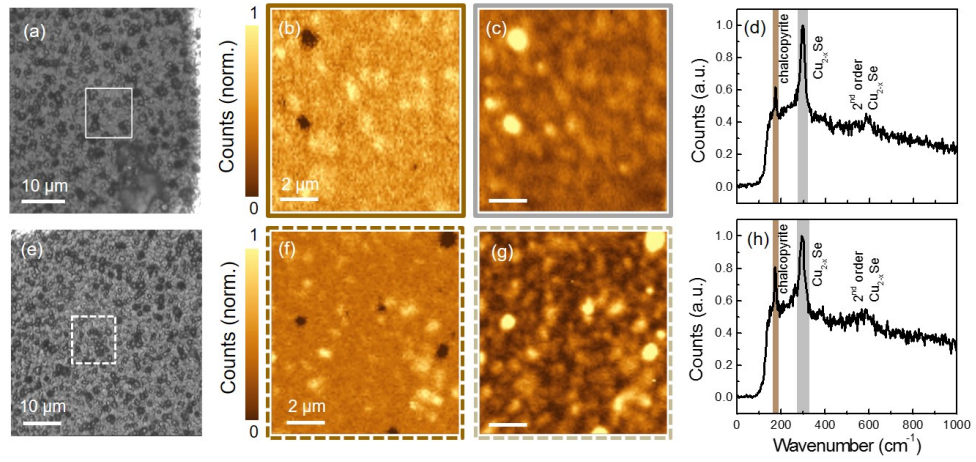


Figure 4.5: **Raman microscopy on CIGS: additional region.**(a,e) Optical micrographs of CIGS solar cell. The white box refers to the $10 \times 10 \mu\text{m}^2$ region where micro-Raman imaging measurements were performed. (b,f) Chalcopyrite peak with Raman shift = 172 cm^{-1} and (c,g) Cu_{2-x}Se peak with Raman shift = 295 cm^{-1} , where each pixel in the images is a spectrum within the brown and gray highlighted region in (d) and (h), respectively. (d,h) Single Raman spectra extracted from the center pixel of its corresponding Raman map.

4.4 Spectrally dependent photovoltage imaging results and discussion

We performed a test measurement to verify the photovoltage signal. For this, the incident laser light was switched ON and OFF, see Figure 4.6. Furthermore, to prove that the voltage variation in these photovoltage measurements were representative and reproducible we acquired maps on a variety of CIGS solar cells as shown in Figure 4.7. Here, we imaged three similarly fabricated devices that all show voltage variations at the same length scale as the composing CIGS grains.

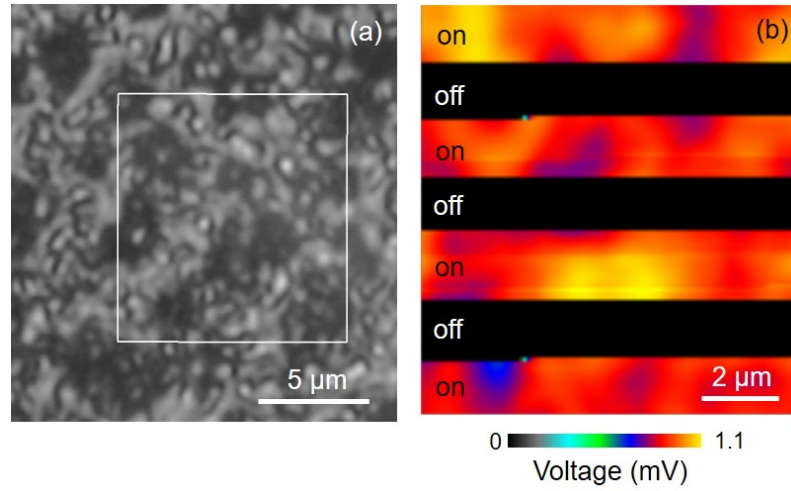


Figure 4.6: **Laser ON/OFF photovoltage signal verification.** (a) Optical micrograph of CIGS solar cell; the white square indicates the region where the voltage scan was performed. (b) Scanning photovoltage map of a typical CIGS solar cell showing spatial variation in voltage. Illumination conditions: 600 nm laser; incident power = $1.44 \mu\text{W}$; objective lens: $100\times$, $\text{NA} = 0.75$.

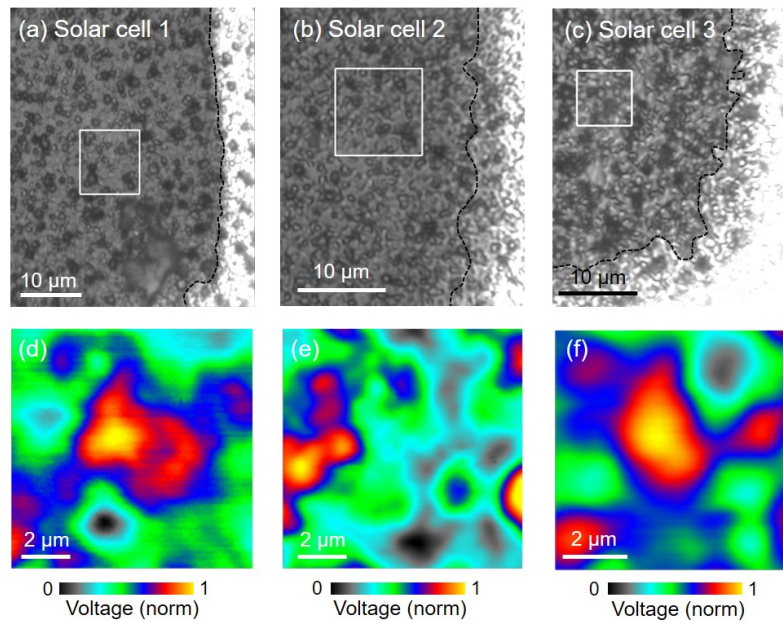


Figure 4.7: **Additional photovoltage mapping on CIGS solar cells.** (a)-(c) Optical micrographs of three different CIGS solar cells where the white square indicates the corresponding scanned photovoltage map below. The bright white region in each micrograph is the top electrical contact; here the black dashed line is a guide for the eye to emphasize the interface between the metal and the semiconductor layers. To ensure effective charge carrier collection we scanned regions $<25 \mu\text{m}$ away from the top macroscopic contact. (d)-(f) Photovoltage maps acquired for solar cells 1, 2 and 3, respectively, with spatial variation on the same length scale as the CIGS grains.

To understand the contribution of the photovoltage generated within the CIGS grains to the overall performance of the solar cell as a function of light penetration depth we spectrally resolve the electrical response of the CIGS sample while mimicking the illumination conditions of a working device. See Figure 4.8(a) and (c) for the 1-sun spectrum at AM1.5G illumination [206] and the EQE, respectively, where the colored dots represent the wavelengths at which the microscopic photovoltage measurements were performed. Figure 4.8(b) shows an optical micrograph of a selected region of the CIGS solar cell. We acquire the photovoltage maps using the same number of incident photons in all cases (Figure 4.8(d)-(u)). The electrical signal continually increases with the wavelength, reaching a maximum value at 950 nm (Figure 4.8(r)), approaching the bandgap of the fabricated CIGS layer (equal to 1.15 eV, as determined by photoluminescence). As expected, beyond the semiconductor bandgap (corresponding to wavelength $\lambda > 1000$ nm) the electrical signal drops dramatically (Figure 4.8(t) and (u)), indicating that the very modest photogenerated voltage is likely due to trap states within the polycrystalline layer [131]. Nevertheless, spatial variations are still observed and are well above the noise level (20 nV) of the photovoltage measurements introduced here. The in depth electrical response of the CIGS layer is obtained without cross-sectioning (destroying) the sample. Although the surface of the sample is being probed, the electrical response of the subsurface grains and interfaces was acquired due to the absorption coefficient of the material. By comparing the spatial variation in photovoltage of individual scans (*e.g.* Figure 4.8(g) and (n)), one notices that the behavior changes as a function of wavelength, demonstrating that the photovoltage signal is resulting from the electrical response within the material (and not its surface only). Thus, through our imaging method we acquire a tomography of the electrical characteristics of the absorbing material where each scan corresponds to a snapshot

of the mesoscale behavior of the grains composing the CIGS layer. The word tomography is used here to emphasize that the device is imaged in 'sections' by illuminating it with different wavelengths, which, by definition, corresponds to a distinct penetration depth within the CIGS layer.

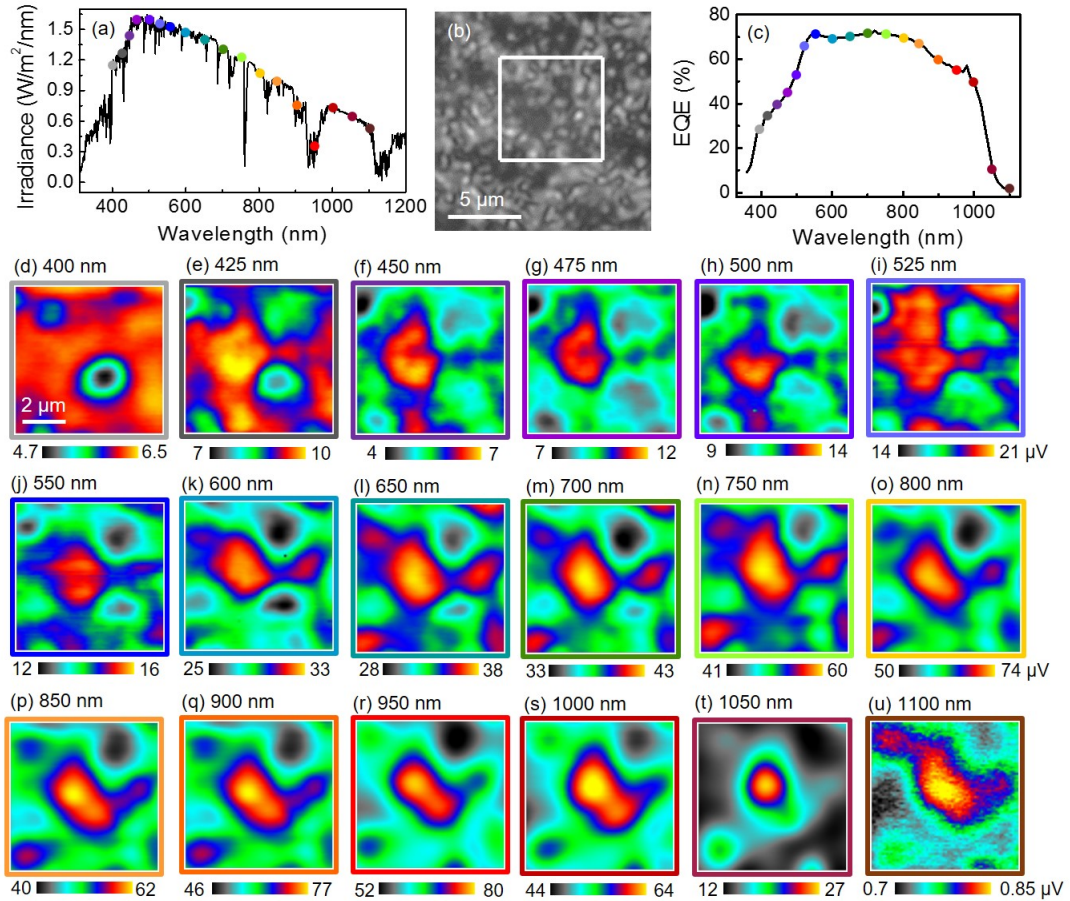


Figure 4.8: **Spectrally dependent voltage maps on CIGS solar cell.** (a) 1-sun AM1.5G spectrum as a function of wavelength. (b) Optical micrograph of CIGS solar cell acquired with $100\times$ objective, $NA = 0.75$, spot size $\sim 1 \mu\text{m}$. The white box highlights the $7 \times 7 \mu\text{m}^2$ area where the photovoltage measurements were performed. (c) EQE measurements. The colored dots in (a) and (c) represent the wavelengths where the microscopic measurements were performed. (d)-(u) Spectrally dependent scanning photovoltage microscopy scans. For each scan: the label indicates the wavelength, and the color scale bar is in μV .

The spatial distribution of the voltage for each scan is used to quantify the occurrence of preferential charge carrier generation/collection sites as a function of wavelength

and, thus, light penetration depth within the CIGS layer. As shown by the histograms in Figure 4.9, the voltage average value and distribution for each map vary as a function of wavelength. While the absorption coefficient is larger for shorter wavelengths (Figure 4.10), a smaller average value of the voltage is obtained. This behavior suggests that carriers generated near the top surface are more likely to recombine non-radiatively, leading to a smaller voltage. This observation is corroborated by the EQE data (Figure 4.1(c)), which also shows a decrease in carrier collection. For longer wavelengths, the absorption occurs deeper within the CIGS layer and leads to increased photovoltage until the bandgap is reached, where the voltage again decreases due to lack of photon absorption. The precise cause of the broadening of the voltage distribution with wavelength is unknown and is currently being investigated.

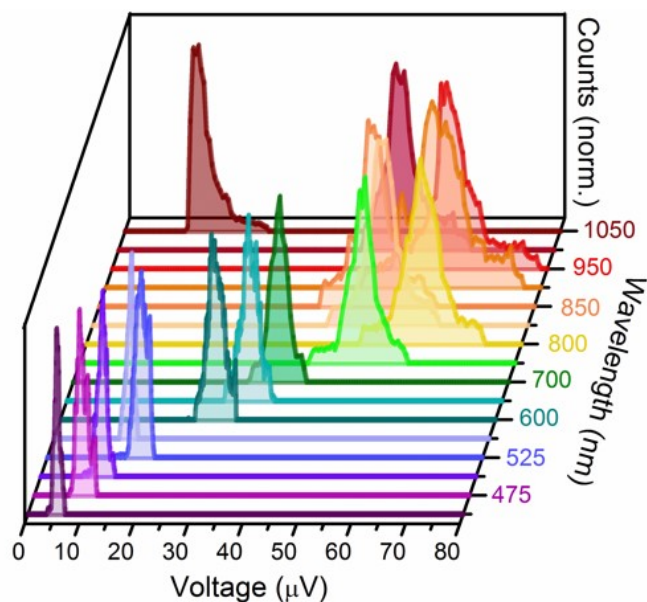


Figure 4.9: **Spectrally dependent voltage histograms.** 3D plot of voltage histograms (normalized) as a function of wavelength for CIGS solar cell, obtained from scanning photovoltage microscopy (shown in Figure 4.8).

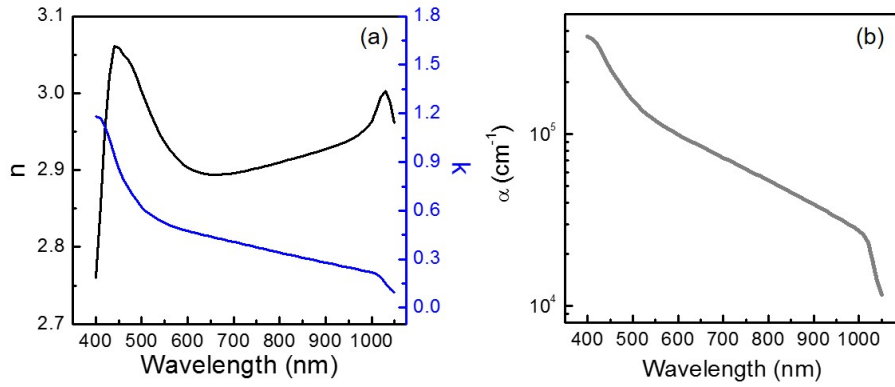


Figure 4.10: **CIGS optical properties.** (a) Index of refraction n and extinction coefficient k as a function of wavelength, as measured by ellipsometry on the polished CIGS sample. (b) Absorption coefficient, α , as a function of wavelength.

The possible contribution of surface roughness and consequent light reflection and scattering to the voltage signal was excluded by a detailed comparison between as-is and polished grains, where spatial variations in photovoltage to occur irrespective of the morphology of the grains. The CIGS sample was chemically polished with aqua regia using a method described in ref [207]. The sample was immersed in a 1:3 solution of HCl:HNO₃ at room temperature for nine seconds, followed by a rinse in DI water. Figure 4.11 shows a cross-section SEM of both as-is and polished grains while Figure 4.12 shows a top-view SEM, optical micrographs, atomic force microscopy scans, and line profiles.

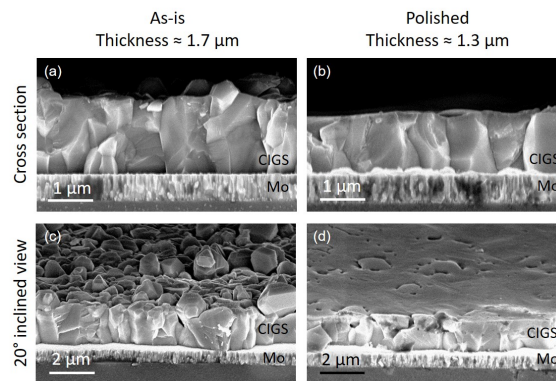


Figure 4.11: **SEM images of as-is vs. polished CIGS grains.** Cross-section SEM images of (a,c) as-is and (b,d) polished CIGS samples.

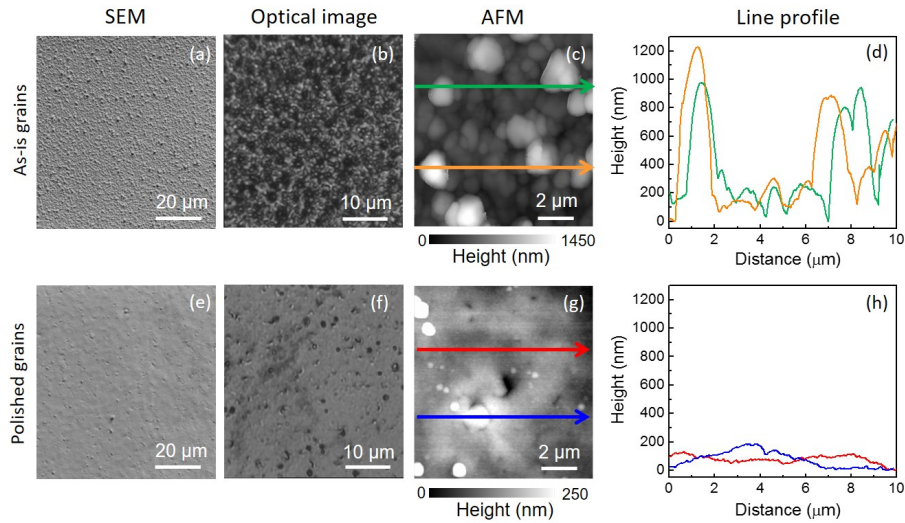


Figure 4.12: **Electron, optical, scanning probe microscopy of as-is and polished CIGS grains.** SEM, optical and AFM images and line scans of (a-d) as-is and (e-h) polished CIGS grains post-sputter fabrication.

In Figure 4.13 the voltage distribution maps for both the as-is and polished samples are shown along with their macroscopic light J - V curves. The non-uniformity of the voltage signal in both as-is and polished CIGS samples demonstrates that different charge carrier dynamics are taking place at the distinct grains. Note that there is no correlation between the spatial variation in the voltage signal and the optical micrographs (reflected light). Light J - V curves of Figure 4.13(c) as-is and Figure 4.13(f) polished solar cells were tested under AM1.5 global illumination (1-sun, 100 mW/cm²). Here, the low voltage from the polished sample results primarily from parasitic shunt resistance (R_{sh}) that reduces the amount of current flowing through the solar cell, which most likely results from surface recombination within the CIGS layer after the chemical polishing. Note that the series resistance (R_s) in both samples is similar, which is not related to the voltage of the device. Although the polished sample has surface roughness of ~ 100 nm (Figure 4.12), we were unable to acquire reliable information about the grains crystallographic orientation by EBSD due to the ZnO 500 nm layer (Figure 4.1(a)). Thus, the precise

correlation between the spatial variations in V_{oc} and the structural properties of the CIGS requires the implementation of a selective chemical etching for removing the oxide layer. Nevertheless, this etching would necessarily be destructive and the exposure of the n -CdS would favor surface recombination, which directly affects the V_{oc} of the device.

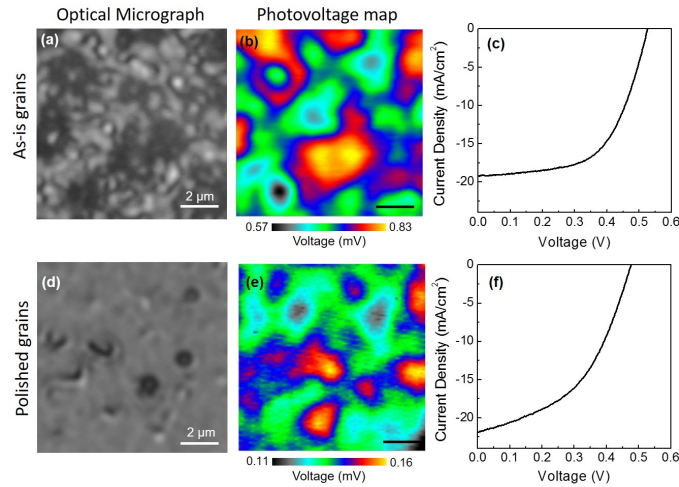


Figure 4.13: **Voltage distribution of a polished CIGS sample.** Optical image of (a) as-is and (d) polished CIGS grains imaged under the same illumination conditions. Scanning photovoltage images for (b) as-is and (e) polished grains, using $100\times$ objective, $NA = 0.75$. In both cases, the scans were acquired $<25 \mu\text{m}$ from the electrical contacts, and were illuminated with $600 \pm 3 \text{ nm}$ laser source at a power = $1.44 \mu\text{W}$.

To further evaluate the spatial inhomogeneity of charge carrier dynamics within the CIGS layer we analyze the voltage enhancement for the set of maps shown in Figure 4.8. Figure 4.14(a) shows a photovoltage scan acquired at 750 nm overlaid on the SEM image for the same $7 \times 7 \mu\text{m}^2$ region. Despite the fact that the scanning photovoltage measurements are limited by diffraction, notable spatial variations were consistently observed. Figure 4.14(b) displays the voltage enhancement as a function of wavelength for the positions (pixels) indicated by the colored circles in Figure 4.8(a). Here, we define the enhancement as the voltage of a pixel, $V_{x,y}$, divided by the average value of the entire region, $\langle V \rangle$, ($52.1 \mu\text{V}$ in this case). Note that both $V_{x,y}$ and $\langle V \rangle$ change for each incident

wavelength (due to the CIGS absorption coefficient, see Figure 4.10).

Surprisingly, some regions of the sample showed a modest voltage improvement of 10% for short wavelengths (400-500 nm), and a remarkable enhancement of 40% close to CIGS bandgap. The low electrical signal (black and cyan circles in Figure 4.14(b)) approaches the average value (green solid line) as the energy of the incident source of excitation nears the bandgap of CIGS. Interestingly, certain regions of the CIGS layer (red points in Figure 4.14(b)) present local voltage that varies 10% below and above the average response of the device, for wavelengths <550 nm and >600 nm, respectively. Near the material bandgap the voltage enhancement reaches 20%. By spectrally and spatially resolving the photovoltage generated by the CIGS solar cell we obtain a qualitative tomography of the local electrical characteristics of the device and probe their limiting factor: the V_{oc} (see Figure 4.14(c)). Here, the maps are displayed on the same voltage scale to emphasize the spatial variations as a function of the incident wavelength, which are likely due to the structural properties of the CIGS layer, instead of composition inhomogeneities between different grains. The longer wavelength voltage maps encompass the near-surface strong light absorption, and the qualitative tomography displays the influence of the each wavelength's light absorption on the photovoltage.

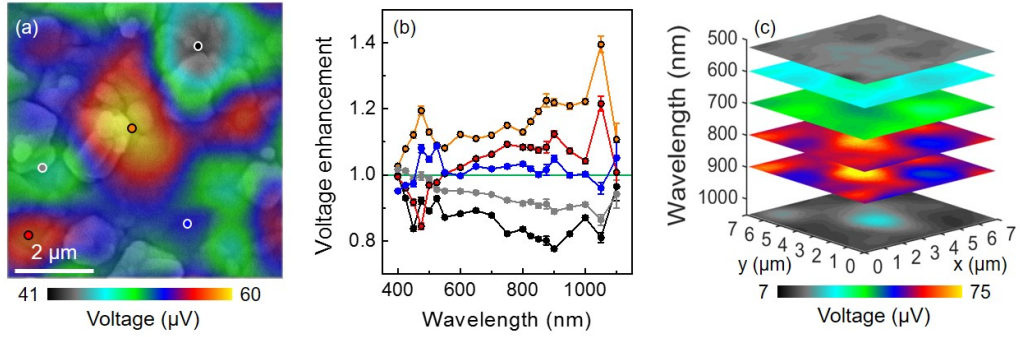


Figure 4.14: **Mapping voltage with high spatial resolution in polycrystalline solar cells.** (a) Voltage map overlaid with SEM image, acquired at $\lambda = 750 \pm 3$ nm and incident power of 59 ± 1 nW. (b) Voltage enhancement as a function of wavelength for selected regions of the map shown in (a). The green line corresponds to the average voltage value of each map, and the error bars refer to the standard deviation of each λ -dependent scan. (c) Qualitative tomography of photovoltage showing spatial variation as a function of λ . For each measurement: $100\times$ objective lens ($NA = 0.75$).

Through a sequence of spectrally dependent photocurrent scans we determine the ΔV_{oc} map for the polished CIGS device under 1-sun illumination (Figure 4.15). This map is obtained by adding the contribution of each photocurrent scan to the overall short-circuit current map $I_{sc,total}$ of the device, weighted by the number of photons incident into the sample at AM1.5G illumination, as:

$$J_{sc,total} = \sum_{\lambda_n} J_{sc,\lambda_n} \quad (4.1)$$

$$J_{sc,\lambda_n} = I_{sc,\lambda_n}^{measured} \times \int_{(\lambda+\lambda_{n-1})/2}^{(\lambda_n+\lambda_{n+1})/2} (\phi_{1-sun} \times \lambda d\lambda) / (P_{inc} \times \lambda_n) \quad (4.2)$$

where J_{sc,λ_n} is the short-circuit current density for each wavelength λ_n where a scan was acquired, $I_{sc,\lambda_n}^{measured}$ is the short-circuit current measured (a map), ϕ_{1-sun} is the irradiance corresponding to 1-sun AM1.5G illumination (from Figure 4.8(a)), and P_{inc} is the incident

power for each measurement (wavelength dependent). Then, the V_{oc} map is determined by using the diode equation, where the ideality factor and the dark saturation current density (J_{dark}) were obtained from macroscopic measurements. The spatially resolved V_{oc} map combines the contribution of the surface and the bulk properties of the grains, weighted by the sun spectrum, mimicking the performance of a solar cell under realistic operation conditions.

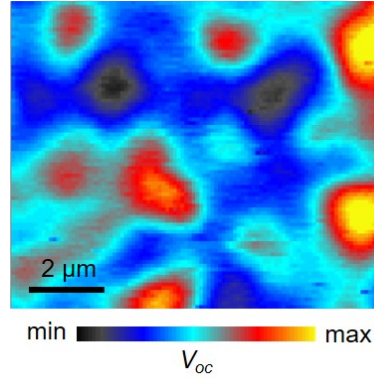


Figure 4.15: **Characterization of the mesoscale behavior of CIGS solar cells.** V_{oc} map for CIGS solar cell, with sub-micron spatial resolution, obtained from a sequence of spectrally dependent scans.

4.5 Conclusion

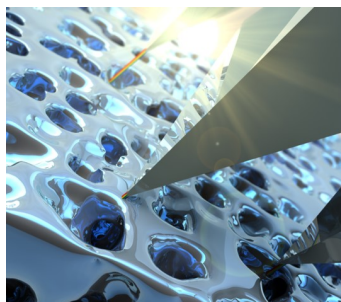
Here, we have implemented a universal, non-destructive imaging method to map the spatial variation of the electrical response of optoelectronic devices in situ that enabled a tomography of the generated photovoltage within the solar cell absorbing layer. The spatial resolution of the diffraction-limited method described in this chapter could be improved by using near-field scanning optical microscopy probes as the source of illumination, [131] which can achieve resolution <100 nm. Nevertheless, the interpretation of the data in these cases often requires the consideration of near-field effects, and possibly the need for 3-dimensional simulations to help us understand the primary near-field

light-matter interactions taking place. This functional characterization reveals how the electrical response of CIGS devices from a quaternary target changes spatially, considering light penetration depth. Further, the sub-micron spatial resolution of the photovoltage scans presented here elucidates a pressing open question in the field of photovoltaics: does the V_{oc} of polycrystalline CIGS devices from a quaternary target vary spatially? Yes.

We demonstrated that the photovoltage of CIGS solar cells from a quaternary target varies locally in $>20\%$, a behavior mapped here for the first time. We used micron-Raman imaging and EDX to determine the chemical composition of the grains. While the distribution of Cu, In, Ga and Se was found to be uniform at the micron-scale, the V_{oc} of these devices is still considerably lower than expected. Scanning photovoltage microscopy was implemented as an in situ functional characterization tool to resolve the local electrical response of CIGS, where remarkable variations in voltage were measured. A sequence of wavelength dependent voltage scans were used to build a tomography of the photovoltage distribution within the CIGS layer; where some regions of the material outperform the average, macroscopic behavior, potentially affecting the performance of the device. Finally, we presented a micron-scale resolved V_{oc} map under broadband illumination, revealing the spatial distribution of voltage for the CIGS solar cell under 1-sun global illumination operation conditions. This functional imaging framework provides a novel tool to map the electrical response of inhomogeneous materials for photovoltaics with micron-scale length grains, such as perovskites, CdTe, and CZTS. Further, this non-destructive method can be expanded to other optoelectronic devices, such as photodetectors and LEDs.

Chapter 5: Nano-imaging of open-circuit voltage in photovoltaics

For most photovoltaic devices, the current density is near its maximum value; however, achieving a large open-circuit voltage has proven difficult for nearly all photovoltaic technologies. Understanding the carrier recombination processes on the nanoscale that lead to this voltage reduction is critical, yet no technique exists to microscopically map recombination and the resulting open-circuit voltage. Here we present a novel metrology to image the open-circuit voltage with spatial resolution <100 nm, more than five orders of magnitude better than previous methods, using a variant of illuminated Kelvin Probe Force Microscopy. We apply this technique to several materials (GaAs, Si, CdTe, and CIGS), and find that the open-circuit voltage varies locally by more than 200 mV, suggesting that spatial variation of non-radiative recombination strongly affects the overall device performance. This technique enables new insights into the loss mechanisms that hinder solar cells and provides a new platform to image device performance with nanoscale resolution. This chapter is adapted from E.M. Tennyson et. al, *Advanced Energy Materials*, **5** 1501142 (2015) **Front Cover** [37]



5.1 Introduction to local voltage mapping in thin-film solar cells

For most photovoltaic devices, the record short-circuit current density (J_{sc}) is near its theoretical limit; however, achieving a large open-circuit voltage (V_{oc}) has proven difficult for nearly all photovoltaic technologies. [7, 208] Understanding the carrier recombination processes, caused by structural or compositional variations at the nanoscale, that lead to this voltage reduction is critical, yet no technique exists to quantitatively map recombination and the resulting V_{oc} at the nanoscale. Here we present a novel metrology to image the V_{oc} with spatial resolution <100 nm, more than five orders of magnitude better than previous methods, using a variant of illuminated Kelvin Probe Force Microscopy. We apply this technique to several materials (GaAs, Si, CdTe, and CIGS), and find that the V_{oc} varies locally by more than 200 mV, suggesting that spatial variation of non-radiative recombination strongly affects the overall device performance. This technique enables new insights into the loss mechanisms that hinder solar cells and provides a new platform to image device performance with nanoscale resolution.

The V_{oc} of a solar cell is a measurement of the maximum voltage generated by the device under illumination, which is proportional to the quasi Fermi level splitting of the semiconductor p - n junction. This generated voltage and the overall electrical behavior of a device strongly depend on the non-radiative recombination rate of the charge carriers within a material, as described in Chapter 1, which is affected by the defects inherently present within the semiconductor. Despite all the effort in developing higher performance thin-film polycrystalline solar cells, such as CdTe, $\text{CuIn}_x\text{Ga}_{(1-x)}\text{Se}_2$ (CIGS), and $\text{Cu}_2\text{ZnSnS}_4$ (CZTS), the difference between the theoretically predicted and the best exper-

imentally achieved V_{oc} is still considerably large, as shown in Chapter 3. For Si, extensive research has been dedicated to design and implement nanostructured light-trapping architectures to boost light absorption [209–212] however, there are very few experiments showing how the V_{oc} is affected. Thus, for any micron- and nano-scale structured PV device, assessing variations in V_{oc} with nanoscale resolution and spatially resolving where recombination occurs within the material can potentially change the pathway for designing higher performance devices.

Imaging methods based on atomic force microscopy (AFM) techniques have been extensively used to characterize the structural and electrical properties of PV materials and full devices. [172, 182, 213–222] In particular, Kelvin probe force microscopy (KPFM) has been implemented to probe the electrical characteristics of a variety of PV materials and devices, ranging from organic materials [223–226] and oxides [227] to III-V semiconductors for multijunction designs [228–230] and polycrystalline thin-films. [184, 219, 231–236] The local optoelectronic properties and changes in material composition have also been mapped using near-field scanning optical microscopy (NSOM) probes as local sources of excitation. [130, 131, 186, 237–240] Recently, photoluminescence has emerged as a promising tool to map charge recombination [129, 241, 242] and carriers diffusion [194] with high spatial resolution. At low-temperature (70 K), photoluminescence imaging with sub-micron resolution has been implemented to map a 10 meV quasi-Fermi level splitting in CIGS solar cells, where variations in the intensity signal were attributed to changes in the material composition. [190] Nevertheless, none of these imaging techniques provide a direct measurement of V_{oc} within the material at operating conditions. A straightforward, universal, and accurate method to measure the V_{oc} (and hence non-radiative recombination processes) with high spatial resolution in PV materials is still missing.

Here we present a new imaging technique based on illuminated-KPFM to map the V_{oc} of optoelectronic devices with nanoscale resolution <100 nm. We map the contact potential difference of a half or fully processed solar cells in the dark and under illumination to determine the quasi Fermi level splitting of the $p-n$ junction. We spatially resolve the V_{oc} of different PV materials, including III-V direct bandgap semiconductors, monocrystalline Si, and polycrystalline thin-films, demonstrating the universality of our platform for imaging devices performance. While single crystalline GaAs and Si solar cells show very uniform V_{oc} maps, CdTe and CIGS present dramatic variations in V_{oc} , larger than 0.2 V, which have never been resolved by other microscopy methods. We find that the local variations in the V_{oc} are due to the fact that different grain orientations can act as distinct centers for recombination within the material. Although KPFM measurements under illumination (named surface photovoltage - SPV) have been realized in a variety of solar cells technology [84, 243–253], here a direct correlation between KPFM measurements (light-minus dark-KPFM) and the V_{oc} of photovoltaic devices, through the measurement of the quasi-Fermi level splitting is demonstrated for the first time. This nanoscale metrology is non-destructive and can be implemented in ambient conditions, allowing for the diagnosis of how the different processing steps can affect the recombination within the material and, therefore, the ultimate performance of an optoelectronic device. For non-uniform semiconductor materials, mapping local variations in V_{oc} is extremely useful to identify which types of interfaces can suppress non-radiative recombination processes.

5.2 Experimental methods

5.2.1 Solar cell fabrication

The GaAs solar cell was obtained from M-Comm. The cells were grown on an n -type GaAs wafer ($300\ \mu\text{m}$ thick, $5 \times 10^{18}\ \text{cm}^{-3}$), and the active regions were cladded by AlGaAs ($E_g = 1.80\ \text{eV}$, $3 \times 10^{18}\ \text{cm}^{-3}$) passivation and back surface field layers. The GaAs solar cell used for system calibration was extremely small ($1 \times 3\ \text{mm}^2$). As a consequence, the ideality factor of the device is particularly high, due to edge surface recombination effects. [254] The monocrystalline Si solar cell is a commercially available device, formed by n - and p -doped Si layers, with pyramidal texturing to enhance light trapping. The commercially available CdTe solar cell measured was formed by the following layers (from top to bottom): 4.0 mm of glass substrate, 550 nm of a bilayer transparent conductive oxide, 50 nm of n -type CdS, and 3.5 μm of p -type CdTe, which was submitted to the standard CdCl_2 treatment. Due to the geometry of the device, the illuminated-KPFM measurements were performed on the exposed p -doped CdTe grains with the original back contact. The CIGS solar cell sample was fabricated by sputtering from a quaternary target, which consistently produces polycrystalline, highly oriented grains with controlled stoichiometry, and a bandgap of 1.1 eV. [167] Soda lime glass coated with 500 nm of Mo was used as the substrate. P -doped CIGS films with 2.0 μm in thickness were deposited by RF magnetron sputtering. A 50 nm thick n -type CdS layer was deposited by chemical bath deposition. For all samples, no anti-reflection coating was added.

5.2.2 KPFM measurements

It has been shown that AM-KPFM is susceptible to internal AC-signal couplings which can lead to a topography-dependent offset in the applied voltage. [255] Thus, to ensure no topography pick-up we measure the cantilever response to electrostatic excitation in both the in- and out-of-phase channels across the entire resonance. The response is that of a simple harmonic oscillator, without any sign of AC coupling. Because the coupling scales with frequency, a cantilever with a low resonance frequency is chosen. Furthermore, the coupling is independent of illumination, so it does not affect the results pertaining to the change in surface potential caused by incident light intensity. The cantilever spatially averages the tip-sample interaction due to the long-range nature of the electrostatic interaction, [256] reducing the spatial voltage variation signal, [257] importantly, this does not change the voltage shift due to illumination.

5.2.3 Macroscopic characterization of devices

Dark and light J - V curves were acquired using a full spectrum solar simulator, with $2.0 \times 2.0 \text{ in}^2$ ($50.8 \times 50.8 \text{ mm}^2$) collimated output, and an Air Mass 1.5G filter. The output power of the xenon lamp was independently controlled, ranging from 0.1 to 1.0-sun (100 mW/cm^2). The light source was calibrated using a $20 \times 20 \text{ mm}^2$ reference monocrystalline Si solar cell with a fused silica window. Light J - V measurements for all the devices measured here are presented in Figure 5.1. A dark J - V measurement of the GaAs solar cell was used to determine the dark current of the device in Figure 5.2.

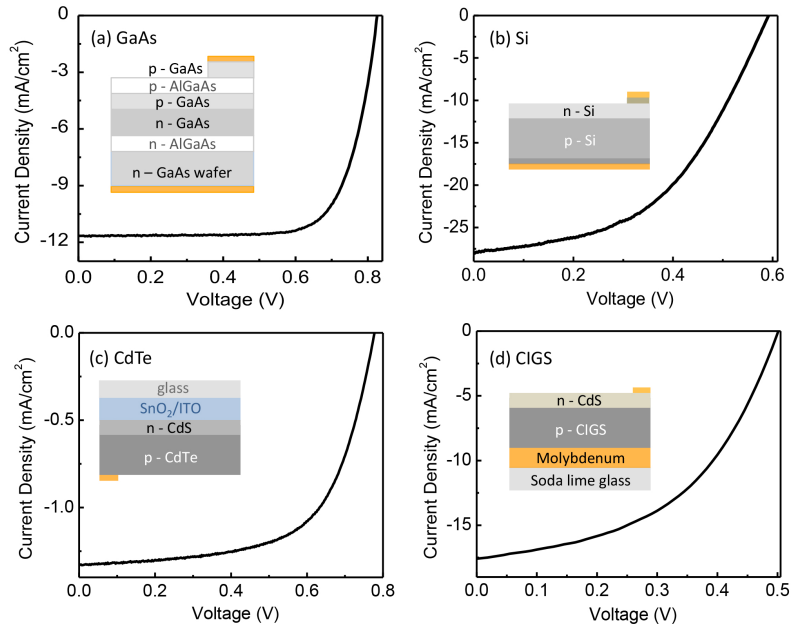


Figure 5.1: **Light J - V curves for four solar cell devices.** (a) GaAs ($V_{oc} = 0.83 \text{ V}$), (b) monocrystalline Si ($V_{oc} = 0.59 \text{ V}$), (c) CdTe ($V_{oc} = 0.56 \text{ V}$), and (d) CIGS ($V_{oc} = 0.50 \text{ V}$). Inset: active layers of each device (out of scale for clarity). For all samples, no anti-reflection coating was added.

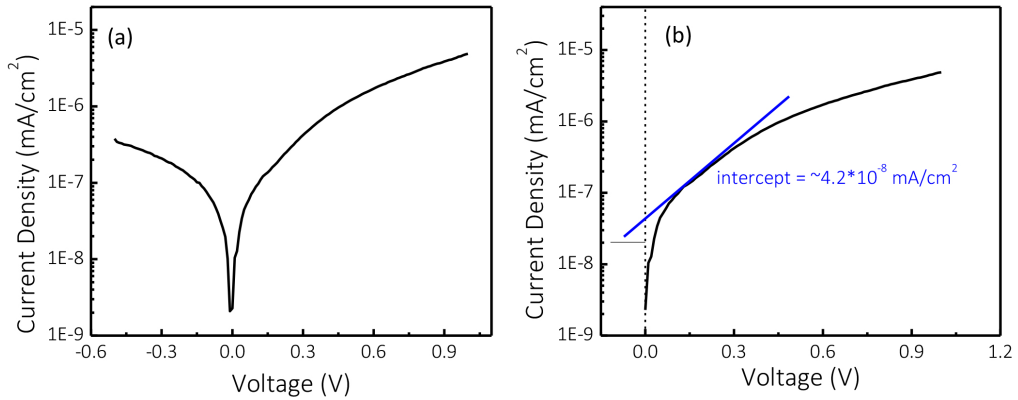


Figure 5.2: **Dark J - V for GaAs solar cell.** (a) Semilog dark J - V and (b) linear fit used to determine J_{dark} .

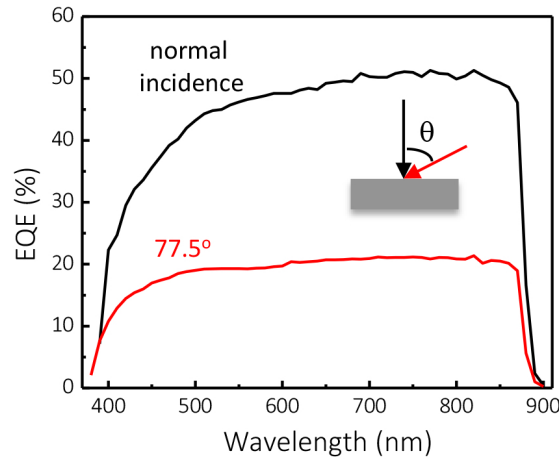


Figure 5.3: **Angle dependence of external quantum efficiency for the GaAs solar cell.** EQE measurements at normal incidence (black) and 77.5° (red) using polarized light, in the same geometry of the illuminated-KPFM measurements.

5.2.4 EQE measurements of GaAs

A xenon arc lamp was directed into a monochromator. Two identical silicon diodes were used to regulate the spectral response of the EQE measurements; one as a reference and the other for calibration. A beam splitter guides half of the output light to the fixed reference diode, the other half was directed through an optical path and collected at the position of the calibration diode or solar cell sample. The ratio of the spectral responses between the reference and calibration diode was computed in 10 nm increments. The EQE of the solar cell was measured from 390 nm and 900 nm. Independent calibrations were performed before each EQE measurement. A polarizer was used to match the polarization of the incident light with the illuminated-KPFM measurements. Figure 5.3 shows the EQE measurement taken on GaAs solar cell used to calculate the calibration constant.

5.2.5 V_{oc} image analysis

The SPV images were corrected for drift using a correlation function which computes the similarity between two topographical scans as they shift in time. The function outputs a value that corresponds to the magnitude in which the image is shifted in x and y directions. Once the topography correction was complete the potential maps of the dark- and illuminated-KPFM scans were subtracted.

5.3 Direct imaging of V_{oc} at the nanoscale: results and discussion

We implement illuminated-KPFM as a new tool to directly map the V_{oc} of photovoltaic materials with nanoscale resolution. In KPFM, the contact potential difference (CPD) is proportional to the work function difference between the tip and the surface of the material under investigation ($qV_{CPD} = W_{tip} - W_s$). For a solar cell, as shown in Figure 5.4(a) and (b), the CPD signal depends on the illumination conditions as:

$$qV_{CPD}^d = W_{tip}^d - W_s^d \text{ (in the dark),} \quad (5.1)$$

and

$$qV_{CPD}^{il} = W_{tip}^{il} - W_s^{il} = qV_{CPD}^d + \Delta\mu \text{ (under illumination)} \quad (5.2)$$

where q is the electron charge, the superscripted d and il refer to dark and illuminated conditions, respectively, and $\Delta\mu$ is the quasi Fermi level splitting. The V_{oc} of the device is:

$$V_{oc} = \frac{\Delta\mu}{q} = V_{CPD}^{il} - V_{CPD}^d \quad (5.3)$$

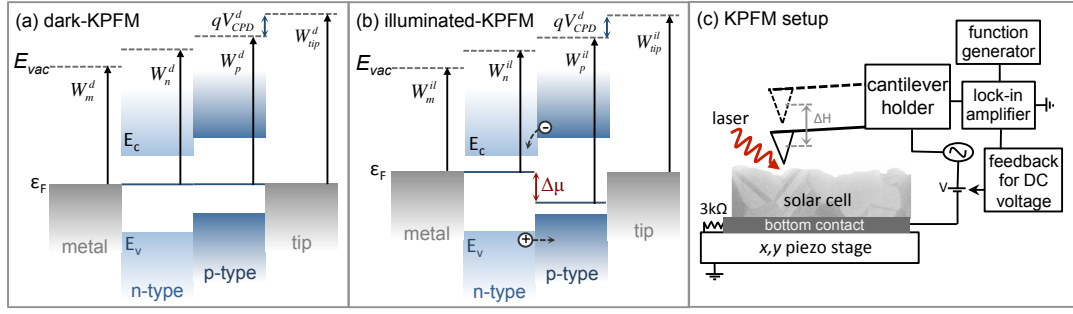


Figure 5.4: **Energy diagram of KPFM measurements.** Band profile of n - p junction (a) in equilibrium (dark) and (b) under illumination. E_{vac} , E_c , E_v , and ϵ_F refer to the energy of the vacuum level, the conduction band, the valence band, and the Fermi level, respectively. $W_n^{d(il)}$ and $W_p^{d(il)}$ are the work function for the dark (illuminated) n - and p -type layers. E_{Fn} , and E_{Fp} refer to the Fermi level splitting $\Delta\mu$ upon illumination. (c) Cross-sectional illustration of illuminated-KPFM setup, used to map open-circuit voltage V_{oc} of photovoltaic materials with nanoscale resolution. The metrology is implemented in ambient environment and only requires the bottom contact of the device. For each scan, the probe passes over the surface twice: in the first one topography is acquired, and in the second one the potential difference is recorded at a height ΔH from the first pass. The illumination source is a 660 nm continuum laser (represented by the red arrow). The surface photovoltage (SPV), difference between the illuminated- and dark-KPFM signals, is proportional to the V_{oc} of the solar cell.

Note that this technique does not require the preceding knowledge of the work function of the sample or the tip, because $\Delta\mu$ is determined by measuring the difference between these two quantities under distinct illumination conditions. Thus, the nanoscale maps of the V_{oc} of partially processed devices are determined from a pair of dark- and illuminated-KPFM images.

Amplitude-modulated (AM) KPFM is implemented using metal-coated Pt probes with mechanical resonance $\frac{\omega}{2\pi} = 86.7$ kHz in ambient conditions - see schematic setup in Figure 5.4(c). For each scan, the probe passes over the surface twice. On the first pass, a feedback loop controls the sample height in order to maintain constant cantilever oscillation amplitude; and topography is acquired in non-contact mode. On the second pass, the cantilever is held at a constant height (ΔH) relative to the path it traced on the first pass – see Figure 5.4(c). The tip oscillates slightly below resonance during

the topographic scan, to maintain stable tapping mode. [258] The amplitude of the tip oscillation is ~ 60 nm (though this value varies slightly from scan to scan, depending on the optical lever sensitivity of the probe).

The V_{oc} of a photovoltaic device is given by:

$$V_{oc} = \frac{nkT}{q} \ln \left(\frac{I_{il}}{I_{dark}} + 1 \right) \cong \frac{nkT}{q} \ln \left(\frac{I_{il}}{I_{dark}} \right) \quad (5.4)$$

where n is the ideality factor, k is Boltzmann's constant, T is the temperature, and I_{il} and I_{dark} are the light generated and the dark saturation current, respectively. For a partially illuminated solar cell the V_{oc} can be written as:

$$V_{oc}^{partial}(\phi) = \frac{nkT}{q} \ln \left(\frac{q * \phi * EQE_o}{J_{dark}} \right) + \ln \left(\frac{\tau * A_{il} * EQE_{\lambda, \Theta}}{A_{cell} * EQE_o} \right) = V_{oc}^{full}(\phi) + \beta \quad (5.5)$$

where $I_{il} = q * \phi * EQE_{(\lambda, \Theta)} * A_{il}$, ϕ is the number of photons per area per time from the light source, EQE_o and $EQE_{\lambda, \Theta}$ are the external quantum efficiencies at normal incidence and at an incident angle Θ for illumination at wavelength λ , J_{dark} is the dark current density, τ is the transmission fraction of the optical setup, A_{il} is the area of the solar cell being illuminated, A_{cell} is the total area of the solar cell, and β is a calibration constant (< 0), given by:

$$\beta = \frac{nkT}{q} \ln \left(\frac{\tau A_{il} EQE_{\lambda, \Theta}}{A_{cell} EQE_o} \right) \quad (5.6)$$

Note that for illumination of the full device, as is the case for a solar simulator measurement, $\beta = 0$. With KPFM, the solar cells are only partially illuminated, and the light generated current is very small compared to the situation of full cell illumination. To determine the expected V_{oc} for full illumination using KPFM:

$$V_{oc}^{full}(\phi) = V_{oc}^{partial}(\phi) + \beta \quad (5.7)$$

where $V_{oc}^{partial}(\phi)$ is the illuminated- minus dark-KPFM voltage signal, *i.e.* the surface photovoltage (SPV) of the cell. Alternatively, if $V_{oc}^{full}(\phi)$ is determined by an independent method, *e.g.* from solar simulator measurements, for the same photon flux as the KPFM measurements, β can be experimentally determined as:

$$\beta \cong V_{oc}^{partial}(\phi) - V_{oc}^{full}(\phi). \quad (5.8)$$

For our calibration of β , ϕ corresponds to 1-sun illumination (see Figure 5.6).

Figure 5.5 shows the macroscopic characterization of a GaAs solar cell, without an anti-reflection coating, used to calibrate and test this new metrology; a schematic of the solar cell is presented in Figure 5.5(a). Figure 5.5(b) shows the external quantum efficiency (EQE) measurement for the device under normal incidence illumination. The dark and light J - V macroscopic measurements were performed using a conventional solar simulator, where we adjust the light intensity to mimic different numbers of suns. The electrical characterization of the device shows good diode behavior, with $V_{oc} = 0.83 \pm 0.01$ V under 1-sun illumination (see Figure 5.5(c)). From the intensity-dependent light J - V curves we infer the V_{oc} dependence with illumination (see Figure 5.5(d)), where the photon

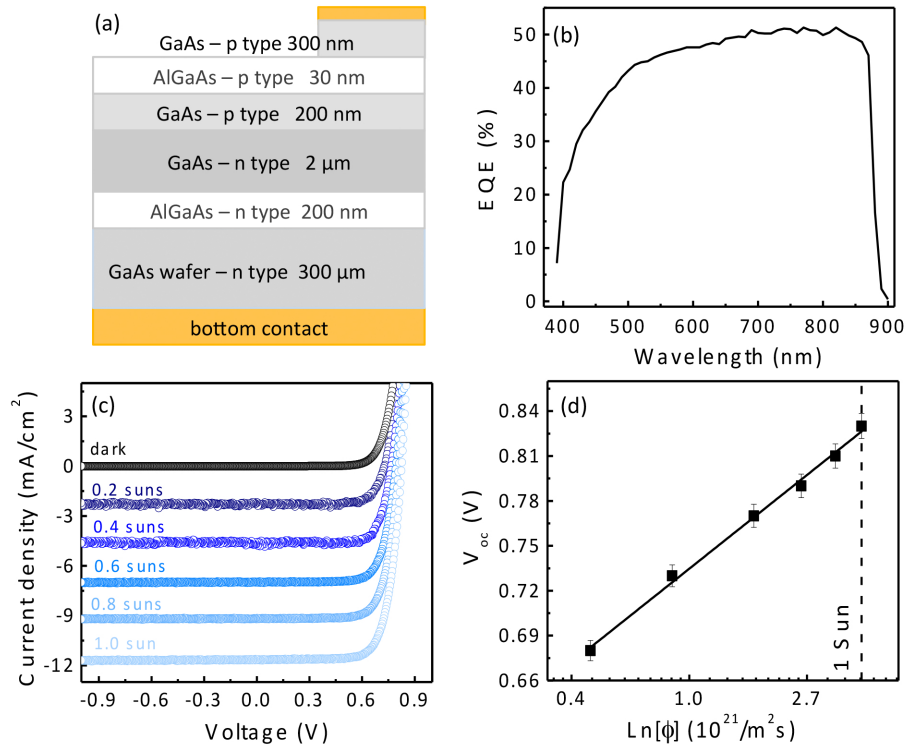


Figure 5.5: **Macroscopic characterization of GaAs.** (a) Schematic of the solar cell. (b) External quantum efficiency measurement. (c) Light J - V curves as a function of illumination (incident power). At AM 1.5G 1-sun illumination, $V_{oc} = 0.83 \pm 0.01$ V. (d) Open-circuit voltage V_{oc} as a function of incident power (photon flux).

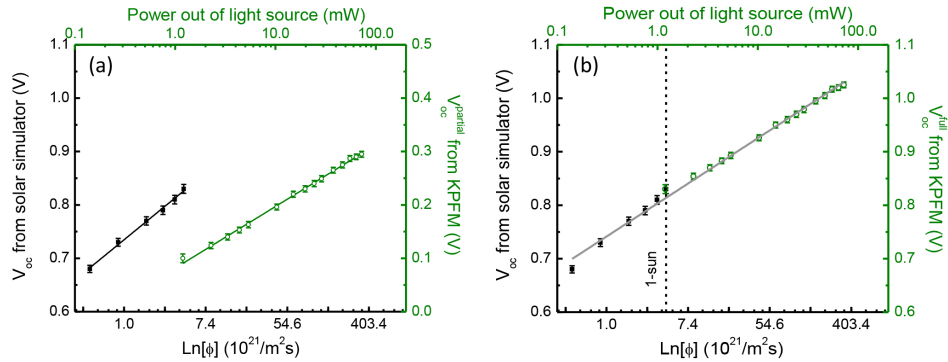


Figure 5.6: V_{oc} vs. **photon flux.** V_{oc} as a function of photon flux (ϕ) obtained from solar simulator (black) and nanoscale KPFM measurements (green) for a GaAs solar cell. (a) V_{oc} of a fully (solar simulator) and partially (KPFM) illuminated device. (b) V_{oc} after correction for calibration factor $\beta = -0.73$ V, to compare with fully illuminated devices. Note that both measurements were performed at the same injection level, allowing for the direct comparison of the voltage dependence on the incident light. The ideality factor, n , equals 1.9 ± 0.2 .

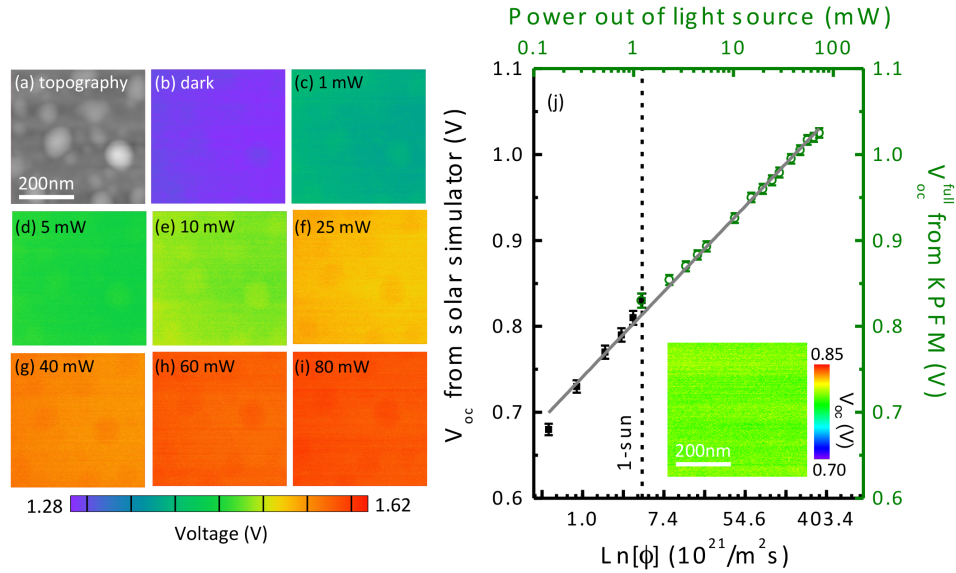


Figure 5.7: **Comparison of macro- and nanoscale V_{oc} measurements.** (a) AFM topography image (peak to valley = 5 nm). (b)-(i) KPFM images (V_{CPD}) for different incident powers (light source: 660 nm laser). (j) V_{oc} determined by macroscopic $J-V$ measurements (black) and by nanoscale KPFM (green) as a function of incident power from the light sources. For the KPFM measurements, the V_{oc} was obtained by averaging over the scanned area, and the error bars refer to the standard deviation. Inset shows uniform V_{oc} map with nanoscale resolution.

flux corresponds to the AM1.5 global illumination, from 0.1 to 1.0-sun ($100 \text{ mW}/\text{cm}^2$).

Figure 5.7 shows a sequence of intensity-dependent KPFM measurements. The GaAs solar cell is ideal to test this method because it is a very uniform sample (single crystal) with minimum height variation (roughness is 5 nm, see Figure 5.7(a)). The CPD (voltage signal) of the device increased with the incident laser power (photon flux) - see Figure 5.7(b)-(i) - indicating that more carriers are generated upon increasing illumination, as expected. In all cases, the voltage was very uniform because the epitaxial GaAs solar cell has an extremely low density of recombination centers. [24] The uniform colored scans shown in Figure 5.7(b)-(i) confirm the constant CPD signal of the cell, expected for a GaAs monocrystalline device with extremely low density of defects. Therefore, the uniform color of the scans indicates that the CPD does not vary within the spatial resolution of the AFM probe (30 nm in diameter). Figure 5.7(j) shows the macroscopic V_{oc} (from solar

simulator measurements) and the V_{oc} signal determined by KPFM, both as a function of the photon flux. For the KPFM measurements, the V_{oc} is the averaged signal obtained from the scans shown in Figures 5.7(b)-(i). The calibration constant is $\beta = -0.73$ V (see Figure 5.6). The KPFM measurements are in excellent agreement with the solar simulator ones: the ideality factor obtained from KPFM is $n = 1.9 \pm 0.2$, which is within 10% (see Experimental Methods). According to the KPFM measurements, the average V_{oc} of the solar cell at 1-sun illumination is $V_{oc} = 0.83 \pm 0.02$ V (spatially resolved in the inset of Figure 5.7(j)). These results demonstrate that by illuminated-KPFM the macroscopic value of the V_{oc} for a device can be determined, and local variations in V_{oc} can be measured with nanoscale resolution. This can be applied to *any* PV material.

The illuminated-KPFM metrology is extended to a variety of solar cell devices, allowing for direct imaging of local variations in V_{oc} (*i.e.* ΔV_{oc}) with nanoscale resolution. The ΔV_{oc} maps do not require system calibration; *i.e.* β is not needed. Figure 5.8 shows the SEM, AFM, dark- and illuminated-KPFM measurements for all samples investigated in this work: GaAs, monocrystalline Si, CdTe and CIGS, with morphologies ranging from epitaxial to granular surfaces. GaAs presents a very uniform V_{oc} (Figure 5.8(q)), with spatial variations within the noise level of the KPFM measurements (~ 10 mV).

The V_{oc} map for Si (Figure 5.8(r)) is also very uniform, as expected for a monocrystalline material. Yet, we investigate the influence of shadowing effects on the V_{oc} values for the textured Si sample – see Figure 5.9. Briefly, we find that to compensate the shadowing effects of the textured facets we simply need to measure illuminated-KPFM under two illumination conditions.

For CdTe (Figure 5.8(s)), different grain interfaces displayed unique V_{oc} responses, indicated by the dashed areas. This result suggests that the grain boundaries act as dis-

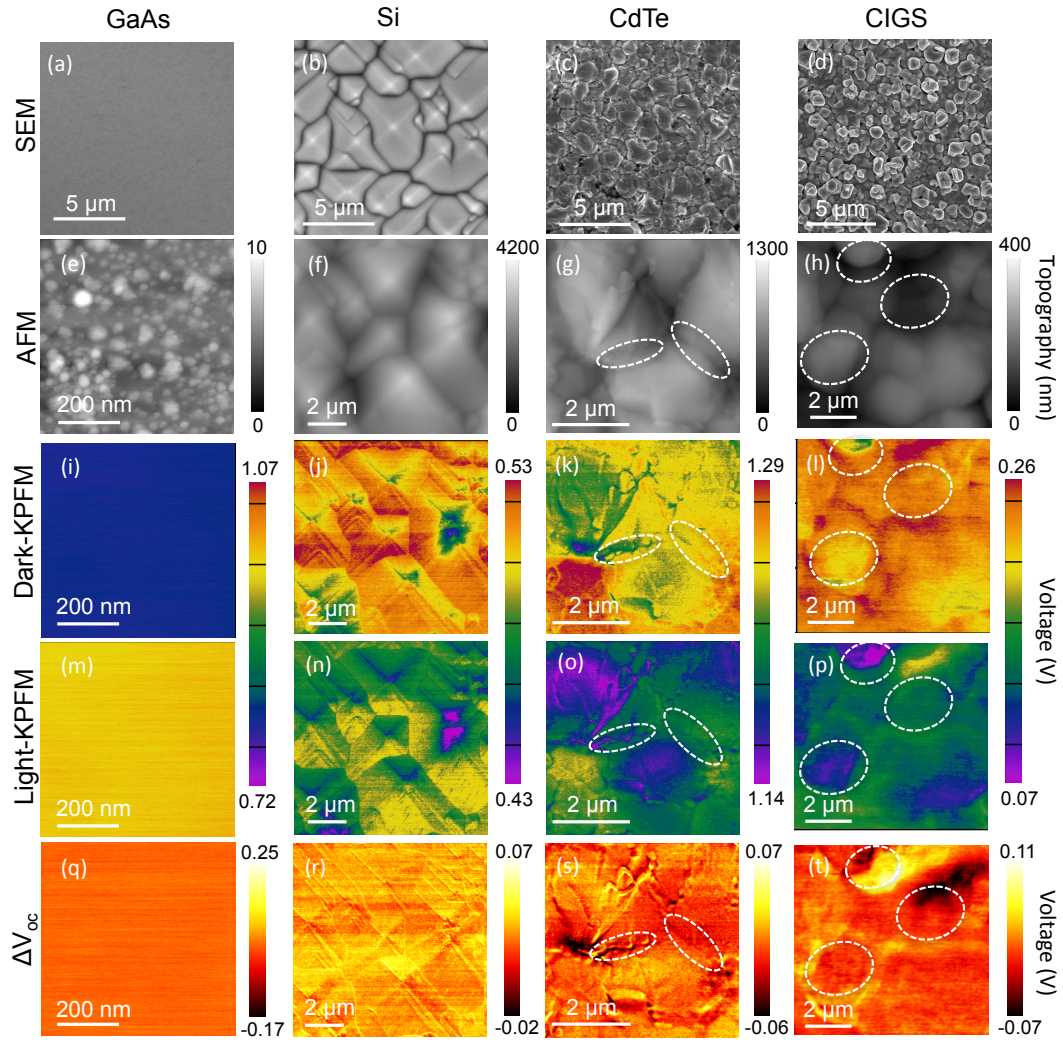


Figure 5.8: **KPFM performed on four solar cell devices.** (a)-(d) SEM images of GaAs, monocrystalline Si, CdTe and CIGS solar cells. (e)-(h) AFM topography images of the same samples. (i)-(l) Dark-KPFM images. (m)-(p) Illuminated-KPFM images using 660 nm laser source with power output = 1 mW, which corresponds to 1-sun illumination ($100 \text{ mW}/\text{cm}^2$). For Si sample, laser output = 10 mW. (q)-(t) Open-circuit voltage variation (ΔV_{oc}) maps with nanoscale resolution. Dashed areas indicate grains and interfaces with local V_{oc} variations only resolved by illuminated-KPFM.

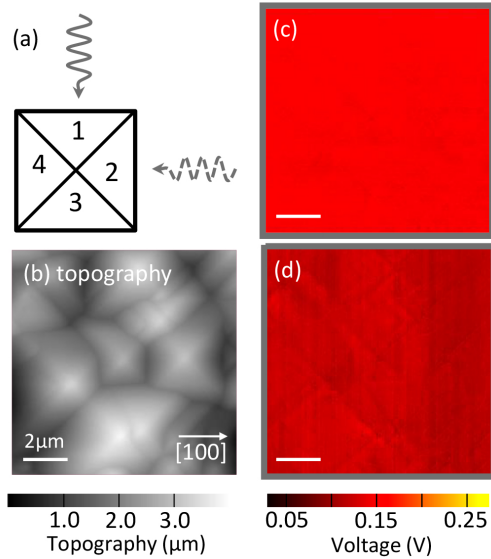


Figure 5.9: **Directional independent KPFM imaging on Si.** (a) Schematic showing two directions of illumination for KPFM measurements on Si solar cells. (b) AFM topography image. ΔV_{oc} maps obtained from two distinct illuminated-KPFM measurements (power out of the light source = 10 and 50 mW) for sample positioned at (c) [100] and (d) [010] directions with respect to the AFM probe. (50 mW-10 mW) voltage signal is equal to 0.152 ± 0.016 V and 0.125 ± 0.012 V, respectively. Image (d) is rotated 90 degrees counter-clockwise to facilitate comparison with (c).

tinct recombination centers. The CIGS grains present remarkable variations in V_{oc} (>200 mV), independent of the material topography, see dashed regions in Figure 5.8(t). Despite the fact that the different facets of a crystal can present distinct work functions, [259] the difference is taken into account because both the light- and dark-KPFM voltage signals are measured for the same facets of the crystal. The analysis of the role of the grain interfaces on the performance of the device is beyond the scope of this paper; however, these measurements demonstrate that nanoscale analysis of V_{oc} in non-uniform materials can resolve and quantify the recombination processes that currently limit the performance of polycrystalline solar cells. [208] Controlled growth of grains with crystal orientation corresponding to the high values of ΔV_{oc} (~ 0.15 V) could potentially boost the overall V_{oc} of the device. Despite the fact that CIGS grains grow preferentially along the $\langle 112 \rangle$ orientation, [167] a distribution of grains is usually observed, and to the best of our knowledge there is no

systematic study correlating different grain orientations with device performance. Note that while the voltage signal increases with illumination for GaAs, it decreases for Si and CdS/CIGS because the scanned layers are *p*- and *n*-doped, respectively. For the *p*-type CdTe surface, the voltage signal decreases with illumination because the work function of CdTe (~ 5.9 eV) is larger than the work function of the Pt-coated probe (~ 5.1 eV) used in the measurements, modifying the band diagram configuration presented in Figure 5.4.

The possible influence of major experimental artifacts was carefully analyzed, and no significant contribution to our measurements was found. A detailed study of the influence of ΔH (and therefore topography) on the SPV signal was performed and is presented in Figure 5.10. In order to minimize the effect of topography on the SPV signal, ΔH was kept constant for all dark and illuminated measurements presented here. Unless indicated otherwise, the probe passed at $\Delta H = 20$ nm above the topographic scan on the second pass.

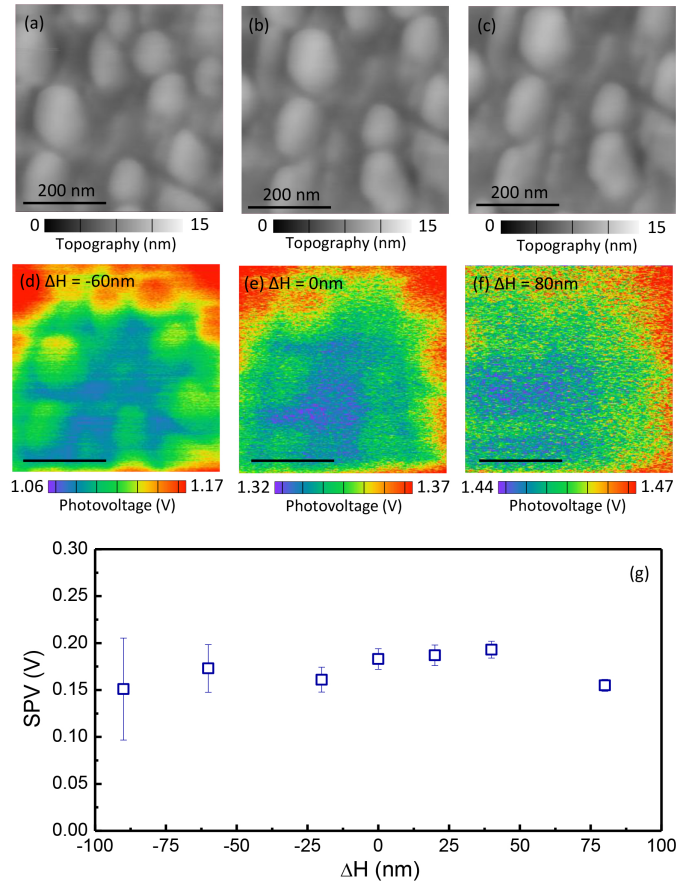


Figure 5.10: **Influence of ΔH on voltage response.** (a)-(c) AFM images of GaAs solar cell and (d)-(f) corresponding KPFM showing topography influence on voltage scan as a function of the difference in sample-probe distance between AFM and KPFM passes (ΔH). Illuminated-KPFM using incident power = 10 mW. At $\Delta H = -60$ nm the topography signal clearly contributes to the voltage scan even for the case of a smooth sample. At $\Delta H = 80$ nm the probe is too far from the surface and the variation in the voltage signal is negligible because this situation is similar to a macroscopic Kelvin probe measurement. (g) Average surface photovoltage (SPV) as a function of ΔH .

We resolve local variations in V_{oc} with spatial resolution <100 nm. Figure 5.11(a) shows a ΔV_{oc} map for the CdTe solar cell, showing a few interfaces that have reduced V_{oc} and, most likely, act as non-radiative recombination centers. The full-width-half-maximum (FWHM) of the line profiles shown in Figures 5.11(b)-(d) for the lateral variation in ΔV_{oc} is consistently below 100 nm. This set of KPFM measurements was acquired using Pt probes with 30 nm in diameter, demonstrating that we can accurately measure and resolve the V_{oc}

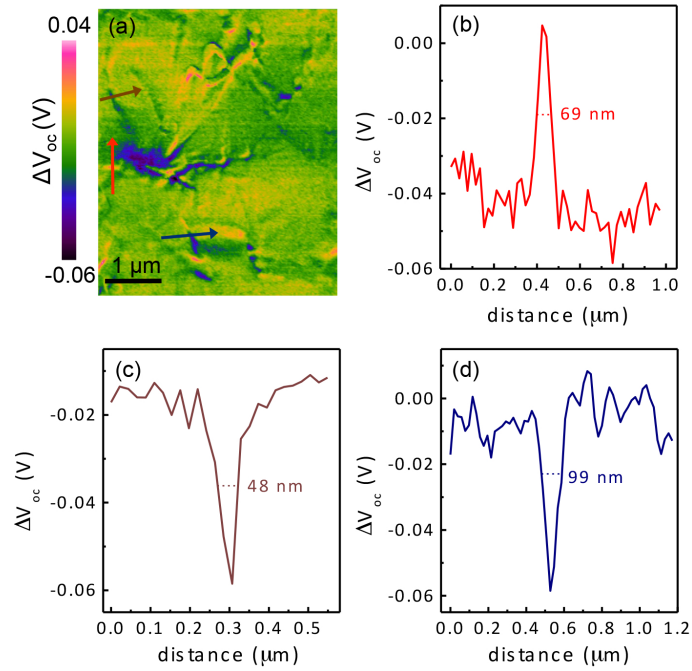


Figure 5.11: **Quantifying KPFM spatial resolution.** (a) ΔV_{oc} map for CdTe solar cell. (b)-(d) Line scans showing consistent spatial resolution <100 nm. The full-width-half-maximum that defines the lateral resolution of the method is indicated in each line profile.

with truly nanoscale resolution. Higher spatial resolution can be achieved by using smaller probes; such as high aspect ratio tips with gold nanoparticles on standard Si tips [260] or Si probes with 2 nm in diameter. [261]

For polycrystalline PV materials, the direct correlation between the structural properties of different grains and the V_{oc} maps can be used to identify the types of grains which should be favored during the thin-film deposition or growth. Further, nanostructured PV can tremendously benefit from this new technique because the identification of non-radiative recombination centers can guide the design of the next generation nano-enabled devices. It is well known that the V_{oc} of a PV device can strongly depend on surface passivation, and therefore spatial variations in the surface properties can lead to local variations in the V_{oc} , which can be accurately measured with our technique. Further, a

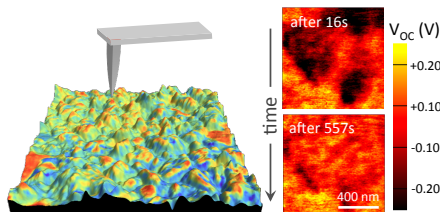
recombination center, which corresponds to a region with very small diffusion length, can be accurately measured by our imaging method. Although the carrier minority diffusion length of inorganic PV materials is greater than 100 nm, it is an average of the distance a carrier can move from point of generation until it recombines. Illuminated-KPFM does not require the preceding knowledge of the sample nor the probe work function because the difference between the work function of the material surface and the probe under illumination and in the dark suffices to determine local variations in V_{oc} .

5.4 Conclusion

In this chapter, we presented a new method to spatially resolve and image the V_{oc} in partially and fully processed optoelectronic devices with nanoscale resolution, <100 nm. The V_{oc} is a key figure of merit to determine the performance of a device; it is an indirect measurement of the recombination processes that take place within the material. The illuminated-KPFM technique is demonstrated in a variety of photovoltaic materials, ranging from epitaxial GaAs to polycrystalline CIGS, where we can resolve V_{oc} variation larger than 200 mV at the nanoscale. This metrology, introduced here for the first time, can be applied to any optoelectronic device, including photovoltaics, LEDs, and photodetectors, does not require full device processing, is non-destructive and works in ambient environment. Moreover, it can be used to determine if specific device processing steps are beneficial or harmful for the ultimate performance of a functional semiconductor material.

Chapter 6: Real-time nanoscale open-circuit voltage dynamics of perovskite solar cells

Hybrid organic-inorganic perovskites are an emerging material with great potential for high-performance and low-cost photovoltaics. However, for perovskites to become a competitive and reliable solar cell technology, their instability and spatial variation must be understood and controlled. While the macroscopic characterization of the devices as a function of time is very informative, a nanoscale identification of their real-time local optoelectronic response is still missing. Here, we implement a 4D imaging method through illuminated heterodyne KPFM to spatially (<50 nm) and temporally (16 seconds/scan) resolve the voltage of perovskite solar cells in a low relative humidity environment. Local V_{oc} images show nanoscale sites with voltage variation >300 mV under 1-sun illumination. Surprisingly, regions of voltage that relax in seconds and after several minutes consistently coexist. Time-dependent changes of the local V_{oc} are likely due to intragrain ion migration and are reversible at low injection level. These results show, for the first time, the real-time transient behavior of the V_{oc} in perovskite solar cells at the nanoscale. This chapter is adapted from J.L. Garrett, E.M. Tennyson et. al, *Nano Letters*, **17** 2554-2560 (2017) [39]



6.1 Introduction to nano-imaging in perovskite solar cells

Recent improvements in power conversion efficiency of perovskite solar cells have brought this class of materials to the same performance level as thin-film CdTe and CIGS photovoltaics, demonstrating its promise as a large-scale technology. [262–265] To date, the world record single-junction perovskite device has a power conversion efficiency of $\eta = 22.7\%$. [35] Moreover, perovskites are ideal for composing dual-junction designs with a Si or a CIGS bottom subcell. [266, 267] The remarkable performance of perovskite solar cells is primarily attributed to their high absorption combined with extremely long carrier diffusion lengths, [268] including one literature report of $>175 \mu\text{m}$. [269] Despite the rapid progress of the field, there is still a lack of understanding of why and how the material is changing/degrading when exposed to light and humidity. [50, 270] Thus, there is a pressing need in the scientific community to elucidate what causes the perovskite active layer to change when the device is operating [271] (exposed to light). Macroscopic electrical measurements, such as light J - V curves as a function of time, are extremely useful to track the device instabilities; [272, 273] however, one cannot infer how much variation exists from grain to grain and within one grain in the perovskite layer, which is needed to determine how the local changes affect the overall device performance.

Microscopy measurements provide a powerful framework for correlating the morphology of the active layers of the solar cells with fundamental physical processes and device performance. [37, 40, 130, 131] In particular, scanning microscopy techniques are ideal for investigating heterogeneity at the nanoscale, [51, 90, 138] such as the spatial domains on MAPbI₃. [51] Recently, micron-scale photoluminescence has been applied to resolve charge carrier recombination and ion migration in perovskite grains. [41, 138, 274]

Through piezo force microscopy, the ferroelectric domains of the perovskites have been observed. [275,276] By time-dependent Kelvin probe measurements it has been suggested that the hysteresis behavior commonly observed in perovskite devices could be related to trapped charges and ion migration across the light absorbing layer. [277] Kelvin probe force microscopy (KPFM) [278,279] has been used to map the electrostatic potential across multiple layers of active devices, [151,280] to measure work function changes during device poling, [281] and to probe the effect of grain boundaries on MAPbI₃. [282] Further, KPFM has been applied to investigate the possible origins of the hysteresis commonly observed in light J - V measurements. [69] Despite these advances, traditional high-resolution variants of atomic force microscopy (AFM) operate too slowly to spatially analyze dynamic events, such as structural changes, light induced chemical reactions, and ion migration.

Here we image, in real-time, the dynamics of perovskite solar cells with nanoscale spatial resolution (<50 nm) by mapping local changes in the open-circuit voltage (V_{oc}) through high-speed illuminated-KPFM (16 seconds/scan), see Figure 6.1(a). For that, we implement a novel KPFM method that preserves the spatial sensitivity while increasing the scan speed by >100 times when compared to conventional frequency-modulated-KPFM, where we map nanoscale voltage domains that vary by >300 mV under 1-sun illumination. The voltage within a perovskite grain changes substantially (both spatially and temporally) post light exposure, where regions out of and in equilibrium co-exist, and are attributed here to intragrain ion migration. We determine the spatial distribution of the local photogenerated voltage, how it varies as a function of time, and we quantify its dynamic behavior as the perovskite solar cell reaches its steady state: over 9 minutes. A time-dependent residual V_{oc} that lasts for minutes is found, resulting from migration, even under dark conditions. Our results demonstrate, for the first time, the transient electrical

behavior of perovskite solar cells with nanoscale spatial resolution.

6.2 Experimental methods

6.2.1 Perovskite solar cell fabrication

The solar cells are fabricated by the sequential spin-coating deposition of the perovskite layer ($\text{CH}_3\text{NH}_3\text{PbI}_3$) and the [6,6]-phenyl C61-butyric acid methyl ester (PCBM) layer. The perovskite layer is fabricated from lead (II) iodide (PbI_2) and methyl ammonium iodide (MAI), each deposited on a glass/ITO/PEDOT substrate by spin coating at 6000 rpm for 35 seconds. After deposition, the sample is thermally annealed at 100°C in a nitrogen dimethylformamide environment, as described elsewhere. [283] A 20 nm layer of PCBM is then deposited on top of the perovskite via spin coating at 6000 rpm for 35 seconds, and the device is annealed at 100°C for 60 minutes. This annealing process is implemented to passivate the perovskite and minimize photocurrent hysteresis. A 20 nm layer of C_{60} is then thermally evaporated to further aid the passivation of the active layer of the device. The macroscopic characterization of the devices (light J - V and EQE) is performed under nitrogen environment to prevent material degradation. The band diagram for the device is presented in Figure 6.1(b), where the approximate values of the energy gaps were obtained from refs [264,284–288]. Here, the PCBM layer functions as the electron transport material (ETM), while the PEDOT layer is the hole transport material (HTM), where the holes are preferentially collected through the indium tin oxide (ITO) electrical contact. The perovskite absorbing layer with nominal thickness of 300 nm is sandwiched by the PEDOT and the PCBM (see Figure 6.2). The perovskite films are composed of grains $\approx 1 \mu\text{m}$ in size and with a low density of pinholes, with $V_{oc} = 1.02 \pm$

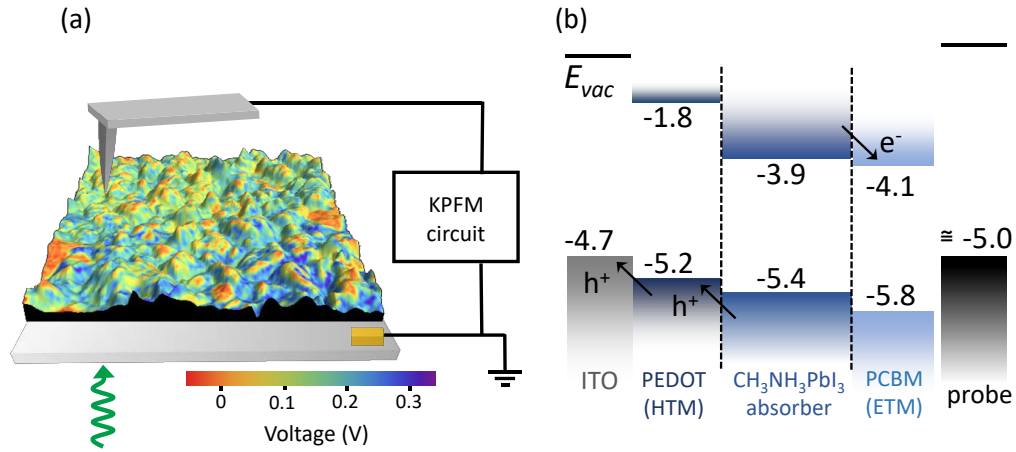


Figure 6.1: **Real-time nanoscale measurements of voltage dynamics in perovskite solar cells.** (a) Schematic of hybrid perovskite solar cells measured by illuminated-KPFM, out of scale for clarity. The local voltage is overlaid with topography, and the green arrow indicates the illumination direction. (b) Energy diagram of perovskite device and AFM probe illustrating the charge separation mechanism within the hybrid solar cell under illumination. E_{vac} refers to the vacuum energy level, and all energy values are in units of eV. The ITO layer is grounded with respect to the KPFM probe; thus, the subtraction of an illuminated- from a dark-KPKM scan provides a map of the open-circuit voltage of the device. ETM electron transport material; HTM hole transport material.

0.02 V (see Figures 6.2 and 6.3 for macroscopic device characterization and SEM images).

6.2.2 Illuminated Kelvin-probe force microscopy V_{oc} derivation

Kelvin probe force microscopy is a scanning probe method based on atomic force microscopy (AFM) that measures surface potential at nanometer length-scales and utilizes AFM to maintain small tip-sample separation, as reviewed in depth in Chapter 3. An AC voltage is applied to a conductive AFM probe, which in turn causes the probe to oscillate, generating a signal proportional to the difference between the voltage of the probe and the surface. A feedback loop then applies a DC voltage (contact potential difference, V_{CPD}) to the probe in order to minimize the KPFM signal, which originates from the cantilevers oscillation. The contact potential difference is defined to be $V_{CPD} = V_{probe} - V_{sample}$. We followed the calibration procedure described in Ref [155] to determine the

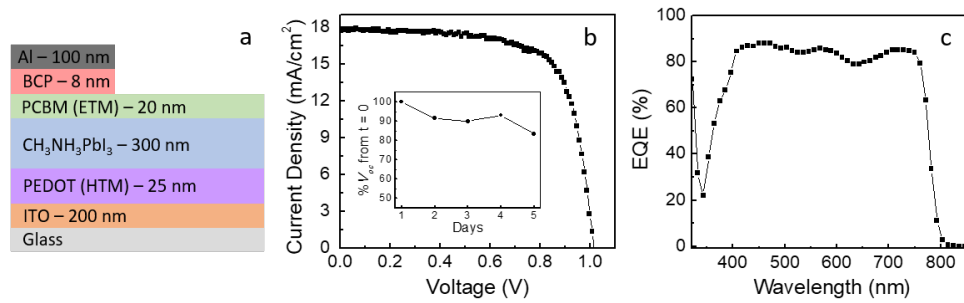


Figure 6.2: **Macroscopic characterization of perovskite solar cell device.** (a) Cross-section schematic of perovskite solar cell (out of scale for clarity). (b) Light J - V performed under 1-sun AM1.5G illumination in reverse bias. $V_{oc} = 1.02$ V, $J_{sc} = 17.72$ mA/cm², FF = 71.56%, $\eta = 12.91\%$. Inset: device V_{oc} variation as a function of time, where $t = 0$ refers to the first light J - V measurement acquired, just after device fabrication. (c) External quantum efficiency (EQE) measurement for the same device.

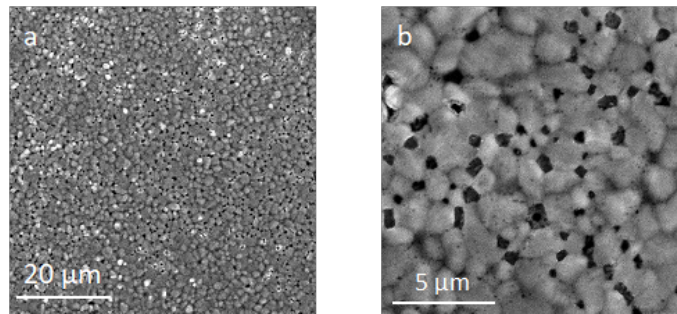


Figure 6.3: **SEM images of perovskite thin film.** (a,b) Scanning electron microscopy images of PCBM layer.

KPFM setpoint, avoiding topographical imprint on the KPFM data. [255] Here, the in-plane spatial variation of V_{CPD} is equal to the spatial variation of the surface potential, because V_{probe} does not depend on probe position.

Two KPFM techniques are used throughout the results presented here: heterodyne (H-) KPFM and frequency modulation (FM-) KPFM. H-KPFM is a newer technique, first developed to increase the sensitivity of KPFM in vacuum, while retaining the spatial resolution of FM-KPFM, [155] but it has recently been shown to operate quickly in air, reaching scan speeds of several frames a minute. [289] Here it is used in single pass mode, to map dynamic processes. It acquires each $(128)^2$ pixel image in 16 seconds and achieves a per-pixel signal standard deviation of about 30 mV. The sequential fast H-KPFM measurements are acquired by alternating top-bottom and bottom-top scans, and no correlation between the scan direction and the voltage signal is detected. FM-KPFM is used to scan rougher regions of the sample, which are observed to disturb the H-KPFM signal. It is configured in the side-band implementation with a modulation frequency of 800 Hz, [278] in the two-pass lift mode; topography is measured on the first pass and the probe is lifted 15 nm above to record the surface potential. The KPFM loop error signal, and 2f-KPFM signal, which is proportional to V_{AC} [155] are also collected, to verify proper functioning of the KPFM loop (see Figure 6.4). Lift mode helps to maintain stability of the FM-KPFM signal on rough topography. Each FM-KPFM image takes about 30 minutes to record, and contains $(256)^2$ pixels. The standard deviation per-pixel due to noise of FM-KPFM is ≈ 20 mV, whether estimated by sensitivity measurements or by sampling a uniform region of the potential.

The V_{oc} map is obtained using the following analysis, as discussed in ref [37] and the previous chapter:

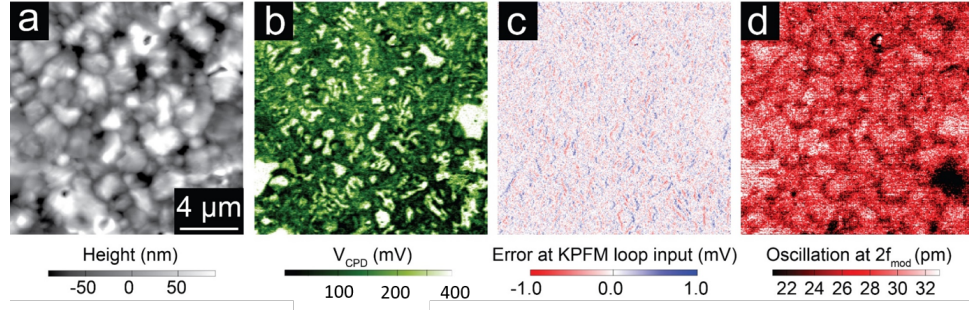


Figure 6.4: **Monitoring all relevant signals during FM-KPFM measurements.** (a) AFM topography shows a homogenous texture of grains. (b) Kelvin probe voltage (V_{CPD}) detected by a feedback loop at a frequency $f_{mod} = 800$ Hz from the first resonance. (c) Error signal in the feedback loop showing extremely small variations (~ 2 mV), which demonstrates the reliability of the method. (d) In FM-KPFM, a second signal at twice the modulation frequency ($2f_{mod}$) is also recorded and is proportional to the tip-sample capacitance. The scan shows how the sensitivity of the KPFM signal varies spatially.

$$\begin{aligned}
 V_{oc}^{partial} &= \frac{nkT}{q} \ln \left(\frac{I_{sc}}{I_{dark}} + 1 \right) = \frac{nkT}{q} \ln \left(\frac{J_{sc} \times A_{il}}{J_{dark} \times A_{cell}} + 1 \right) \\
 &= \frac{nkT}{q} \ln \left(\frac{J_{sc}}{J_{dark}} \right) + \frac{nkT}{q} \ln \left(\frac{A_{il}}{A_{cell}} + \frac{J_{dark}}{J_{sc}} \right)
 \end{aligned} \tag{6.1}$$

$$V_{oc}^{full} = V_{oc}^{partial} - \frac{nkT}{q} \ln \left(\frac{A_{il}}{A_{cell}} + \frac{J_{dark}}{q(EQE)\phi} \right) = V_{oc}^{partial} - \beta'(\phi) \tag{6.2}$$

$$\beta'(\phi) = \frac{nkT}{q} \ln \left(\frac{A_{il}}{A_{cell}} + \frac{J_{dark}}{q(EQE)\phi} \right) \tag{6.3}$$

Here, the superscripts partial and full refer to the illumination conditions, n (= 1.34) is determined from the slope of Figure 6.7(f), J_{sc} and J_{dark} are the short-circuit and the dark current densities, respectively, and $\beta'(\phi)$ depends on the illumination conditions (photon flux, ϕ) of the measurements. At 1-sun ($\phi = \phi(1\text{-sun})$), the short-circuit current term is given by: $J_{sc} = q(EQE)\phi(1 - sun)$, which is determined by a light J - V measure-

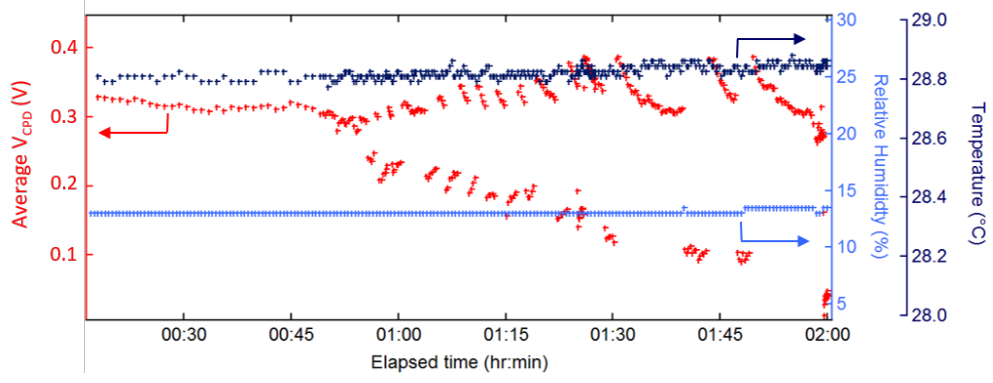


Figure 6.5: **Controlling the environmental conditions during *in situ* imaging of device performance.** Average value of voltage (V_{CPD}) for a sequence of alternating dark- and illuminated-KPFM scans as a function of time (red). The relative humidity (light blue) and the temperature (navy) of the environment inside the AFM chamber were both precisely controlled and monitored while performing the KPFM measurements.

ment (see Figure 6.2). When the device is under full illumination: $\beta' = 0$, as $A_{il} = A_{cell}$ and $J_{dark} \ll J_{sc}$.

6.2.3 KPFM implementation

For the measurements presented here, a Cypher AFM (Asylum Research) is used, with HQ:CSC37/Pt-B probes (Pt-coated Si-doped probe with <30 nm in radius and 0.3 N/m force constant, μ masch). Dry air is pumped into the microscope to maintain a low relative humidity ($<15\%$) and constant temperature (see Figure 6.5). The topography of the PCBM layer is observed to be stable during the time scale of our measurements (Figure 6.6). The ITO layer (bottom contact) is grounded with respect to the conductive probe for the KPFM measurements. A supercontinuum laser (WhiteLase, Fianium) with variable power density is used for the illuminated measurements at 500 nm wavelength, and neutral density filters are used for the smallest illumination intensities (<30 nW). FM-KPFM was used to acquire Figures 6.1, 6.7, and 6.8(b), while H-KPFM is implemented for Figures 6.8(c)-(h), 6.10, and 6.11.

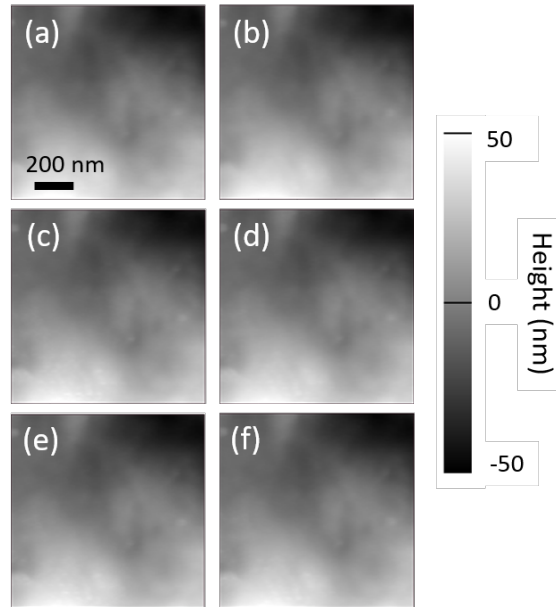


Figure 6.6: **AFM topography images.** (a)-(f) The morphology of the PCBM layer does not change within the time interval of the fast H-KPFM measurements (corresponding to Figure 6.8(c)-(h)).

We implement two types of KPFM to spatially resolve nanoscale changes of the voltage in the perovskite solar cell. KPFM measures the contact potential difference voltage signal (V_{CPD}), which is proportional to the difference between the work function of the conductive probe and the surface of the sample being scanned. To map the local voltage response in large areas of the device, frequency-modulated KPFM [290–292] can be used. To increase the scan speed of AFM techniques, common approaches include the use of polymeric cantilevers [293] or to reduce the size of the cantilevers while imaging the sample in an aqueous solution. [294] Although these methods are extremely useful to probe the topography of a variety of materials, they cannot be implemented to accurately measure voltage. Thus, to investigate the perovskites electrical properties in real-time upon illumination, we realize a variant of heterodyne-KPFM, which enables fast scanning (16 seconds/scan) while maintaining high spatial resolution. [155] Briefly, the frequency at which the voltage is detected is separated from the frequencies of both the topography

feedback loop and the applied voltage [155, 289] (see Figure 6.4 for maps of all relevant signals).

6.2.4 Image analysis

The KPFM images are analyzed using Igor Pro software. We used a linear drift correction software code, [295] based on the correlation of topography scans for the calculations of V_{oc} .

6.3 Fast-KPFM results and discussion

In order to better understand the voltage changes that occur under illumination, we perform light intensity dependent in situ measurements of the photogenerated voltage on a large, $16 \mu\text{m}^2$, area of the perovskites using KPFM. Figure 6.7(b)-(e) shows a sequence of illuminated-KPFM images from 2 nW to $54 \mu\text{W}$ (corresponding to low injection level). As the power of the incident light increases, so does the magnitude of the average V_{CPD} (despite the local variations in voltage, as discussed later in this manuscript). Figure 6.7(f) shows the expected linear increase of the averaged change in V_{CPD} under illumination, as a function of light intensity.

As derived in the Experimental Methods section, KPFM has been recently demonstrated as a novel method to map the local V_{oc} of half and fully processed photovoltaic devices with nanoscale spatial resolution, where V_{oc} is the voltage across a solar cell at open-circuit condition. In the illuminated- and dark-KPFM measurements presented here, the voltage on the conductive probe is referenced to the grounded ITO bottom contact. As a result, when the device is illuminated the splitting of the quasi-Fermi level (propor-

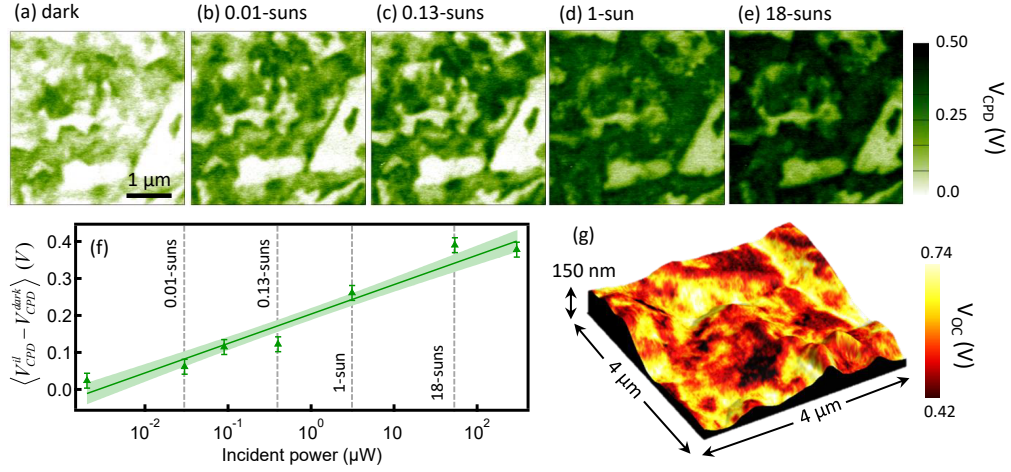


Figure 6.7: **Imaging nanoscale variations in the V_{oc} of perovskite solar cells.** (a) Dark-KPFM and (b-e) intensity dependent illuminated-KPFM scans measured on a perovskite device showing local variations in voltage. (f) Scan-averaged illuminated minus dark voltage ($V_{CPD}^{il} - V_{CPD}^{dark}$) as a function of incident power (light intensity). The error bars refer to the standard deviation of the averaged values, the green line is the best fit, and the green region represents two deviations from the mean. (g) Absolute V_{oc} map with nanoscale spatial resolution at 1-sun illumination, overlaid with topography.

tional to the V_{oc} of the solar cell) is directly measured by subtracting an illuminated- from a dark-KPFM scan. Here, we illuminate a well-defined area of the solar cell at normal incidence and, thus, the local V_{oc} can be expressed as: [37]

$$V_{oc}(x, y) = [V_{CPD}^{il}(x, y) - V_{CPD}^{dark}(x, y)] - \beta', \quad (6.4)$$

where (x, y) are the spatial coordinates, il and $dark$ refer to illuminated and dark conditions, respectively, and

$$\beta' = \frac{nkT}{q} \ln \left(\frac{A_{il}}{A_{cell}} + \frac{J_{dark}}{J_{sc}} \right), \quad (6.5)$$

at 1-sun illumination, where n is the ideality factor (obtained from the slope of the curve shown in Figure 6.7(f)), k is Boltzmann's constant, T is the temperature, and $A_{cell} = 1.0 \text{ cm}^2$, $A_{il} = 2.0 \times 10^{-3} \text{ cm}^2$ are the total cell and illuminated areas, respectively, and J_{dark}

and J_{sc} are the dark current and short-circuit current densities. The coefficient β' ($= -0.22 \pm 0.03$ V) is a calibration factor that depends on the illumination conditions and on the area of the device being probed. Note that when the whole cell is illuminated: $\beta' = 0$, as $A_{il} = A_{cell}$ and $J_{sc} \gg J_{dark}$. Figure 6.7(g) shows a representative V_{oc} map for the perovskite solar cell under 1-sun local illumination, which exhibits spatial variations >300 mV. These remarkable changes in photovoltage demonstrate that the materials electrical characteristics vary locally from grain to grain and within a single grain. The average value of the V_{oc} measured by KPFM is smaller than the initial value obtained by macroscopic light J - V measurements immediately after fabrication (Figure 6.2), which primarily results from the V_{oc} decay of the sample at a rate of $\sim 5\%$ per day (see the inset of Figure 6.2).

Figure 6.8(a,b) show representative topography and KPFM scans in a $16 \mu\text{m}^2$ region of the perovskite device in the dark (at equilibrium). The V_{CPD} varies spatially with a standard deviation of 80 mV (substantially greater than the noise) and is independent of the morphology of the sample. These spatial variations could be due to inhomogeneities either within the perovskite or within the PCBM layer, caused by the spin coating deposition process used to fabricate the sample. During all measurements presented here, the temperature was kept at 28-29 °C and the relative humidity $<15\%$ inside the AFM enclosure, see Figure 6.5 for stability of the environment inside the AFM chamber during dark and illuminated measurements. Figure 6.8(c)-(h) show the in situ changes in the voltage before, during and after illumination, obtained by fast-KPFM (16 seconds/scan), with $54 \mu\text{W}$ of incident power at wavelength of 500 nm. According to the KPFM initial dark scan, areas of both high and low surface potential co-exist (Figure 6.8(c)), with an average V_{CPD} of 0.2 V. Upon illumination, Figure 6.8(d), the surface potential increases substantially, to 0.4 V on average, as a result of the photogenerated voltage. No change

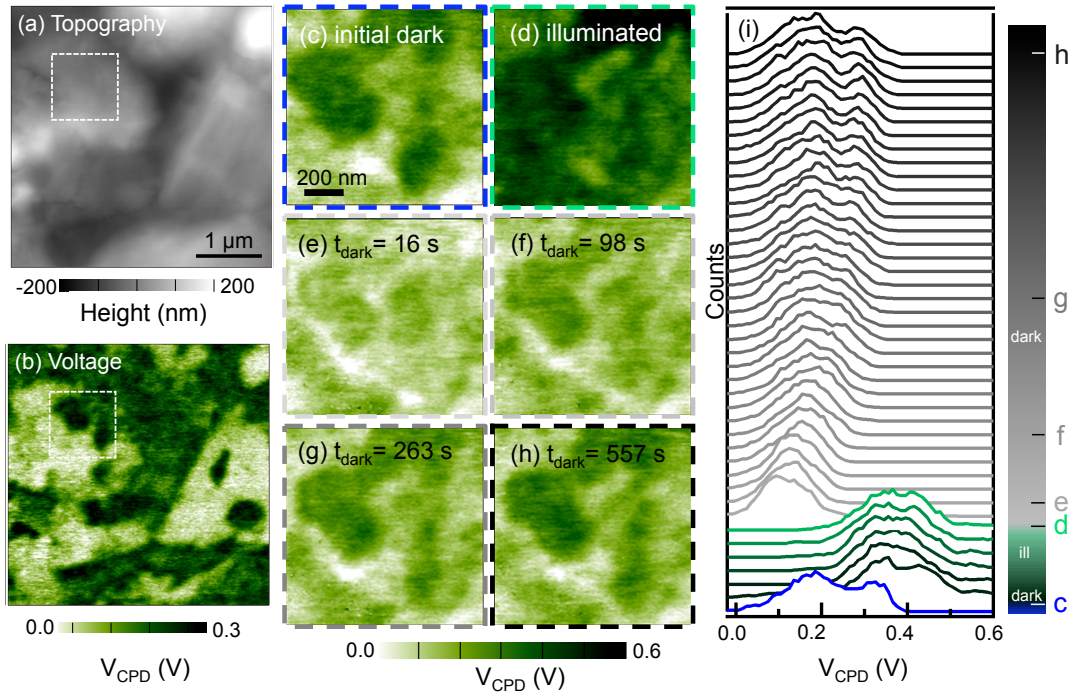


Figure 6.8: **Dynamics of perovskite solar cells at the nanoscale.** (a) Topography and (b) dark-KPFM measurements on a representative area of a perovskite photovoltaic device. A sequence of fast-KPFM measurements were acquired on the region highlighted by the white dashed square in (a,b): (c) dark-KPFM, (d) illuminated-KPFM, (e-h) dark-KPFM scans as a function of time. Note that after exposure to light (scan (d)), it takes the material \approx nine minutes to return to equilibrium (scan (h)). (i) Histograms of voltage distribution as a function of time for 42 KPFM scans (dark and illuminated) showing reversible dynamics upon a sequence of dark scans. Illumination conditions: 500 nm laser light at 54 μ W. Relative humidity <15%.

in topography is observed during the KPFM scans (see Figure 6.6), indicating that these perovskite devices are morphologically stable during this time frame, under the illumination conditions and the environment used in this experiment. Surprisingly, after turning the light back OFF, a transient decay of the voltage is observed, see Figure 6.8(e)-(h). Over time, the voltage returns towards its initial profile, where it takes \approx 9 min for the material to achieve its original surface potential spatial distribution (Figure 6.8(h)).

Through the voltage histograms displayed in Figure 6.8 we quantify this complex transient behavior of the perovskite's voltage. Each pixel in a 128×128 pixel map is binned according to its voltage value to produce the histograms. Note how the spatial

distribution of the voltage changes with time until the device reaches equilibrium again. In particular, the histograms reveal that the initial dark voltage distribution (blue) is quite broad, with a peak around 0.2 V, and under illumination this distribution increases to 0.4 V (green curves). However, after turning the laser OFF, the potential immediately becomes a single, fairly narrow Gaussian (light grey curve). As time progresses, the V_{CPD} broadens again, primarily by extending to higher voltages (dark grey curves). This behavior is also observed after exposing the perovskite to different illumination intensities (ranging from 2.0 nW to 4.2 mW, see Figure 6.9). These results demonstrate that after exposing the perovskite to light, its voltage changes as a function of time even under dark conditions.

Another striking observation about these perovskite solar cells is that upon removing the illumination, the V_{oc} does not immediately return to zero. Instead, a non-zero average voltage persists for several minutes, with a sign is opposite of the V_{oc} under illumination. This behavior is consistent with trap filling and subsequent ion migration, which have been observed to take minutes to equilibrate on the macroscale. [49, 296] To quantify the time-dependent voltage response within the perovskite solar cell, we analyze the spatial variation of this residual V_{oc} obtained by subtracting the equilibrium dark-KPFM image, Figure 6.8(h), from the post-illumination dark-KPFM scans, see for example Figure 6.8(e)-(g). Figure 6.10 displays the residual V_{oc} images for the perovskite solar cell for a series of snapshots. The dark measurement immediately after turning the laser OFF shows a transient electrical behavior (Figure 6.10(a)), most likely resulting from a reversible electronic process within the material. The representative scans shown in Figure 6.10(a)-(e) have two very distinct regions, with initial $V_{oc} = -0.2$ V (red) and $V_{oc} = 0$ V (blue), revealing a strong bimodal voltage distribution on the electrical response of the device,

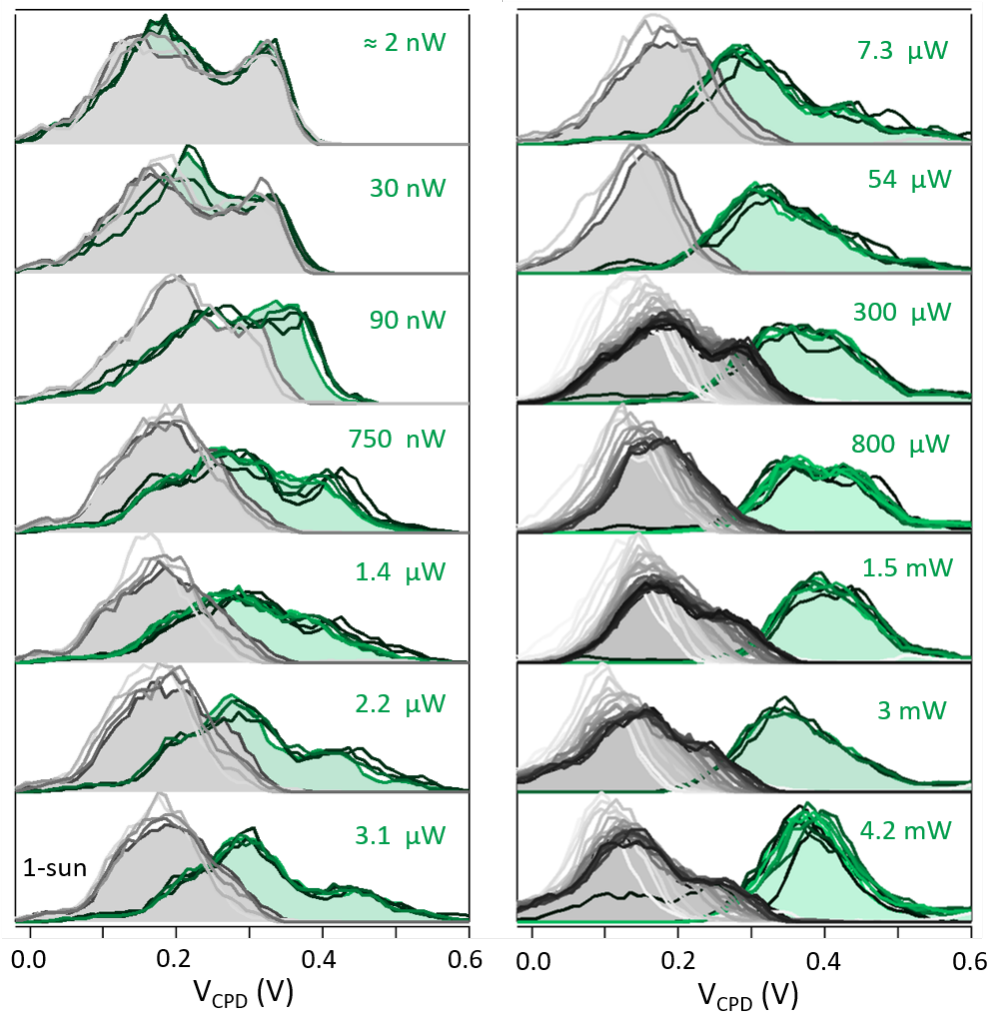


Figure 6.9: **Voltage profile for fast H-KPFM illumination scans.** Histogram of V_{CPD} for sequential H-KPFM scans showing signal variation as a function of illumination, using 500 nm (green curves) and under dark conditions (grey/black curves). Each histogram corresponds to one scan, acquired in 16 seconds in the same $1.0 \mu\text{m}^2$ area. The incident illumination power is listed on the right. Lines representing dark (light) scans become darker (lighter) the longer the light is OFF (ON), as shown in grey and green, respectively.

not resolved by conventional macroscopic electrical measurements or by standard AFM-based methods. As the system approaches equilibrium, the V_{oc} in the initially red region approaches zero, see voltage scans in Figure 6.10(b)-(e), while the blue regions remain unchanged. Figure 6.10(f) shows the averaged V_{oc} as a function of time for the entire scanned area shown in (a)-(e) (black curve) and the voltage for the regions highlighted by the white squares (red and blue curves). Each point on the graph corresponds to the averaged value (either within the white squares or for the entire scanned region). Here, the variance is calculated by considering each pixel in each box as an individual measurement with 30 mV standard deviation, and it is plotted at three standard deviations. The blue curve is constant under dark conditions (laser OFF), indicating that either some regions of the PCBM layer do not suffer any post-illumination driven electrical changes or that these regions return to equilibrium in less than 16 seconds. Nevertheless, the red curve shows that an out-of-equilibrium state persists for several minutes. These time-dependent measurements reveal that the voltage equilibration has a spatial dependence at the nanoscale that could be responsible for the light-dependent instability observed in perovskites. [297]

Because no net current flows out of the device at open-circuit conditions, an additional current term must balance the diode dark current (I_{dark}) to enable a residual voltage to exist without illumination. We explain this behavior using a simple diode model with an additional time-dependent current term, $I_{ion}(t)$, which could arise as a result of ion migration and/or a change in the density of trap states:

$$I(V) = I_L - I_{dark} \left(e^{\frac{qV}{nkT}} - 1 \right) + I_{ion}(t), \quad (6.6)$$

where I_L is the light-generated current of the solar cell. In the dark ($I_L = 0$), and at

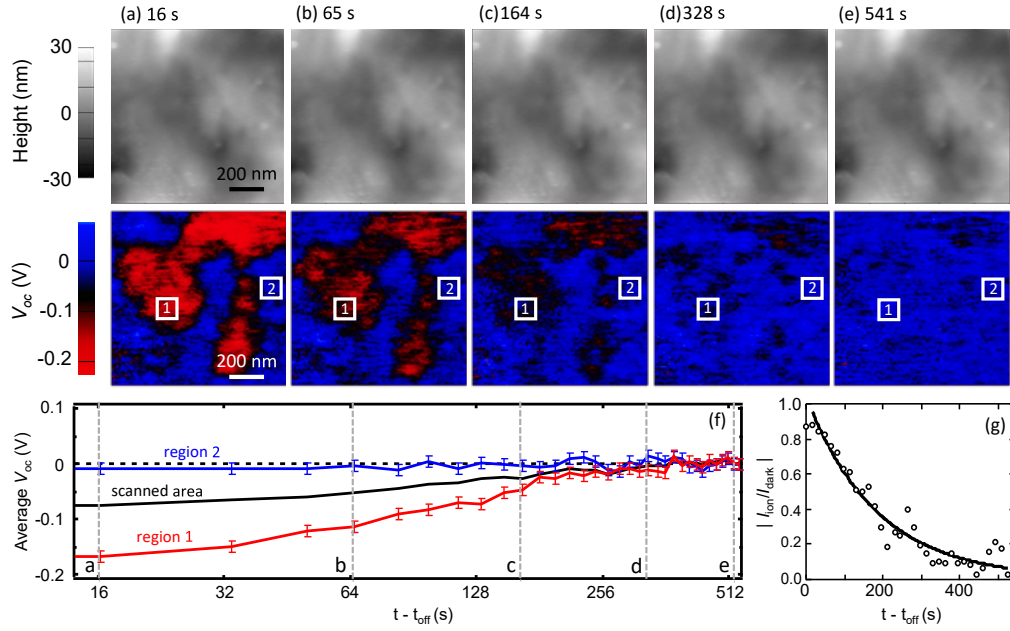


Figure 6.10: **Spatial and temporal variation of the residual photogenerated voltage within perovskite solar cells.** Topography and V_{oc} scans acquired after the solar cell is illuminated and brought back to dark conditions after (a) 16 s, (b) 65 s, (c) 164 s, (d) 328 s and (e) 541 s. Note that immediately after illumination, two distinct regions are observed, one with V_{oc} equal zero (blue) and another with $V_{oc} = -0.2$ V (red). (f) Averaged V_{oc} as a function of time for the entire scanned area shown in (a-e) (black), and for regions 1 and 2 (highlighted by the white squares). The error bars refer to three standard deviations from the averaged values. The vertical grey dashed lines correspond to the time interval where the scans (a-e) are performed. (g) Ratio of current due to ion migration (I_{ion}) and dark current (I_{dark}) as a function of time. Black line is an exponential fit to the experimental data resulting in a time constant of 185 ± 27 s.

open-circuit conditions, we have

$$I_{ion}(t) = I_{dark} \left(e^{\frac{qV_{oc}(t)}{nkT}} - 1 \right), \quad (6.7)$$

where $V_{oc}(t)$ is the time-dependent residual open-circuit voltage. Post-illumination, $I_{ion}(t)$ opposes the original dark current and tends toward zero on the time scale of minutes. Figure 6.10(g), shows the decay of $I_{ion}(t)$ as the device reaches equilibrium, resulting in a time constant of 185 ± 27 s.

As one of the primary limiting factors of perovskite photovoltaics is the material instability when exposed to light, we also measure the time-dependent local changes in V_{oc} under illumination, as presented in Figure 6.11. Here, we determine ΔV_{oc} by the difference between two illuminated KPFM maps, where each resulting scan corresponds to an instant of time subtracted from the last illuminated one in Figure 6.8(i), in light green. The sequence of ΔV_{oc} maps show the local spatial variation in the photogenerated voltage. As previously observed, [296] when the perovskite material is illuminated, the trap states due to vacancies are filled by electrons. As a result, the ions move away from these sites (due to electrostatic repulsion). We track this ion migration process, in real-time, by spatially resolving changes in the local voltage (ΔV_{oc}) that take place during material illumination. We hypothesize that ions migrate away from the PCBM layer (electron transport layer) due to the built-in electric field. Regions with $\Delta V_{oc} > 0$ and < 0 co-exist, strongly indicating that there is an accumulation of ions and vacancies within the illuminated area of the cell, which varies in time. At low injection level, this migration process is reversible and does not lead to material degradation. Yet, it changes the electrical behavior of the device locally, which ultimately affects the overall performance of the solar cells.

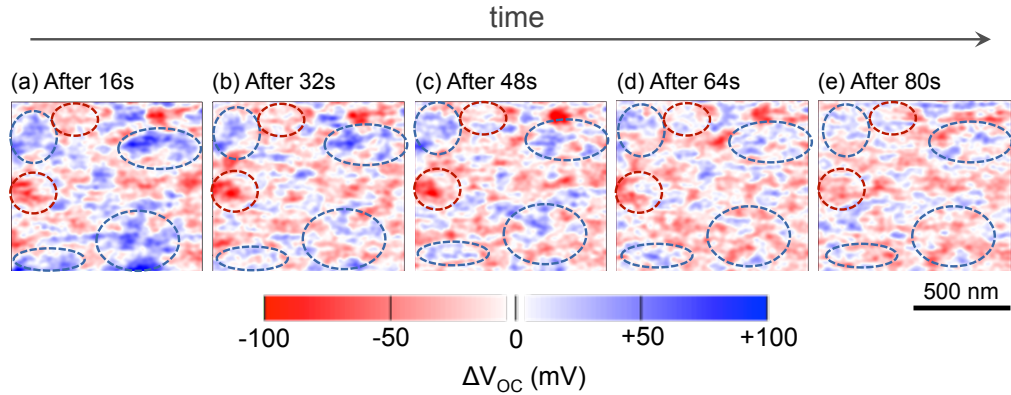


Figure 6.11: **Real-time nanoscale V_{oc} dynamics of perovskite photovoltaics.** Sequence of ΔV_{oc} maps as a function of time after (a) 16 s, (b) 32 s, (c) 48 s, (d) 64 s, and (e) 80 s of illumination. Each scan is subtracted from an illuminated one after 96 s (from 6.8i). The blue and red dashed areas highlight regions with transient voltage response. The scans size is $1 \times 1 \mu\text{m}^2$.

We attribute the dynamic behavior of the local electrical response of the perovskite solar cell mapped here to intragrain ion migration: [41, 282] charge accumulation takes place when the material is illuminated, and charge migration when the solar cell is no longer in operation (dark conditions). This photo-induced ion migration is primarily driven by the movement of to regions with depleted ions, as observed in prior photoluminescence experiments. [41] We demonstrate that this phenomenon is fully reversible at low illumination injection level (Figure 6.7) and does not result in permanent material degradation. Further, the spatial variations in the local electrical response are not accompanied by any changes in morphology (see Figure 6.6 for sequence of topography maps during material illumination), but the nanoscale time-dependent variations are most likely responsible for macroscopic instabilities observed in these perovskite solar cells. The diffusion of ions under dark conditions leads to a time-dependent local residual $V_{oc}(t)$, mapped here for the first time. Our results indicate that free carriers are probably responsible for the observed transient voltage. Once the material is under dark conditions again, some ions continuously move until the perovskite layer achieves an equilibrium state, which

takes place in several minutes for the material probed in this work (as shown in Figure 6.8).

6.4 Conclusion

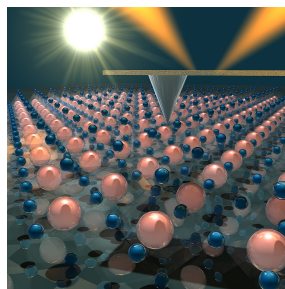
The real-time functional imaging method reported here can be combined with other scanning probe microscopies and big data analysis [298] to probe additional relevant phenomena that currently describes the unique illumination dependent behavior of perovskites, such as structural transformation, [299] ferroelectric domains, [275, 300] poling, [296] and piezoelectric behavior. [275] For instance, to map structural and chemical composition changes, fast-KPFM could be combined with tip-enhanced Raman spectroscopy. Likewise, to investigate the possible effects of long lived traps [301] on the devices local electrical response, our novel imaging method could be combined with pump-probe EFM/KPFM techniques, [302, 303] which measures voltage at microsecond timescales. Further, spectrally dependent fast-KPFM could help elucidating the mechanism responsible for light-induced self-poling in perovskites.

In summary, we imaged and quantified the real-time voltage dynamics of perovskite solar cells at the nanoscale (<50 nm) under illumination and post-illumination conditions by fast KPFM (16 seconds/scan) in a low relative humidity environment. 1-sun local V_{oc} maps of the perovskites revealed absolute variations >300 mV between and within grains. Under illumination, the photogenerated voltage of the perovskite varied spatially within one grain. After illumination, it took the material ≈ 9 min to reach its equilibrium state. This transient electrical behavior, most likely resulting from reversible ion migration within the perovskite layer, cannot be revealed by conventional macroscopic electrical measurements. The real-time nanoscale imaging experiments presented here demonstrate that the

V_{oc} of perovskite photovoltaics varies locally, and that light-induced reversible ion migration could be responsible for the time-dependent transient behavior of most perovskite photovoltaics. Substantial effort lies ahead to acquire a full picture of the mechanism(s) responsible for the light-induced physical and chemical processes frequently observed in this class of materials, and their effects on the maximum attainable V_{oc} . Nevertheless, our nanoscale time-dependent measurement represents a new imaging method to diagnose the local electrical response of perovskites, ranging from lead-free $\text{CsBrI}_x\text{Br}_{3-x}$ alternatives to mixed cation and halide compositions for optimized dual-junction solar cells. Thus, mapping the spatial and time dynamics of perovskite materials will likely impact the design of next-generation stable perovskite solar cells with reliable voltage response.

Chapter 7: Perovskite composition-dependent nanoscale voltage response

Perovskite solar cells that incorporate small concentrations of Cs in their A-site demonstrate a boost in both stability as well as overall device performance. Yet, how the Cs cation influences the electrical properties at the nanoscale of the photovoltaic material is still unknown. In this chapter, we determine how the composition affects the short- and long-term electrical stabilities of three perovskites under 1-sun illumination, MAPbBr₃, MAPbI₃, and Cs-mixed, with <50 nm spatial resolution. An anomalous irreversible electrical signature on MAPbBr₃ is mapped at the mesoscale, which results in entire grains with no contribution to the V_{oc} . These measurements verify the necessity of high spatial resolution mapping. Conversely, Cs-mixed perovskites exhibit fully reversible voltage, ultimately proving that the desired electrical output of this composition persists even at the nanoscale. Further, this material presents no spatial variation in V_{oc} as a function of illumination, as ion motion is restricted. Finally, we reveal that the performance of the Cs-mixed thin film remains stable as a function of four weeks. These results show that the nanoscale electrical behavior of the perovskites is intimately connected to their chemical composition and macroscopic response.



7.1 Introduction

The remarkable progress and research effort that has happened to improve perovskite solar cells in the past decade is unprecedented. [153, 304] This PV material has now achieved power-conversion efficiencies (η) for both single-junction [35, 305] and tandem devices containing perovskites [144, 306] $>22\%$. These advancements demonstrate researchers ripening comprehension of perovskites, and thus, the fabrication processes for higher quality materials, such as electronic charge carrier transport layers and film interfaces, are being refined. [307–309] While such advances are necessary to develop commercial PV devices, short- and long-term stability under realistic atmosphere environments and perovskites inability to pass accelerated ageing tests remain challenging. [152]

The heterogeneity and dynamics of the electrical behavior in perovskites begin at the nanoscale, [28, 34, 39, 151] and locally revealing the primary performance parameters with high spatial resolution can potentially be correlated to the beneficial, parasitic, and/or transient response and the overall device performance. For instance, under illumination, perovskites have local variations in V_{oc} , [37, 39, 90] photocurrent, [51] and photoluminescence signal [41, 310, 311] as a function of both space and time. The primary culprit of the heterogeneity is still under debate, but the strongest hypothesis thus far suggests halide ion migration. [49, 106, 312–314] Recently, triple-cation perovskites containing methylammonium (MA), formamidinium (FA), and Cs have been presented as a promising alternative, due to experimental evidence that Cs incorporation improves thermal, [315] moisture, [316, 317] and photoelectrical stabilities. [318] Simultaneously, the devices can maintain its output η , suitable for the future, large-scale deployment of this PV material. It has been lately observed that the addition of Cs affects the structural properties of the

absorbing layer by decreasing its lattice constant, while simultaneously preventing ion migration. [319] Nevertheless, it is currently unknown how the electrical signal of the grains constituting these perovskites changes upon illumination and if this composition suffers from ion motion at the nanoscale.

Here we elucidate how the presence of Cs-incorporated triple cations lead to a fully reversible nanoscale voltage response in perovskite solar cells for both short- and long-term stabilities. By implementing Kelvin probe force microscopy (KPFM), one can directly image spatial variations in V_{oc} under 1-sun illumination of three perovskites with different compositions. The sample that incorporates Cs yields a uniform and steady V_{oc} upon light treatment, irrespective of grains and grain boundaries. The MAPbBr₃ composition shows an anomalous, non-reversible light-induced electrical behavior. For this material, illumination under 1-sun results in >10% of the material with “zero-voltage” regions ranging from single grains to clusters, while no morphological variations are observed. Further, through spatially and temporally resolving the light-induced changes in the MAPbBr₃ sample, we demonstrate the effect of ion motion in these solar cells V_{oc} , which is responsible for the observed dynamics. These results show that the Cs-mixed perovskite is the only stable composition measured here at both the nano- and macroscale. The V_{oc} measurements presented can be applied to other perovskites, with alternative chemical compositions to track material degradation, and can be used in different atmospheres.

7.2 Experimental methods

7.2.1 ToF-SIMS characterization

Using a focused Ga^+ ion beam and scanning electron microscope dual-beam system, depth profiles are acquired, presented in Figure 7.1. Both the positive and negative secondary ions were generated by ionizing the species from the sample using a 20 keV Ga^+ ion beam with current at ~ 1.1 nA. The ToF-SIMS signals were recorded by a mass spectrometer. During the measurements, the vacuum level was kept below 10^{-4} Torr at all times. Three distinct locations were measured for each perovskite sample for statistical purposes. Areas of $20 \times 20 \mu\text{m}^2$ were sputtered while $10 \times 10 \mu\text{m}^2$ central regions were analyzed to avoid any edge effect.

7.2.2 Raman spectroscopy and microscopy

Raman spectra and maps for the MAPbBr_3 sample were acquired with a 650 nm laser excitation source and spectrometer, using a $100\times$ objective lens in a confocal optical microscopy setup. The Cs-mixed and MAPbI_3 samples were measured with a NT-MDT atomic force microscope, using an excitation source of 532 nm laser. Each pixel in the Raman map represents the integrated area under the peak, highlighted in Figure 7.2. All Raman maps are $5 \times 5 \mu\text{m}^2$ and were performed after the KPFM maps were measured.

7.2.3 Solar cell synthesis

Fluorine doped tin oxide coated glass slides (Sigma-Aldrich, $7\Omega/\square$) were cleaned by sonication in 2% Hellmanex solution for 15 minutes. After rinsing with deionized

water and ethanol, the substrates were again sonicated with isopropanol for 15 minutes and rinsed with acetone. The substrates were treated with UV-ozone for 5 minutes, and a 50 nm thick TiO₂ electron selective layer was deposited by spray pyrolysis at 450°C from a precursor solution of titanium diisopropoxide bis(acetylacetonate) (0.6 ml) and acetylacetone (0.4 ml) in anhydrous ethanol (9 mL). After the spraying, the substrates were left at 450°C for 30 min and left to cool down to room temperature. Mesoporous TiO₂ films were spin-coated (4000 rpm, 20 s) from a 1:10 solution of TiO₂ paste (30 NR-D, Dyesol) in anhydrous ethanol. The films were annealed on a programmable hotplate (2000 W, Harry Gestigkeit GmbH) using a 45 minute ramp to 450°C followed by a dwell time of 30 minutes. Perovskite films were deposited from a precursor solution; MAPbBr₃: MABr (1.2 M) and PbBr₂ (1.2 M) in anhydrous DMF:DMSO 4:1 (v:v); MAPbI₃: MAI (1.2 M) and PbBr₂ (1.2 M) in DMSO; Cs_{0.06}(MA_{0.17}FA_{0.83})_{0.94}Pb(I_{0.83}Br_{0.17})₃: FAI (1 M), PbI₂ (1.1 M), MABr (0.2 M), PbBr₂ (0.2 M) and CsI (0.075 M) in anhydrous DMF:DMSO 4:1 (v:v). The perovskite solution was spin-coated in a two-step program at 1000 and 6000 rpm for 10 and 20 s respectively. During the second step, 100 μl of chlorobenzene was poured onto the spinning substrate five seconds prior the end of the program. The substrates were then annealed at 100°C for one hour in a N₂ glove box. Subsequently, the substrates were cooled down for a few minutes and a PTAA (EM Index) solution (10 mg/ml in chlorobenzene) doped with bis(trifluoromethylsulfonyl)imide lithium salt (Li-TFSI, Aldrich) and 4-tert-butylpyridine (TBP, Aldrich) was spun at 4000 rpm for 20 s, as according to the literature. [146, 320] For the solar cells, 80 nm of Au was thermally evaporated under high vacuum for the top contact of the devices.

7.2.4 Macroscopic measurements

For the power conversion efficiency measurements, a solar simulator from ABET Technologies (Model 11016 Sun 2000) with a xenon arc lamp was used, and the solar cell response was recorded using a Metrohm PGSTAT302N Autolab. The intensity of the solar simulator was calibrated to 100 mW/cm^2 using a Si reference cell from ReRa Solutions (KG5 filtered). J - V curves were measured in ambient environment at room temperature, and under reverse bias (from high to low voltages) conditions, at a scan rate of 10 mV/s . The active area of the cells was 0.09 cm^2 and cells were measured two days after their preparation.

7.2.5 Kelvin probe force microscopy experiments

The KPFM measurements were performed using an atomic force microscope (AFM). A conductive Pt-coated Si probe is used with a 35-nm tip to measure the work function difference and topography of each sample simultaneously. Due to the geometry of the perovskite half-devices, in all cases the surface of the 50-nm thick PTAA hole transport layer was scanned. To neglect the influence of moisture during the KPFM measurements, piping connected to a dry air source was fed into the AFM chamber, which maintained a humidity level within the microscope to $<10\%$ relative humidity, see Figure 7.5. The samples were illuminated with a power-tunable 532 nm laser (1-sun), directed into the AFM. A small glass prism was placed underneath the perovskite thin film, and reflected light up toward the sample, producing a spot with 0.5 mm in diameter. Heterodyne-KPFM mode was implemented during the experiment, which measures the contact potential difference (V_{CPD}) of the tip-sample at the second resonance of the cantilever; see refs [39, 155] for de-

tails. The line-noise of 50 mV was quantified by examining voltage line profiles. Between experiments, the perovskite samples were stored in a low-humidity desiccant chamber, with the average humidity level between <10%.

7.3 Composition analysis of perovskites

Perovskites are, in most cases, an organic-inorganic hybrid material blend with a chemical formula of ABX_3 (A = monovalent cation, B = inorganic cation, and X = halide anion). The constituents of this structural form have been researchers primary tuning knob used to alter the optoelectronic properties of perovskites as well as improve the thermal, structural, and photo stability. [119, 150, 321, 322] The most common compounds for each lattice position are: A-site: methylammonium (MA = $CH_3NH_3^+$), formamidinium (FA = $HC(NH_2)_2^+$) and inorganic Cs^+ ; B-site: Pb^{2+} , which has the best performance in this location (although very recent studies show that a partial substitution of Co^{2+} or Bi^{3+} could boost output power) [321, 323]; and X_3 site: I^- , Br^- , and/or Cl^- .

We investigate three perovskite thin-films with different compositions. First, the conventional $MAPbI_3$ (with bandgap = 1.58 eV) is selected because its electronic properties are well documented, and therefore, it is an ideal candidate for systematic testing of the chemical composition contribution to the nanoscale electrical response. Another pure halide, $MAPbBr_3$, is analyzed; this perovskite has a higher bandgap (2.2 eV) and, thus, larger V_{oc} and limited photocurrent, and it could be utilized in tandem PV devices. The overall electrical performance (macroscopic) of pure-halide perovskites has been observed to degrade with exposure to either light and/or moisture, especially when the sole A-site compound is MA. [153, 324, 325] Cation engineering is implemented by adding a small amount of an inorganic component, Cs^+ , to a mixture of MA and FA, and also use a

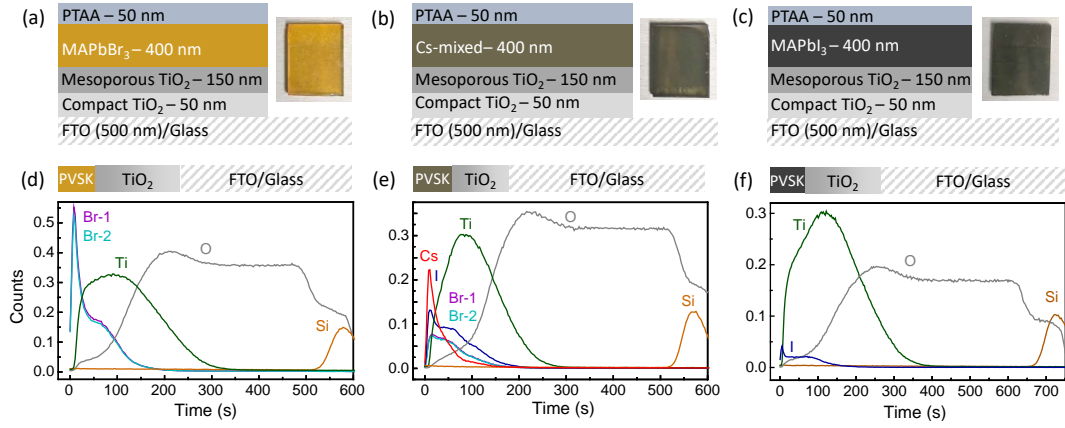


Figure 7.1: **Chemical composition analysis of perovskites by ToF-SIMS.** Schematic and real-color photographs of perovskite samples: (a) MAPbBr₃, (b) Cs-mixed, and (c) MAPbI₃. Samples size = $1.2 \times 1.5 \text{ cm}^2$. (d)-(f), Representative depth profiles of ToF-SIMS measurements acquired for each sample.

mixture of halide atoms. This approach has been observed to improve the stability in ambient environments substantially. [146, 318] The third sample investigated here has a mixed A-site and X-site perovskite material: $\text{Cs}_{0.06}(\text{MA}_{0.17}\text{FA}_{0.83})_{0.94}\text{Pb}(\text{I}_{0.83}\text{Br}_{0.17})_3$ (i.e. Cs-mixed, also with bandgap $\approx 1.58 \text{ eV}$). [146, 326] See the Methods section for detailed information about the perovskite thin film/device fabrication steps. Half-devices are fabricated, which are composed of PTAA/perovskite/TiO₂/FTO/glass, to perform nanoscale electrical measurements through KPFM, as will be presented later in this chapter.

To confirm the existence of each species within all perovskite compositions, time-of-flight secondary ion mass spectroscopy (ToF-SIMS) are performed and the depth profiles of the relevant elements are collected. Figure 7.1 displays a schematic of the perovskite samples and their corresponding thicknesses, plus the respective real color photographs (Figure 7.1(a)-(c)), which are an indicator of their bandgaps. The elemental depth profiles obtained by ToF-SIMS (Figure 7.1(d)-(f)) validate the presence of the constituent elements in the perovskite films with minimal diffusion throughout the other thin-film layers, see the experimental methods.

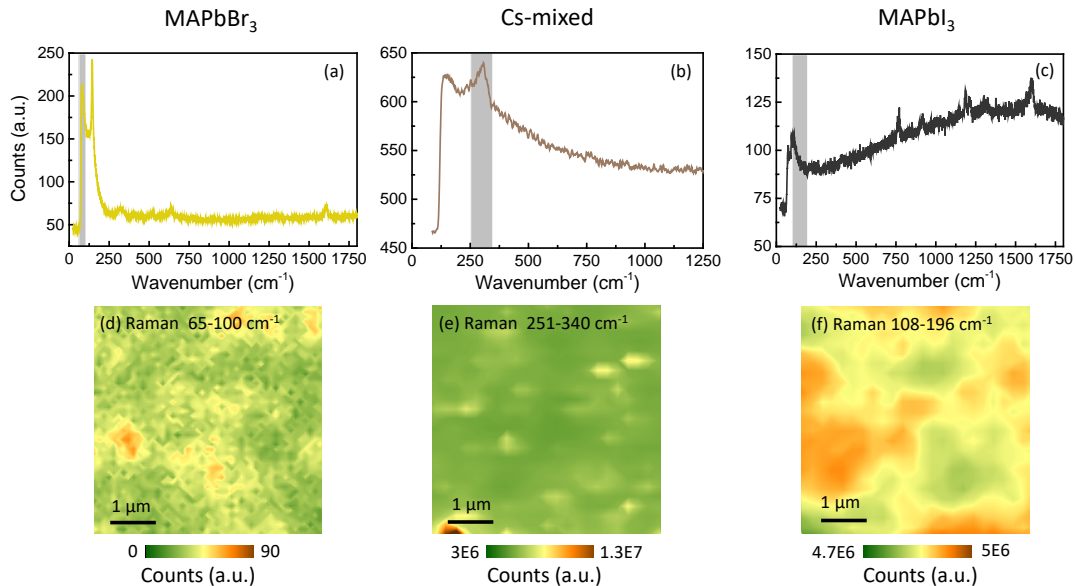


Figure 7.2: **Raman microscopy on perovskite thin films.** (a)-(c), Raman spectra and (d)-(f), their corresponding Raman maps. Each pixel in the $5 \times 5 \mu\text{m}^2$. Raman map is the integration of the Raman peak highlighted by gray in the spectrum above, where the range in cm^{-1} is indicated within the maps. Raman peak identification (a)-(c): $\text{Br}_3\text{-Pb-Br}_3$ stretching, asymmetric; MA torsion, and Pb-I_3 stretching symmetric, respectively. [327, 328]

As desired, Br (two isotopes shown as Br-1 and Br-2 in Figure 7.1), Cs, and I are all confined to the perovskite layer of the samples. Further, the chemical composition is uniform throughout each layer. This uniform distribution in the composition is in agreement with our Raman microscopy chemical imaging, see Figure 7.2.

7.4 Probing perovskites' electrical response at the nanoscale

Each perovskite thin-film investigated here also has a full device counterpart. Light J - V curves and η vs. time plots are presented in Figure 7.3, detailing the average performance parameters of the investigated films (see Methods for parameter specification). From the macroscopic measurements, it is clear that the Cs-mixed sample has the highest η at 18.6% while concurrently having excellent short-term performance stability (Figure

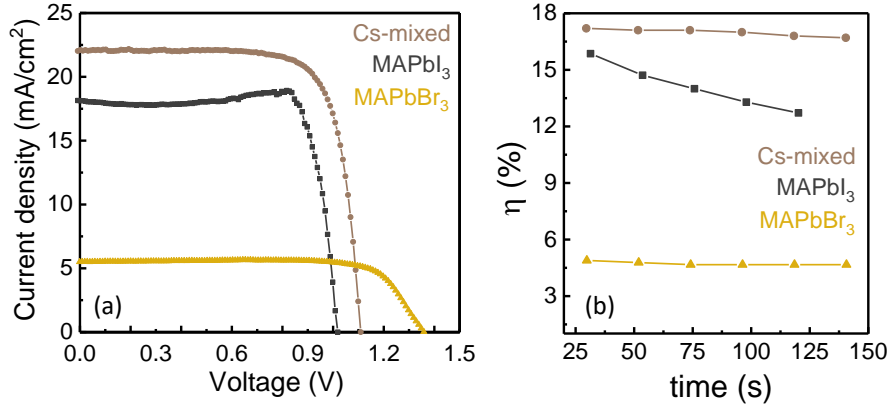


Figure 7.3: **Macroscopic performance and short-term stability of perovskite solar cells.** (a) Light J - V curves for all the perovskite solar cells investigated here (color-coded). For Cs-mixed, MAPbI₃, and MAPbBr₃: $V_{oc} = 1.11, 1.02,$ and 1.36 V, $J_{sc} = 22.1, 18.1,$ and 5.5 mA/cm², FF = 76, 85, and 76%, and $\eta = 18.6, 15.7,$ and 5.7%, respectively. (b) η vs. time for each perovskite device. The Cs-mixed sample shows the highest performance and stability while the MAPbI₃ device degrades rapidly with time.

7.3(b)). The MAPbBr₃ solar cell has the lowest efficiency at 5.7% despite having the largest V_{oc} (due to its wide bandgap) and also maintains an unchanged electrical output with time, see Figure 7.3(b). Yet the MAPbI₃ device, which initially has a promising $\eta = 15.7\%$, rapidly falls to $<13\%$ in two minutes, signifying that this perovskite composition is the least electrically stable. Furthermore, despite the larger fill factor (FF), the MAPbI₃ light J - V curve contains an undesirable bump between 0.8-0.9 V, which is attributed to charge build-up close to the electrical contacts. [49] For these reasons, we have chosen to focus these high-resolution mapping experiments on the MAPbBr₃ and Cs-mixed perovskite compositions, to understand how their nanoscale voltage behavior influences the materials electrical stability.

The nanoscale, real-time V_{oc} response of the perovskites is imaged by Kelvin-probe force microscopy (KPFM) under 1-sun illumination conditions and extremely low humidity. A schematic of the KPFM experimental setup is presented in Figure 7.4. The samples

are illuminated from the bottom using a 532-nm laser beam incident on a glass prism, which reflects an equivalent photon flux of 1-sun up towards the sample. Briefly, KPFM measures the work function difference between the atomic force microscope (AFM) probe and the sample surface. [28] Upon illumination, the perovskite absorbs photons, which generate charge carriers, introducing quasi-Fermi level splitting (directly proportional to the V_{oc}) [37] and thus, changing the work function of the material. By subtracting an illuminated KPFM scan by a dark one performed in the same location, and maintaining a common electrical ground between the probe and the perovskite samples back electrode (FTO in this case), we image V_{oc} with spatial resolution <50 nm. [37, 39] The relative humidity in the AFM chamber is held $<8\%$ (Figure 7.5) by continuously flowing dry air into the microscope through a piping system. See the experimental methods section for more details on experimental parameters. The nanoscale voltage response of perovskite samples before, during, and after illumination are mapped, termed here $\text{Dark}_{(1)}$, Light , and $\text{Dark}_{(2)}$, respectively.

7.4.1 Irreversible nanoscale electrical response in MAPbBr_3

Figure 7.6 displays measurements of the nanoscale voltage response of the MAPbBr_3 perovskite under 1-sun illumination, where an irreversible response is observed upon the material's first exposure to light. During the entirety of our experiments, no topography changes are observed (Figure 7.6(a)-(c)), indicating that any variations in the electrical signal are due to non-morphological properties of the perovskites. It also demonstrates that during the scans the AFM probe is kept intact (and all changes in tip-sample interactions are due to changes in the electrical output of the perovskites). The MAPbBr_3 perovskite presents extraordinary, irreversible light-induced electrical behavior at the nanoscale, with

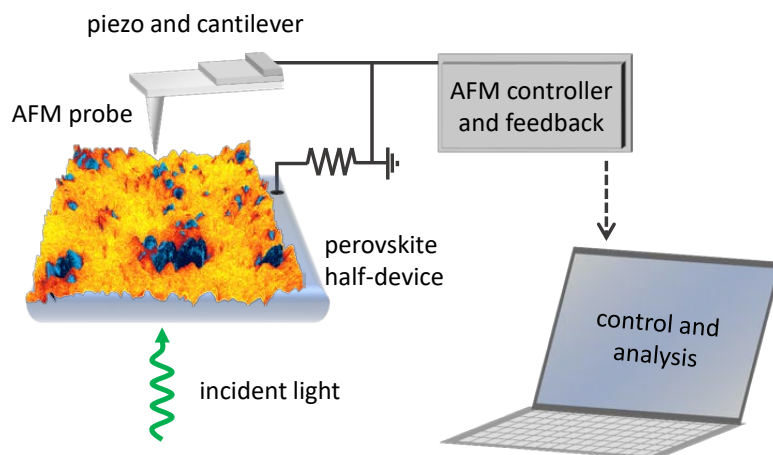


Figure 7.4: **Imaging the V_{oc} response in perovskites at the nanoscale.** Schematic of the illuminated-KPFM experimental setup, where the perovskite samples are back illuminated, and the local voltage signal is measured by an AFM probe using Kelvin-probe force microscopy. Because the perovskite back contact is grounded with respect to the tip, the data acquired under illumination is proportional to the V_{oc} of the solar cell.

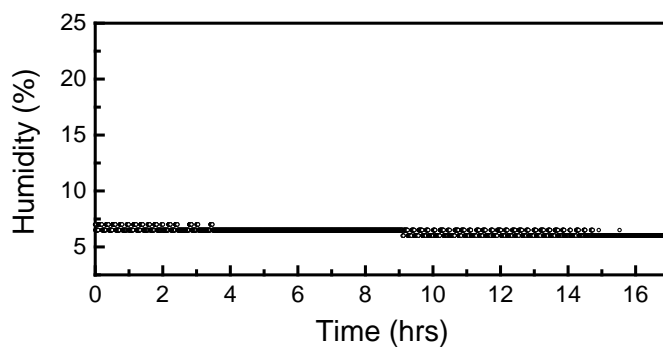


Figure 7.5: **Relative humidity during KPFM measurements.** The humidity level inside the AFM chamber was monitored every 30 seconds during the experiments. A constant dry air flow was pumped into the chamber to maintain low moisture content.

no morphological changes. Before this sample is exposed to light, the voltage is nearly uniform, see Dark₍₁₎ image in Figure 7.6(d), with an average voltage equal to 1.04 V. Upon illumination (Figure 7.6(e)), the an inhomogeneous photovoltage response which differentiates itself from the distribution of the initial dark scan. After sample illumination (Figure 7.6(f)), a new electrical and reversible state emerges, termed as Dark₍₂₎. There are two distinct regions within the MAPbBr₃ voltage maps in Figure 7.6(d)-(f): (i) the background, where the light-induced voltage shows the largest increase (very light green, voltage = 1.84 V), and (ii) unique perovskite grain and grains clusters which have become inactive photovoltage sites, viewed as the medium-green color in Figure 7.6(e) and (f) (voltage = 1.49 V in both cases). Note that after the initial illumination of the MAPbBr₃ sample (shown in Figure 7.6(e)) the voltage responses, both Light and Dark, become reversible.

To quantify the actual effect of the high and low voltage regions on the V_{oc} of MAPbBr₃, we subtract a Dark_(x) image from a Light-KPFM scan, and obtain V'_{oc} maps, as indicated in Figure 7.6. Here V'_{oc} is defined as an effective V_{oc} because it results from the partial illumination of the perovskite (laser is focused and, thus, the excitation of carriers is localized) using a single wavelength, and considers the dark current contribution of the entire sample area. Thus, as expected, V'_{oc} differs from the macroscopic V_{oc} , where the volume of carriers excited is much larger. Two contrasting areas are immediately apparent when comparing the $V'_{oc(1)}$ and $V'_{oc(2)}$ maps (Figure 7.6(g) and (h), respectively), as locally, the $V'_{oc(2)}$ value drops to zero (dark red regions). Because the electrical response does not change post-illumination, the photovoltage generation is now inactive at these sites, harming the local and, thus, macroscopic performance of devices. These parasitic regions cover approximately 12% of the scanned area shown here. Surprisingly, despite the

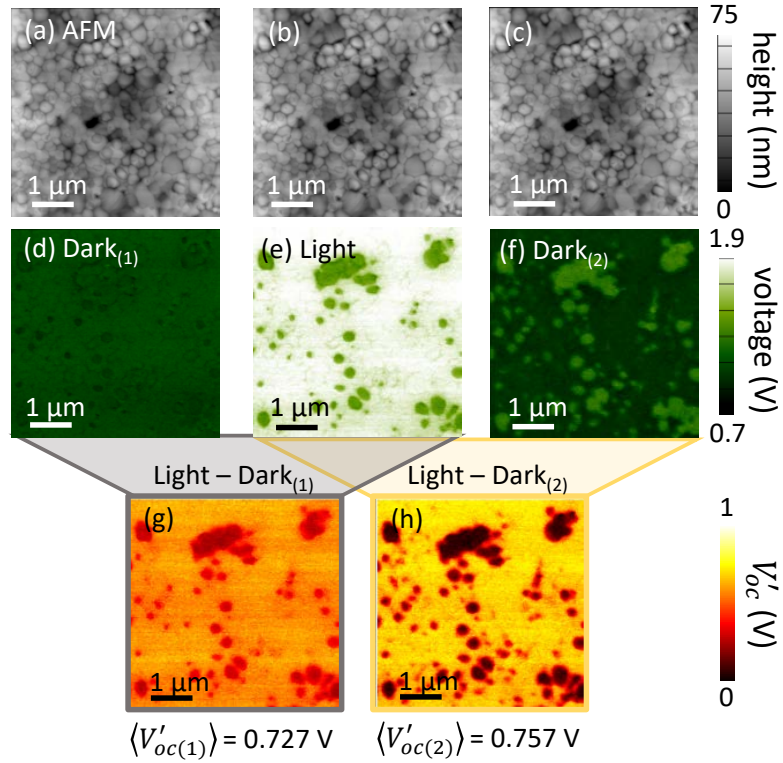


Figure 7.6: **Nanoscale irreversible voltage response in MAPbBr₃ perovskites.** (a)-(c) AFM topography maps of the MAPbBr₃ sample and their respective (d)-(f) voltage images under sequential dark, illuminated, and dark conditions. Here, despite consistent topography, an irreversible electrical process occurs within the MAPbBr₃ perovskite film. (g,h) Spatial variation in open-circuit voltage under local illumination where: $V'_{oc(1)} = \text{Light} - \text{Dark}_{(1)}$, and $V'_{oc(2)} = \text{Light} - \text{Dark}_{(2)}$. For all measurements relative humidity <8%, and for all light-KPFM scans the illumination conditions are a 532-nm laser under 1-sun incident photon flux.

zero-voltage grains in the $V'_{oc(2)}$ map, the average V'_{oc} value of the entire scanned region ($\langle V'_{oc(x)} \rangle$), quoted underneath Figure 7.6(g) and (h)) increases by 30 mV after illumination. Note that a macroscopic measurement would not capture such irreversible behavior and could inadvertently lead to the conclusion that there is an overall enhancement in performance, when this is not the full story. We hypothesize that this irreversible electrical process is caused by Br^- ion motion within the perovskite film. [329–331] Because Br is a negatively charged ion, it tends to move towards the electron transport material during operation conditions (meaning, during illumination). The movement of these ions away from the surface (i.e. PTAA, the hole transport layer) is likely the reason for the observed heterogeneous depletion of voltage at the tip-sample junction.

Through fast-KPFM we determine the immediate changes that take place in the perovskites electrical response upon illumination in two representative regions within the scanned area of Figure 7.6, see Figures 7.7 and 7.8. Briefly, in fast-KPFM, the real-time voltage is measured, where each map is acquired in 16 seconds. [155] As the laser is turned ON/OFF, the transient and asymmetric voltage response of this perovskite is captured, as displayed in the maps presented in Figure 7.7 and in the corresponding voltage histograms. Once the sample is illuminated under 1-sun (Figure 7.6(c)) the electrical signal changes substantially, corresponding to the photo-generated voltage. Here, the ‘slow’ voltage increase that takes place in $\sim 2\text{-}3$ minutes (red-color histograms) results from ion motion within the perovskite. As the material is illuminated the electrons fill in the existing trap states.¹² Consequently, the Br^- anions now have a preferential motion direction — away from these filled states. Upon turning the laser OFF a residual positive voltage response is measured for ~ 10 min (see gradual change in signal from Figure 7.7(f) to (i) and red to purple histograms in Figure 7.7(j)). Here, the dynamic voltage signal

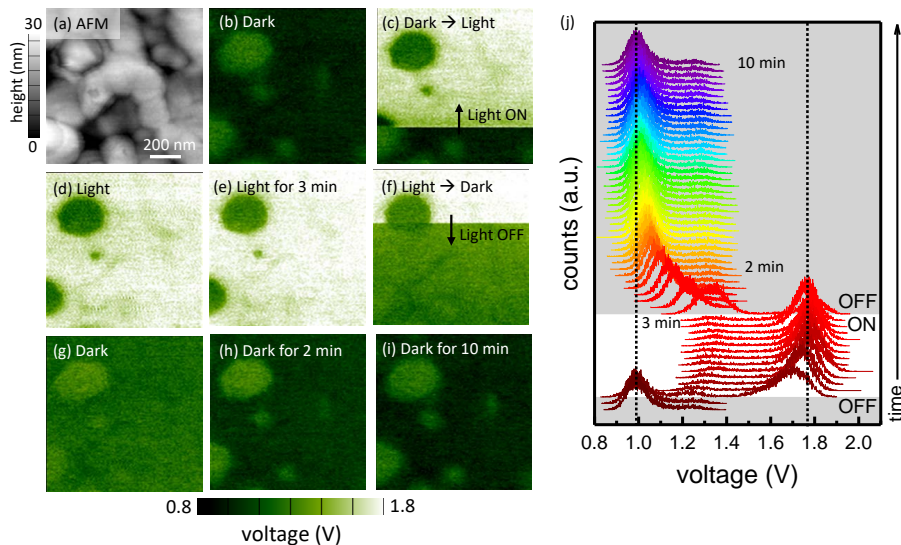


Figure 7.7: **Dynamic, reversible electrical response after the first illumination of MAPbBr₃.** (a) Topography map. (b)-(i) Fast Dark- and Light-KPFM scans (16 sec/scan) shown in chronological order, demonstrating the slow reversibility of the voltage response in 10 minutes post illumination. During scan (c) the 532 nm laser at 1-sun is turned ON, scan direction bottom to top. During scan (f) the illumination source is turned OFF, scan direction from top to bottom. (j) Corresponding voltage histograms for the entire fast KPFM series.

at open-circuit conditions results from the now reversible electron and Br⁻ motion. Yet, there is a hysteresis in the nanoscale voltage, where it takes more than 2× longer for the voltage to equilibrate under dark conditions. Note that this time-dependent voltage behavior could not be resolved by conventional KPFM methods, as they would not capture the short-time voltage changes.

7.4.2 Fully reversible and stable Cs-incorporated triple cation perovskites

The macroscopic electrical performance and stability of solar cells, shown in Figure 7.3, can be traced down to their nanoscale constructs. Therefore, revealing the relevant local voltage responses will help answer the open-question of: “Why does Cs-incorporation significantly improve overall device efficiency and stability?” Thus, we dedicate this section to the effect of cation engineering on the material at short- and long-term time scales.

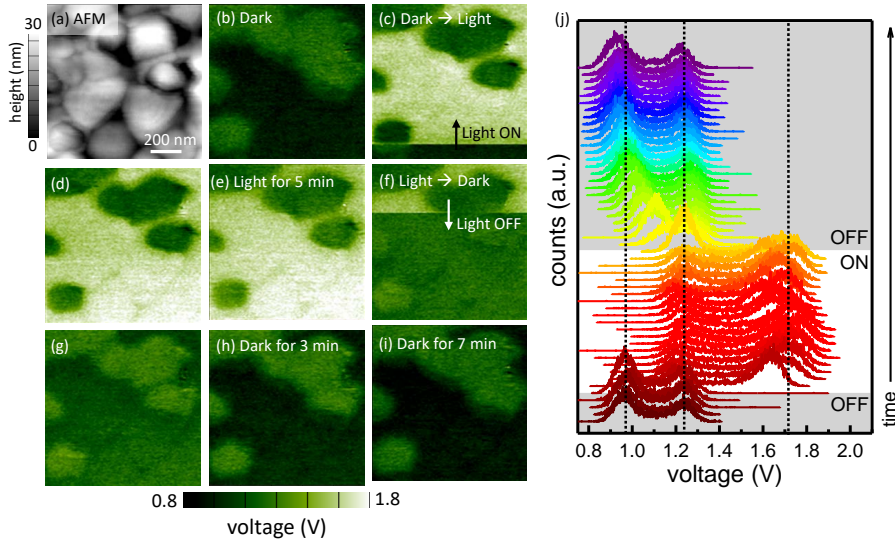


Figure 7.8: **Dynamic electrical response after illumination of MAPbBr₃ region 2.** (a) Topography map. (b)-(i) Fast Dark- and Light- KPFM scans (16 sec/scan) acquired, shown in chronological order, demonstrating the slow reversibility of the voltage response in ~ 10 minutes post illumination. During scan (c) the 532 nm laser at 1-sun is turned ON, scan direction bottom to top. During scan (f), the illumination source is turned OFF, scan direction from top to bottom. (j) Corresponding voltage histograms for the entire fast KPFM series.

In Figure 7.9 the morphology (which is constant as a function of time and illumination, Figure 7.9(a)-(c)) and electrical signal of Cs-mixed composition at the nanoscale is shown. We measure a very uniform voltage distribution (Figure 7.9(d)-(f)) under both dark and light conditions, irrespective of the interfaces between the grains. This is desirable for large-scale solar cell deployment, and a distinct difference from the behavior of MAPbBr₃. The Cs-mixed sample also presents fully reversible voltage response (under the experimental conditions tested here) determined by extracting the difference between the $V'_{oc(1)}$ and $V'_{oc(2)}$ maps (= 9 mV), see Figure 7.9(g)-(h), which is well within the line-noise level of our KPFM measurements. The ion motion suppression in the Cs-mixed perovskites is further confirmed by applying fast-KPFM, as shown in Figure 7.10. As a region consisting of several grains undergoes illumination cycling, the nanoscale voltage response is fully reversible, and it immediately changes upon turning the laser ON/OFF. It is important

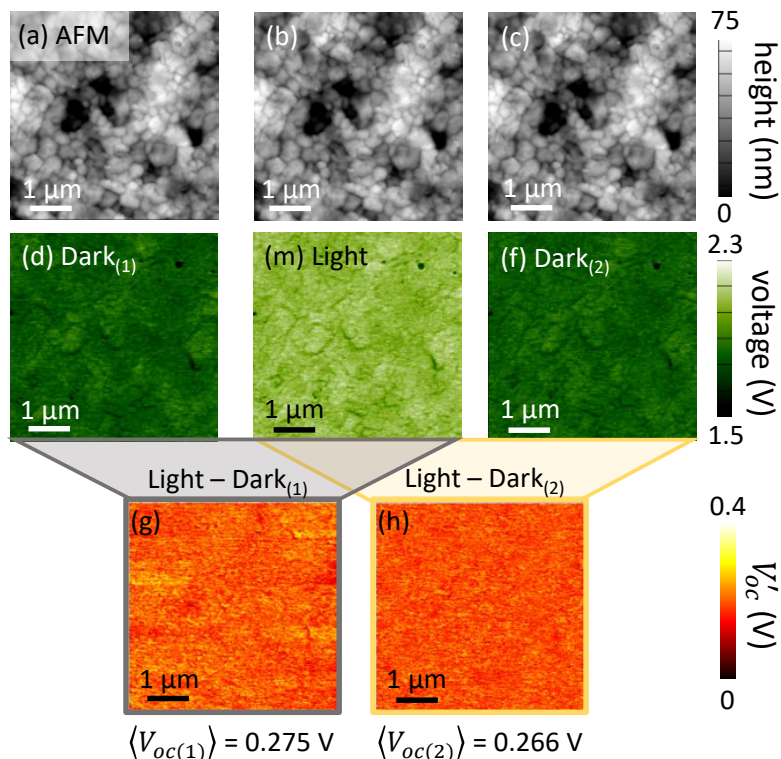


Figure 7.9: **Nanoscale reversible voltage responses in Cs-mixed perovskites.** (a)-(c), Topography and (d)-(f), KPFM maps of the Cs-mixed sample showing fully reversible voltage and no significant spatial variations. (g,h) V'_{oc} maps, where the difference in the average value between the two images is within the noise level of the KPFM measurements. For light-KPFM scans, the illumination conditions = 532-nm laser at 1-sun incident photon flux. All measurements held relative humidity <10%.

to reiterate that, as expected, the absolute value of the V'_{oc} for the Cs-mixed sample is lower than the MAPbBr_3 one due to its smaller bandgap energy, see Figure 7.3. Yet, the differences in the perovskites electrical behavior can only be attributed to their compositions, as the experimental parameters, grain morphology, and thin film stacking layers are all similar. Through our scanning probe microscopy experiments we elucidate that the presence of Cs prevents the degradation of the perovskites at the nanoscale, ultimately leading to the stable macroscopic response observed in this system. [317,318]

Figure 7.11 shows the stability of all samples investigated here after four weeks of KPFM experiments. As described in other reports, [146, 319, 326] by incorporating Cs into the A-site position (which has a smaller radius than both MA and FA), [332] halide

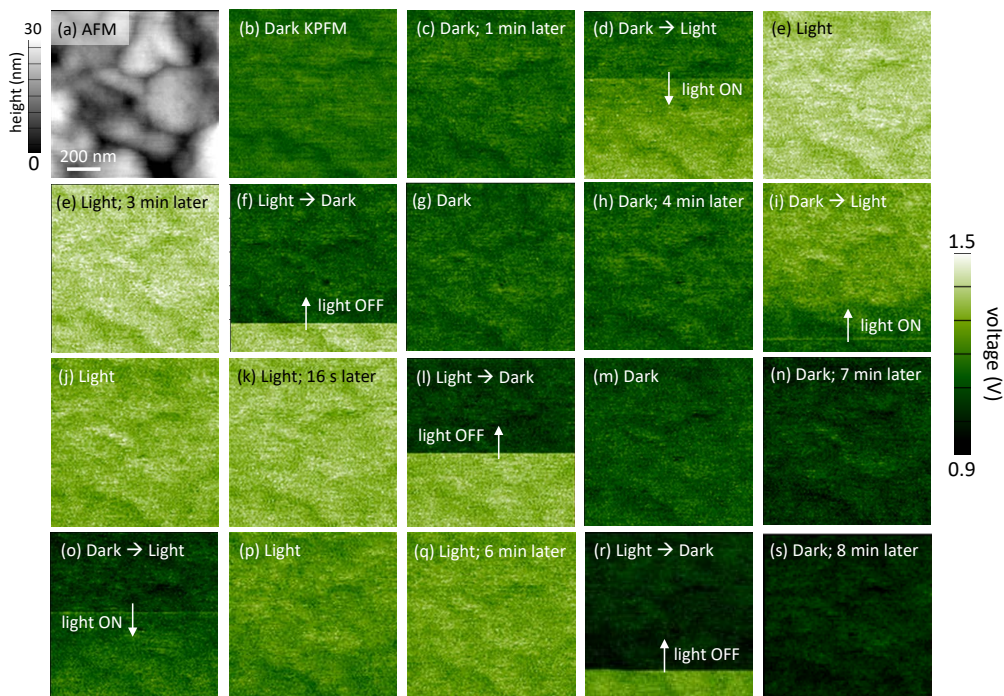


Figure 7.10: **Dynamic electrical response after illumination of Cs-mixed perovskite.** (a) Topography map. (b)-(s), Fast Dark- and Light- KPFM scans (16 sec/scan) acquired, shown in chronological order, demonstrating the reversible and uniform voltage response of the Cs-mixed perovskite half-device in a $1 \times 1 \mu\text{m}^2$ region. During scans (d), (i), and (o), the 532 nm laser at 1-sun is turned ON, and for scans (f), (l), and (r) the illumination source is turned OFF. The scan direction is indicated by the white arrows within the voltage map. The entire dataset is not shown as this would comprise of $>100+$ images, therefore, we have selected time snapshots which either (1) show a change in illumination state or (2) are representative of the voltage distribution during a given illumination state.

migration is inhibited because both MA and FA are compressed in these cases. The histograms in Figure 7.11 display the time-dependence of the V_{oc} of all the perovskite compositions obtained by the KPFM maps, where the error bars correspond to the line-noise level of the measurements. It is clear that the MAPbI₃ perovskite decays week-after-week, signifying material degradation. Meanwhile, the MAPbBr₃ and Cs-mixed samples remain stable throughout the entirety of the experiments, although MAPbBr₃ does show higher volatility. This phenomenon could be related to the measured irreversible electrical signal and zero-voltage sites in the MAPbBr₃, which in this case, are likely caused by light-induced, mobile organic cation and/or bromine ions. [329, 330] In comparison with the other pure halide options, the Cs-mixed perovskite has superior electrical behavior.

The significance of spatially resolving the V_{oc} of inhomogeneous materials, such as perovskites, lies in revealing changes in the optoelectronic behavior of grains and within grains related to charge carrier recombination that dominates the overall device stability and performance. Ultimately, elucidating the driving forces for material degradation upon exposure to light (in this case), moisture, oxygen, temperature and bias will advance our understanding of what triggers the dynamic response commonly observed in perovskites. To date, microscopic measurements of perovskites through scanning probe and electron microscopy-based methods have shown significant spatial variations in the photocurrent and photovoltage generated by MA and FA perovskites, and are likely related to physical and chemical processes that take place once the material is exposed to ambient environment or operation conditions. Thus, identifying the response of novel perovskites, such as (RbCsMAFA)PbI₃ and Bismuth-halide double perovskites, [333] to the parameters above-mentioned is critical to elucidate which chemical compositions can be implemented as solar cell modules.

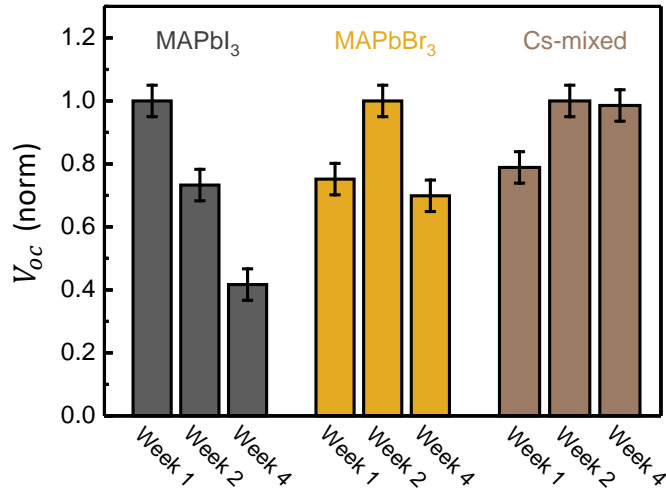


Figure 7.11: **Analysis of perovskites nanoscale electrical stability.** Histograms of V_{oc} , extracted from the nanoscale KPFM experiments, normalized as a function of the first week for each perovskite sample. The superior long-term voltage stability of the Cs-mixed composition is evident by its steady V_{oc} signal over four weeks.

7.5 Conclusion

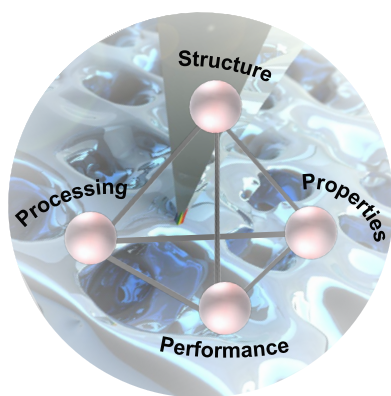
We determined the influence of chemical composition on the nanoscale V_{oc} stability for three types of perovskites: MAPbI₃, MAPbBr₃, and Cs-mixed. By performing KPFM imaging under 1-sun illumination conditions we discovered an irreversible photovoltage response within the MAPbBr₃ perovskite, demonstrating the need for high spatial resolution mapping. Regions of zero-photovoltage coexist with active areas upon material illumination. The MAPbI₃ conventional perovskite presented the lowest stability among the three compositions at multiple time scales. Meanwhile, we measured a fully reversible and uniform voltage response in Cs-mixed perovskites, which is linked to the suppression of ion motion. The differences between the three samples' V_{oc} behavior are due to the existence and suppression of ion migration: as Cs is incorporated into the perovskite lattice, the movement of ions is inhibited due to strain. As a result, the nanoscale V_{oc} is homogeneous at the length scale of individual grains. Yet, for the MAPbBr₃ perovskite, the

motion of Br^- ions causes a hysteresis on the V_{oc} response as a function of illumination.

This nanoscale V_{oc} imaging/analysis can be expanded to probe the real-time response of emerging perovskites, including options for multi-junction solar cells [306] and light-emitting devices. For instance, by implementing fast-KPFM one can identify the role of different atmospheres, such as N_2 , O_2 , and H_2O , on the dynamic electrical properties of these materials. Moreover, the KPFM measurements can be combined with other AFM-based methods, such as photoconductive-AFM, to provide a complete picture of the electrical (voltage and current) characteristics of the perovskites. As the search for reliable perovskites accelerates, defining the chemical compositions that lead to stable devices is key for the future deployment of high-performance and low-cost optoelectronics based on this class of material. Because they are composed by nanoscale constructs, resolving their individual contribution to the overall material behavior through microscopic methods will enable the understanding of the relevant processes responsible for the dynamic response often observed in perovskites.

Chapter 8: Perspective on functional imaging of PV materials

Further global adoption of photovoltaic energy conversion technologies is contingent on sustained progress towards widespread grid-parity. For that, solar cell materials composed of micro-scale grains and nanoscale boundaries show the highest potential due to their large theoretical efficiency and low-cost fabrication methods. Here we outline the current challenges facing hybrid perovskites and prevalent thin film polycrystalline materials for photovoltaics. We offer an perspective on how mesoscale functional imaging can enable a complete understanding of the physical and chemical processes restricting their performance, completing the materials science structure-properties-processing-performance tetrahedron. We provide a discussion about how novel imaging methods based on electron and scanning probe microscopies can be realized to provide quantitative information about the relevant parameters (figures-of-merit) that define solar cell performance. Finally, we offer our vision for the upcoming years, wherein correlative functional microscopy will lead to a complete narrative of the electrical, optical, structural, and chemical properties of these materials, including their surface and bulk properties. This chapter is adapted from E.M. Tennyson et. al, *ACS Energy Letters*, **2** 1825 (2017) [34]



8.1 Introduction

In this chapter, we provide insight about how cutting-edge functional nano-imaging methods can be implemented to advance our understanding of the fundamental physical and chemical processes governing these non-uniform materials, including the use of both electrons and photons as the excitation source for charge carriers. Second, we discuss the need for real-time microscopic methods to probe the degradation mechanisms of perovskite solar cells, still not well understood. Finally, we briefly analyze the relevance of big data to effectively correlate the information acquired by a set of microscopic methods.

We suggest the implementation of high spatial resolution microscopy methods beyond their standard operation mode as a functional imaging platform to directly resolve the role of the grains and interfaces on solar cell performance. To emulate PV device operation conditions, both electrons and photons can be employed as the carrier excitation source. Therefore, we discuss the primary advantages and limitations of selected microscopy approaches and how they can be modified to offer quantitative information about device figures-of-merit at the nanoscale.

8.2 Electrons as a source of excitation

Electron microscopy has proven to be an indispensable tool to acquire structural, electrical, and chemical information of PV materials with nanoscale and atomic spatial resolution. SEM-based measurements are typically performed in a high vacuum atmosphere, minimizing sample contamination. The interaction of the electron beam (e-beam) with the material can generate secondary and back-scattered electrons, X-rays, and cathodoluminescence (CL), portrayed in Figure 8.1(a). A commonly used electrical measurement

in a SEM is termed electron-beam-induced current (EBIC), where the e-beam acts as a local source of excitation of carriers. As the e-beam rasters across the sample, it produces a map of the generated current with spatial resolution primarily determined by the beam size. [196] This characterization method is frequently performed on cross-sections to determine the relative changes in charge carrier collection across p - n junctions and other important interfaces. These measurements are especially important for perovskite devices, as they do not have a conventional, well-defined p - n junction. However, the use of electrons as the carrier excitation source is prone to severe image artifacts, mainly caused by: (i) e-beam penetration path and depth, and (ii) damage to the sample.

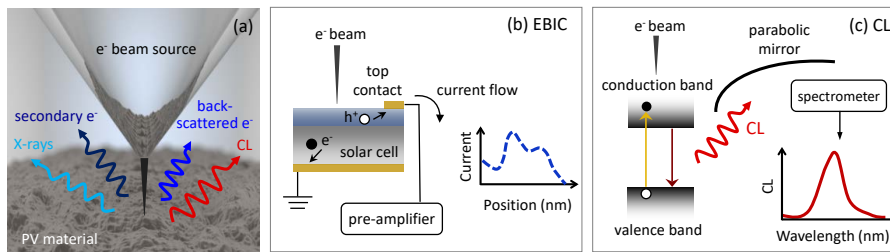


Figure 8.1: **Electrons as a source of excitation for high-resolution functional imaging of solar cells.** (a) Illustration of the main radiation signals generated from an e-beam upon interaction with a material. (b) Schematic of e-beam induced current (EBIC), where the generated current is spatially resolved. (c) Illustration of cathodoluminescence (CL) resulting from the radiative recombination of charge carriers.

Cathodoluminescence (CL) is the physical phenomenon defined by the emission of photons (electromagnetic radiation) within the UV-IR range, occurring when electrons relax to their fundamental state, resulting from a material excitation by an e-beam [334,335] - see Figure 8.1(c). Thus, information about where radiative recombination takes place within a PV material can be obtained by CL. The spatial resolution is, in principle, defined by the size of the e-beam in the SEM. CL imaging has been implemented in the investigation of a variety of solar cell materials. [336–339] The successful acquisition of reliable

data heavily depends on the instrumentation used for light detection. A parabolic mirror, inserted between the specimen and the pole piece, focuses the photons emitted from the solar cell into a well-defined point on the detection system. Then, the collected radiation is spectrally analyzed/resolved for every e-beam position using a high sensitivity CCD detector and a two-dimensional emission map is recorded. In this manner, the spectrally and spatially resolved optical response is acquired. CL has recently been implemented to probe the optical response of the fully processed device. As an example, the CdCl₂-treatment during CdTe fabrication has been shown to reduce non-radiative recombination in all types of GBs, as the overall intensity of the CL spectrum increases after this passivation step. [55] One unique feature of CL is the fact that it does not require device processing. In other words, electrical contacts are not required for mapping the radiative recombination rate of carriers within a thin film. Nevertheless, analogous to EBIC, CL suffers from the similar limitations (see Table 8.1), due to the excitation source.

imaging technique	applications	limitations
Electrons as a source of excitation		
EBIC	maps of generated current	E-beam induced artifacts due to sample damage, strong dependence on accelerating voltage, primarily a surface signal.
CL	radiative recombination of charge carriers	Resolution is limited to e-beam volume interaction and excess carrier diffusion.
Photons as a source of excitation		
pcAFM	photocurrent, relative nanoscale J - V characterization	Removal of conductive coating on probe due to sample contact, slow scan speeds, and effect of contact size.
illuminated-KPFM	quantitative, nanoscale V_{oc}	Topographic artifacts due to surface roughness.
NSOM LBIC	photocurrent beyond diffraction limit	Decouple the evanescent field around probe aperture and near-field sample-probe interactions.
NSOM PL	radiative recombination of charge carriers beyond diffraction limit	
Tr-PL through NSOM	minority carrier lifetime with subwavelength spatial resolution	

Table 8.1: Selected nanoscale functional imaging methods performed on PV materials along with their primary applications and limitations

Though the imaging methods described above have been extensively used to characterize non-uniform solar cell materials, a combinatorial SEM-based functional imaging platform is necessary to describe the full picture of the fundamental physics of charge carriers. Thus, both EBIC and CL are beginning to be used in conjunction with other SEM-based imaging capabilities to gain information about additional material properties (e.g. chemical or structural). X-rays produced by the e-beam (Figure 8.1(a)) are used for compositional mapping, by employing energy dispersive X-ray spectroscopy (EDX). [340] Alternative chemical imaging techniques include electron energy loss spectroscopy (EELS), [341] and time-of-flight secondary-ion mass spectroscopy (ToF-SIMS). [41] Additionally, the orientation of the grains and the types of interfaces present in a sample can be mapped by electron backscattering diffraction (EBSD). Recently, EBIC, transmission electron microscopy with selected area diffraction (TEM-SAD), and atom probe tomography (APT) were united to investigate the $\text{CdSe}_x\text{Te}_{1-x}$ alloy that forms upon annealing of CdTe devices. [38] Here, the zinc blende phase showed superior photo-response of when compared to wurzite. Although very informative, EBIC measurements do not provide quantitative information regarding current collection, nor has the generated current been compared to macroscopic light J - V measurements.

We foresee correlative SEM and TEM approaches becoming widespread over the coming years, as the dynamics of the charge carrier processes responsible for high (low) PV performance is strongly related to the structural and chemical characteristics of the grains composing the thin-film devices. To date, most of the work using SEM techniques has focused on capturing the relative variations in current; however, measurements of J_{sc} , a key figure-of-merit for solar cells, are still missing. While a photon generates only one electron-hole pair, an electron can generate up to thousands of electron-hole pairs. The

volume in which the carrier excitation event occurs depends on the e-beam current and voltage, the material density, band gap energy, its backscatter coefficient, atomic weight, atomic number, and the quantum efficiency for generating an electron-hole pair. [342] Thus, the volume of excitation, which is defined by the trajectory of the electrons within the solid, must be calculated for a quantitative comparison between EBIC and J_{sc} . For that, the role of the contact size must also be taken into consideration. [179] Although the contribution of each individual atom is not as relevant as the mesoscale behavior of the material, if atomic resolution becomes needed, we expect TEM-based EBIC to be implemented. In this case, besides all considerations mentioned above, one must also determine the possible overestimated contribution of surface recombination due to the very large surface area-to-volume ratio of the samples (as a result of the lamella sample size).

8.3 Photons as a source of excitation

The nanoscale functional imaging of PV using photons as the excitation source requires researchers to use atomic force microscopy (AFM) or near-field scanning optical microscopy (NSOM). Both platforms offer spatial resolution beyond the diffraction limit, <100 nm, enabling the elucidation of the local electrical and optical properties of solar cells. In this section, we summarize the operation principles of selected AFM- and NSOM-based methods that provide invaluable insights about the material optoelectronic response and focus on how they can provide quantitative information about the figures-of-merit of the solar cells, with nanoscale spatial resolution.

Scanning probe microscopy methods have demonstrated exceptional versatility when mapping the electrical response of PV with nanometer spatial resolution, as reviewed in

Chapter 3. [37,71] A common AFM mode used to determine the electrical response of solar cells is photoconductive (pc) AFM. Here, a conductive metal probe acts as the top local electrical contact of the PV device, as illustrated in Figure 8.2(a). Upon device illumination by an external light source, the probe directly collects the generated photocurrent while recording the topography of the sample in contact mode. The potential beneficial role of grain boundaries in CdTe, CIGS, and CZTS devices as current collectors has been broadly investigated through pcAFM. [94, 192, 343] However, it is still unknown how the grain boundaries affect charge carrier recombination, which requires mapping V_{oc} , as will be discussed later. pcAFM has been applied to perovskites [344] and recently integrated with voltage biasing to produce spatially resolved J - V curves of the devices. [51] In these measurements, individual maps of J - V parameters can be obtained, extremely valuable to estimate relative changes in all figures-of-merit, with nanoscale spatial resolution. In order to translate this information into macroscopic device parameters, one needs to take into consideration (1) the extremely small volume of excitation when light focusing is used, (2) the effect of the probe size as a current collector and charge carrier diffusion length, (3) the photon flux in single wavelength measurements, (4) spatial variations in the absorption coefficient of the material under investigation (which will necessarily affect charge carrier generation), (5) and the possible optical losses of the experimental setup.

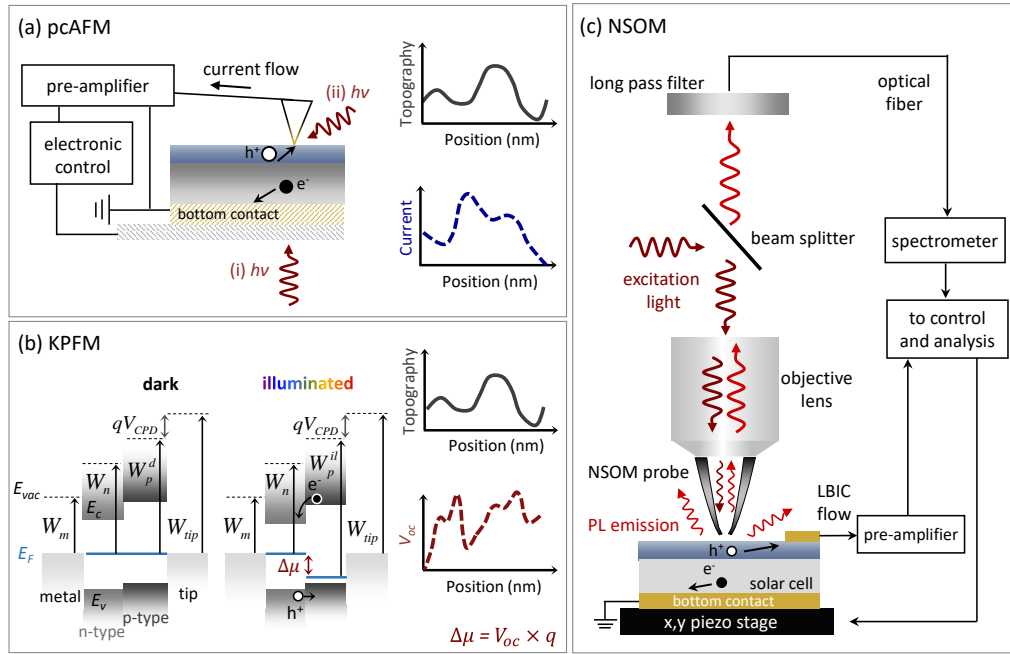


Figure 8.2: **Photons as a source of excitation to nano-image PV functionality through scanning probe microscopy.** (a) In photoconductive-AFM (pcAFM) a conductive probe acts as a local electrical contact. An external light source is used, where the illumination direction, (i) or (ii), depends on device configuration. Both surface topography and current are measured simultaneously. (b) Kelvin probe force microscopy (KPFM) measures the work function (W) difference (or contact potential difference, V_{CPD}) between the probe and the sample surface when grounded with respect to one another. In the dark, d , the solar cell is in equilibrium and all the Fermi levels are equal. Under illumination (il) there is a splitting of the quasi-Fermi level ($\Delta\mu$). The V_{oc} is, thus, determined by subtracting dark- from light-KPFM scans. E_{vac} , E_c , E_{Fn} , E_{Fp} , and E_v denote the vacuum, conduction, the quasi-Fermi level for e^- and h^+ , and valence band energies, respectively. Adapted from [37]. (c) Near-field scanning optical microscopy (NSOM) schematic showing two possible types of measurements with spatial resolution beyond the diffraction limit: photoluminescence (PL) and laser-beam-induced current (LBIC) microscopy.

While extensive efforts have been made to increase the J_{sc} of thin-film polycrystalline solar cells, higher efficiencies are still limited by the V_{oc} (see Chapter 3). The local variations of V_{oc} within these materials can be determined by a much less explored and equally powerful AFM-based method: Kelvin probe force microscopy (KPFM). [37, 39] As previously explained, the work function difference between the sample surface and the probe is measured, as illustrated in Figure 8.2(b). By subtracting an illuminated-KPFM scan from a dark one, the *quasi*-Fermi level splitting ($\Delta\mu$), and therefore, the local V_{oc} gen-

erated by the material is obtained. This universal approach only requires a half-processed device and can be performed in ambient conditions. With proper system calibration, the quantitative V_{oc} obtained from focused illumination is converted into a 1-sun V_{oc} map under AM1.5 global illumination. We anticipate V_{oc} mapping through KPFM to be combined with pcAFM (on the very same grains and boundaries) to quantify where charge carrier recombination and collection take place, respectively. Combined, these measurements enable the deconvolution of both processes, critical to identify which mechanism is limiting the performance of the device under investigation. Further, by implementing a correlative microscopy approach, where the SPM methods are combined with ex situ EBSD, one can elucidate which interfaces and grain orientations in polycrystalline materials are responsible for the modest V_{oc} of the technologies discussed earlier.

Functional imaging through NSOM has been applied less frequently to solar cells when compared to AFM-based methods. Here, evanescent waves are used to break the far-field diffraction limit. By keeping the distance between the probe and the sample surface considerably smaller than the wavelength of light (at least two orders of magnitude), it is possible to map the solar cells optical response with true nanoscale spatial resolution. In NSOM, a probe or an optical fiber with a hollow center (approximately 60-200 nm in diameter) is used as the excitation and/or collection source, as depicted in Figure 8.2(c). One electrical measurement option using NSOM is laser-beam induced current (LBIC). In this configuration, the photons transmitted through the probe induce photocurrent in a highly localized region of the solar cell. This method has been applied to identify the diffusion of sulfur in CdTe, [237] to spatially resolve the external quantum efficiency (EQE) of CdTe solar cells, determining the contribution of grains and boundaries to the overall signal of the device, [130,131,345] and the photo-response of grain and GBs in CIGS. [238]

For the quantitative comparison between the LBIC signal and the macroscopic J_{sc} of a device, one must accurately determine the contribution of the dark saturation current of the entire sample (whole device area), and extricate possible topographic artifacts due to near-field light coupling. One attractive application of NSOM for perovskites is to realize spectrally dependent LBIC scans to spatially monitor the existence of trap states within the material, where ion migration seems to be a major contributor in their local electrical response. [39]

A powerful alternative measurement is to use the NSOM probe for both the excitation of carriers and the collection of emitted photons (photoluminescence, PL), resulting from radiative recombination. The collection of the PL signal strongly depends on light-probe coupling, and considerable effort has focused on designing optimized probes for capturing the emitted photons. For instance, campanile tips have been identified as an excellent geometry to enhance the coupling efficiency between far and near fields, allowing for PL signal imaging of nanoscale features in InP nanowires for PV applications. [129] PL microscopy with nanoscale spatial resolution can be realized to probe the impact of GaAs polycrystals' facets on carrier recombination. Note that device processing is not required here. Different than InP, GaAs is a material that is not self-passivated. Thus, one could use PL through NSOM to identify the effect of distinct surface passivation processes (e.g. Na_2S and Si_3N_4) to the recombination rate within the different facets composing the GaAs polycrystals. Although unconventional, NSOM can also be integrated into a SEM. In this dual probe approach the NSOM tip collects the near-field CL emission caused by the e-beam to image the energy transport mechanisms without being limited by photon recycling or excess carrier diffusion. [346] We foresee that combining LBIC and PL signals with simulations of the electrodynamics at the near-field regime could enable a

tomography of charge carrier generation, recombination, and collection, resolving the role of the mesoscale constructs within polycrystalline solar cells to their macroscopic device performance.

Time-resolved PL (tr-PL) is an extremely powerful method to quantify the minority carriers lifetime within a material. Here, the carriers that recombine radiatively (PL signal) are detected by a time-correlating photon counting system. tr-PL spectroscopy has been widely implemented to resolve the effect of passivation methods on the lifetime of polycrystalline materials for PV, [347, 348] as well as the role of precursor solution concentration (and band gap) in halide perovskites. [349, 350] When combined with an NSOM microscope, it provides maps of the temporal dynamics of the PL signal, with sub-wavelength spatial resolution. tr-PL through confocal optical microscopy [351, 352] or NSOM [353] could be implemented to investigate the spatial distribution of minority carrier lifetimes in perovskite grains and its photo-instability. A primary advantage of tr-PL microscopy is that it enables measurements in a film, not requiring any device processing.

8.4 Probing the degradation of perovskite solar cells

The commonly observed degradation of perovskite solar cells is the main barrier for this emerging material to become a reliable PV technology, as previously mentioned in Chapters 6 and 7. Thus, measuring and controlling the physical and chemical processes responsible for the transient electrical behavior of perovskites is critical for its widespread deployment. [50] we foresee pCAFMs and illuminated-KPFMs being implemented to track material degradation. For instance, MAPbX_3 ($X = \text{Br}$ or I) is unstable under illumination, and can suffer from structural phase transition at low temperatures ($<60^\circ\text{C}$), and

often degrades upon exposure to moisture. [146] Thus, SPM under controlled illumination, humidity, and temperature conditions will help elucidate the driving forces behind the material degradation commonly observed in perovskites. For example, spectrally dependent KPFM will likely reveal the possible presence of trap states within the material, and how their density varies from grain to grain. The reversibility of the electrical response of perovskites can also be probed by tuning the humidity (low, high, low) upon sequential SPM measurements. Here, pcAFM and KPFM could resolve how both J_{sc} and V_{oc} change as the perovskite is exposed to moisture. The advantage of using microscopic methods to probe perovskite solar cells lies in quantifying spatial variations within the samples, which could be associated with chemical composition deviations from grain to grain.

The dynamic electrical behavior of the perovskites has been measured both in plane-view and in cross-section by pcAFM [90] and KPFM. [39, 151] However, there is still a pressing need for scientists to discover the driving forces responsible for the devices transient behavior when the material is exposed to light and humidity. This dynamic response likely requires the further development of time-dependent functional microscopy methods that will provide 4-dimensional (4D) information, space and time, at relevant length scales. Mimicking realistic operation conditions (including the environment) of perovskite devices during operando measurements is necessary to identify why and how the material is degrading. Preferably, these 4D measurements should be combined with chemical imaging to establish a correlation between device behavior and the changes in chemical composition. The combination of illuminated-KPFM (as described earlier) with Raman imaging and other AFM-based chemical mapping is a promising route to elucidate the effect of photo-induced chemical reactions in device degradation. As recently demonstrated, [39] fast-KPFM scans (16 second/frame) that allow real-time measurements of local V_{oc} have

revealed (1) substantial ion migration during perovskites illumination, and (2) a residual post-illumination voltage resulting from a time dependent ion migration current never measured before. These fast scans can be extended to lead-free perovskite films, [354] e.g. MASnI_3 [355] or $\text{Cs}_2\text{BiAgCl}_6$, [53] as well as new compounds for multi-junction PV, such as $\text{Rb-FA}_{0.75}\text{MA}_{0.15}\text{Cs}_{0.1}\text{PbI}_2\text{Br}$, [356] to determine their dynamic response and, thus, material stability when exposed to light.

8.5 Correlative microscopy and the need for big data analytics

We foresee that the use of combined functional imaging microscopies will produce large amounts of data that must be effectively analyzed for an understanding of the material behaviors under investigation. An emerging investigation pathway is big data, which encompasses the analysis of all data to identify critical patterns and associations (*e.g.* correlation between grain boundaries and low V_{oc}). Big data analytics involves evaluating the detected signals with approaches from multivariate statistics and machine learning to identify meaningful relationships between material properties, obtained from a set of microscopy measurements in this case. [357] Ultimately, the main advantage of the available paradigms [298] is to gain insight into complex phenomena while minimizing computational time. For example, using principal component analysis (PCA), [358] one can determine which dimensions of the data account for the most variance in an imaging dataset. Note that in this situation, each physical quantity is assigned as one data dimension. This method has already proven useful when combined with band excitation magnetic force microscopy; PCA provided the same qualitative insight as the simple harmonic oscillator

model while requiring $\sim 10^4$ less computation time. [358] Machine learning approaches will likely help scientists determine which defects and grain boundaries in polycrystalline PV materials contribute most to performance deficiencies. For instance, a combination of NSOM LBIC and ex situ EBSD data acquired at the same region of a sample could train an algorithm to predict the electrical signal based solely on the angle between two adjacent grain boundaries. Data mining may also identify degradation mechanisms in perovskite solar cells. Namely, factor analysis can be applied to a combination of illuminated-KPFM and tip-enhanced Raman spectroscopy under a controlled atmosphere to establish how the electrical and chemical responses vary as a function of relative humidity. Further, time-dependent photocurrent and photovoltage measurements of emerging lead-free perovskite alternatives could provide a roadmap for stable materials. For the reasons outlined, we anticipate the use of big data analytics on information produced by combinatorial functional microscopy.

8.6 Outlook

In perovskites, device stability is currently the main barrier towards implementing a reliable technology, followed by the pressing need to identify non-toxic lead-free, stable options. The full potential of thin-film polycrystalline materials for PV is primarily limited by their V_{oc} , which is strongly related to non-radiative recombination events within the material. As the grains and boundaries forming the devices are acknowledged to affect their electrical response it is imperative that we identify which types of grains and interfaces contribute to charge carrier non-radiative recombination. In order to determine the local electrical properties of the mesoscale constituents of both perovskites and inorganic thin-film PV, researchers must implement microscopy techniques beyond their standard

operation modes, quantifying the figures-of-merit (and, hence, the device performance) at relevant length scales. Further, the large amount of generated data must be analyzed in an effective manner using approaches based on big data analytics, leading to quantitative information about the devices under investigation.

We expect the realization of correlative microscopy and the functional imaging of materials/devices at the mesoscale to finally elucidate some critical open questions in the field, such as: What are the light-induced chemical reactions responsible for perovskites' degradation under 1-sun illumination? What is the role of humidity in perovskite's performance? Which types of interfaces in CdTe, CIGS, and CZTS are responsible for the low carrier radiative recombination rate that limits their V_{oc} ? How do the different facets composing GaAs polycrystals affect charge carrier generation, recombination, and collection? Is the diode ideality factor for all grain boundaries the same in a polycrystalline PV device? To answer these questions, among many others, it is essential to determine the physical behavior of the mesoscale constructs when the devices are in operando. Functional imaging methods will likely act as the central "covalent bond" between the materials science structure-properties-processing-performance tetrahedron cornerstones, providing unprecedented correlative insights into materials for PV at the mesoscale. In turn, these sophisticated measurements can potentially allow the rational design of higher performance PV devices based on low-cost materials/methods.

8.7 Future work

An exciting next direction for this research project will be to implement correlative microscopy, as described above, to investigate how the local chemical distribution within a perovskite material effects the dynamic nanoscale voltage response, which we previously

measured and quantified in Chapters 6 and 7. For this, I recently performed photothermal infrared resonance (PTIR) microscopy (also known as AFM-IR discussed in Chapter 3, Section 3.2.3), on a perovskite thin-film sample that contains an additional solution, termed additive, see Figure 8.3. The inclusion of the additive shows an increase in the macroscopic V_{oc} , however, how it influences the electrical properties at the nanoscale is still unknown.

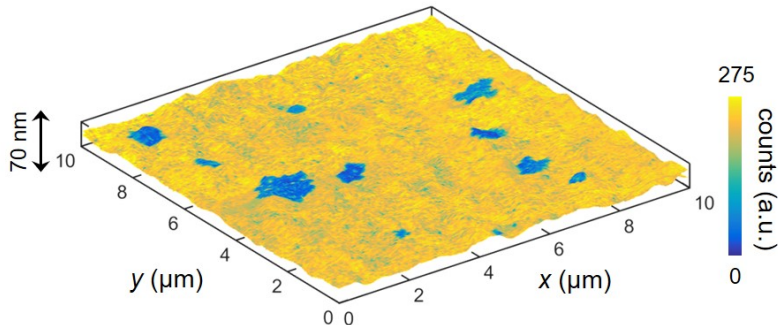


Figure 8.3: **Imaging the nanoscale chemical distribution of a perovskite thin-film.** AFM topography overlaid with the chemical map that was simultaneously measured, here, the sample was excited by wavenumber = 1609 cm^{-1} .

The preliminary measurements reveal $\sim 1 \times 1 \mu\text{m}^2$ regions of distinct chemical variations induced by the presence of the additive; this was proven by acquiring AFM-IR on a sample without the additional solution (not shown here). A clear next step will be to apply the illuminated-KPFM technique developed in this thesis on the same sample to correlate the chemical variations to the nanoscale V_{oc} .

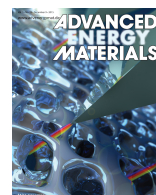
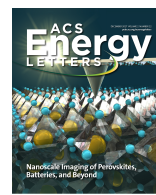
Appendix A: Products of this research

A.1 Awards and honors

19. MRS Graduate Student Award (Silver)	10/2017
18. IEEE 44 th Photovoltaic Specialist Conference Best Student Paper Finalist	05/2017
17. OSA Student Poster Competition - honorable mention	04/2017
16. UMD All-S.T.A.R. fellowship	04/2017
15. UMD graduate student summer research fellowship 2017	04/2017
14. ARPA-e student program at the energy innovation summit, Washington, D.C.	01/2017
13. OSA Student Leadership Conference, Rochester, NY - UMD representative	10/2016
12. Graduate Student Deans Dissertation Fellowship	04/2016
11. Selected for Joint US-Africa Materials Institute (JUAMI) 2016	04/2016
10. Hulka Energy Research Fellowship	02/2016
9. MRS Graduate Student Exchange at NC - Chapel Hill Seminar, invited talk	02/2016
8. Institute of Research in Electronics and Applied Physics (IREAP) - best speaker	12/2015
7. UMD ResearchFest 2015 - overall winner	06/2015
6. UMD graduate student summer research fellowship 2015	04/2015
5. OSA student chapter poster competition - 1 st place poster	04/2015
4. NSF graduate research fellowship program honorable mention	04/2015
3. UMD Jacob K. Goldhaber travel grant	01/2015
2. IEEE 40 th Photovoltaic Specialist Conference (PVSC) - best poster	06/2014
1. UMD Dean's Fellowship	08/2013 – 05/2017

A.2 Publications

8. J. M. Howard, **E. M. Tennyson**, S. Barik, E. Waks, M. Toney, A. F. Nogueira, B. R. A. Neves, M. S. Leite, *Humidity-dependent Photoluminescence Hysteresis in Cs-containing Perovskite Thin Films* – in progress
7. **E. M. Tennyson**, B. Roose, J. L. Garrett, C. Gong, J. N. Munday, A. Abate, M. S. Leite, *Caesium-incorporated triple cation perovskites deliver fully reversible and stable nanoscale voltage response* – in progress
6. **E. M. Tennyson**, C. Gong, M. S. Leite, *Imaging Energy Harvesting and Storage Systems at the Nanoscale*, ACS Energy Letters, **2**, 2761-2777 (2017) – **invited review, front cover**
5. **E. M. Tennyson**, J. M. Howard, M. S. Leite, *Mesoscale Functional Imaging of Materials for Photovoltaics*, ACS Energy Letters, **2**, 1825-1834 (2017) – **invited perspective**
4. J.L. Garrett, **E. M. Tennyson**, J.N. Munday, M.S. Leite, *Real-time Nanoscale open-circuit voltage dynamics of perovskite solar cells*, Nano Letters, **17**, 2554-2560, (2017)
3. **E. M. Tennyson**, J.A. Frantz, J.M. Howard, W.B. Gunnarsson, J.D. Myers, R.Y. Bekele, S. Na, M.S. Leite, *Photovoltage tomography in polycrystalline solar cells*, ACS Energy Letters, **1**, 899-905 (2016)



2. **E. M. Tennyson**, J.L. Garrett, J.A. Frantz, J.D. Myers, R.Y. Bekele, J.S. Sanghera, J.N. Munday, M.S. Leite, *Nanoimaging of open-circuit voltage in photovoltaic devices*, *Advanced Energy Materials*, **5**, 1501142 (2015) – **front cover**
1. **E. M. Tennyson**, M.S. Leite, *Mapping the performance of solar cells with nanoscale resolution*, SPIE Newsroom doi:10.1117/2.1201509.006097 (2015)

Conference Proceedings:

5. **E. M. Tennyson**, M.S. Leite, 44th IEEE PVSC Proceedings: *Nano-imaging of Performance in Photovoltaics* (06/2017)
4. **E. M. Tennyson**, J. L. Garrett, J. N. Munday, M. S. Leite, 43rd IEEE PVSC Proceedings: *Mapping V_{oc} in Polycrystalline Solar Cells with Nanoscale Spatial Resolution* (06/2016)
3. **E. M. Tennyson**, J.L. Garrett, C. Gong, J.A. Frantz, J.D. Myers, R.Y. Bekele, J.S. Sanghera, J.N. Munday, M.S. Leite, SPIE 9561, *Thin Films for Solar and Energy Technology VII Proceedings: A novel method for mapping open-circuit voltage in solar cells with nanoscale resolution* (10/2015)
2. **E. M. Tennyson**, J.A. Frantz, J.D. Myers, R.Y. Bekele, J.S. Sanghera, S. Na, M.S. Leite, 42nd IEEE PVSC Proceedings: *Imaging EQE in CIGS solar cells with high spatial resolution* (06/2015)
1. **E. M. Tennyson**, J.L. Garrett, C. Gong, J.A. Frantz, J.D. Myers, R.Y. Bekele, J.S. Sanghera, J.N. Munday, M.S. Leite, 40th IEEE PVSC Proceedings: *Assessing local voltage in CIGS solar cells by nanoscale resolved Kelvin probe force microscopy and sub-micron photoluminescence* (06/2014)

A.3 Presentations

29. **E. M. Tennyson**, M. S. Leite, *Functional Imaging of Photovoltaics at the Nanoscale: from Perovskites to Polycrystalline Materials*. Fall MRS 2017 (11/2017) talk and MRS Graduate Student Silver Award winner
28. **E. M. Tennyson**, J. L. Garrett, J. N. Munday, M. S. Leite, *Real-Time Mapping of Perovskite Intragrain Instabilities at the Nanoscale*. Fall MRS 2017 (11/2017) talk
27. **E. M. Tennyson**, M.S. Leite, *Imaging photovoltaic functionality of polycrystalline and perovskite solar cells at the nanoscale*. ACS 254th National Meeting (08/2017) talk and poster
26. **E. M. Tennyson**, M.S. Leite, *Nano-imaging of Performance in Photovoltaics*. 44th IEEE PVSC (06/2017) best student award finalist talk
25. **E. M. Tennyson**, M.S. Leite, *Imaging the mesoscale electrical response of polycrystalline and perovskite solar cells*. UMD ResearchFest 2017 (06/2017) poster
24. **E. M. Tennyson**, M.S. Leite, *Mapping the performance of polycrystalline and perovskite solar cells with nanoscale spatial resolution*. OSA poster competition (04/2017) poster
23. **E. M. Tennyson**, M.S. Leite, *Open-circuit voltage mapping of next-generation solar cells*. IREAP Graduate Student Seminar (04/2017) talk
22. **E. M. Tennyson**, M.S. Leite, *High spatial resolution performance mapping in thin-film solar cells*. IREAP Graduate Student Seminar (11/2016) talk
21. **E. M. Tennyson**, M.S. Leite, *Mapping the local voltage response of polycrystalline solar cells with nanoscale resolution*. Frontier in Optics Conference (10/2016) poster
20. **E. M. Tennyson**, M.S. Leite, *Spectrally dependent photovoltage tomography map for charge carrier recombination study in CIGS solar cells*. IREAP Graduate Student Seminar (04/2016) talk
19. **E. M. Tennyson**, M.S. Leite, *Imaging the electrical properties of thin-film solar cells with high spatial resolution*. UMD Nanoday (04/2016) poster
18. **E. M. Tennyson**, M.S. Leite, *Spectrally dependent photovoltage tomography map for charge carrier recombination study in CIGS solar cells*. IREAP Graduate Student Seminar (04/2016) talk

17. **E. M. Tennyson**, M.S. Leite, *Kelvin probe force microscopy: mapping the local open-circuit voltage of solar cells with nanoscale resolution*. NC Chapel Hill Seminar (03/2016) invited talk
16. **E. M. Tennyson**, J.L. Garrett, J.N. Munday, M.S. Leite *Resolving local voltage variations in opto-electronic devices with Kelvin probe force microscopy*. APS Baltimore (03/2016) talk
15. **E. M. Tennyson**, M.S. Leite *High resolution mapping of the local performance parameters in solar cells*. Center for Nanophysics and Advanced Materials Seminar (02/2016) talk
14. **E. M. Tennyson**, M.S. Leite *Resolving electrical performance variations of polycrystalline solar cells at the nanoscale*. IREAP Graduate Student Seminar (10/2015) talk
13. **E. M. Tennyson**, J.L. Garrett, J.A. Frantz, J.D. Myers, R.Y. Bekele, J.S. Sanghera, J.N. Munday, M.S. Leite, *Mapping efficiency in solar cells with nanoscale resolution*. SPIE Optics and Photonics (08/2015) talk
12. **E. M. Tennyson**, J.L. Garrett, J.A. Frantz, J.D. Myers, R.Y. Bekele, J.S. Sanghera, J.N. Munday, M.S. Leite *High resolution mapping of the open-circuit voltage of solar cells using Kelvin probe force microscopy*. IEEE Photonics: Women in Photonics event (06/2015) invited talk
11. **E. M. Tennyson**, J.L. Garrett, J.A. Frantz, J.D. Myers, R.Y. Bekele, J.S. Sanghera, J.N. Munday, M.S. Leite *Mapping the open-circuit voltage of solar cells with nanoscale resolution*. UMD ResearchFest 2015 (06/2015) poster and talk
10. **E. M. Tennyson**, J.A. Frantz, J.D. Myers, R.Y. Bekele, J.S. Sanghera, S.M. Na, A. Flatau, M.S. Leite, *Imaging EQE in CIGS solar cells with high spatial resolution*. 42nd IEEE PVSC (06/2015) talk
9. **E. M. Tennyson**, J.L. Garrett, J.A. Frantz, J.D. Myers, R.Y. Bekele, J.S. Sanghera, J.N. Munday, M.S. Leite *Mapping the open-circuit voltage of solar cells with nanoscale resolution*. Annual Science Fair and Graduate Student Poster Award Dinner for NCS-OSA and DC-N. Virginia IEEE photonics societies (05/2015) poster
8. **E. M. Tennyson**, M.S. Leite, *High resolution mapping of solar cell functionality*. Electrical and Computer Engineering Graduate Student Seminar (05/2015) talk
7. **E. M. Tennyson**, M.S. Leite, *High resolution mapping of solar cell functionality*. Institute of Research in Electronics and Applied Physics Graduate Student Seminar (05/2015) talk
6. **E. M. Tennyson**, J.L. Garrett, J.A. Frantz, J.D. Myers, R.Y. Bekele, J.S. Sanghera, J.N. Munday, M.S. Leite, *Imaging open-circuit voltage and external quantum efficiency in solar cells with nanoscale resolution*. Materials Research Society meeting (04/2015) talk
5. **E.M. Tennyson**, J.L. Garrett, J.A. Frantz, J.D. Myers, R.Y. Bekele, J.S. Sanghera, J.N. Munday, M.S. Leite *Quantitative imaging of open-circuit voltage in opto-electronic devices with nanoscale resolution*. SPIE Sensing Technology + Applications conference (04/2015) talk
4. **E. M. Tennyson**, J.L. Garrett, J.A. Frantz, J.D. Myers, R.Y. Bekele, J.S. Sanghera, J.N. Munday, M.S. Leite, *Mapping the open-circuit voltage of solar cells with nanoscale resolution*. OSA poster competition (04/2015) poster
3. **E. M. Tennyson**, J.L. Garrett, J.A. Frantz, J.D. Myers, R.Y. Bekele, J.S. Sanghera, J.N. Munday, M.S. Leite, *Kelvin probe force microscopy: Imaging open-circuit voltage in optoelectronic devices*. American Physical Society March Meeting (03/2015) talk
2. **E. M. Tennyson**, *Characterization of solar cells with nano-scale resolution*. IREAP Graduate Student Seminar (10/2014) talk
1. **E. M. Tennyson**, J.L. Garrett, C. Gong, J.A. Frantz, J.D. Myers, R.Y. Bekele, J.S. Sanghera, J.N. Munday, M.S. Leite, *Assessing local voltage in CIGS solar cells by nanoscale resolved Kelvin probe force microscopy and sub-micron photoluminescence*. 40th IEEE PVSC (06/2014) **best poster**

Appendix B: Additional publications

2. Y. Xu, **E. M. Tennyson**, J. Kim, S. Barik, J. Murray, E. Waks, M. S. Leite, and J. N. Munday, *Active control of photon recycling for tunable optoelectronic device*, Advanced Optical Materials, (2018) DOI: 10.1002/adom.201701323
1. L. J. Kraye, **E. M. Tennyson**, M. S. Leite, J. N. Munday, *Near-IR imaging based on hot carrier generation in nanometer-scale optical coatings*, ACS Photonics, (2018) DOI: 10.1021/acsphotonics.7b01021 – **front cover**

Appendix C: University of Maryland service

C.1 Contributions

- | | |
|--|----------------------------------|
| 10. Vice President of OSA Student Chapter at UMD | July 2017 - May 2018 |
| 9. Restricted research sub-committee member | Aug. 2016 - Feb. 2017 |
| 8. Volunteer for Women in Engineering DREAM conference | Years 2015, 2016, and 2017 |
| 7. Short talk (10 min) at Materials Science and Engineering alumni event | April 2015 |
| 6. Presented at MSE open house for prospective PhD students | March 2015 |
| 5. Participant in Women in Engineering day | Years 2014, 2015, 2016, and 2017 |
| 4. Volunteer for Maryland Day | Years 2014, 2015, 2016 and 2017 |
| 3. Socialized with prospective PhD students at open house dinners | Years 2014, 2015, 2015, and 2017 |
| 2. Organized UMD ResearchFest | June 2014 |
| 1. President of Materials Science Graduate Society | Spring 2014 |

Bibliography

- [1] National Renewable Energy Laboratories. Renewable Electricity Futures Study. http://www.nrel.gov/analysis/re_futures, 2016. [Online; accessed 20-Oct-2016].
- [2] D. J. Norris and E. S. Aydil. Getting Moore from solar cells. *Science*, 338(6107):625–626, 2012.
- [3] Solar Energy Industries Assosiaton. Solar Industry Data. <http://www.seia.org/Research-Resources/Solar-Industry-Data>, 2016. [Online; accessed 20-Oct-2016].
- [4] M. A. Green, Y. Hishikawa, W. Warta, E. D. Dunlop, D. H. Levi, J. Hohl-Ebinger, and A. W. Y. Ho-Baillie. Solar cell efficiency tables (version 50). *Progress in Photovoltaics: Research and Applications*, 25(7):668–676, 2017.
- [5] National Renewable Energy Laboratories. NREL Best Research-Cell Efficiencies. <https://www.nrel.gov/pv/assets/images/efficiency-chart.png>, 2018. [Online; accessed 04-Feb-2018].
- [6] W. Shockley and H.J. Queisser. Detailed balance limit of p - n junction solar cells. *Journal of Applied Physics*, 32:510, 1961.
- [7] P. K. Nayak, J. Bisquert, and D. Cahen. Assessing possibilities and limits for solar cells. *Advanced Materials*, 23(25):2870–2876, 2011.
- [8] H. Xin, J. K. Katahara, I. L. Braly, and H. W. Hillhouse. 8% efficient $\text{Cu}_2\text{ZnSn}(\text{S},\text{Se})_4$ solar cells from redox equilibrated simple precursors in DMSO. *Advanced Energy Materials*, 4(11):1301823, 2014.
- [9] W. Ki and H. W. Hillhouse. Earth-abundant element photovoltaics directly from soluble precursors with high yield using a non-toxic solvent. *Advanced Energy Materials*, 1(5):732–735, 2011.
- [10] Y.-T. Hsieh, Q. Han, C. Jiang, T.-B. Song, H. Chen, L. Meng, H. Zhou, and Y. Yang. Efficiency enhancement of $\text{Cu}_2\text{ZnSn}(\text{S},\text{Se})_4$ solar cells via alkali metals doping. *Advanced Energy Materials*, 6(7):1502386, 2016.
- [11] W.-C. Hsu, H. Zhou, S. Luo, T.-B. Song, Y.-T. Hsieh, H.-S. Duan, S. Ye, W. Yang, C.-J. Hsu, C. Jiang, B. Bob, and Y. Yang. Spatial element

distribution control in a fully solution-processed nanocrystals-based 8.6% $\text{Cu}_2\text{ZnSn}(\text{S},\text{Se})_4$ device. *ACS Nano*, 8(9):9164–9172, 2014.

- [12] V. Steinmann, R. E. Brandt, and T. Buonassisi. Photovoltaics: Non-cubic solar cell materials. *Nature Photonics*, 9(6):355–357, 2015.
- [13] Y. Zhou, L. Wang, S. Chen, S. Qin, X. Liu, J. Chen, D.-J. Xue, M. Luo, Y. Cao, Y. Cheng, E. H. Sargent, and J. Tang. Thin-film Sb_2Se_3 photovoltaics with oriented one-dimensional ribbons and benign grain boundaries. *Nature Photonics*, 9(6):409–415, 2015.
- [14] J. H. Yun, K. H. Kim, M. S. Kim, B. T. Ahn, S. J. Ahn, J. C. Lee, and K. H. Yoon. Fabrication of CIGS solar cells with a Na-doped Mo layer on a Na-free substrate. *Thin Solid Films*, 515(15):5876–5879, 2007.
- [15] W. Jaegermann, A. Klein, and T. Mayer. Interface engineering of inorganic thin-film solar cells - materials-science challenges for advanced physical concepts. *Advanced Materials*, 21(42):4196–4206, 2009.
- [16] A. Romeo, M. Terheggen, D. Abou-Ras, D. L. Bätzner, F.-J. Haug, M. Kälin, D. Rudmann, and A. N. Tiwari. Development of thin-film $\text{Cu}(\text{In},\text{Ga})\text{Se}_2$ and CdTe solar cells. *Progress in Photovoltaics: Research and Applications*, 12:93–111, 2004.
- [17] M. Kaelin, D. Rudmann, F. Kurdesau, H. Zogg, T. Meyer, and A. N. Tiwari. Low-cost CIGS solar cells by paste coating and selenization. *Thin Solid Films*, 480:486–490, 2005.
- [18] T. Nakada, Y. Hirabayashi, T. Tokado, D. Ohmori, and T. Mise. Novel device structure for $\text{Cu}(\text{In},\text{Ga})\text{Se}_2$ thin film solar cells using transparent conducting oxide back and front contacts. *Solar Energy*, 77(6):739–747, 2004.
- [19] N. Kohara, S. Nishiwaki, Y. Hashimoto, T. Negami, and T. Wada. Electrical properties of the $\text{Cu}(\text{In},\text{Ga})\text{Se}_2/\text{MoSe}_2/\text{Mo}$ structure. *Solar Energy Materials and Solar Cells*, 67(1-4):209–215, 2001.
- [20] K. Orgassa, H. W. Schock, and J. H. Werner. Alternative back contact materials for thin film $\text{Cu}(\text{In},\text{Ga})\text{Se}_2$ solar cells. *Thin Solid Films*, 431:387–391, 2003.
- [21] K. D. Dobson, I. Visoly-Fisher, G. Hodes, and D. Cahen. Stability of CdTe/CdS thin-film solar cells. *Solar Energy Materials and Solar Cells*, 62(3):295–325, 2000.
- [22] W. Monch. Barrier heights of real Schottky contacts explained by metal-induced gap states and lateral inhomogeneities. *Journal of Vacuum Science and Technology B*, 17(4):1867–1876, 1999.

- [23] Jenny Nelson. *The Physics of Solar Cells (Properties of Semiconductor Materials)*. Imperial College Press, 2003.
- [24] O. D. Miller, E. Yablonovitch, and S. R. Kurtz. Strong internal and external luminescence as solar cells approach the Shockley-Queisser limit. *IEEE Journal of Photovoltaics*, 2:303–311, 2012.
- [25] R. T. Ross. Some thermodynamics of photochemical systems. *Journal of Chemical Physics*, 46:45904593, 1967.
- [26] M. A. Green. Radiative efficiency of state-of-the-art photovoltaic cells. *Progress in Photovoltaics: Research and Applications*, 20:472476, 2012.
- [27] L. C. Hirst and N. J. Ekins-Daukes. Fundamental losses in solar cells. *Progress in Photovoltaics: Research and Applications*, 19:286–293, 2011.
- [28] E. M Tennyson, C. Gong, and M. S. Leite. Imaging energy harvesting and storage systems at the nanoscale. *ACS Energy Letters*, 2(12):27612777, 2017.
- [29] G. Binnig, H. Rohrer, C. Gerber, and E. Weibel. Surface studies by scanning tunneling microscopy. *Physical Review Letters*, 49(1):57–61, 1982.
- [30] G. Binnig, C. F. Quate, and C. Gerber. Atomic force microscope. *Physical Review Letters*, 56(9):930–933, 1986.
- [31] F. J. Giessibl. Advances in atomic force microscopy. *Reviews of Modern Physics*, 75(3):949–983, 2003.
- [32] R. Garcia and E. T. Herruzo. The emergence of multifrequency force microscopy. *Nature Nanotechnology*, 7(4):217–226, 2012.
- [33] M. Z. Baykara, T. C. Schwendemann, E. I. Altman, and U. D. Schwarz. Three-dimensional atomic force microscopy – taking surface imaging to the next level. *Advanced Materials*, 22(26-27):2838–2853, 2010.
- [34] E. M. Tennyson, J. M. Howard, and M. S. Leite. Mesoscale functional imaging of materials for photovoltaics. *ACS Energy Letters*, 2:1825–1834, 2017.
- [35] M. A. Green, Y. Hishikawa, E. D. Dunlop, D. H. Levi, J. Hohl-Ebinger, and A. W.Y. Ho-Baillie. Solar cell efficiency tables (version 51). *Progress in Photovoltaics: Research and Applications*, 26(1):3–12, 2018.
- [36] Department of Energy: From quanta to the continuum: Opportunities for mesoscale science. (2012).
- [37] E. M. Tennyson, J. L. Garrett, J. A. Frantz, J. D. Myers, R. Y. Bekele, Jasbinder S. Sanghera, J. N. Munday, and M. S. Leite. Nanoimaging of open-circuit voltage in photovoltaic devices. *Advanced Energy Materials*, 5(23):1501142, 2015.

- [38] J. D. Poplawsky, W. Guo, N. Paudel, A. Ng, K. More, D. Leonard, and Y. Yan. Structural and compositional dependence of the $\text{CdTe}_x\text{Se}_{1-x}$ alloy layer photoactivity in CdTe-based solar cells. *Nature Communications*, 7:12537, 2016.
- [39] J. L. Garrett, E. M. Tennyson, M. Hu, J. Huang, J. N. Munday, and M. S. Leite. Real-time nanoscale open-circuit voltage dynamics of perovskite solar cells. *Nano Letters*, 17(4):2554–2560, 2017.
- [40] E. M. Tennyson, J. A. Frantz, J. M. Howard, Gunnarsson W. B., J. D. Myers, R. Y. Bekele, S. M. Na, and M. S. Leite. Tomography of charge carrier collection in polycrystalline solar cells. *ACS Energy Letters*, 1:899–905, 2016.
- [41] D. W. de Quilettes, W. Zhang, V. M. Burlakov, D. J. Graham, T. Leijtens, A. Osherov, V. Bulovic, H. J. Snaith, D. S. Ginger, and S. D. Stranks. Photo-induced halide redistribution in organic-inorganic perovskite films. *Nature Communications*, 7, 2016.
- [42] Y. Xie, F. Shao, Y. Wang, T. Xu, D. Wang, and F. Huang. Enhanced performance of perovskite $\text{CH}_3\text{NH}_3\text{PbI}_3$ solar cell by using $\text{CH}_3\text{NH}_3\text{I}$ as additive in sequential deposition. *ACS Applied Materials & Interfaces*, 7(23):12937–12942, 2015.
- [43] D.-H. Son, D.-H. Kim, S.-N. Park, K.-J. Yang, D. Nam, H. Cheong, and J.-K. Kang. Growth and device characteristics of CZTSSe thin-film solar cells with 8.03% efficiency. *Chemistry of Materials*, 27(15):5180–5188, 2015.
- [44] A. L. Greenaway, M. C. Sharps, J. W. Boucher, L. E. Strange, M. G. Kast, S. Aloni, and S. W. Boettcher. Selective area epitaxy of GaAs microstructures by close-spaced vapor transport for solar energy conversion applications. *ACS Energy Letters*, 1(2):402–408, 2016.
- [45] A. Kojima, K. Teshima, Y. Shirai, and T. Miyasaka. Organometal halide perovskites as visible-light sensitizers for photovoltaic cells. *Journal of the American Chemical Society*, 131(17):6050–6051, 2009.
- [46] J. Seo, J. H. Noh, and S. I. Seok. Rational strategies for efficient perovskite solar cells. *Accounts of Chemical Research*, 49(3):562–572, 2016.
- [47] T.-B. Song, T. Yokoyama, S. Aramaki, and M. G. Kanatzidis. Performance enhancement of lead-free tin-based perovskite solar cells with reducing atmosphere-assisted dispersible additive. *ACS Energy Letters*, 2(4):897–903, 2017.
- [48] J. Bisquert, Y. Qi, T. Ma, and Y. Yan. Advances and obstacles on perovskite solar cell research from material properties to photovoltaic function. *ACS Energy Letters*, 2(2):520–523, 2017.

- [49] W. Tress, N. Marinova, T. Moehl, S. M. Zakeeruddin, Mohammad Khaja Nazeeruddin, and M. Grätzel. Understanding the rate-dependent J - V hysteresis, slow time component, and aging in $\text{CH}_3\text{NH}_3\text{PbI}_3$ perovskite solar cells: the role of a compensated electric field. *Energy & Environmental Science*, 8(3):995–1004, 2015.
- [50] J. Berry, T. Buonassisi, D. A. Egger, G. Hodes, L. Kronik, Y.-L. Loo, I. Lubomirsky, S. R. Marder, Y. Mastai, J. S. Miller, D. B. Mitzi, Y. Paz, A. M. Rappe, I. Riess, B. Rybtchinski, O. Stafsudd, V. Stevanovic, M. F. Toney, D. Zitoun, A. Kahn, D. Ginley, and D. Cahen. Hybrid organic-inorganic perovskites (HOIPs): Opportunities and challenges. *Advanced Materials*, 27:5102–5112, 2015.
- [51] Y. Kutes, Y. Zhou, J. L. Bosse, J. Steffes, N. P. Padture, and B. D. Huey. Mapping the photoresponse of $\text{CH}_3\text{NH}_3\text{PbI}_3$ hybrid perovskite thin films at the nanoscale. *Nano Letters*, 16(6):3434–3441, 2016.
- [52] E. Edri, S. Kirmayer, S. Mukhopadhyay, K. Gartsman, G. Hodes, and D. Cahen. Elucidating the charge carrier separation and working mechanism of $\text{CH}_3\text{NH}_3\text{PbI}_{3-x}\text{Cl}_x$ perovskite solar cells. *Nature Communications*, 5, 2014.
- [53] F. Giustino and H. J. Snaith. Toward lead-free perovskite solar cells. *ACS Energy Letters*, 1(6):1233–1240, 2016.
- [54] Y. Zhao, M. Boccard, S. Liu, J. Becker, X.-H. Zhao, C. M. Campbell, E. Suarez, M. B. Lassise, Z. Holman, and Y.-H. Zhang. Monocrystalline CdTe solar cells with open-circuit voltage over 1V and efficiency of 17%. *Nature Energy*, 1:16067, 2016.
- [55] J. Moseley, W. K. Metzger, H. R. Moutinho, N. Paudel, H. L. Guthrey, Y. Yan, R. K. Ahrenkiel, and M. M. Al-Jassim. Recombination by grain-boundary type in CdTe. *Journal of Applied Physics*, 118(2):025702, 2015.
- [56] D. Abou-Ras, S. S. Schmidt, N. Schäfer, J. Kavalakkatt, T. Rissom, T. Unold, R. Mainz, A. Weber, T. Kirchartz, E. Simsek Sanli, P. A. van Aken, Q. M. Ramasse, H.-J. Kleebe, D. Azulay, I. Balberg, O. Millo, O. Cojocar-Mirédin, D. Barragan-Yani, K. Albe, J. Haarstrich, and C. Ronning. Compositional and electrical properties of line and planar defects in $\text{Cu}(\text{In,Ga})\text{Se}_2$ thin films for solar cells. *physica status solidi (RRL) Rapid Research Letters*, pages 1–13, 2016.
- [57] R. Kamada, T. Yagioka, S. Adachi, A. Handa, K. F. Tai, T. Kato, and H. Sugimoto. New world record $\text{Cu}(\text{In,Ga})(\text{Se,S})_2$ thin film solar cell efficiency beyond 22%. In *2016 IEEE 43rd Photovoltaic Specialists Conference (PVSC)*, pages 1287–1291.

- [58] A. Walsh, S. Chen, S.-H. Wei, and X.-G. Gong. Kesterite thin-film solar cells: Advances in materials modelling of $\text{Cu}_2\text{ZnSnS}_4$. *Advanced Energy Materials*, 2(4):400–409, 2012.
- [59] A. Polizzotti, I. L. Repins, R. Noufi, S.-H. Wei, and D. B. Mitzi. The state and future prospects of kesterite photovoltaics. *Energy & Environmental Science*, 6(11):3171–3182, 2013.
- [60] W. Wang, M. T. Winkler, O. Gunawan, T. Gokmen, T. K. Todorov, Y. Zhu, and D. B. Mitzi. Device characteristics of CZTSSe thin-film solar cells with 12.6% efficiency. *Advanced Energy Materials*, 4(7):1301465, 2014.
- [61] C.-Y. Su, C. Yen Chiu, and J.-M. Ting. $\text{Cu}_2\text{ZnSnS}_4$ absorption layers with controlled phase purity. *Scientific Reports*, 5:9291, 2015.
- [62] M. S. Leite, R. L. Woo, W. D. Hong, D. C. Law, and H. A. Atwater. Wide-band-gap InAlAs solar cell for an alternative multijunction approach. *Applied Physics Letters*, 98(9):093502, 2011.
- [63] H. Cotal, C. Fetzer, J. Boisvert, G. Kinsey, R. King, P. Hebert, H. Yoon, and N. Karam. III-V multijunction solar cells for concentrating photovoltaics. *Energy & Environmental Science*, 2(2):174–192, 2009.
- [64] M. S. Leite, R. L. Woo, J. N. Munday, W. D. Hong, Sh. Mesropian, D. C. Law, and H. A. Atwater. Towards an optimized all lattice-matched InAlAs/InGaAsP/InGaAs multijunction solar cell with efficiency $>50\%$. *Applied Physics Letters*, 102(3):033901, 2013.
- [65] A. J. Ritenour, R. C. Cramer, S. Levinrad, and S. W. Boettcher. Efficient n -GaAs photoelectrodes grown by close-spaced vapor transport from a solid source. *ACS Applied Materials & Interfaces*, 4(1):69–73, 2011.
- [66] A. J. Ritenour, J. W. Boucher, R. DeLancey, A. L. Greenaway, S. Aloni, and S. W. Boettcher. Doping and electronic properties of GaAs grown by close-spaced vapor transport from powder sources for scalable III-V photovoltaics. *Energy & Environmental Science*, 8(1):278–285, 2015.
- [67] K. Kamon, M. Shimazu, K. Kimura, M. Mihara, and M. Ishii. Orientation dependence of GaAs growth in low-pressure OMVPE. *Journal of Crystal Growth*, 84(1):126–132, 1987.
- [68] S. D. Hersee, E. Barbier, R. Blondeau, and R. Blondeau. A study of the orientation dependence of Ga(Al)As growth by MOVPE. *Journal of Crystal Growth*, 77(13):310–320, 1986.
- [69] Y. C. Kim, N. J. Jeon, J. H. Noh, W. S. Yang, J. Seo, J. S. Yun, A. Ho-Baillie, S. Huang, M. A. Green, J. Seidel, T. K. Ahn, and S. I. Seok. Beneficial effects of PbI_2 incorporated in organo-lead halide perovskite solar cells. *Advanced Energy Materials*, 6(4):1502104, 2016.

- [70] P. A. Cox, M. S. Glaz, J. S. Harrison, S. R. Peurifoy, D. C. Coffey, and D. S. Ginger. Imaging charge transfer state excitations in polymer/fullerene solar cells with time-resolved electrostatic force microscopy. *The Journal of Physical Chemistry Letters*, 6(15):2852–2858, 2015.
- [71] M. Tuteja, A. B. Mei, V. Palekis, A. Hall, S. MacLaren, C. S. Ferekides, and A. A. Rockett. CdCl₂ treatment-induced enhanced conductivity in CdTe solar cells observed using conductive atomic force microscopy. *The Journal of Physical Chemistry Letters*, 7(24):4962–4967, 2016.
- [72] A. Kento, I. Yutaka, A. Yoshio, and M. Takuya. Fine structures of organic photovoltaic thin films probed by frequency-shift electrostatic force microscopy. *Japanese Journal of Applied Physics*, 55(7):070305, 2016.
- [73] M. Koji, F. Takaya, I. Hiroshi, and F. Daisuke. Characterization of carrier concentration in cigs solar cells by scanning capacitance microscopy. *Measurement Science and Technology*, 25(4):044020, 2014.
- [74] Lord Kelvin. On electric machines founded on induction and convection. *Philosophical Magazine*, 46(82):66–73, 1898.
- [75] Nonnenmacher M., M.P. OBoyle, and H. K. Ickramasinghe. Kelvin probe force microscopy. *Applied Physics Letters*, 58:2921–2923, 1991.
- [76] W. Melitz, J. Shen, A.C. Kummel, and S Lee. Kelvin probe force microscopy and its application. *Surface Science Reports*, 66:1–27, 2011.
- [77] S. Sadewasser, T. Glatzel, S. Schuler, S. Nishiwaki, R. Kaigawa, and M. Ch Lux-Steiner. Kelvin probe force microscopy for the nano scale characterization of chalcopyrite solar cell materials and devices. *Thin Solid Films*, 431:257–261, 2003.
- [78] W. Melitz, J. Shen, S. Lee, J. S. Lee, A. C. Kummel, R. Droopad, and E. T. Yu. Scanning tunneling spectroscopy and Kelvin probe force microscopy investigation of fermi energy level pinning mechanism on InAs and InGaAs clean surfaces. *Journal of Applied Physics*, 108(2):023711, 2010.
- [79] S. Yogev, R. Matsubara, M. Nakamura, U. Zschieschang, H. Klauk, and Y. Rosenwaks. Fermi level pinning by gap states in organic semiconductors. *Physical Review Letters*, 110(3):036803, 2013.
- [80] Y. Zhang, D. Ziegler, and M. Salmeron. Charge trapping states at the SiO₂-Oligothiophene monolayer interface in field effect transistors studied by Kelvin probe force microscopy. *ACS Nano*, 7(9):8258–8265, 2013.
- [81] P. A. Fernández Garrillo, L. Borowik, F. Caffy, R. Demadrille, and B. Grévin. Photo-carrier multi-dynamical imaging at the nanometer scale in organic and inorganic solar cells. *ACS Applied Materials and Interfaces*, 8(45):31460–31468, 2016.

- [82] H. Lepage, N. Chevalier, D. Mariolle, and O. Renault. Measuring the lifetime of silicon nanocrystal solar cell photo-carriers by using Kelvin probe force microscopy and x-ray photoelectron spectroscopy. *Nanotechnology*, 25(26):265703, 2014.
- [83] M. Takihara, T. Takahashi, and T. Ujihara. Minority carrier lifetime in polycrystalline silicon solar cells studied by photoassisted Kelvin probe force microscopy. *Applied Physics Letters*, 93(2):021902, 2008.
- [84] G. Shao, M. S. Glaz, F. Ma, H. Ju, and D. S. Ginger. Intensity-modulated scanning Kelvin probe microscopy for probing recombination in organic photovoltaics. *ACS Nano*, 8(10):10799–10807, 2014.
- [85] P. Girard. Electrostatic force microscopy: Principles and some applications to semiconductors. *Nanotechnology*, 12(4):485–490, 2001.
- [86] J. W. Hong, K. H. Noh, Sang-il Park, S. I. Kwun, and Z. G. Khim. Surface charge density and evolution of domain structure in triglycine sulfate determined by electrostatic-force microscopy. *Physical Review B*, 58(8):5078–5084, 1998.
- [87] V. K. Sangwan, D. Jariwala, I. S. Kim, K.-S. Chen, T. J. Marks, L. J. Lauhon, and M. C. Hersam. Gate-tunable memristive phenomena mediated by grain boundaries in single-layer MoS₂. *Nature Nanotechnology*, 10(5):403–406, 2015.
- [88] D. C. Coffey and D. S. Ginger. Time-resolved electrostatic force microscopy of polymer solar cells. *Nature Materials*, 5:735–740, 2006.
- [89] M. Jaquith, E. M. Muller, and J. A. Marohn. Time-resolved electric force microscopy of charge trapping in polycrystalline pentacene. *The Journal of Physical Chemistry B*, 111(27):7711–7714, 2007.
- [90] S. Y. Leblebici, L. Leppert, Y. Li, S. E. Reyes-Lillo, S. Wickenburg, E. Wong, J. Lee, M. Melli, D. Ziegler, D. K. Angell, D. F. Ogletree, P.D Ashby, F. M. Toma, J. B. Neaton, I. D. Sharp, and A. Weber-Bargioni. Facet-dependent photovoltaic efficiency variations in single grains of hybrid halide perovskite. *Nature Energy*, 1:16093, 2016.
- [91] J.-J. Li, J.-Y. Ma, Q.-Q. Ge, J.-S. Hu, D. Wang, and L.-J. Wan. Microscopic investigation of grain boundaries in organolead halide perovskite solar cells. *ACS Applied Materials & Interfaces*, 7(51):28518–28523, 2015.
- [92] N. Bich Phuong, K. Gee Yeong, J. William, K. Byeong Jo, and J. Hyun Suk. Trapping charges at grain boundaries and degradation of CH₃NH₃Pb(I_{1-x}Br_x)₃ perovskite solar cells. *Nanotechnology*, 28(31):315402, 2017.

- [93] J. Luria, Y. Kutes, A. Moore, L. Zhang, E. A. Stach, and B. D. Huey. Charge transport in CdTe solar cells revealed by conductive tomographic atomic force microscopy. *Nature Energy*, 1(16150):16150, 2016.
- [94] N. Muhunthan, O. P. Singh, V. Toutam, and V. N. Singh. Electrical characterization of grain boundaries of CZTS thin films using conductive atomic force microscopy techniques. *Materials Research Bulletin*, 70:373–378, 2015.
- [95] T. A. Bull, L. S. C. Pingree, S. A. Jenekhe, D. S. Ginger, and C. K. Luscombe. The role of mesoscopic PCBM crystallites in solvent vapor annealed copolymer solar cells. *ACS Nano*, 3(3):627–636, 2009.
- [96] X.-D. Dang, A. B. Tamayo, J. Seo, C. V. Hoven, B. Walker, and T.-Q. Nguyen. Nanostructure and optoelectronic characterization of small molecule bulk heterojunction solar cells by photoconductive atomic force microscopy. *Advanced Functional Materials*, 20(19):3314–3321, 2010.
- [97] W. C. Tsoi, P. G. Nicholson, J. S. Kim, D. Roy, T. L. Burnett, C. E. Murphy, J. Nelson, D. D. C. Bradley, J.-S. Kim, and F. A. Castro. Surface and subsurface morphology of operating nanowire:fullerene solar cells revealed by photoconductive-AFM. *Energy & Environmental Science*, 4(9):3646–3651, 2011.
- [98] M. Guide, X.-D. Dang, and T.-Q. Nguyen. Nanoscale characterization of tetrabenzoporphyrin and fullerene-based solar cells by photoconductive atomic force microscopy. *Advanced Materials*, 23(20):2313–2319, 2011.
- [99] L. Letertre, O. Douhret, M. Bougouma, T. Doneux, R. Lazzaroni, C. Buess-Herman, and P. Leclre. Nanoscale study of MoSe₂/Poly(3-Hexylthiophene) bulk heterojunctions for hybrid photovoltaic applications. *Solar Energy Materials and Solar Cells*, 145(Part 2):116–125, 2016.
- [100] B. E. McCandless, I. Youm, and R. W. Birkmire. Optimization of vapor post-deposition processing for evaporated CdS/CdTe solar cells. *Progress in Photovoltaics: Research and Applications*, 7(1):21–30, 1999.
- [101] K. Kobayashi, H. Yamada, and K. Matsushige. Dopant profiling on semiconducting sample by scanning capacitance force microscopy. *Applied Physics Letters*, 81(14):2629–2631, 2002.
- [102] I. Visoly-Fisher, S. R. Cohen, and D. Cahen. Direct evidence for grain-boundary depletion in polycrystalline CdTe from nanoscale-resolved measurements. *Applied Physics Letters*, 82(4):556–558, 2003.
- [103] F. Takaya, M. Koji, I. Hiroshi, and F. Daisuke. Analytical procedure for experimental quantification of carrier concentration in semiconductor devices by using electric scanning probe microscopy. *Measurement Science and Technology*, 25(4):044021, 2014.

- [104] N. Nicoara, T. Lepetit, L. Arzel, S. Harel, N. Barreau, and S. Sadewasser. Effect of the KF post-deposition treatment on grain boundary properties in Cu(In, Ga)Se₂ thin films. *Scientific Reports*, 7:41361, 2017.
- [105] A. Dazzi and C. B. Prater. AFM-IR: Technology and applications in nanoscale infrared spectroscopy and chemical imaging. *Chemical Reviews*, 117(7):5146–5173, 2017.
- [106] S. J. Yoon, M. Kuno, and P. V. Kamat. Shift happens. how halide ion defects influence photoinduced segregation in mixed halide perovskites. *ACS Energy Letters*, 2:1507–1514, 2017.
- [107] J. Chae, Q. Dong, J. Huang, and A. Centrone. Chloride incorporation process in CH₃NH₃PbI_{3-x}Cl_x perovskites via nanoscale bandgap maps. *Nano Letters*, 15(12):8114–8121, 2015.
- [108] D. Nowak, W. Morrison, H. K. Wickramasinghe, J. Jahng, E. Potma, L. Wan, R. Ruiz, T. R. Albrecht, K. Schmidt, J. Frommer, D. P. Sanders, and S. Park. Nanoscale chemical imaging by photoinduced force microscopy. *Science Advances*, 2(3):e1501571, 2016.
- [109] X. Wang, D. Zhang, K. Braun, H.-J. Egelhaaf, C. J. Brabec, and A. J. Meixner. High-resolution spectroscopic mapping of the chemical contrast from nanometer domains in P3HT:PCBM organic blend films for solar-cell applications. *Advanced Functional Materials*, 20(3):492–499, 2010.
- [110] T. Schmid, L. Opilik, C. Blum, and R. Zenobi. Nanoscale chemical imaging using tip-enhanced raman spectroscopy: A critical review. *Angewandte Chemie International Edition*, 52(23):5940–5954, 2013.
- [111] S. Zaleski, A. J. Wilson, M. Mattei, X. Chen, G. Goubert, M. F. Cardinal, K. A. Willets, and R. P. Van Duyne. Investigating nanoscale electrochemistry with surface- and tip-enhanced raman spectroscopy. *Accounts of Chemical Research*, 49(9):2023–2030, 2016.
- [112] N. Jiang, D. Kurouski, E. A. Pozzi, N. Chiang, M. C. Hersam, and R. P. Van Duyne. Tip-enhanced raman spectroscopy: From concepts to practical applications. *Chemical Physics Letters*, 659:16–24, 2016.
- [113] G. Nicholson Patrick and A. Castro Fernando. Organic photovoltaics: Principles and techniques for nanometre scale characterization. *Nanotechnology*, 21(49):492001, 2010.
- [114] B.-S. Yeo, J. Stadler, T. Schmid, R. Zenobi, and W. Zhang. Tip-enhanced raman spectroscopy - its status, challenges and future directions. *Chemical Physics Letters*, 472(1):1–13, 2009.

- [115] S. Ghosh, N. A. Kouamé, L. Ramos, S. Remita, A. Dazzi, A. Deniset-Besseau, P. Beaunier, F. Goubard, P.-H. Aubert, and H. Remita. Conducting polymer nanostructures for photocatalysis under visible light. *Nature Materials*, 14(5):505–511, 2015.
- [116] I. Rajapaksa, K. Uenal, and H. K. Wickramasinghe. Image force microscopy of molecular resonance: A microscope principle. *Applied Physics Letters*, 97(7):073121, 2010.
- [117] I. Rajapaksa and H. K. Wickramasinghe. Raman spectroscopy and microscopy based on mechanical force detection. *Applied Physics Letters*, 99(16):161103, 2011.
- [118] J. Jahng, D. A. Fishman, S. Park, D. B. Nowak, W. A. Morrison, H. K. Wickramasinghe, and E. O. Potma. Linear and nonlinear optical spectroscopy at the nanoscale with photoinduced force microscopy. *Accounts of Chemical Research*, 48(10):2671–2679, 2015.
- [119] D. J. Slotcavage, H. I. Karunadasa, and M. D. McGehee. Light-induced phase segregation in halide-perovskite absorbers. *ACS Energy Letters*, 1(6):1199–1205, 2016.
- [120] A. Dazzi, R. Prazeres, F. Glotin, and J. M. Ortega. Local infrared microspectroscopy with subwavelength spatial resolution with an atomic force microscope tip used as a photothermal sensor. *Optics Letters*, 30(18):2388–2390, 2005.
- [121] Cho. H., J. R. Felts, M.-F. Yu, L. A. Bergman, A. F. Vakakis, and W. P. King. Improved atomic force microscope infrared spectroscopy for rapid nanometer-scale chemical identification. *Nanotechnology*, 24(44):444007, 2013.
- [122] A. Dazzi, F. Glotin, and R. Carminati. Theory of infrared nanospectroscopy by photothermal induced resonance. *Journal of Applied Physics*, 107(12):124519, 2010.
- [123] J. R. Felts, K. Kjoller, M. Lo, C. B. Prater, and W. P. King. Nanometer-scale infrared spectroscopy of heterogeneous polymer nanostructures fabricated by tip-based nanofabrication. *ACS Nano*, 6(9):8015–8021, 2012.
- [124] B. Lahiri, G. Holland, and A. Centrone. Chemical imaging: Chemical imaging beyond the diffraction limit: Experimental validation of the PTIR technique. *Small*, 9(3):439–445, 2013.
- [125] E. Strelcov, Q. Dong, T. Li, J. Chae, Y. Shao, Y. Deng, A. Gruverman, J. Huang, and A. Centrone. $\text{CH}_3\text{NH}_3\text{PbI}_3$ perovskites: Ferroelasticity revealed. *Science Advances*, 3(4):e1602165, 2017.

- [126] C. Gong, M. R. S. Dias, G. C. Wessler, J. A. Taillon, L. G. Salamanca-Riba, and M. S. Leite. Fully alloyed noble metal nanoparticles via physical deposition for plasmonics. *Advanced Optical Materials*, 5, 2017.
- [127] B. Hecht, B. Sick, U. P. Wild, V. Deckert, R. Zenobi, O. J. F. Martin, and D. W. Pohl. Scanning near-field optical microscopy with aperture probes: Fundamentals and applications. *The Journal of Chemical Physics*, 112(18):7761–7774, 2000.
- [128] Y. Zhang, Y. Wang, Z.-Q. Xu, J. Liu, J. Song, Y. Xue, Z. Wang, J. Zheng, L. Jiang, C. Zheng, F. Huang, B. Sun, Y.-B. Cheng, and Q. Bao. Reversible structural swell-shrink and recoverable optical properties in hybrid inorganic-organic perovskite. *ACS Nano*, 10(7):7031–7038, 2016.
- [129] W. Bao, M. Melli, N. Caselli, F. Riboli, D. S. Wiersma, M. Staffaroni, H. Choo, D. F. Ogletree, S. Aloni, J. Bokor, S. Cabrini, F. Intonti, M. B. Salmeron, E. Yablonovitch, P. J. Schuck, and A. Weber-Bargioni. Mapping local charge recombination heterogeneity by multidimensional nanospectroscopic imaging. *Science*, 338(6112):1317–1321, 2012.
- [130] M. S. Leite, M. Abashin, H. J. Lezec, A. G. Gianfrancesco, A. A. Talin, and N. B. Zhitenev. Nanoscale imaging of photocurrent and efficiency in CdTe solar cells. *ACS Nano*, 8(11):11883–11890, 2014.
- [131] M. S. Leite, M. Abashin, H. J. Lezec, A. G. Gianfrancesco, A. Alec Talin, and N. B. Zhitenev. Mapping the local photoelectronic properties of polycrystalline solar cells through high resolution laser-beam-induced current microscopy. *IEEE Journal of Photovoltaics*, 4(1):311–316, 2014.
- [132] U. W. Paetzold, S. Lehnen, K. Bittkau, U. Rau, and R. Carius. Nanoscale observation of waveguide modes enhancing the efficiency of solar cells. *Nano Letters*, 14(11):6599–6605, 2014.
- [133] E. H. Synge. XXXVIII. a suggested method for extending microscopic resolution into the ultra-microscopic region. *The London, Edinburgh, and Dublin Philosophical Magazine and Journal of Science*, 6(35):356–362, 1928.
- [134] U. Dürig, D. W. Pohl, and F. Rohner. Near-field optical-scanning microscopy. *Journal of Applied Physics*, 59(10):3318–3327, 1986.
- [135] A. Lewis, M. Isaacson, A. Harootunian, and A. Muray. Development of a 500 Å spatial resolution light microscope. *Ultramicroscopy*, 13(3):227–231, 1984.
- [136] J.-H. Kim and K.-B. Song. Recent progress of nano-technology with NSOM. *Micron*, 38(4):409–426, 2007.

- [137] D. F. Ogletree, P. J. Schuck, A. F. Weber-Bargioni, N. J. Borys, S. Aloni, W. Bao, S. Barja, J. Lee, M. Melli, K. Munechika, S. Whitelam, and S. Wickenburg. Revealing optical properties of reduced-dimensionality materials at relevant length scales. *Advanced Materials*, 27(38):5693–5719, 2015.
- [138] M. Vrućnić, C. Matthiesen, A. Sadhanala, G. Divitini, S. Cacovich, S. E. Dutton, C. Ducati, M. Atatre, H. Snaith, R. H. Friend, H. Sirringhaus, and F. Deschler. Local versus long-range diffusion effects of photoexcited states on radiative recombination in organic-inorganic lead halide perovskites. *Advanced Science*, 2(9):1500136, 2015.
- [139] K. Okamoto, A. Scherer, and Y. Kawakami. Near-field scanning optical microscopic transient lens for carrier dynamics study in InGaN/GaN. *Applied Physics Letters*, 87(16):161104, 2005.
- [140] K. Nakayama, K. Tanabe, and H. A. Atwater. Plasmonic nanoparticle enhanced light absorption in GaAs solar cells. *Applied Physics Letters*, 93(12):121904, 2008.
- [141] J. Das Anshuman, R. Shivanna, and K. S. Narayan. Photoconductive NSOM for mapping optoelectronic phases in nanostructures. *Nanophotonics*, 3(1-2):19–31, 2014.
- [142] J. M. Atkin, S. Berweger, A. C. Jones, and M. B. Raschke. Nano-optical imaging and spectroscopy of order, phases, and domains in complex solids. *Advances in Physics*, 61(6):745–842, 2012.
- [143] A. Bek, R. Vogelgesang, and K. Kern. Apertureless scanning near field optical microscope with sub-10nm resolution. *Review of Scientific Instruments*, 77(4):043703, 2006.
- [144] Imec. <https://www.imec-int.com/en/articles/imec-reports>, 2017.
- [145] G. Grancini, C. Roldn-Carmona, I. Zimmermann, E. Mosconi, X. Lee, D. Martineau, S. Narbey, F. Oswald, F. De Angelis, M. Graetzel, and Mohammad Khaja Nazeeruddin. One-year stable perovskite solar cells by 2d/3d interface engineering. *Nature Communications*, 8:15684, 2017.
- [146] M. Saliba, Taisuke M., J.-Y. Seo, K. Domanski, J.-P. Correa-Baena, M. K. Nazeeruddin, S. M. Zakeeruddin, W. Tress, A. Abate, A. Hagfeldt, and M. Grätzel. Cesium-containing triple cation perovskite solar cells: Improved stability, reproducibility and high efficiency. *Energy & Environmental Science*, 9(6):1989–1997, 2016.
- [147] R. E. Beal, D. J. Slotcavage, T. Leijtens, A. R. Bowring, R. A. Belisle, W. H. Nguyen, G. F. Burkhard, E. T. Hoke, and M. D. McGehee. Cesium lead halide perovskites with improved stability for tandem solar cells. *The Journal of Physical Chemistry Letters*, 7(5):746–751, 2016.

- [148] D. Bryant, N. Aristidou, S. Pont, I. Sanchez-Molina, T. Chotchunangatchaval, S. Wheeler, J. R. Durrant, and S. A. Haque. Light and oxygen induced degradation limits the operational stability of methylammonium lead triiodide perovskite solar cells. *Energy & Environmental Science*, 9(5):1655–1660, 2016.
- [149] D. Yang, J. Lv, X. Zhao, Q. Xu, Y. Fu, Y. Zhan, A. Zunger, and L. Zhang. Functionality-directed screening of Pb-free hybrid organic-inorganic perovskites with desired intrinsic photovoltaic functionalities. *Chemistry of Materials*, 29(2):524–538, 2017.
- [150] L. Li, N. Liu, Z. Xu, Q. Chen, X. Wang, and H. Zhou. Precise composition tailoring of mixed-cation hybrid perovskites for efficient solar cells by mixture design methods. *ACS Nano*, 11(9):88048813, 2017.
- [151] V. W. Bergmann, S. A. L. Weber, F. Javier Ramos, M. K. Nazeeruddin, M. Grätzel, D. Li, A. L. Domanski, I. Lieberwirth, S. Ahmad, and R. Berger. Real-space observation of unbalanced charge distribution inside a perovskite-sensitized solar cell. *Nature Communications*, 5:6001, 2014.
- [152] M. I. Asghar, J. Zhang, H. Wang, and P. D. Lund. Device stability of perovskite solar cells - a review. *Renewable and Sustainable Energy Reviews*, 77:131–146, 2017.
- [153] N.-G. Park, M. Grätzel, T. Miyasaka, K. Zhu, and K. Emery. Towards stable and commercially available perovskite solar cells. *Nature Energy*, 1:16152, 2016.
- [154] L. Wang, H. Wang, M. Wagner, Y. Yan, D. S. Jakob, and X. G. Xu. Nanoscale simultaneous chemical and mechanical imaging via peak force infrared microscopy. *Science Advances*, 3(6):1–11, 2017.
- [155] J. L. Garrett and J. N. Munday. Fast, high-resolution surface potential measurements in air with heterodyne Kelvin probe force microscopy. *Nanotechnology*, 27(24):245705, 2016.
- [156] L. Collins, M. Ahmadi, T. Wu, B. Hu, S. V. Kalinin, and S. Jesse. Breaking the time barrier in Kelvin probe force microscopy: Fast free force reconstruction using the G-mode platform. *ACS Nano*, 11(9):87178729, 2017.
- [157] Y. Miyahara and Peter G. Force-gradient sensitive Kelvin probe force microscopy by dissipative electrostatic force modulation. *Applied Physics Letters*, 110(16):163103, 2017.
- [158] J. B. Kim and W. S. Chang. Design and fabrication of a tip-on-aperture probe for resolution enhancement of optical patterning. *Microelectronic Engineering*, 151:24–29, 2016.

- [159] F. Huth, A. Chuvilin, M. Schnell, I. Amenabar, R. Krutokhvostov, S. Lopatin, and R. Hillenbrand. Resonant antenna probes for tip-enhanced infrared near-field microscopy. *Nano Letters*, 13(3):1065–1072, 2013.
- [160] A. L. Greenaway, J. W. Boucher, S. Z. Oener, C. J. Funch, and S. W. Boettcher. Low-cost approaches to III-V semiconductor growth for photovoltaic applications. *ACS Energy Letters*, pages 2270–2282, 2017.
- [161] H. R. Moutinho, R. G. Dhere, C. S. Jiang, Y. F. Yan, D. S. Albin, and M. M. Al-Jassim. Investigation of potential and electric field profiles in cross sections of CdTe/CdS solar cells using scanning Kelvin probe microscopy. *Journal of Applied Physics*, 108(7):074503, 2010.
- [162] M. A. Green. Commercial progress and challenges for photovoltaics. *Nature Energy*, 1:15015, 2016.
- [163] A. Chirilă, P. Reinhard, F. Pianezzi, P. Bloesch, A. R. Uhl, C. Fella, L. Kranz, D. Keller, C. Gretener, H. Hagendorfer, D. Jaeger, R. Erni, S. Nishiwaki, S. Buecheler, and A. N. Tiwari. Potassium-induced surface modification of Cu(In,Ga)Se₂ thin films for high-efficiency solar cells. *Nature Materials*, 12(12):1107–1111, 2013.
- [164] P. Jackson, R. Wuerz, D. Hariskos, E. Lotter, W. m Witte, and M. Powalla. Effects of heavy alkali elements in Cu(In,Ga)Se₂ solar cells with efficiencies up to 22.6%. *physica status solidi (RRL) Rapid Research Letters*, 10(8):583–586, 2016.
- [165] C.-H. Liu, C.-H. Chen, S.-Y. Chen, Y.-T. Yen, W.-C. Kuo, Y.-K. Liao, J.-Y. Juang, H.-C. Kuo, C.-H. Lai, L.-J. Chen, and Y.-L. Chueh. Large scale single-crystal Cu(In,Ga)Se₂ nanotip arrays for high efficiency solar cell. *Nano Letters*, 11(10):4443–4448, 2011.
- [166] T. B. Harvey, I. Mori, C. J. Stolle, T. D. Bogart, D. P. Ostrowski, M. S. Glaz, J. Du, D. R. Pernik, V. A. Akhavan, H. Kesrouani, D. A. Vanden Bout, and B. A. Korgel. Copper indium gallium selenide photovoltaic devices made using multistep selenization of nanocrystal films. *ACS Applied Materials and Interfaces*, 5(18):9134–9140, 2013.
- [167] J. A. Frantz, R. Y. Bekele, V. Q. Nguyena, J. S. Sanghera, A. Bruce, S. V. Frolov, M. Cyrus, and I. D. Aggarwal. Cu(In,Ga)Se₂ thin films and devices sputtered from a single target without additional selenization. *Thin Solid Films*, (519):7763–7765, 2011.
- [168] J. H. Shi, Z. Q. Li, D. W. Zhang, Q. Q. Liu, Z. Sun, and S. M. Huang. Fabrication of Cu(In,Ga)Se₂ thin films by sputtering from a single quaternary chalcogenide target. *Progress in Photovoltaics: Research and Applications*, 19(2):160–164, 2011.

- [169] L. Ouyang, D. Zhuang, M. Zhao, N. Zhang, X. Li, L. Guo, R. Sun, and M. Cao. Cu(In,Ga)Se₂ solar cell with 16.7% active-area efficiency achieved by sputtering from a quaternary target. *physica status solidi (a)*, pages 1–5, 2015.
- [170] N. G. Dhere. Scale-up issues of CIGS thin film PV modules. *Solar Energy Materials and Solar Cells*, 95(1):277–280, 2011.
- [171] N. E. Gorji. Degradation sources of CdTe thin film PV: CdCl₂ residue and shunting pinholes. *Applied Physics A*, 116(3):1347–1352, 2014.
- [172] K. Durose, S. E. Asher, W. Jaegermann, D. Levi, B. E. McCandless, W. Metzger, H. Moutinho, P. D. Paulson, C. L. Perkins, J. R. Sites, G. Teeter, and M. Terheggen. Physical characterization of thin-film solar cells. *Progress in Photovoltaics*, 12(2-3):177–217, 2004.
- [173] T. Kirchartz and U. Rau. *Advanced Characterization Techniques for Thin Film Solar Cells*, pages 1–547. Wiley-VCH, 2011.
- [174] D. P. Ostrowski, M. S. Glaz, B. W. Goodfellow, V. A. Akhavan, M. G. Panthani, B. A. Korgel, and D. A. V. Bout. Mapping spatial heterogeneity in Cu(In_{1-x}Ga_x)Se₂ nanocrystal-based photovoltaics with scanning photocurrent and fluorescence microscopy. *Small*, 6(24):2832–2836, 2010.
- [175] S. L. Howell, S. Padalkar, K.-H. Yoon, Q. Li, D. D. Koleske, J. J. Wierer, G. T. Wang, and L. J. Lauhon. Spatial mapping of efficiency of GaN/InGaN nanowire array solar cells using scanning photocurrent microscopy. *Nano Letters*, 13:51235128, 2013.
- [176] D. Josell, R. Debnath, J. Y. Ha, J. Guyer, M. A. Sahiner, C. J. Reehil, W. A. Manners, and N. V. Nguyen. Windowless CdSe/CdTe solar cells with differentiated back contacts: JV, EQE, and photocurrent mapping. *ACS Applied Materials and Interfaces*, 6(18):15972–15979, 2014.
- [177] M. Nichterwitz, D. Abou-Ras, K. Sakurai, J. Bundesmann, T. Unold, R. Scheer, and H. W. Schock. Influence of grain boundaries on current collection in Cu(In,Ga)Se₂ thin-film solar cells. *Thin Solid Films*, 517(7):2554–2557, 2009.
- [178] P. O. Grabitz, U. Rau, B. Wille, G. Bilger, and J. H. Werner. Spatial inhomogeneities in Cu(In,Ga)Se₂ solar cells analyzed by electron beam induced voltage measurements. In *Photovoltaic Energy Conversion, Conference Record of the 2006 IEEE 4th World Conference on*, volume 1, pages 424–427, 2006.
- [179] H. P. Yoon, P. M. Haney, D. Ruzmetov, H. Xu, M. S. Leite, B. H. Hamadani, A. A. Talin, and N. B. Zhitenev. Local electrical characterization of cadmium telluride solar cells using low-energy electron beam. *Solar Energy Materials and Solar Cells*, 117:499–504, 2013.

- [180] J.-H. Kim, S.-Y. Kim, C.-S. Jiang, K. Ramanathan, and M. M. Al-Jassim. Direct imaging of enhanced current collection on grain boundaries of Cu(In,Ga)Se₂ solar cells. *Applied Physics Letters*, 104(6):063902, 2014.
- [181] D. Azulay, O. Millo, I. Balberg, H.-W. Schock, I. Visoly-Fisher, and D. Cahen. Current routes in polycrystalline CuInSe₂ and Cu(In,Ga)Se₂ films. *Solar Energy Materials and Solar Cells*, 91(1):85–90, 2007.
- [182] D.C. Coffey, O.G. Reid, D.B. Rodovsky, G.P. Bartholomew, and D. S. Ginger. Mapping local photocurrents in polymer/fullerene solar cells with photoconductive atomic force microscopy. *Nano Letters*, 7:738–744, 2007.
- [183] Y. Kutes, B. A. Aguirre, J. L. Bosse, J. L. Cruz-Campa, D. Zubia, and B. D. Huey. Mapping photovoltaic performance with nanoscale resolution. *Progress in Photovoltaics: Research and Applications*, 24(3):315–325, 2015.
- [184] T. Dittrich, A. Gonzales, T. Rada, T. Rissom, E. Zillner, S. Sade-wasser, and M. Lux-Steiner. Comparative study of Cu(In,Ga)Se₂/CdS and Cu(In,Ga)Se₂/In₂S₃ systems by surface photovoltage techniques. *Thin Solid Films*, 535:357–361, 2013.
- [185] M. Tuteja, P. Koirala, S. MacLaren, R. Collins, and A. Rockett. Direct observation of electrical properties of grain boundaries in sputter-deposited CdTe using scan-probe microwave reflectivity based capacitance measurements. *Applied Physics Letters*, 107(14):142106, 2015.
- [186] C. R. McNeill, H. Frohne, J. L. Holdsworth, J. E. Furst, B. V. King, and P. C. Dastoor. Direct photocurrent mapping of organic solar cells using a near-field scanning optical microscope. *Nano Letters*, 4(2):219–223, 2004.
- [187] L. Gütay, R. Pomraenke, C. Lienau, and G. H. Bauer. Subwavelength inhomogeneities in Cu(In,Ga)Se₂ thin films revealed by near-field scanning optical microscopy. *physica status solidi (a)*, 206(5):1005–1008, 2009.
- [188] U. Rau, K. Taretto, and S. Siebentritt. Grain boundaries in Cu(In,Ga)(Se,S)₂ thin-film solar cells. *Applied Physics A*, 96(1):221–234, 2009.
- [189] D. Abou-Ras, C. T. Koch, V. Kstner, P. A. van Aken, U. Jahn, M. A. Contreras, R. Caballero, C. A. Kaufmann, R. Scheer, T. Unold, and H. W. Schock. Grain-boundary types in chalcopyrite-type thin films and their correlations with film texture and electrical properties. *Thin Solid Films*, 517(7):2545–2549, 2009.
- [190] K. Bothe, G. H. Bauer, and T. Unold. Spatially resolved photoluminescence measurements on Cu(In,Ga)Se₂ thin films. *Thin Solid Films*, 403404(0):453–456, 2002.

- [191] L. Gütay and G. H. Bauer. Spectrally resolved photoluminescence studies on Cu(In,Ga)Se₂ solar cells with lateral submicron resolution. *Thin Solid Films*, 515(15):6212–6216, 2007.
- [192] L. Lombez, M. Soro, A. Delamarre, N. Naghavi, N. Barreau, D. Lincot, and J.-F. Guillemoles. Revisiting the interpretation of biased luminescence: Effects on Cu(In,Ga)Se₂ photovoltaic heterostructures. *Journal of Applied Physics*, 116(064504):6, 2014.
- [193] G. H. Bauer, R. Bruggemann, S. Tardon, S. Vignoli, and R. Kniese. Quasi-fermi level splitting and identification of recombination losses from room temperature luminescence in Cu(In_{1-x}Ga_x)Se₂ thin films versus optical band gap. *Thin Solid Films*, 480481:410–414, 2005.
- [194] K. Alberi, B. Fluegel, H. Moutinho, R. G. Dhere, J. V. Li, and A. Mascarenhas. Measuring long-range carrier diffusion across multiple grains in polycrystalline semiconductors by photoluminescence imaging. *Nature Communications*, 4:1–7, 2013.
- [195] O. Neumann, R. Bruggemann, D. Hariskos, W. Witte, and G. H. Bauer. Photoluminescence studies of polycrystalline Cu(In,Ga)Se₂: Lateral inhomogeneities beyond abbe’s diffraction limit. *Journal of Applied Physics*, 118(18):185311, 2015.
- [196] C. Li, Y. Wu, J. Poplawsky, T. J. Pennycook, N. Paudel, W. Yin, S. J. Haigh, M. P. Oxley, A. R. Lupini, M. Al-Jassim, S. J. Pennycook, and Y. Yan. Grain-boundary-enhanced carrier collection in CdTe solar cells. *Physical Review Letters*, 112(15):156103, 2014.
- [197] R. Chakraborty, J. Serdy, B. West, M. Stuckelberger, B. Lai, J. Maser, M. I. Bertoni, M. L. Culpepper, and T. Buonassisi. Development of an in-situ temperature stage for synchrotron x-ray spectromicroscopy. *Review of Scientific Instruments*, 86(11):1–6, 2015.
- [198] R. Mainz, E. Simsek Sanli, H. Stange, D. Azulay, S. Brunken, D. Greiner, S. Hajaj, M. D. Heinemann, C. A. Kaufmann, M. Klaus, Q. M. Ramasse, H. Rodriguez-Alvarez, A. Weber, I. Balberg, O. Millo, P. A. van Aken, and D. Abou-Ras. Annihilation of structural defects in chalcogenide absorber films for high-efficiency solar cells. *Energy and Environmental Science*, pages 1–10, 2016.
- [199] C. Xue, D. Papadimitriou, Y. S. Raptis, W. Richter, N. Esser, S. Siebentritt, and M. Ch. Lux-Steiner. Micro-raman study of orientation effects of Cu_xSe-crystallites on cu-rich CuGaSe₂ thin films. *Journal of Applied Physics*, 96(4):1963–1966, 2004.
- [200] A. Luque and S. Hegedus. *Handbook of Photovoltaic Science and Engineering*. John Wiley and Sons, Ltd, West Sussex, 2011.

- [201] A. Fantoni, M. Vieira, J. Cruz, R. Schwarz, and R. Martins. A two-dimensional numerical simulation of a non-uniformly illuminated amorphous silicon solar cell. *Journal of Physics D: Applied Physics*, 29(12):3154, 1996.
- [202] A. Cuevas and S. Lopez-Romero. The combined effect of non-uniform illumination and series resistance on the open-circuit voltage of solar cells. *Solar Cells*, 11(2):163–173, 1984.
- [203] S. Nomura, S. Ouchi, and S. Endo. Raman spectra of ordered vacancy compounds in the Cu-In-Se system. *Japanese Journal of Applied Physics*, 36(8B):1075–1077, 1997.
- [204] W. Witte, R. Kniese, and M. Powalla. Raman investigations of Cu(In,Ga)Se₂ thin films with various copper contents. *Thin Solid Films*, 517(2):867–869, 2008.
- [205] M. Gloeckler, J. R. Sites, and W. K. Metzger. Grain-boundary recombination in Cu(In,Ga)Se₂ solar cells. *Journal of Applied Physics*, 98(11):113704, 2005.
- [206] National Renewable Energy Laboratories. Standard am1.5 global sun spectrum (2012), 2012.
- [207] A. Slobodskyy, T. Slobodskyy, T. Ulyanenkova, S. Doyle, M. Powalla, T. Baumbach, and U. Lemmer. In-depth analysis of the CuIn_{1-x}GaxSe₂ film for solar cells, structural and optical characterization. *Applied Physics Letters*, 97(251911), 2010.
- [208] M. A. Green, K. Emery, Y. Hishikawa, W. Warta, and E. D. Dunlop. Solar cell efficiency tables (version 46). *Progress in Photovoltaics: Research and Applications*, 23(7):805–812, 2015.
- [209] K.R. Catchpole and A. Polman. Plasmonic solar cells. *Optics Express*, 16(26):21793–21800, 2008.
- [210] P. Campbell and M. A. Green. Light trapping properties of pyramidally textured surfaces. *Journal of Applied Physics*, 62(1):243–249, 1987.
- [211] J. N. Munday and H. A. Atwater. Large integrated absorption enhancement in plasmonic solar cells by combining metallic gratings and antireflection coatings. *Nano Letters*, 11(6):2195–2201, 2010.
- [212] M. L. Brongersma, Y. Cui, and S. Fan. Light management for photovoltaics using high-index nanostructures. *Nature Materials*, 13(5):451–460, 2014.
- [213] H. R. Moutinho, R. G. Dhere, C. S. Jiang, M. M. Al-Jassim, and L. L. Kazmerski. Electrical properties of CdTe/CdS solar cells investigated with conductive atomic force microscopy. *Thin Solid Films*, 514(1-2):150–155, 2006.

- [214] I. Visoly-Fisher, S. R. Cohen, K. Gartsman, A. Ruzin, and D. Cahen. Understanding the beneficial role of grain boundaries in polycrystalline solar cells from single-grain-boundary scanning probe microscopy. *Advanced Functional Materials*, 16(5):649–660, 2006.
- [215] H. Sakaguchi, F. Iwata, A. Hirai, A. Sasaki, and T. Nagamura. Nanometer-scale photoelectric property of organic thin films investigated by a photoconductive atomic force microscope. *Japanese Journal of Applied Physics*, 38(65):3908–3911, 1999.
- [216] C. Ballif, H. R. Moutinho, and M. M. Al-Jassim. Cross-sectional electrostatic force microscopy of thin-film solar cells. *Journal of Applied Physics*, 89(2):1418–1424, 2001. Ballif, C Moutinho, HR Al-Jassim, MM.
- [217] M. J. Romero, C. S. Jiang, J. Abushama, H. R. Moutinho, M. M. Al-Jassim, and R. Noufi. Electroluminescence mapping of CuGaSe₂ solar cells by atomic force microscopy. *Applied Physics Letters*, 89:143120, 2006.
- [218] H. R. Moutinho, R. G. Dhere, C. S. Jiang, T. Gessert, A. Duda, M. Young, W. K. Metzger, and M. M. Al-Jassim. Role of Cu on the electrical properties of CdTe/CdS solar cells: A cross-sectional conductive atomic force microscopy study. *Journal of Vacuum Science & Technology B*, 25(2):361–367, 2007.
- [219] W. Melitz, J. Shen, A.C. Kummel, and S Lee. Kelvin probe force microscopy and its application. *Surface Science Reports*, 66:1–27, 2011.
- [220] P. Sutter, E. Sutter, and T. R. Ohno. High-resolution mapping of nonuniform carrier transport at contacts to polycrystalline CdTe/CdS solar cells. *Applied Physics Letters*, 84(12):2100–2102, 2004.
- [221] P. Eyben, F. Seidel, T. Hantschel, A. Schulze, A. Lorenz, A. U. De Castro, D. Van Gestel, J. John, J. Horzel, and W. Vandervorst. Development and optimization of scanning spreading resistance microscopy for measuring the two-dimensional carrier profile in solar cell structures. *physica status solidi (a)*, 208(3):596–599, 2011.
- [222] O. G. Reid, G. E. Rayermann, D. C. Coffey, and D. S. Ginger. Imaging local trap formation in conjugated polymer solar cells: A comparison of time-resolved electrostatic force microscopy and scanning Kelvin probe imaging. *The Journal of Physical Chemistry C*, 114(48):20672–20677, 2010.
- [223] E. J. Spadafora, R. Demadrille, B. Ratier, and B. Grévin. Imaging the carrier photogeneration in nanoscale phase segregated organic heterojunctions by Kelvin probe force microscopy. *Nano Letters*, 10(9):3337–3342, 2010.
- [224] H. Hoppe, T. Glatzel, M. Niggemann, A. Hinsch, M. Ch Lux-Steiner, and N. S. Sariciftci. Kelvin probe force microscopy study on conjugated polymer/fullerene bulk heterojunction organic solar cells. *Nano Letters*, 5(2):269–274, 2005.

- [225] S. Watanabe, Y. Fukuchi, M. Fukasawa, T. Sassa, A. Kimoto, Y. Tajima, M. Uchiyama, T. Yamashita, M. Matsumoto, and T. Aoyama. In situ KPFM imaging of local photovoltaic characteristics of structured organic photovoltaic devices. *ACS Applied Materials and Interfaces*, 6(3):1481–1487, 2014.
- [226] V. Palermo, G. Ridolfi, A. M Talarico, L. Favaretto, G. Barbarella, N. Camaioni, and P. Samor. A Kelvin probe force microscopy study of the photo-generation of surface charges in all-thiophene photovoltaic blends. *Advanced Functional Materials*, 17(3):472–478, 2007.
- [227] A. Soudi, C.-H. Hsu, and Y. Gu. Diameter-dependent surface photovoltage and surface state density in single semiconductor nanowires. *Nano Letters*, 12(10):5111–5116, 2012.
- [228] C.-S. Jiang, D. J. Friedman, J. F. Geisz, H. R. Moutinho, M. J. Romero, and M. M. Al-Jassim. Distribution of built-in electrical potential in GaInP₂/GaAs tandem-junction solar cells. *Applied Physics Letters*, 83(8):1572–1574, 2003.
- [229] C.-S. Jiang, H. R. Moutinho, D. J. Friedman, J. F. Geisz, and M. M. Al-Jassim. Measurement of built-in electrical potential in III-V solar cells by scanning Kelvin probe microscopy. *Journal of Applied Physics*, 93(12):10035–10040, 2003.
- [230] A. Schwarzman, E. Grunbaum, E. Strassburg, E. Lepkifker, A. Boag, Y. Rosenwaks, T. Glatzel, Z. Barkay, M. Mazzer, and K. Barnham. Nanoscale potential distribution across multiquantum well structures: Kelvin probe force microscopy and secondary electron imaging. *Journal of Applied Physics*, 98(8):–, 2005.
- [231] R. Baier, C. Leendertz, M. C. Lux-Steiner, and S. Sadewasser. Toward quantitative Kelvin probe force microscopy of nanoscale potential distributions. *Physical Review B*, 85(16), 2012.
- [232] H. R. Moutinho, R. G. Dhere, C. S. Jiang, Y. F. Yan, D. S. Albin, and M. M. Al-Jassim. Investigation of potential and electric field profiles in cross sections of CdTe/CdS solar cells using scanning Kelvin probe microscopy. *Journal of Applied Physics*, 108(7):074503, 2010.
- [233] M. Hafemeister, S. Siebentritt, J. Albert, M. C. Lux-Steiner, and S. Sadewasser. Large neutral barrier at grain boundaries in chalcopyrite thin films. *Physical Review Letters*, 104(19), 2010.
- [234] Masaki Takihara, Takashi Minemoto, Youichi Wakisaka, and Takuji Takahashi. An investigation of band profile around the grain boundary of Cu(In,Ga)Se₂ solar cell material by scanning probe microscopy. *Progress in Photovoltaics: Research and Applications*, 21(4):595–599, 2013.

- [235] S. S. Schmidt, D. Abou-Ras, S. Sadewasser, W. Yin, C. Feng, and Y. Yan. Electrostatic potentials at Cu(In,Ga)Se₂ grain boundaries: Experiment and simulations. *Physical Review Letters*, 109(9):095506, 2012. PRL.
- [236] H. Mönig, Y. Smith, R. Caballero, C. A. Kaufmann, I. Lauermann, M. Ch Lux-Steiner, and S. Sadewasser. Direct evidence for a reduced density of deep level defects at grain boundaries of CuGaSe₂ thin films. *Physical Review Letters*, 105(11):116802, 2010. PRL.
- [237] M. K. Herndon, A. Gupta, V. Kaydanov, and R. T. Collins. Evidence for grain-boundary-assisted diffusion of sulfur in polycrystalline CdS/CdTe heterojunctions. *Applied Physics Letters*, 75(22):3503–3505, 1999.
- [238] A. A. McDaniel, J. W. P. Hsu, and A. M. Gabor. Near-field scanning optical microscopy studies of Cu(In,Ga)Se₂ solar cells. *Applied Physics Letters*, 70(26):3555–3557, 1997. McDaniel, AA Hsu, JWP Gabor, AM.
- [239] M. J. Romero, K. Alberi, I. T. Martin, K. M. Jones, D. L. Young, Y. Yan, C. Teplin, M. M. Al-Jassim, P. Stradins, and H. M. Branz. Nanoscale measurements of local junction breakdown in epitaxial film silicon solar cells. *Appl. Phys. Lett.*, 97(9):092107, 2010.
- [240] K. Bittkau and T. Beckers. Near-field study of light scattering at rough interfaces of a-si:h/mu c-si:h tandem solar cells. *Physica Status Solidi a-Applications and Materials Science*, 207(3):661–666, 2010.
- [241] W. Bao, M. Staffaroni, J. Bokor, M. B. Salmeron, E. Yablonovitch, S. Cabrini, A. Weber-Bargioni, and P.J. Schuck. Plasmonic near-field probes: a comparison of the campanile geometry with other sharp tips. *Optics Express*, 21(7):8166–8176, 2013.
- [242] P. J. Schuck, A. Weber-Bargioni, P. D. Ashby, D. F. Ogletree, A. Schwartzberg, and S. Cabrini. Life beyond diffraction: Opening new routes to materials characterization with next-generation optical near-field approaches. *Advanced Functional Materials*, 23(20):2539–2553, 2013.
- [243] R. D. Berger, Weber A.L, and Stefan A. L. Electrical characterization of organic solar cell materials based on scanning force microscopy. *European Polymer Journal*, 49(8):1907–1915, 2013.
- [244] A. Castaldini, D. Cavalcoli, A. Cavallini, and M. Rossi. Scanning Kelvin probe and surface photovoltage analysis of multicrystalline silicon. *Materials Science and Engineering: B*, 91-92(0):234–238, 2002.
- [245] Q. Chen, H. Zhou, T.-B. Song, S. Luo, Z. Hong, H.-S. Duan, L. Dou, Y. Liu, and Y. Yang. Controllable self-induced passivation of hybrid lead iodide perovskites toward high performance solar cells. *Nano Letters*, 14(7):4158–4163, 2014.

- [246] M. Chiesa, L. Bürgi, J.-S. Kim, R. Shikler, R. H. Friend, and H. Sirringhaus. Correlation between surface photovoltage and blend morphology in polyfluorene-based photodiodes. *Nano Letters*, 5(4):559–563, 2005.
- [247] J. Heo and S. Won. Scanning probe study on the photovoltaic characteristics of a si solar cell by using Kelvin force microscopy and photoconductive atomic force microscopy. *Thin Solid Films*, 546(0):353–357, 2013.
- [248] C. S. Jiang, H. R. Moutinho, R. G. Dhere, and M. M. Al-Jassim. The nanometer-resolution local electrical potential and resistance mapping of CdTe thin films. *IEEE Journal of Photovoltaics*, 3(4):1383–1388, 2013.
- [249] C.-S. Jiang, R. Noufi, K. Ramanathan, H. R. Moutinho, and M. M. Al-Jassim. Electrical modification in Cu(In,Ga)Se₂ thin films by chemical bath deposition process of cds films. *Journal of Applied Physics*, 97(5):053701, 2005.
- [250] M. Salvador, S. M. Vorpahl, H. Xin, W. Williamson, G. Shao, D.s U. Karatay, H. W. Hillhouse, and D. S. Ginger. Nanoscale surface potential variation correlates with local S/Se ratio in solution-processed CZTSSe solar cells. *Nano Letters*, 14(12):6926–6930, 2014.
- [251] C. Yang, Y. Pyekh, and S. Danyluk. Surface potential imaging of PV cells with a Kelvin probe. *Solar Energy Materials and Solar Cells*, 102(0):167–172, 2012.
- [252] C. Loppacher, U. Zerweck, S. Teich, E. Beyreuther, T. Otto, S. Grafström, and L. M. Eng. FM demodulated Kelvin probe force microscopy for surface photovoltage tracking. *Nanotechnology*, 16(3):S1, 2005.
- [253] W. Bergbauer, T. Lutz, W. Frammelsberger, and G. Benstetter. Kelvin probe force microscopy - an appropriate tool for the electrical characterisation of LED heterostructures. *Microelectronics Reliability*, 46(911):1736–1740, 2006.
- [254] M. S. Carpenter, M. R. Melloch, M. S. Lundstrom, and S. P. Tobin. Effects of Na₂S and (NH₄)₂S edge passivation treatments on the dark current-voltage characteristics of GaAs *p-n* diodes. *Applied Physics Letters*, 52(25):2157–2159, 1988.
- [255] S. Barbet, M. Popoff, H. Diesinger, D. Deresmes, D. Theron, and T. Melin. Cross-talk artefacts in Kelvin probe force microscopy imaging: A comprehensive study. *Journal of Applied Physics*, 115(144313):1–11, 2014.
- [256] H. O. Jacobs, P. Leuchtmann, O. J. Homan, and A. Stemmer. Resolution and contrast in Kelvin probe force microscopy. *Journal of Applied Physics*, 84(3):1168–1173, 1998.
- [257] U. Zerweck, C. Loppacher, T. Otto, S. Grafström, and L. M. Eng. Accuracy and resolution limits of Kelvin probe force microscopy. *Physical Review B*, 71(12):125424, 2005.

- [258] R. Garca and A. San Paulo. Attractive and repulsive tip-sample interaction regimes in tapping-mode atomic force microscopy. *Physical Review B*, 60(7):4961–4967, 1999.
- [259] S. Sadewasser and T. Glatzel. *Kelvin Probe Force Microscopy: Measuring and Compensating Electrostatic Forces*. Springer, 2011.
- [260] S. Hormeño, M. Penedo, C. V. Manzano, and M. Luna. Gold nanoparticle coated silicon tips for Kelvin probe force microscopy in air. *Nanotechnology*, 24(39):395701, 2013.
- [261] M. Cohen, R. Shavit, and Z. Zalevsky. Observing optical plasmons on a single nanometer scale. *Scientific Reports*, 4, 2014.
- [262] M. A. Green, A. Ho-Baillie, and H. J. Snaith. The emergence of perovskite solar cells. *Nature Photonics*, 8(7):506–514, 2014.
- [263] T. M. Brenner, D. A. Egger, L. Kronik, G. Hodes, and D. Cahen. Hybrid organic-inorganic perovskites: low-cost semiconductors with intriguing charge-transport properties. *Nature Reviews Materials*, 1:15007, 2016.
- [264] P. Gao, M. Grätzel, and M. K. Nazeeruddin. Organohalide lead perovskites for photovoltaic applications. *Energy & Environmental Science*, 7(8):2448–2463, 2014.
- [265] M. Sessolo and H. J. Bolink. Perovskite solar cells join the major league. *Science*, 350(6263):917–917, 2015.
- [266] J. P. Mailoa, C. D. Bailie, E. C. Johlin, E. T. Hoke, A. J. Akey, W. H. Nguyen, M. D. McGehee, and T. Buonassisi. A 2-terminal perovskite/silicon multijunction solar cell enabled by a silicon tunnel junction. *Applied Physics Letters*, 106(12):121105, 2015.
- [267] C. D. Bailie, M. G. Christoforo, J. P. Mailoa, A. R. Bowring, E. L. Unger, W. H. Nguyen, J. Burschka, N. Pellet, J. Z. Lee, M. Grätzel, R. Noufi, T. Buonassisi, A. Salleo, and M. D. McGehee. Semi-transparent perovskite solar cells for tandems with silicon and CIGS. *Energy & Environmental Science*, 8(3):956–963, 2015.
- [268] D. Shi, V. Adinolfi, R. Comin, M. Yuan, E. Alarousu, A. Buin, Y. Chen, S. Hoogland, A. Rothenberger, K. Katsiev, Y. Losovyj, X. Zhang, P. A. Dowben, O. F. Mohammed, E. H. Sargent, and O. M. Bakr. Low trap-state density and long carrier diffusion in organolead trihalide perovskite single crystals. *Science*, 347(6221):519–522, 2015.
- [269] Q. Dong, Y. Fang, Y. Shao, P. Mulligan, J. Qiu, L. Cao, and J. Huang. Electron-hole diffusion lengths $> 175 \mu\text{m}$ in solution-grown $\text{CH}_3\text{NH}_3\text{PbI}_3$ single crystals. *Science*, 347(6225):967–970, 2015.

- [270] G. Niu, X. Guo, and L. Wang. Review of recent progress in chemical stability of perovskite solar cells. *Journal of Materials Chemistry A*, 3(17):8970–8980, 2015.
- [271] J. You, L. Meng, T.-B. Song, T.-F. Guo, Y. M. Yang, W.-H. Chang, Z. Hong, H. Chen, H. Zhou, and Q. Chen. Improved air stability of perovskite solar cells via solution-processed metal oxide transport layers. *Nature nanotechnology*, 11(1):75–81, 2016.
- [272] H. J. Snaith, A. Abate, J. M. Ball, G. E. Eperon, T. Leijtens, N. K. Noel, S. D. Stranks, J. T.-W. Wang, K. Wojciechowski, and W. Zhang. Anomalous hysteresis in perovskite solar cells. *The journal of physical chemistry letters*, 5(9):1511–1515, 2014.
- [273] W. Qiu, U. W. Paetzold, R. Gehlhaar, V. Smirnov, H.-G. Boyen, J. G. Tait, B. Conings, W. Zhang, C. B. Nielsen, I. McCulloch, L. Froyen, P. Heremans, and D. Cheyns. An electron beam evaporated TiO₂ layer for high efficiency planar perovskite solar cells on flexible polyethylene terephthalate substrates. *Journal of Materials Chemistry A*, 2015.
- [274] D. W. de Quilletes, S. M. Vorpahl, S. D. Stranks, H. Nagaoka, G. E. Eperon, M. E. Ziffer, H. J. Snaith, and D. S. Ginger. Impact of microstructure on local carrier lifetime in perovskite solar cells. *Science*, 348(6235):683–686, 2015.
- [275] Y. Kutes, L. Ye, Y. Zhou, S. Pang, B. D. Huey, and N. P. Padture. Direct observation of ferroelectric domains in solution-processed CH₃NH₃PbI₃ perovskite thin films. *The Journal of Physical Chemistry Letters*, 5(19):3335–3339, 2014.
- [276] J. Beilsten-Edmands, G. E. Eperon, R. D. Johnson, H. J. Snaith, and P. G. Radaelli. Non-ferroelectric nature of the conductance hysteresis in CH₃NH₃PbI₃ perovskite-based photovoltaic devices. *Applied Physics Letters*, 106(17):173502, 2015.
- [277] V. W. Bergmann, Yu. Guo, H. Tanaka, I. M. Hermes, D. Li, A. Klasen, S. A. Bretschneider, E. Nakamura, R.r Berger, and S.A.L. Weber. Local time-dependent charging in a perovskite solar cell. *ACS applied materials & interfaces*, 8(30):19402–19409, 2016.
- [278] U. Zerweck, C. Loppacher, T. Otto, S. Grafström, and L. M Eng. Accuracy and resolution limits of Kelvin probe force microscopy. *Physical Review B*, 71(12):125424, 2005.
- [279] J. M. R. Weaver and D. W. Abraham. High resolution atomic force microscopy potentiometry. *Journal of Vacuum Science & Technology B: Microelectronics and Nanometer Structures Processing, Measurement, and Phenomena*, 9(3):1559–1561, 1991.

- [280] C.-S. Jiang, M. Yang, Y. Zhou, B. To, S. U. Nanayakkara, J. M. Luther, W. Zhou, J. J. Berry, J. van de Lagemaat, N. P. Padture, K. Zhu, and M. M. Al-Jassim. Carrier separation and transport in perovskite solar cells studied by nanometre-scale profiling of electrical potential. *Nature Communications*, 6:8397, 2015.
- [281] Z. Xiao, Y. Yuan, Y. Shao, Q. Wang, Q. Dong, C. Bi, P. Sharma, A. Gruverman, and J. Huang. Giant switchable photovoltaic effect in organometal trihalide perovskite devices. *Nature Materials*, 14(2):193–198, 2015.
- [282] R. Sheng, A. W. Y. Ho-Baillie, S. Huang, M. Keevers, X. Hao, L. Jiang, Y.-B. Cheng, and M. A. Green. Four-terminal tandem solar cells using $\text{CH}_3\text{NH}_3\text{PbBr}_3$ by spectrum splitting. *The journal of physical chemistry letters*, 6(19):3931–3934, 2015.
- [283] Z. Xiao, C. Bi, Y. Shao, Q. Dong, Q. Wang, Y. Yuan, C. Wang, Y. Gao, and J. Huang. Efficient, high yield perovskite photovoltaic devices grown by interdiffusion of solution-processed precursor stacking layers. *Energy & Environmental Science*, 7(8):2619–2623, 2014.
- [284] H.-B. Kim, H. Choi, J. Jeong, S. Kim, B. Walker, S. Song, and J. Y. Kim. Mixed solvents for the optimization of morphology in solution-processed, inverted-type perovskite/fullerene hybrid solar cells. *Nanoscale*, 6(12):6679–6683, 2014.
- [285] W. Shenghao, S. Takeaki, K. Ryusuke, and A. Katsuhiko. Energy level alignment of C_{60} / Ca interface with bathocuproine as an interlayer studied by ultraviolet photoelectron spectroscopy. *Japanese Journal of Applied Physics*, 51(10S):10NE32, 2012.
- [286] I. Eiji and S. Toshiki. Relationship between work function of hole collection electrode and temperature dependence of open-circuit voltage in multilayered organic solar cells. *Japanese Journal of Applied Physics*, 51(2S):02BK14, 2012.
- [287] J.-Y. Jeng, Y.-F. Chiang, M.-H. Lee, S.-R. Peng, T.-F. Guo, P. Chen, and T.-C. Wen. $\text{CH}_3\text{NH}_3\text{PbI}_3$ perovskite/fullerene planar-heterojunction hybrid solar cells. *Advanced Materials*, 25(27):3727–3732, 2013.
- [288] M. Hu, C. Bi, Y. Yuan, Z. Xiao, Q. Dong, Y. Shao, and J. Huang. Distinct exciton dissociation behavior of organolead trihalide perovskite and excitonic semiconductors studied in the same system. *Small*, 11(18):2164–2169, 2015.
- [289] Y. Sugawara, L. Kou, Z. Ma, T. Kamijo, Y. Naitoh, and Y. Jun Li. High potential sensitivity in heterodyne amplitude-modulation Kelvin probe force microscopy. *Applied Physics Letters*, 100(22):223104, 2012.
- [290] S. Jesse, N. Balke, E. Eliseev, A. Tselev, N. J. Dudney, A. N. Morozovska, and S. V. Kalinin. Direct mapping of ionic transport in a Si anode on the

- nanoscale: time domain electrochemical strain spectroscopy study. *ACS Nano*, 5(12):9682–9695, 2011.
- [291] A. Kumar, T. M. Arruda, A. Tselev, I. N. Ivanov, J. S. Lawton, T. A. Zawodzinski, O. Butyaev, S. Zayats, S. n Jesse, and S. V. Kalinin. Nanometer-scale mapping of irreversible electrochemical nucleation processes on solid lithium electrolytes. *Scientific Reports*, 3:1621, 2013.
- [292] N. Balke, S. Jesse, A. N. Morozovska, E. Eliseev, D. W. Chung, Y. Kim, L. Adamczyk, R. E. Garcia, N. Dudney, and S. V. Kalinin. Nanoscale mapping of ion diffusion in a lithium-ion battery cathode. *Nature Nanotechnology*, 5(10):749–754, 2010.
- [293] J. D. Adams, B. W. Erickson, J. Grossenbacher, J. Brugger, A. Nievergelt, and G. E. Fantner. Harnessing the damping properties of materials for high-speed atomic force microscopy. *Nature Nanotechnology*, 11(2):147–151, 2016.
- [294] T. Ando, N. Kodera, E. Takai, D. Maruyama, K. Saito, and A. Toda. A high-speed atomic force microscope for studying biological macromolecules. *Proceedings of the National Academy of Sciences*, 98(22):12468–12472, 2001.
- [295] Milan Sonka, Vaclav Hlavac, and Roger Boyle. *Image Processing, Analysis, and Machine Vision, 4th Edition*. 2015.
- [296] Y. Deng, Z. Xiao, and J. Huang. Light-induced self-poling effect on organometal trihalide perovskite solar cells for increased device efficiency and stability. *Advanced Energy Materials*, 5(20), 2015.
- [297] J. Yang, B. D. Siempelkamp, D. Liu, and T. L. Kelly. Investigation of $\text{CH}_3\text{NH}_3\text{PbI}_3$ degradation rates and mechanisms in controlled humidity environments using in situ techniques. *ACS Nano*, 9(2):1955–1963, 2015.
- [298] E. Strelcov, A. Belianinov, Y.-H. Hsieh, S. Jesse, A. P. Baddorf, Y.-H. Chu, and S. V. Kalinin. Deep data analysis of conductive phenomena on complex oxide interfaces: Physics from data mining. *ACS Nano*, 8(6):6449–6457, 2014.
- [299] R. Gottesman, E. Haltzi, L. Gouda, S. Tirosh, Y. Bouhadana, A. Zaban, E. Mosconi, and F. De Angelis. Extremely slow photoconductivity response of $\text{CH}_3\text{NH}_3\text{PbI}_3$ perovskites suggesting structural changes under working conditions. *The journal of physical chemistry letters*, 5(15):2662–2669, 2014.
- [300] J. M. Frost, K. T. Butler, F. Brivio, C. H. Hendon, M. Van Schilfgaarde, and A. Walsh. Atomistic origins of high-performance in hybrid halide perovskite solar cells. *Nano Letters*, 14(5):2584–2590, 2014.
- [301] T. Leijtens, S. D. Stranks, G. E. Eperon, R. Lindblad, E. M. J. Johansson, I. J. McPherson, H. Rensmo, J. M. Ball, M. M. Lee, and H. J. Snaith. Electronic properties of meso-superstructured and planar organometal halide

- perovskite films: Charge trapping, photodoping, and carrier mobility. *ACS Nano*, 8(7):7147–7155, 2014.
- [302] Durmus U. Karatay, Jeffrey S. Harrison, Micah S. Glaz, Rajiv Giridharagopal, and David S. Ginger. Fast time-resolved electrostatic force microscopy: Achieving sub-cycle time resolution. *Review of Scientific Instruments*, 87(5):053702, 2016.
- [303] J. Murawski, T. Graupner, P. Milde, R. Raupach, U. Zerweck-Trogisch, and L. M. Eng. Pump-probe Kelvin-probe force microscopy: Principle of operation and resolution limits. *Journal of Applied Physics*, 118(15):154302, 2015.
- [304] J. P. Correa-Baena, A. Abate, M. Saliba, W. Tress, T. J. Jacobsson, M. Gratzel, and A. Hagfeldt. The rapid evolution of highly efficient perovskite solar cells. *Energy & Environmental Science*, 10(3):710–727, 2017.
- [305] W. S. Yang, B.-W. Park, E. H. Jung, N. J. Jeon, Y. C. Kim, D. U. Lee, S. S. Shin, J. Seo, E. K. Kim, J. H. Noh, and S. I. Seok. Iodide management in formamidinium-lead-halide-based perovskite layers for efficient solar cells. *Science*, 356(6345):1376–1379, 2017.
- [306] Y.-L. Wu, D. Yan, J. Peng, T. Duong, Y. Wan, S. P. Phang, H. Shen, N. Wu, C. Barugkin, X. Fu, S. Surve, D. Grant, D. Walter, T. P. White, K. R. Catchpole, and K. J. Weber. Monolithic perovskite/silicon-homojunction tandem solar cell with over 22% efficiency. *Energy & Environmental Science*, 10:2472–2479, 2017.
- [307] J. Peng, Y. Wu, W. Ye, D. A. Jacobs, H. Shen, X. Fu, Y. Wan, T. Duong, N. Wu, C. Barugkin, H. T. Nguyen, D. Zhong, J. Li, T. Lu, Y. Liu, M. N. Lockrey, K. J. Weber, K. R. Catchpole, and T. P. White. Interface passivation using ultrathin polymer-fullerene films for high-efficiency perovskite solar cells with negligible hysteresis. *Energy & Environmental Science*, 10(8):1792–1800, 2017.
- [308] Z. Wang, Q. Lin, F. P. Chmiel, N. Sakai, L. M. Herz, and H. J. Snaith. Efficient ambient-air-stable solar cells with 2D3D heterostructured butylammonium-caesium-formamidinium lead halide perovskites. *Nature Energy*, 6:17135, 2017.
- [309] M. He, B. Li, X. Cui, B. Jiang, Y. He, Y. Chen, D. O’Neil, P. Szymanski, M. A. Ei-Sayed, J. Huang, and Z. Lin. Meniscus-assisted solution printing of large-grained perovskite films for high-efficiency solar cells. *Nature Communications*, 8:16045, 2017.
- [310] R. Brenes, D. Guo, A. Osherov, N. K. Noel, C. Eames, E. M. Hutter, S. K. Pathak, F. Niroui, R. H. Friend, M. S. Islam, H. J. Snaith, V. Bulović, T. J. Savenije, and S. D. Stranks. Metal halide perovskite polycrystalline films exhibiting properties of single crystals. *Joule*, 1(1):155–167, 2017.

- [311] A. Ummadisingu, L. Steier, J.-Y. Seo, T. Matsui, A. Abate, W. Tress, and M. Grätzel. The effect of illumination on the formation of metal halide perovskite films. *Nature*, 545(7653):208–212, 2017.
- [312] C. Eames, J. M. Frost, P. R. F. Barnes, B. C. O'Regan, A. Walsh, and M. S. Islam. Ionic transport in hybrid lead iodide perovskite solar cells. *Nature Communications*, 6:7497, 2015.
- [313] S. J. Yoon, S. Draguta, J. S. Manser, O. Sharia, W. F. Schneider, M. Kuno, and P. V. Kamat. Tracking iodide and bromide ion segregation in mixed halide lead perovskites during photoirradiation. *ACS Energy Letters*, 1(1):290–296, 2016.
- [314] Z. Li, C. Xiao, Y. Yang, S. P. Harvey, D. H. Kim, J. A. Christians, M. Yang, P. Schulz, S. U. Nanayakkara, C.-S. Jiang, J. M. Luther, J. J. Berry, M. C. Beard, M. M. Al-Jassim, and K. Zhu. Extrinsic ion migration in perovskite solar cells. *Energy & Environmental Science*, 10(5):1234–1242, 2017.
- [315] O. A. Syzgantseva, M. Saliba, M. Grätzel, and U. Rothlisberger. Stabilization of the perovskite phase of formamidinium lead triiodide by methylammonium, Cs, and/or Rb doping. *The Journal of Physical Chemistry Letters*, 8(6):1191–1196, 2017.
- [316] Q. Ma, S. Huang, S. Chen, M. Zhang, C. F. J. Lau, M. N. Lockrey, H. K. Mulmudi, Y. Shan, J. Yao, J. Zheng, X. Deng, K. Catchpole, M. A. Green, and A. W. Y. Ho-Baillie. The effect of stoichiometry on the stability of inorganic cesium lead mixed-halide perovskites solar cells. *The Journal of Physical Chemistry C*, 121(36):19642–19649, 2017.
- [317] Y. Hu, M. F. Aygüler, M. L. Petrus, T. Bein, and P. Docampo. Impact of rubidium and cesium cations on the moisture stability of multiple-cation mixed-halide perovskites. *ACS Energy Letters*, 2(10):2212–2218, 2017.
- [318] J.-W. Lee, D.-H. Kim, H.-S. Kim, S.-W. Seo, S. M. Cho, and N.-G. Park. Formamidinium and cesium hybridization for photo- and moisture-stable perovskite solar cell. *Advanced Energy Materials*, 5(20):1501310, 2015.
- [319] T. Matsui, J.-Y. Seo, M. Saliba, S. M. Zakeeruddin, and M. Grätzel. Room-temperature formation of highly crystalline multication perovskites for efficient, low-cost solar cells. *Advanced Materials*, 29(15):1606258, 2017.
- [320] M. Saliba, T. Matsui, K. Domanski, J.-Y. Seo, A. Ummadisingu, S. M. Zakeeruddin, J.-P. Correa-Baena, W. R. Tress, A. Abate, and A. Hagfeldt. Incorporation of rubidium cations into perovskite solar cells improves photovoltaic performance. *Science*, 354(6309):206–209, 2016.
- [321] M. T. Klug, A. Osherov, A. A. Haghighirad, S. D. Stranks, P. R. Brown, S. Bai, J. T. W. Wang, X. Dang, V. Bulovic, H. J. Snaith, and A. M. Belcher. Tailoring

- metal halide perovskites through metal substitution: influence on photovoltaic and material properties. *Energy & Environmental Science*, 10(1):236–246, 2017.
- [322] T. J. Jacobsson, J.-P. Correa-Baena, M. Pazoki, M. Saliba, K. Schenk, M. Grätzel, and A. Hagfeldt. Exploration of the compositional space for mixed lead halogen perovskites for high efficiency solar cells. *Energy & Environmental Science*, 9(5):1706–1724, 2016.
- [323] Y. Hu, F. Bai, X. Liu, Q. Ji, X. Miao, T. Qiu, and S. Zhang. Bismuth incorporation stabilized α -CsPbI₃ for fully inorganic perovskite solar cells. *ACS Energy Letters*, pages 2219–2227, 2017.
- [324] S. Yang, W. Fu, Z. Zhang, H. Chen, and C.-Z. Li. Recent advances in perovskite solar cells: efficiency, stability and lead-free perovskite. *Journal of Materials Chemistry A*, 5(23):11462–11482, 2017.
- [325] T. A. Berhe, W.-N. Su, C.-H. Chen, C.-J. Pan, J.-H. Cheng, H.-M. Chen, M.-C. Tsai, L.-Y. Chen, A. A. Dubale, and B.-J. Hwang. Organometal halide perovskite solar cells: degradation and stability. *Energy & Environmental Science*, 9(2):323–356, 2016.
- [326] D. P. McMeekin, G. Sadoughi, W. Rehman, G. E. Eperon, M. Saliba, M. T. Hörlantner, A. Haghighirad, N. Sakai, L. Korte, B. Rech, M. B. Johnston, L. M. Herz, and H. J. Snaith. A mixed-cation lead mixed-halide perovskite absorber for tandem solar cells. *Science*, 351(6269):151–155, 2016.
- [327] R. G. Niemann, A. G. Kontos, D. Palles, E. I. Kamitsos, A. Kaltzoglou, F. Brivio, P. Falaras, and P. J. Cameron. Halogen effects on ordering and bonding of CH₃NH₃⁺ in CH₃NH₃PbX₃ (X = Cl, Br, I) hybrid perovskites: A vibrational spectroscopic study. *The Journal of Physical Chemistry C*, 120(5):2509–2519, 2016.
- [328] M. Ledinský, P. Löper, B. Niesen, J. Holovský, S.-J. Moon, J.-H. Yum, S. De Wolf, A. Fejfar, and C. Ballif. Raman spectroscopy of organic-inorganic halide perovskites. *The Journal of Physical Chemistry Letters*, 6(3):401–406, 2015.
- [329] J. M. Azpiroz, E. Mosconi, J. Bisquert, and F. De Angelis. Defect migration in methylammonium lead iodide and its role in perovskite solar cell operation. *Energy & Environmental Science*, 8(7):2118–2127, 2015.
- [330] S. Ghosh, S. K. Pal, K. J. Karki, and T. Pullerits. Ion migration heals trapping centers in CH₃NH₃PbBr₃ perovskite. *ACS Energy Letters*, pages 2133–2139, 2017.
- [331] A. M. Tirmzi, R. P. Dwyer, T. Hanrath, and J. A. Marohn. Coupled slow and fast charge dynamics in cesium lead bromide perovskite. *ACS Energy Letters*, 2(2):488–496, 2017.

- [332] J.-P. Correa-Baena, M. Saliba, T Buonassisi, M. Grätzel, A. Abate, W. Tress, and A. Hagfeldt. Promises and challenges of perovskite solar cells. *Science*, 358(6364):739–744, 2017.
- [333] A. H. Slavney, L. Leppert, D. Bartesaghi, A. Gold-Parker, M. F. Toney, T. J. Savenije, J. B. Neaton, and H. I. Karunadasa. Defect-induced band-edge reconstruction of a bismuth-halide double perovskite for visible-light absorption. *Journal of the American Chemical Society*, 139(14):5015–5018, 2017.
- [334] T. Coenen, S. V. den Hoedt, and A. Polman. A new cathodoluminescence system for nanoscale optics, materials science, and geology. *Microscopy Today*, 24(03):12–19, 2016.
- [335] D. Abou-Ras, T. Kirchartz, and U. Rau. *Advanced Characterization Techniques for Thin Film Solar Cells*. Wiley-VCH Verlag GmbH Co, 2011.
- [336] M. Müller, S. Ribbe, T. Hempel, F. Bertram, J. Christen, W. Witte, S. Paeltel, and M. Powalla. Investigation of vertical compositional gradients in Cu(In,Ga)Se₂ by highly spatially and spectrally resolved cathodoluminescence microscopy. *Thin Solid Films*, 535(0):270–274, 2013.
- [337] V. Consonni, N. Baier, O. Robach, C. Cayron, F. Donatini, and G. Feuillet. Local band bending and grain-to-grain interaction induced strain nonuniformity in polycrystalline cdte films. *Physical Review B*, 89(3):035310, 2014.
- [338] C. G. Bischak, E. M. Sanehira, J. T. Precht, J. M. Luther, and N. S. Ginsberg. Heterogeneous charge carrier dynamics in organic-inorganic hybrid materials: Nanoscale lateral and depth-dependent variation of recombination rates in methylammonium lead halide perovskite thin films. *Nano Letters*, 15(7):4799–4807, 2015.
- [339] M. I. Dar, G. Jacopin, M. Hezam, N. Arora, S. M. Zakeeruddin, B. Deveaud, M. K. Nazeeruddin, and M. Grätzel. Asymmetric cathodoluminescence emission in CH₃NH₃PbI_{3-x}Br_x perovskite single crystals. *ACS Photonics*, 3(6):947–952, 2016.
- [340] H. Guthrey, S. Johnston, D. N. Weiss, S. Grover, K. Jones, A. Blossie, and M. Al-Jassim. Three-dimensional minority-carrier collection channels at shunt locations in silicon solar cells. *Solar Energy*, 135:163–168, 2016.
- [341] A. Belghachi. *Theoretical Calculation of the Efficiency Limit for Solar Cells*. InTech, 2015.
- [342] J. Sempau, E. Acosta, J. Baro, J. M. Fernandez-Varea, and F. Salvat. An algorithm for monte carlo simulation of coupled electron-photon transport. *Nuclear Instruments and Methods in Physics Research Section B: Beam Interactions with Materials and Atoms*, 132(3):377–390, 1997.

- [343] Y. Kutes, B. A. Aguirre, J. L. Bosse, J. L. Cruz-Campa, D. Zubia, and B. D. Huey. Mapping photovoltaic performance with nanoscale resolution. *Progress in Photovoltaics: Research and Applications*, 24(3):315–325, 2016.
- [344] G. E. Eperon, D. Moerman, and D. S. Ginger. Anticorrelation between local photoluminescence and photocurrent suggests variability in contact to active layer in perovskite solar cells. *ACS Nano*, 10(11):10258–10266, 2016.
- [345] S. Smith, P. Zhang, T. Gessert, and A. Mascarenhas. Near-field optical beam-induced currents in CdTe/CdS solar cells: Direct measurement of enhanced photoresponse at grain boundaries. *Applied Physics Letters*, 85(17):3854–3856, 2004.
- [346] N. M. Haegel. Integrating electron and near-field optics: Dual vision for the nanoworld. *Nanophotonics*, 3(1-2):75–89, 2014.
- [347] S. Shirakata and T. Nakada. Time-resolved photoluminescence in Cu(In,Ga)Se₂ thin films and solar cells. *Thin Solid Films*, 515(15):6151–6154, 2007.
- [348] Teodor K. Todorov, Jiang Tang, Santanu Bag, Oki Gunawan, Tayfun Gokmen, Yu Zhu, and David B. Mitzi. Beyond 11Cu₂ZnSn(S,Se)₄ solar cells. *Advanced Energy Materials*, 3(1):34–38, 2013.
- [349] V. D’Innocenzo, S. R. A. Kandada, M. De Bastiani, M. Gandini, and A. Petrozza. Tuning the light emission properties by band gap engineering in hybrid lead halide perovskite. *Journal of the American Chemical Society*, 136(51):17730–17733, 2014.
- [350] D. W. de Quilletes, S. Koch, S. Burke, R. K. Paranjy, A. J. Shropshire, M. E. Ziffer, and D. S. Ginger. Photoluminescence lifetimes exceeding 8 μ s and quantum yields exceeding 30% in hybrid perovskite thin films by ligand passivation. *ACS Energy Letters*, 1(2):438–444, 2016.
- [351] E. S. Barnard, E. T. Hoke, S. T. Connor, J. R. Groves, T. Kuykendall, Z. Yan, E. C. Samulon, E. D. Bourret-Courchesne, S. Aloni, P. J. Schuck, C. H. Peters, and B. E. Hardin. Probing carrier lifetimes in photovoltaic materials using subsurface two-photon microscopy. *Scientific Reports*, 3:2098, 2013.
- [352] W. Chen, X. Wen, M. Latzel, M. Heilmann, J. Yang, X. Dai, S. Huang, S. Shrestha, R. Patterson, S. Christiansen, and G. Conibeer. Nanoscale characterization of carrier dynamic and surface passivation in InGaN/GaN multiple quantum wells on GaN nanorods. *ACS Applied Materials & Interfaces*, 8(46):31887–31893, 2016.
- [353] A. Richter, G. Behme, M. Sptitz, Ch Lienau, T. Elsaesser, M. Ramsteiner, R. Ntzel, and K. H. Ploog. Real-space transfer and trapping of carriers into single GaAs quantum wires studied by near-field optical spectroscopy. *Physical Review Letters*, 79(11):2145–2148, 1997.

- [354] S. Chakraborty, W. Xie, N. Mathews, M. Sherburne, R. Ahuja, M. Asta, and S. G. Mhaisalkar. Rational design: A high-throughput computational screening and experimental validation methodology for lead-free and emergent hybrid perovskites. *ACS Energy Letters*, 2(4):837–845, 2017.
- [355] Z. Shi, J. Guo, Y. Chen, Q. Li, Y. Pan, H. Zhang, Y. Xia, and W. Huang. Lead-free organic-inorganic hybrid perovskites for photovoltaic applications: Recent advances and perspectives. *Advanced Materials*, 29(16):1605005, 2017.
- [356] T. Duong, Y. Wu, H. Shen, J. Peng, X. Fu, D. Jacobs, E.-C. Wang, T. C. Kho, K. C. Fong, M. Stocks, E. Franklin, A. Blakers, N. Zin, K. McIntosh, W. Li, Y.-B. Cheng, T. P. White, K. Weber, and K. Catchpole. Rubidium multication perovskite with optimized bandgap for perovskite-silicon tandem with over 26% efficiency. *Advanced Energy Materials*, page 1700228, 2017.
- [357] S. V. Kalinin, B. G. Sumpter, and R. K. Archibald. Big-deep-smart data in imaging for guiding materials design. *Nature Materials*, 14(10):973–980, 2015.
- [358] S. Jesse and S. V. Kalinin. Principal component and spatial correlation analysis of spectroscopic-imaging data in scanningprobe microscopy. *Nanotechnology*, 20(8):085714, 2009.